Properties of Iron-Sulfur Clusters in Heterodisulfide Reductase

by

Carly Engel

A dissertation submitted to the Graduate Faculty of
Auburn University
in partial fulfillment of the
requirements for the Degree of
Doctor of Philosophy

Auburn, Alabama
August 3, 2019

Keywords: heterodisulfide reductase, iron-sulfur clusters, electron paramagnetic resonance,
redox studies, rapid freeze quench

Approved by

Evert Duin, Chair, Professor of Biochemistry
Doug Goodwin, Associate Professor of Biochemistry
Holly Ellis, William P. Molette Professor of Biochemistry
Anne Gorden, Associate Professor of Chemistry
Robert Pantazes, Assistant Professor of Chemical Engineering

Abstract

Global warming is a continuing crisis today. It has caused great damage to our planet and health. One of the leading causes of this issue originates from humans releasing an enormous amount of greenhouse gases into the air, in particular CO_2 and CH_4. Infrared radiation produced by the sun become trapped by these molecules and, therefore, increases the Earth's temperature drastically. Ultimately, the source of most of the CH_4 is biological. One enzyme known to aid in the production of methane is heterodisulfide reductase (Hdr). Hdr recycles the substrates used by the enzyme that catalyzes the methane formation. In addition, reduced ferredoxin (Fd^{RED}) is produced and used to push the first step in methanogenesis. The goal of this research is to understand the role of the cofactors, iron-sulfur clusters, and flavin adenine dinucleotide (FAD) in catalysis, with emphasis on the flavin-based electron bifurcation process and heterodisulfide (HDS) reduction.

Redox titrations of methyl-viologen hydrogenase: heterodisulfide reductase (Mvh:Hdr) yielded multiple midpoint potentials for different $[4Fe\text{-}4S]^+$ and $[2Fe\text{-}2S]^+$ clusters. In addition, rapid freeze quench was performed on the whole complex. This allowed the detection of several redox active species, calculation of midpoint potential (E_m), and the development of a model of Hdr with assignment of electron paramagnetic resonance (EPR) signal and E_m values to specific cofactors in the Hdr complex. Due to the presence of a total of 14 clusters it was not always possible to discern individual signals in the whole Mvh:Hdr complex. Therefore, similar experiments were executed on the isolated HdrB, and HdrBC subunits.

The HdrB subunit is the site of the HDS reduction. HdrB2 and HdrB2C2 were cloned by Dr. James "Greg" Ferry's group from *Methanosarcina acetivorans* into *Escherchia coli*. Two non-cuboidal clusters were expected in the HdrB subunit. Our preparation contained one [2Fe-2S] cluster and one non-cuboidal [4Fe-4S] cluster. Through further site-directed mutagenesis both sites could be studied separately. The data showed that the non-cuboidal [4Fe-4S] clusters do not show a 1+/2+ transition. In the presence of substrate, a 2+/3+ transition is detected. Surprisingly the HdrB2 and HdrB2C2 preparations are active although only one non-cuboidal cluster is present.

Table of Contents

List of Tables

List of Figures

List of Schemes

List of Equations

List of Abbreviations

Fmd	Formylmethanofuran dehydrogenase
H_4MPT	Tetrahydromethanopterin
Ftr	Formylmethanofuran: H_4MPT formyltransferase
Mch	Methenyl-H_4MPT cyclohydrolase
Hmd	H_2-forming methylene-H_4MPT dehydrogenase
Mer	F_{420}-dependent methylene-H_4MPT reductase
CoM	Coenzyme M
Mtr	Methyl-H_4MPT: CoM methyltransferase
Mcr	Methyl-CoM reductase
Hdr	Heterodisulfide reductase
CoB	Coenzyme B
HDS	Heterodisulfide
EPR	Electron paramagnetic resonance
kHz	Kilohertz
mV	Millivolts
ms	Milliseconds
Nif	Nitrogen fixation
Isc	Iron-sulfur cluster
Suf	Sulfur utilization factor
mT	Millitesla

NHE	Normal hydrogen electrode
FAD	Flavin adenine dinucleotide
NAD	Nicotinamide adenine dinucleotide
M. marburgensis	*Methanothemobacter marburgensis*
M. maripaludis	*Methanococcus maripaludis*
Ferredoxin	Fd
E. coli	*Escherichia coli*
WT	Wild-Type

Chapter 1: Literature Review

1.1 Methanogens

What are known as extremophiles, methanogens were believed to be one of the few organisms that lived on Earth billions of years ago when oxygen was absent.[1] Originally, methanogens were classified in the phylum *Euryarchaeota* and put into five orders: *Methanococcales, Methanobacteriales, Methanosarcinales, Methanomicrobiales,* and *Methanopyrales*.[2] Later, between 2008-2012, two other orders, *Methanocellales* and *Methanomassiliicoccales*, were discovered.[2] Though CO_2 is a main electron acceptor source for methanogens, these orders are split into groups based on other types of organic material they utilize as alternative electron donating sources. For example, hydrogenotrophic methanogens use H_2, aceticlastic methanogens use acetate, and methylotrophic methanogens use methylated compounds such as methanol, methylamines and methylated thiols.[2] All groups of methanogens are still found in environments with little oxygen present today but are under the phylum *Archaea*. Eukaryotes and archaea are very similar to one another but discovered archaea do not contain many attributes eukaryotes contain such as a nuclear membrane, Golgi apparatus, cytoskeleton, and an endoplasmic reticulum.[3] Scientists, thus, determined archaea needed to be classified in their own group.[3]

Organisms such as these are found in extreme environments such as hydrothermal vents and saline lakes or non-extreme environments such as rice fields and the intestines of ruminal animals.[2] These organisms can even be found in human dental plaque.[2] Some of the non-natural habitants methanogens thrive in are landfills or biogas plants due to the breakdown of complex polymers and fermentation which provide the necessary organic materials for these organisms. With the diverse habitats methanogens cultivate in, they require different growth conditions.[2] Most are mesophilic organisms (*Methanosarcina, Methanobacterium,* and *Methanococcus*) but there are

some which are thermophilic and hyperthermophilic (*Methanothermobacter thermautotrophicus and Methanocaldococcus jannaschii*) that can grow in temperatures up to 75-86°C.[2] For the high salt environments, these organisms prevent themselves from dying using two methods: 1) synthesizing glutamate when NaCl concentrations reach 400 mM and N-acetyl-β-lysine along with glutamate when NaCl concentrations reach 800 mM or 2) influxing potassium and chloride into the cytoplasm.[2] Lastly, the different pH levels in the habitats of methanogens are different from one another as well. Most methanogens grow at neutral pH; however, *Methanocalculus alkaliphilus* and *Methanosalsum natronophilum* are the only methanogens capable of growing at a pH of 9.5 while *Methanoregula booneii* grows at a pH of 5.1. Today, researchers study methanogens to understand how they produce methane.[4–6]

Though the chemical pathway by which methanogens produce methane is known, how some of their enzymes perform this process, mechanistically, remains unknown.[7] One reason for this is the sensitivity of methanogens toward oxygen which requires elaborate methods and equipment for cultivation.[7] Another reason was the limited genetic methods available for these delicate organisms. Luckily, this has changed in the past years and model organisms, *Methanococcus maripaludis* and *Methanosarcina acetivorans*, have become ideal for genetic analysis and cloning purposes.[2] The mechanistic studies are important to develop inhibitors or convert methane into a biofuel to aid in eliminating the greenhouse effect.[8]

1.1.1 Methanogenesis

Methanogenesis is the enzymatic process in which methanogens produce methane from either CO_2, acetate, or formate.[8] CO_2 will be discussed in this section for the hydrogenotrophic mechanistic pathway of methanogenesis.[9] The pathway starts with CO_2 being reduced by ferredoxin (Fd_{red}) to form a bond to methanofuran (**1**) by formylmethanofuran dehydrogenase

(**Fmd**) to create formyl-methanofuran (**2**).[9] Next, the formyl group is transfered to 5-formyl-tetrahydromethanopterin (H_4MPT, **3**) by formylmethanofuran: H_4MPT formyltransferase (**Ftr**) to create 5,10-methenyltetrahydromethanopterin (**4**). The formyl group is hydrolyzed to create a cyclic ring between the nearby nitrogens by methenyl-H_4MPT cyclohydrolase (**Mch**) to form 5,10-methylene-tetrahydromethanopterin (**5**).[9] This compound is then dehydrated by H_2-forming methylene-H_4 MPT dehydrogenase (**Hmd**) and reduced by F_{420}-dependent methylene-H_4MPT reductase (**Mer**) using reduced F_{420} (F_{420}^{red}) to synthesize N^5-methyltetrahydromethanopterin (**6**) and tetrahydromethanopterin (**7**) respectively. The methyl group is transferred to coenzyme M (CoM, **8**) by methyl-H_4 MPT: coenzyme M methyltransferase (**Mtr**) to generate methyl-CoM (**9**). This methyl group is then reduced by methyl-coenzyme M reductase (**Mcr**) to form methane and heterodisulfide (HDS, CoM-S-S-CoB; **11**).[9] Lastly, and possibly the most important step, compound **11** is reduced by heterodisulfide reductase (**Hdr**) to recreate compounds **8** and **10.**

The reduction of HDS back to CoM and CoB is probably the most important step in this process. As a result, the substrates are replenished to begin the methanogenesis process over again. In addition, some methanogens contain Hdr and Fmd as one complex allowing direct transfer of electrons between the two reactions.[10] If this step failed to occur during methanogenesis, CoM would not be available for **Mtr** to methylate and methane would not be created by **Mcr**. Thauer came up with the name "Wolfe Cycle" which implies methanogenesis is a cyclic process thanks to the contributions of **Hdr**.[11] Methanogens would be incapable of producing the enormous amount of methane if methanogenesis was not a cyclic process.[2,11] This proposal implicates **Hdr** as an important target for inhibition to prevent methanogens from releasing too much methane into the atmosphere.

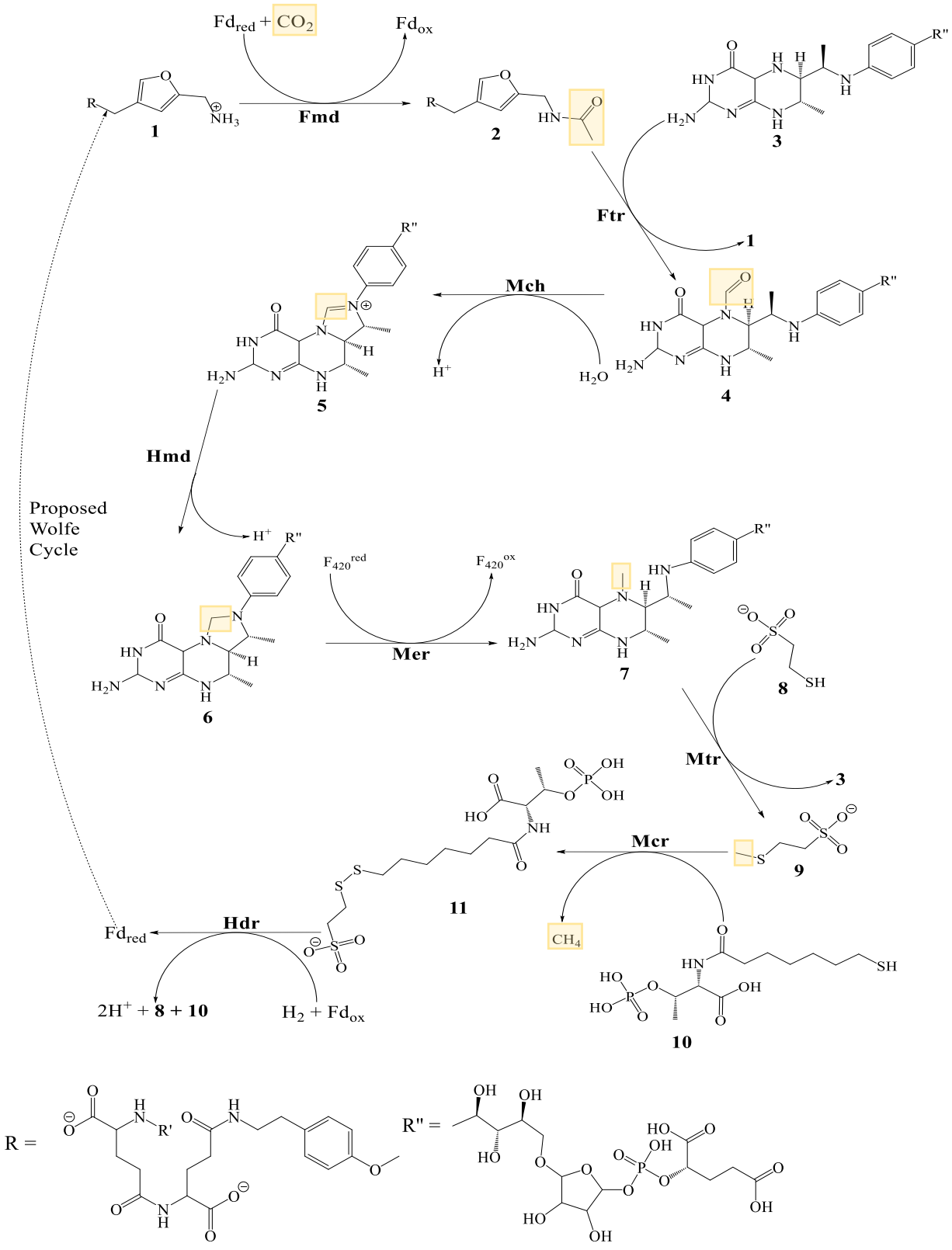

Figure 1.1: Hydrogenotrophic pathway in methanogens (See section 1.1.1 for description).[9]

1.2 Electron Paramagnetic Resonance (EPR) Spectroscopy

Iron-sulfur containing proteins are highly abundant in methanogens.[12] Iron-sulfur clusters are oxygen sensitive which makes studying these enzymes more difficult.[12] The number of instruments to study these enzymes become more selective as well. This makes EPR spectroscopy the ideal instrument to study metalloenzymes. Samples are analyzed frozen which, therefore, prevents oxygen from oxidizing the iron-sulfur clusters. This section will discuss EPR spectroscopy into further detail in how the instrument operates and the kind of experiments that can be conducted with the help of this technique.

1.2.1 History of Unpaired Electron Studies

In the 1920s, Stern and Gerlach developed an experiment to study an electron magnetic moment in an atom that can only take on discrete orientations in a magnetic field.[13] From there, Uhlenbeck and Goudsmit linked the electron magnetic moment with the concept of electron spin angular momentum using a hydrogen atom as the model.[13,14] The atom has an additional angular momentum which comes from the proton in the nucleus. Later, Breit and Rabi described the resulting energy levels of the hydrogen atom in a magnetic field and studied the transitions between levels induced by the oscillating magnetic field which became the first observation of magnetic resonance. The first resonance peak was not seen until 1945 by Zavoisky when he detected a radiofrequency absorbance line from a $CuCl_2*H_2O$ sample.[13] From then on, EPR studies grew at a rapid speed in the United States and England.[13] Pulsed spin-excitation schemes and ultra-rapid-reaction techniques became more feasible and are now commonly utilized techniques to study a vast number of elements and compounds with unpaired electrons.[13]

1.2.2 Operations of EPR

An overlay diagram of a continuous-wave EPR instrument is shown in **Figure 1.2**.[15] EPR involves studying the spin of unpaired electrons. An electron, even without outside forces, has an angular momentum (S) due to its charge. As a result, the electron acts similar to a little magnet or magnetic dipole which creates a magnetic momentum (μ).[15] When the electron is placed in an external magnetic field (B_0), its spin aligns itself with the field, known as the Zeeman effect.[16] Similar to the function of a compass, the magnetic moment aligning to the north requires energy and represents the least favorite compared to aligning to the south which requires less energy (**Figure 1.3**).[16] Utilizing quantum mechanics, the magnetic field is capable of distinguishing between these two energies (ΔE) based on the spins which assume two orientations in the external field along the z-axis, $m_s=1/2$ or $m_s=-1/2$. 'β' is the Bohr conversion factor known as the Bohr magneton and 'g_e' is the g-value of the unpaired electron equal to 2.0023. Therefore, the individual energies of the unpaired electrons can be calculated by **Equation 1.1**.[15,16] To add to the situation, at times an electron may have other outside forces influencing its spin. One common source comes from an atom or molecule which gives it some orbital momentum (L). This momentum depends greatly on the paramagnetism and the size of the nuclei interacting with the unpaired electron.[15,16] As a result, this spin-orbit changes the g-value and creates more unique and specific signals for the compounds being studied. When the electron resides in a nucleus with an electron spin, the associate field can add or subtract to the applied outside field and cause the EPR signal to split.[15,16] This is known as hyperfine. When a ligand nucleus with a nuclear spin is present, a similar split is observed, known as super hyperfine.

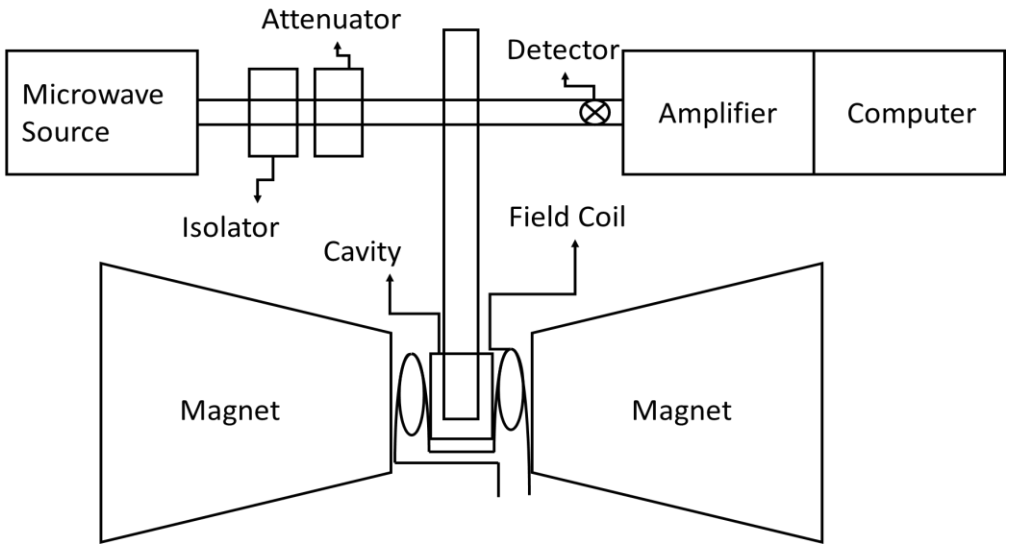

Figure 1.2: X-band EPR diagram overlay.[15]

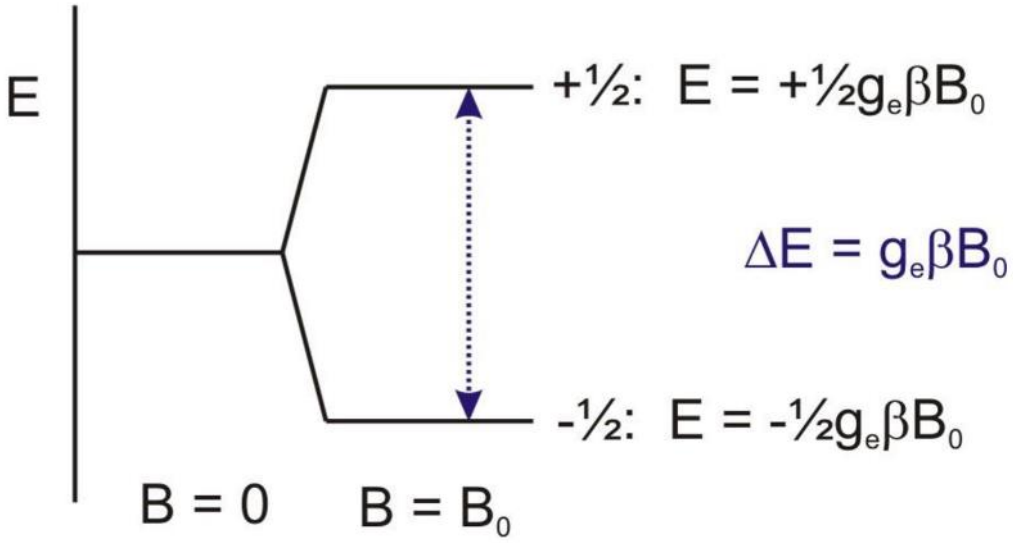

Figure 1.3: Energy diagram representing energy levels of an electron spin and the resonance condition (Adapted from Brudvig).[15,17]

$$E_1 = \frac{1}{2} g_e \beta B_0 \; ; \; E_2 = -\frac{1}{2} g_e \beta B_0$$

$$\Delta E = g_e \beta B_0$$

Equation 1.1: Energy difference calculation of an unpaired electron. ±1/2 is the spin of the electron, g_e represents the g-value of the electron/radical (2.0023), β represents the Bohr's constant, and B_0 represents the magnetic field.[15]

1.2.3 Energies Used for EPR

The most convenient energy used for EPR in inorganic and biochemistry fields is in the microwave region around 9.4 GHz, known as an X-band (**Table 1.1**). This wavelength size is similar in dimension as the internal cavity in which they resonate. In addition, this band requires a simple electromagnet and still provides high sensitivity and a feasible sample amount to work with. There are frequencies stronger in energy that are utilized for EPR. Even though stronger energies allow for a better resolution, they require smaller wavelengths which means the cavity must also be smaller. For convenience purposes, X-band EPR monitored-experiment studies were performed for this research and will be discussed in detail in later chapters.

Table 1.1: Various bandwidths and their corresponding frequency strengths of EPR instruments.

EPR Frequencies	
Band	Approximate Frequencies (GHz)
L	1
S	3
X	9.4
P	15
K	18
Q	35
W	94

1.2.4 Line Shapes of EPR Signals

EPR signals are based on absorbance but to help in the sensitivity, the first derivative is measured (**Figure 1.4**).[15] This procedure is done by modulating the magnetic field. The Helmholtz coils surrounding the sample are placed in line with the external field. These coils amplify the field to change a small amount at a set frequency (most commonly at 100 kHz) and ensues the first derivative of the signal.[15] Signals are based on the interactions of the unpaired electron and its surroundings. Four different types of signals can be found for a paramagnet with one unpaired electron which indicate the type of interactions occurring. Isotropic occurs when the g_{zyx} are all equal in value while rhombic has no g_{zyx} equal to one another. Axial shapes will have the g_{yx} equal to one another and will be greater than or less than g_z (**Figure 1.4**).[15] These shapes are the basic shapes that can be detected. The spectra become more complex when interactions with other electron species or nuclear spins are present.

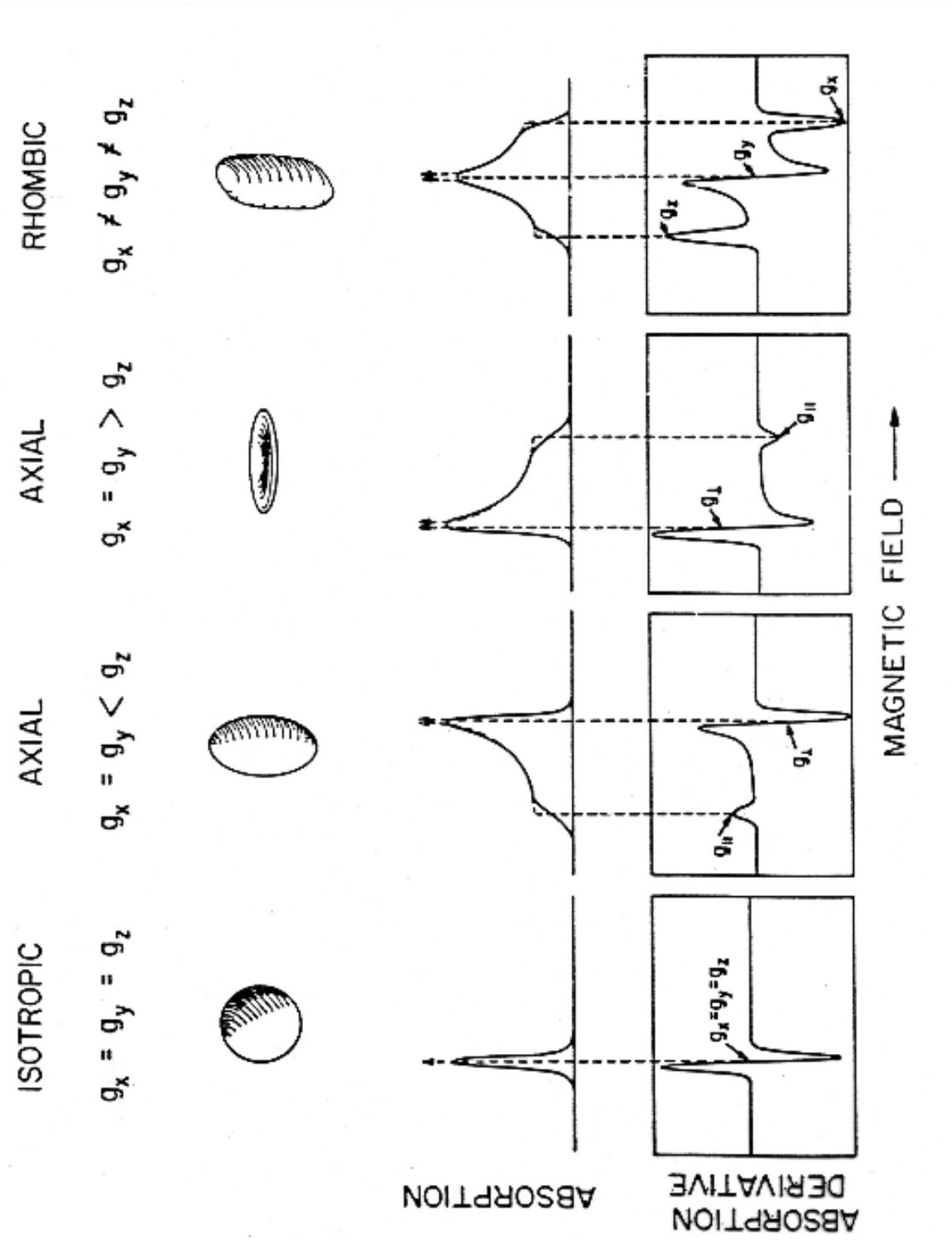

Figure 1.4: The common shapes of basic EPR signals (Adapted from Palmer).[18]

1.2.5 EPR-Monitored Experiments

Redox-active cofactors can have different redox states of which some are paramagnetic and detectable in EPR spectroscopy.[16] To access all the different possible redox states, redox titrations are performed. This experiment involves mixing the enzyme with a variety of redox dyes which stabilize the potential of the solution. A reductant or oxidant are added to change the potential in steps of 30 mV. Samples are aliquoted out and frozen in liquid nitrogen to be further analyzed by EPR.

For fast reactions, one needs fast detection and/or ways to trap signals. To study these, rapid freeze quench techniques are required to track the flow of electrons in multi-cluster (or cofactor) enzyme systems. A two-syringe setup is shown in **Figure 1.5**. This two-syringe setup contains the enzyme in one and the substrate in the other. These two solutions are mixed and guided through an incubation loop. Once the incubation time is complete, the solution is sent into a cold isopentane (-153°C) mixture to ensure the reaction halts by freezing it. These samples are packed to be analyzed by EPR. The RFQ-3 system is computerized and automatically selects one of seven aging loops and the speed of the ram, allowing reaction times of 4.6 ms and up.

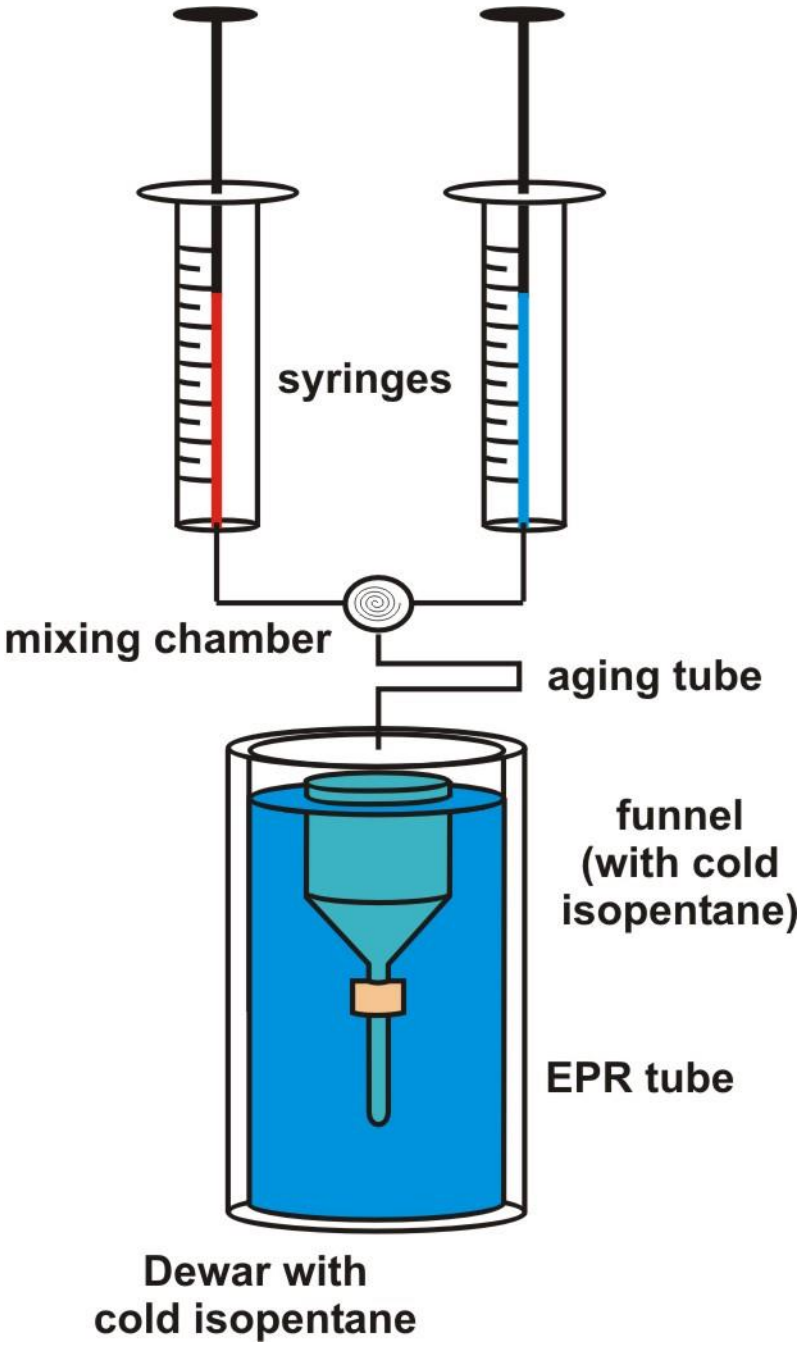

Figure 1.5: Stop flow instrument diagram. Syringe **A** contains the substrate solution while syringe **B** contains the enzyme solution. These solutions are sent through the reaction loop which incubates the mixture on a millisecond time scale and then sends this through the exit loop where the mixture is frozen instantaneously.

1.3 Iron-Sulfur Clusters

In the 1960s, scientists learned organisms did not utilize oxygen or water to survive during the times of evolution.[19] Instead, they depended on carbon sources such as methane, acetate and carbon monoxide. How this was possible was difficult to determine until studies found many organisms used iron-sulfur clusters. These clusters are formed utilizing iron cations partially coordinated to sulfide anions to form square or cuboidal shapes.[20] In proteins, the thiol group of one or more cysteine residues coordinate the Fe and S ions together. The four roles of iron-sulfur clusters in proteins are electron carrying, enzymatic catalysis, structural, and/or gene regulation.[21] In this section, details of iron-sulfur clusters will be discussed pertaining to the types of clusters formed in nature, the different amino acids which help bind these clusters together, and how redox studies provide useful information on electron transport between the clusters.

1.3.1 Initial Iron-Sulfur Cluster Studies

Nitrogenase was one of the first enzymes to help shine light on how iron-sulfur clusters are biosynthetically made. This enzyme catalyzes the nucleotide-dependent reduction of dinitrogen (nitrogen fixation).[22] Analysis of the genes in the nitrogenase's makeup was performed to understand which ones make iron-sulfur clusters and how the process is done. Studies showed NifS uses L-cysteine to mobilize the elemental S for the iron-sulfur cluster formation while NifU accommodates the formation of transient iron-sulfur clusters.[22] Since then, two other iron-sulfur cluster biosynthetic systems have been discovered: Isc and Suf. Isc (iron-sulfur cluster) aids in iron-sulfur cluster maturation whereas Suf (sulfur utilization factor) aids in the maturation when Fe is limited.[22]

1.3.2 Types of Iron-Sulfur Cluster

Figure 1.6 shows the basic forms of iron-sulfur clusters and **Table 1.2** gives the sequence motifs that identify an iron-sulfur cluster present in a protein. Typical clusters utilize cysteines to bind them in the protein. Histidines are common ligands found as alternatives for cysteines.[23] Unlike cysteine, the distal nitrogen on histidine can exist in a neutral, protonated, or a de-protonated form which enables the molecule to handle a larger range of pH levels.[23] The iron-sulfur clusters containing histidines as ligands can, as a result, contain a large range of midpoint potentials at which they are detected.

Iron-sulfur clusters accept and distribute single electrons to other iron-sulfur clusters and redox active cofactors throughout the protein due to the redox properties of these clusters.[21,23] This allows for paramagnetic studies by certain instruments which will be discussed later in this section.

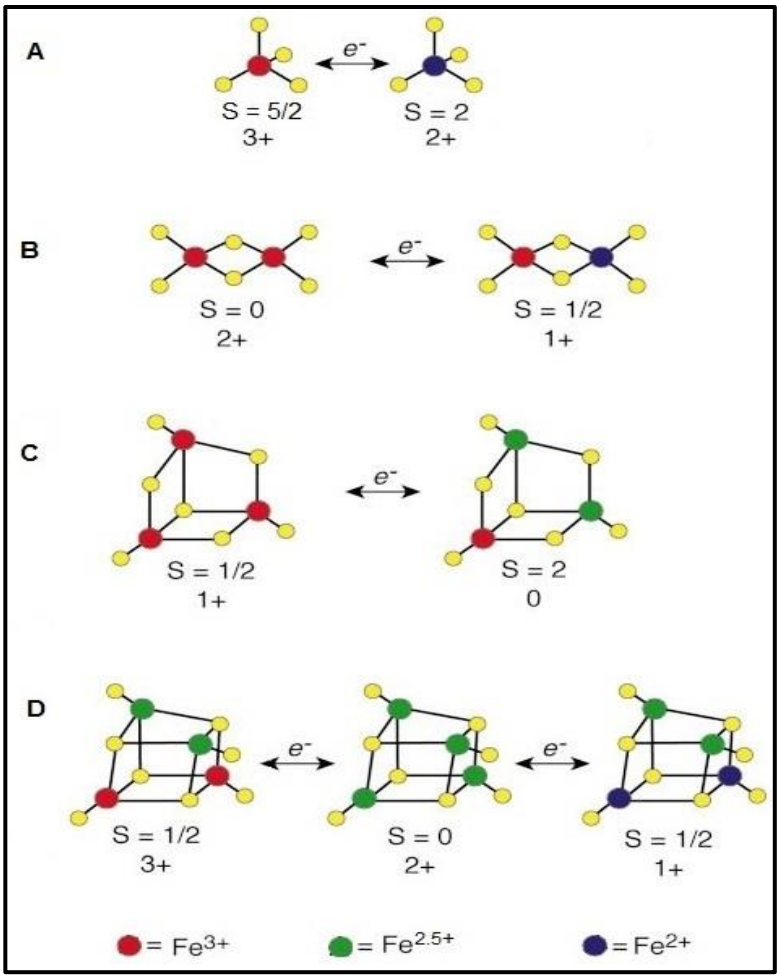

Figure 1.6: The common types of iron-sulfur clusters and their spin states at different oxidation states. [14,24]

Table 1.2: Iron-sulfur clusters and their common sequence motives.

Type of Iron-Sulfur Cluster	Sequence Motif[8]
$[2Fe\text{-}2S]^{+}$	$CX_4CX_2CX_{29}CP$
$[3Fe\text{-}4S]^{+}$	$CX_{5\text{-}7}CX_nCP$
$[4Fe\text{-}4S]^{+}$	$CX_2CX_3CX_2CP$
$[4Fe\text{-}4S]^{3+}$	$CX_2CX_{16}CX_{13}CP$

1.3.3 Breakdown of Iron-Sulfur Clusters by Molecular Oxygen

Iron-sulfur clusters are oxygen sensitive and potentially lose an iron when O_2 reacts with them.[21] This is normally detrimental to the function of the protein but it can also be used as a system to sense O_2 levels. Bacteria grow in more aerobic environments, but the mechanism of this process is still being elucidated. They found the fumarate and nitrate reduction (FNR) enzyme act as an O_2-sensing DNA-binding proteins to coordinate the switch between aerobic and anaerobic metabolism.[21] In *Escherichia coli* specifically, the $[4Fe\text{-}4S]^{2+}$ cluster of FNR converts into a $[2Fe\text{-}2S]^{2+}$ cluster when reacting with O_2. This causes a conformational change in the protein and leads to monomerization and loss of high affinity DNA binding.[21]

The first step releases Fe^{2+} to generate the $[3Fe\text{-}4S]^{1+}$ intermediate by performing a one electron oxidation of the $[4Fe\text{-}4S]^{2+}$ cluster. This yields an unstable $[4Fe\text{-}4S]^{3+}$ which causes the release of a Fe^{2+} ion. In step two, $[3Fe\text{-}4S]^{1+}$ species is unstable and does not need O_2 to convert to $[2Fe\text{-}2S]^{2+}$. The Fe^{3+} is ejected while the two sulfide ions undergo two electron oxidation to form sulfane (S^0) and react to cysteine side chains to give persulfide (RSS^-) which coordinate the [2Fe-2S] cluster.[21]

1.3.4 EPR Signals of Iron-Sulfur Clusters

Most iron-sulfur clusters have rhombic EPR signals due to the cysteines and H-bonds interacting with different parts of the cluster. The cysteinyl-S will coordinate the Fe ions due to the protein environment. This results in highly different angles causing the electronic environment to be very different in the x, y, and z directions causing a rhombic EPR line shape.[15] Each type of iron-sulfur cluster has a different temperature range in which they can be detected due to the presence or absence of higher lying energy levels (**Figure 1.7**).[15]

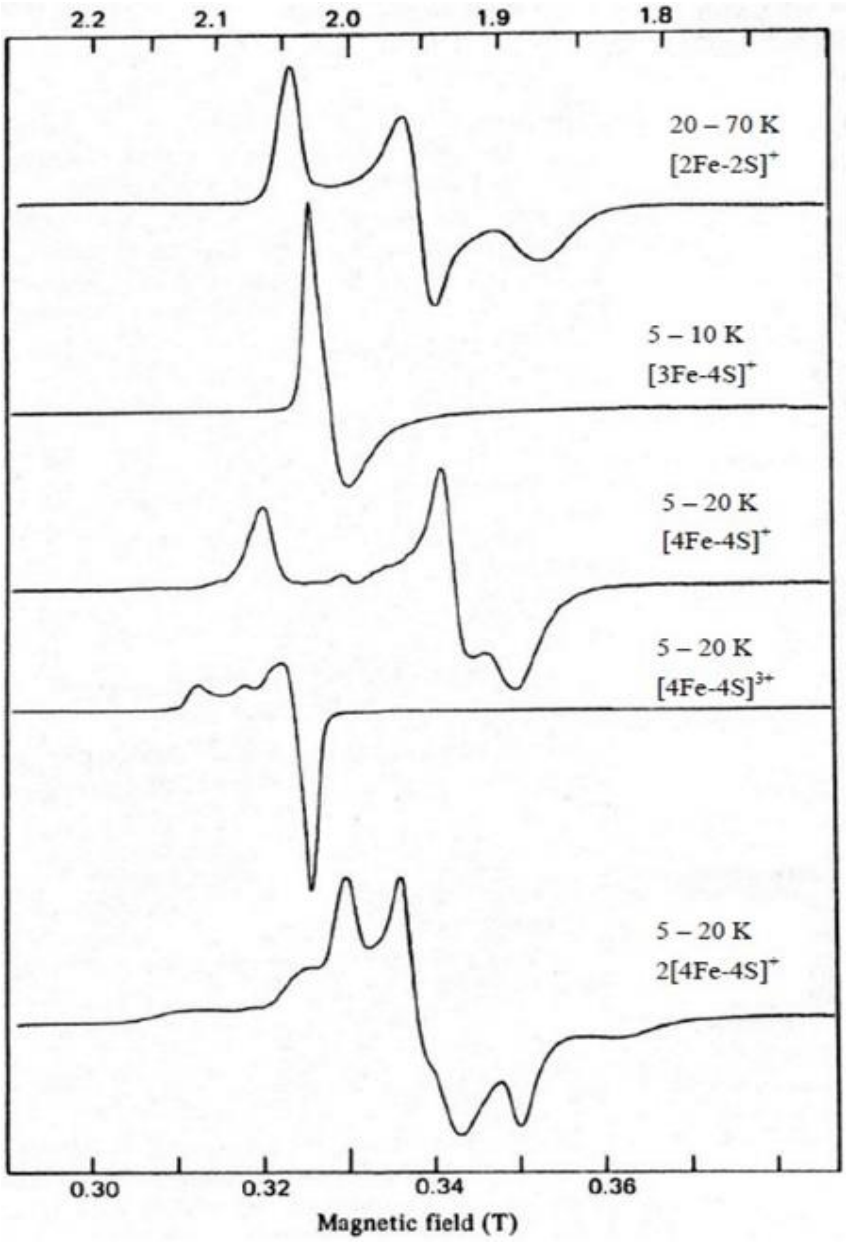

Figure 1.7: Common EPR signals of iron-sulfur clusters and their optimal temperature detections. (Adapted from Cammack et al.)[25]

1.3.5 Redox Studies and Properties for Iron-Sulfur Clusters

Iron-sulfur clusters and iron-sulfur containing proteins have been a part of redox chemistry during the evolutionary times. As seen in **Figure 1.8**, the common iron-sulfur clusters have unique redox potential ranges, covering the full range from +500 to -600 mV (NHE).[23] pH dependency plays a role in cluster mostly due to hydrogen bonding, specifically in Rieske clusters. As discussed previously, His ligands can be protonated which increases a protein's reduction potential up to 300 mV more compared to a cluster with only Cys. This is due to this ligand's resonance which stabilizes the oxidation state of the iron-sulfur cluster. The midpoint potential can be determined for individual iron-sulfur clusters by performing redox studies. Once analyzed by EPR, the intensities are plotted, and the Nernst curve equation is applied to calculate the midpoint potential. **Equation 1.2** represents Nernst curve equation used to plot a reduced EPR-active species while **Equation 1.3** represents the Nernst curve equation used to plot an oxidized species. 'I' represents the maximum intensity, 'n' represents the number of electrons involved, 'x' is the potential values obtained during the titration, 'E' is the midpoint potential, and '38.92' is the value of F/RT (F=96484.6 C/mol, R=8.31441 J/(mol*K), T=298.15 K).

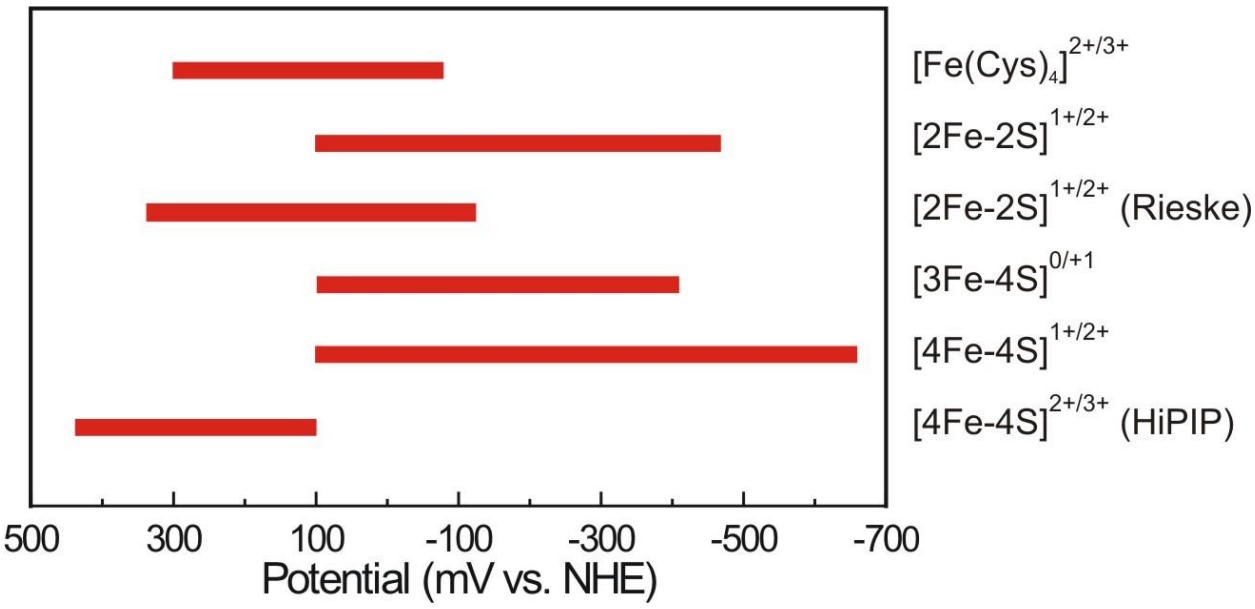

Figure 1.8: Redox potential ranges of the common types of iron-sulfur clusters. 'R' stands for Rieske in this figure. (Adapted from Johnson et al.)[20]

Equation 1.2: Nernst curve equation used to plot a reduced EPR-active species.[15]

$$y = \frac{I}{1 + \exp\big(n * 38.92 * (x - E)\big)}$$

Equation 1.3: Nernst curve equation used to plot an oxidized EPR-active species.[15,26]

$$y = \frac{I}{1 + \exp\big(n * 38.92 * (E - x)\big)}$$

1.4 Hydrogenases

Hoppe-Seyler was the first to note that bacteria in river mud were responsible for converting formate into H_2 and CO_2 in 1887. Later, Stephenson and Stickland named these bacterial enzymes 'hydrogenases.'[27] The majority of organisms containing hydrogenases grow strictly under anaerobic conditions. Hydrogenases play a significant role in methanogens by

reducing two protons to yield hydrogen gas and/or oxidizing this gas to produce two protons.[20] There are two types of hydrogenases known today: [Ni-Fe] and [Fe] (commonly known as FeFe or Fe only) (**Figure 1.9**). In the next sections, [Ni-Fe] hydrogenases will be discussed in detail due to the connection this enzyme has with methanogens.

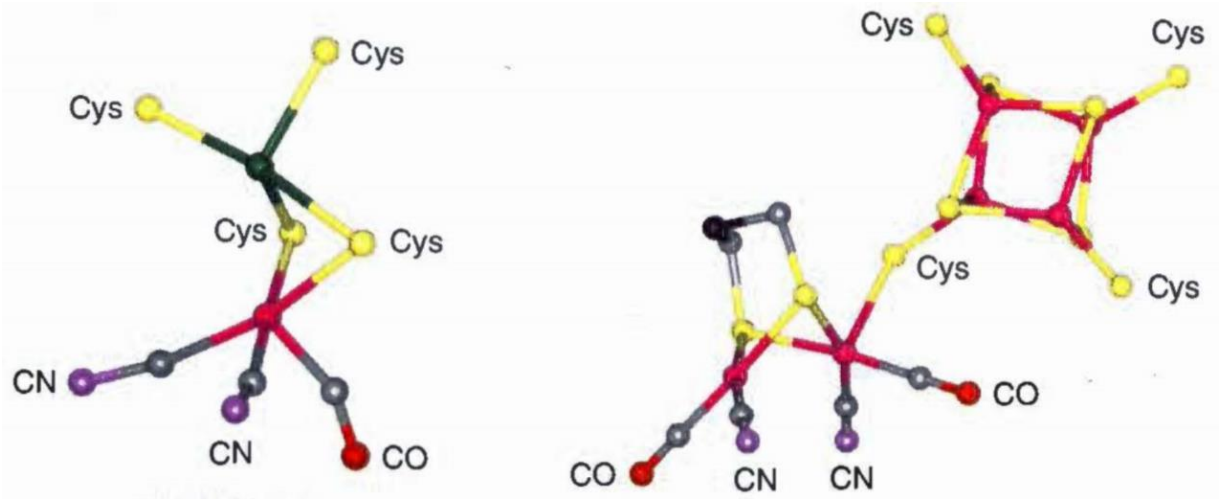

Figure 1.9: Active site cofactors of [Ni-Fe] hydrogenase (Left) and [Fe-Fe] hydrogenase (Right). Figure adapted from Johnson and Smith.[20]

1.4.1 [Ni-Fe] and [NiFeSe] Hydrogenase Properties

[Ni-Fe] hydrogenases oxidize H_2 to achieve two electrons and two protons compared to [Fe] hydrogenases which produce H_2.[27] [Ni-Fe] hydrogenases contain two CN^- and one CO molecule to coordinate the Fe atom while two Cys thiolates coordinate the Ni atom. In a subgroup, [NiFeSe] hydrogenases, however, a selenocysteine is in place of one of those Cys. The Se/S atoms function as a base to accept protons during the proton transfer and H_2 activation. In addition, these hydrogenases contain conserved Arg, His, and Glu residues which create exchangeable sites near or within the H-bonding distance to the Ni-Fe cluster. These hydrogenases typically are comprised

of 2-3 subunits: the large subunit containing the [Ni-Fe]-catalytic site, the small subunit with three highly conserved iron-sulfur clusters, and the last subunit contains one [2Fe-2S] cluster. [Ni-Fe] hydrogenases can be separated into four groups corresponding to their physiological role.[28]

Group 1 correlates to the hydrogenases that are membrane bound and use H_2 as an energy source.[29] Cytochrome *b* typically anchors this enzyme to the membrane and allows electron transfer between it and the quinone pool.[28] This group couples the oxidation of H_2 to the reduction of electron acceptors such as oxygen, nitrate, sulfate, CO_2 or oxidized sulfur compounds.[28] Group 2 contains two subgroups of hydrogenases: one involves the hydrogenases found in cyanobacteria which fixes N_2 using nitrogenases while the other consists of H_2-sensing regulatory hydrogenases that signal H_2 availability.[29] The second subgroup is typically affiliated with Group 1 H_2 oxidizing enzymes. Group 3 contains four subgroups of hydrogenases. This first subgroup relates to the F_{420}-reducing hydrogenases found in methanogenic archaea. These organisms couple the oxidation of H_2 to the reduction of cofactor F_{420} which can donate electrons to different process including the conversion of CO_2 into methane (**Figure 1.1**) .[28] The second one contains the enzymes that are tetrameric ($\alpha\beta\gamma\delta$) and found in thermophilic archaea. The α and δ subunits represent the minimal [Ni-Fe] hydrogenase structure while the β and γ subunits contain iron-sulfur clusters and a NAD(P)/FAD binding domain. The third subgroup couples an endergonic reduction to an exergonic reduction.[30] Finally, the last subgroup contains homology to the NADH input module of Complex I.[28] These hydrogenases are bidirectional heteromultimeric that are associated with an additional NADH oxidoreductase.[28] Lastly, group 4 involve the other membrane bound hydrogenases which are Fd-dependent enzymes. These hydrogenases can generate H_2 from Fd^{RED} with the generation/utilization of a proton gradient.[31]

1.4.2 Redox States of [Ni-Fe] Hydrogenase

The [Ni-Fe] cofactor contains a Ni and an Fe ion that are bridged by two cysteinyl-S ligands. Three additional cysteinyl-S ligands coordinate the Ni and two CN and one CO coordinate the Fe. This enzyme contains multiple forms known as the 'ready,' 'unready,' and 'silent' forms.[27] The 'ready' (Ni-C, Ni-L) forms are the stages in which the Ni^{+} binds H_2 to oxidize the gas. The 'unready' forms (Ni-A, Ni-B) Ni^{3+} do not bind H_2. The Ni^{2+} state is referred to as the 'silent' form (Ni-SI) due to the lack of signal detection by EPR.[27,32]

A third bridge that coordinates the Ni and Fe atom distinguishes the different states of the [Ni-Fe] hydrogenase (**Figure 1.10**). Ogata et al crystallized a protein structure that showed evidence of how H_2 is oxidized. **Figure 1.10** gives an adapted form of what the authors suggested the pathway for when the [Ni-Fe] hydrogenase goes from the 'unready' state to the 'ready' state. They never said anything about Ni-A but what is known from other studies is Ni-A occurs when this bridge is open in preparation of H_2 or possible hydroxyl groups to coordinate to the Ni and Fe atoms.[27] If a hydroxyl group is present (typically from water), Ni-B occurs and coordinates the hydroxyl group to the Ni and Fe. If the hydroxyl group leaves and an electron is lost from the Ni, the cluster changes to Ni-SI where SI represents the EPR silent form. From there, H_2 can bind to the hydrogenase. Ni-R represents the state in which the hydride coordinates to the Ni and Fe while the proton is coordinated to a nearby base which is a Cys.[32] Once this H-atom (H^{+} + 1 e^{-}) leaves, Ni-C is formed. If the cluster is exposed to light for a long period of time, the bond between the hydride and the two metals breaks and the proton moves to the nearby base to create Ni-L.[33]

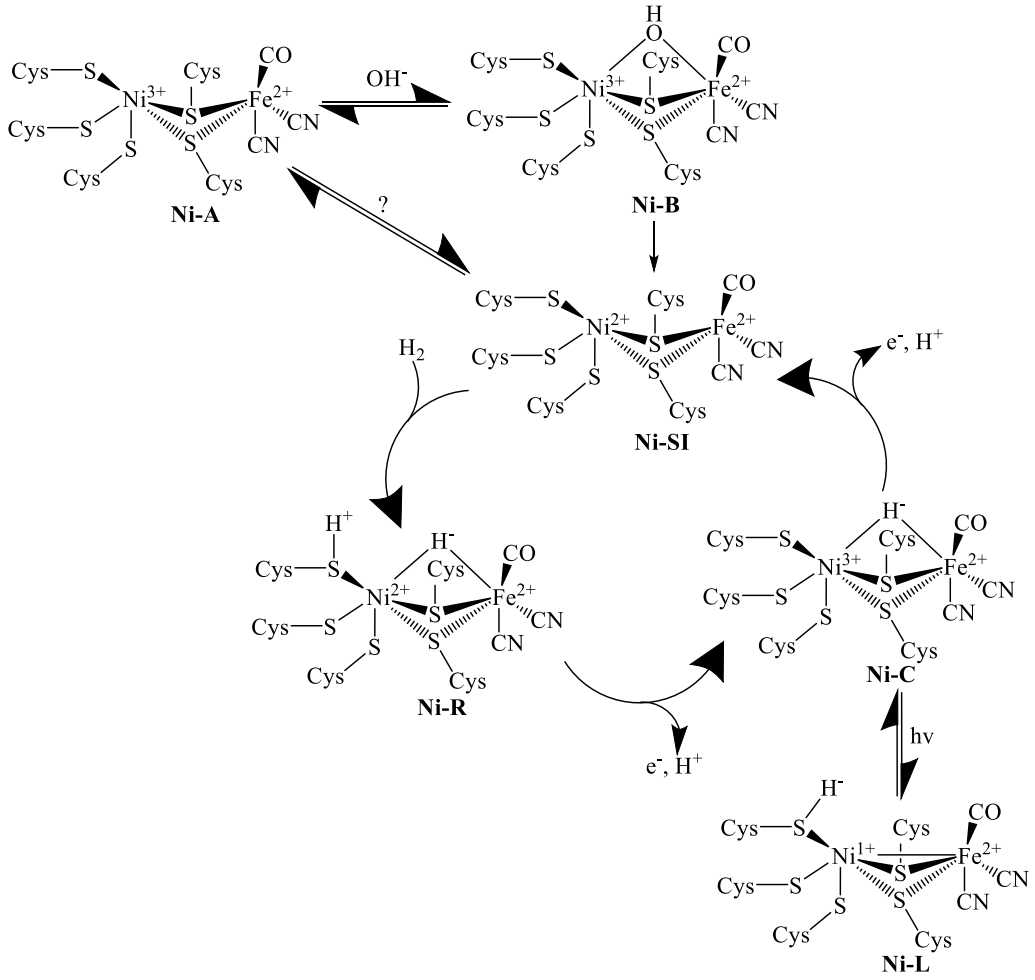

Figure 1.10: An adapted pathway from Ogata et al. starting from the oxidative state (Ni-B) and going into the catalytic cycle starting at Ni-SI.[32] Once H_2 is introduced, the state goes to Ni-R and with the loss of a proton and electron Ni-C forms. Ni-A and Ni-L were not discussed in this article but what is known is Ni-A also contains Ni with a 3+ oxidation state and Ni-L is formed due to long exposure to light. This exposure will cause the hydride group to move to a local base.[33]

1.4.3 EPR Signals

With the vast studies performed on [Ni-Fe] hydrogenases, EPR signals and g-values have been determined for the 'ready' and 'unready' forms (**Figure 1.11**). The majority of these states are EPR active and give rhombic signals due to Ni^{3+} and Ni^{+}. Ni^{2+} in Ni-R is EPR silent. Ni-C has

g_{zyx}-values of 2.19, 2.15, and 2.01. Even though Ni-L is similar to Ni-C, its g-values and EPR signal were significantly different. The g_{yx}-values were slightly different at 2.13 and 2.045 respectively while the g_z-values had two signals given the values of 2.27 and 2.29. Ni-A and Ni-B are similar to one another that their g-values tend to overlap one another. The main difference is at the g_y-value which is 2.24 and 2.14 respectively (g_z-value is 2.33 and g_x-value is 2.02).[27]

In addition to these EPR signals, the Mvh complex was studied by Stojanowic et al. to determine the connection between Mvh and Hdr. After genetic analysis, researchers saw *mvhD* was fused to *hdrA* homologue. This homologue perfectly aligned with a known HdrA sequence and also contained the same cofactors which suggested Mvh and Hdr worked together.[30] To analyze the iron-sulfur cluster in MvhD further, they purified Mvh from *M. marburgensis* and reduced the protein with sodium dithionite. **Figure 1.12** shows the EPR signal of Mvh after being reduced with g_{zyx}-values of 2.006, 1.936, 1.912 which could be observed at 10-80 K.[30] This signal proved to be a $[2Fe\text{-}2S]^+$ cluster because of these conditions.

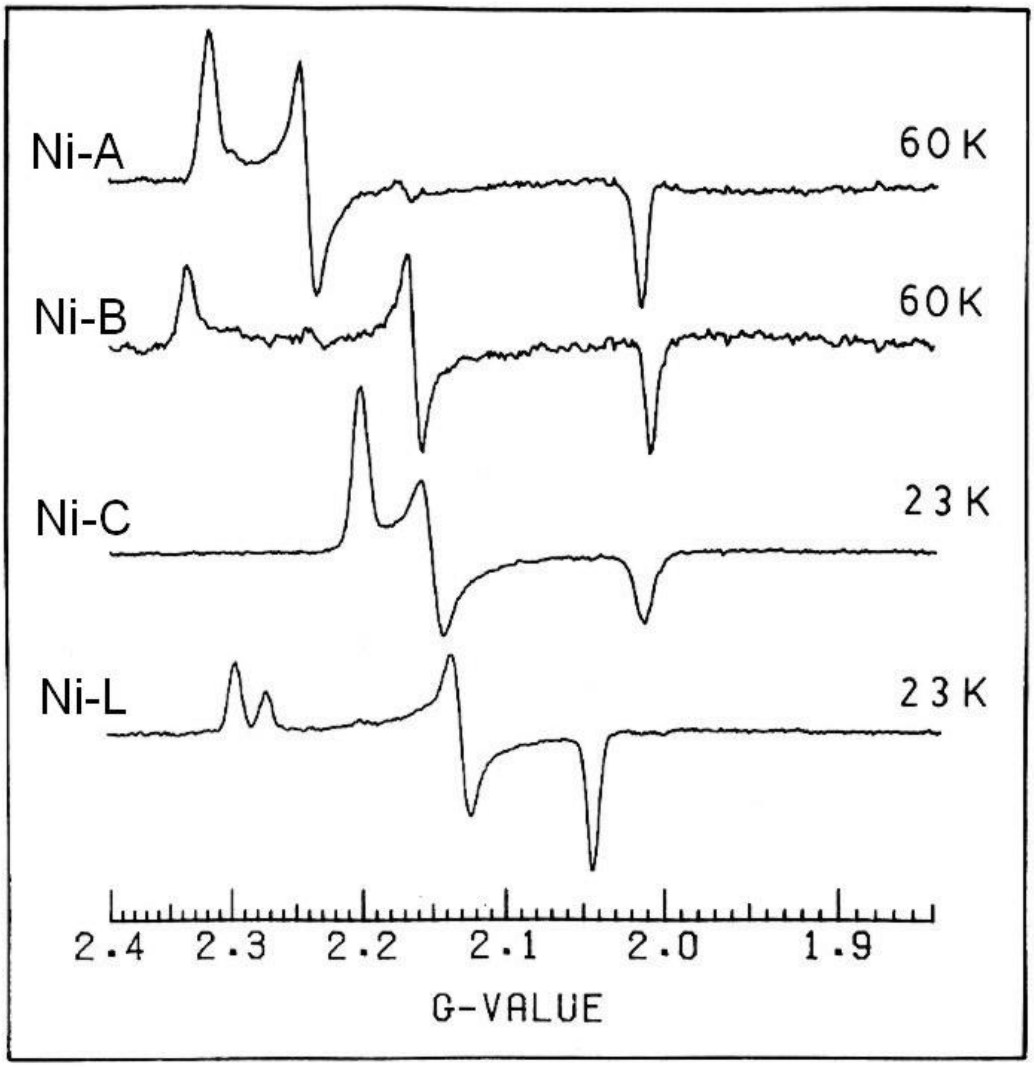

Figure 1.11: EPR signals of the various [Ni-Fe] hydrogenase states (Adapted from Cammack).[27]

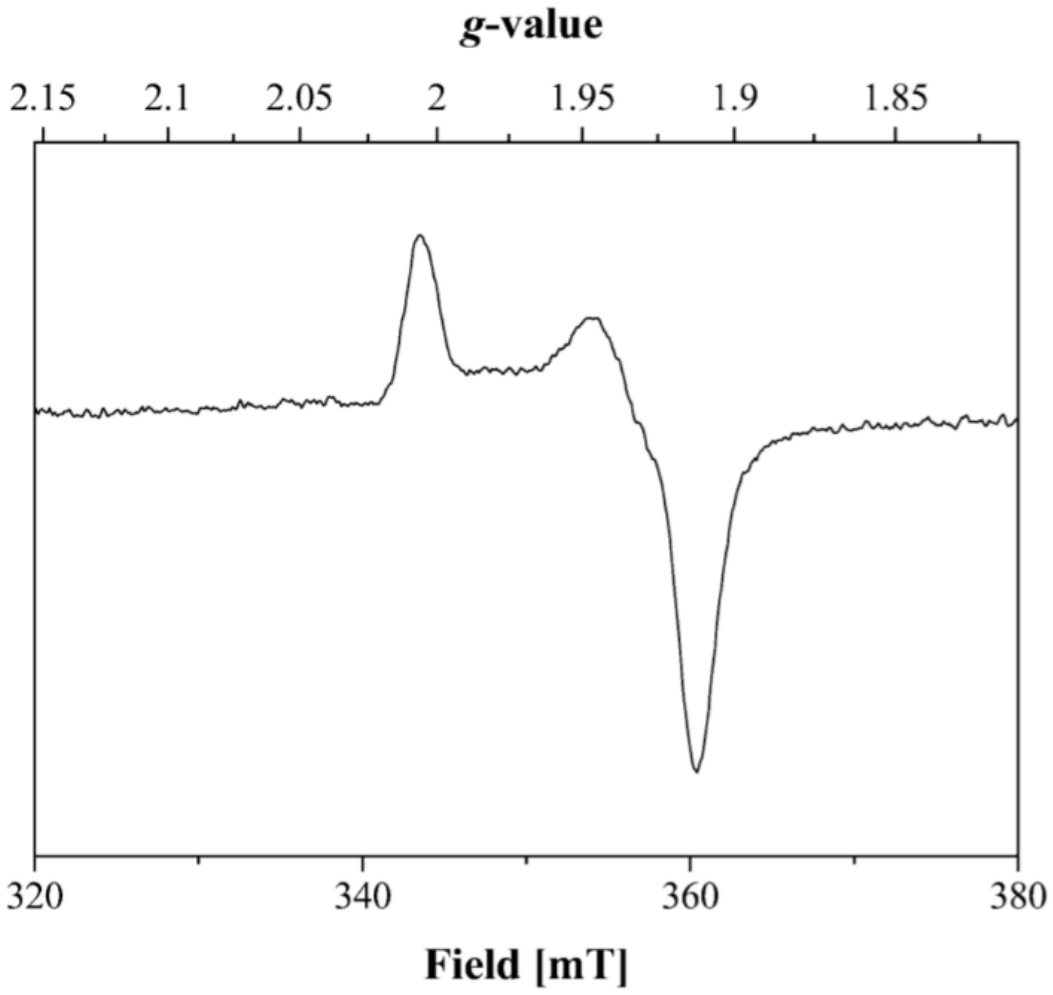

Figure 1.12: EPR of reduced Mvh.[30]

1.5 Heterodisulfide Reductase

Heterodisulfide reductase (Hdr) is an enzyme which reduces HDS to CoM and CoB in the hydrogenotrophic pathway. Both the recycling of CoB and CoM and the indirect coupling to the first reaction step make this enzyme essential to the whole methanogenic pathway.[11] There are two types of Hdr: membrane bound and cytosolic. The membrane complex couples the oxidation of molecular hydrogen and reduction of HDS to the pumping of sodium ions which, in turn, can be used by other complexes for ATP production or more importantly generation of reduced

ferredoxin. The Hdr studied for this research, however, is not membrane bound and is found in the cytoplasm instead. This brings the question of how this enzyme reduces HDS without coupling to ATP synthase. The answer was found within one of the enzyme's subunits.

In *M. marburgensis* Hdr is present as a larger complex together with methyl viologen-reducing hydrogenase (Mvh, **Figure 1.13**). The MvhA subunit contains the [Ni-Fe]-catalytic site which oxidizes H_2 to obtain the electrons.[27] The smaller subunit, MvhG, accepts the electrons and transfers these through three [4Fe-4S] clusters that are commonly called the proximal, medial, and distal clusters based on their positions within the subunit. The last subunit of Mvh, MvhD, only contains a single [2Fe-2S] cluster. From there, the electron flows to Hdr. HdrA is proposed to be the initial Hdr subunit. This subunit alone has 6 [4Fe-4S] clusters and a flavin adenine dinucleotide (FAD) which performs flavin-based electron bifurcation. The mechanism of the bifurcation remains unknown, but theories have been developed in the lab which are discussed below. From HdrA, electrons flow to either ferredoxin or HdrC. HdrC, the second subunit of Hdr, contains two [4Fe-4S] clusters and passes the electrons to the active site in HdrB, the third subunit of Hdr. HdrB for many years was believed to only contain one [4Fe-4S] cluster; however, crystallization studies revealed two [4Fe-4S] clusters but they are uniquely shaped and named non-cuboidal [4Fe-4S] clusters.[34] The next sections will discuss in detail all about Hdr, the non-cuboidal clusters found in HdrB, and flavin-based electron bifurcation.

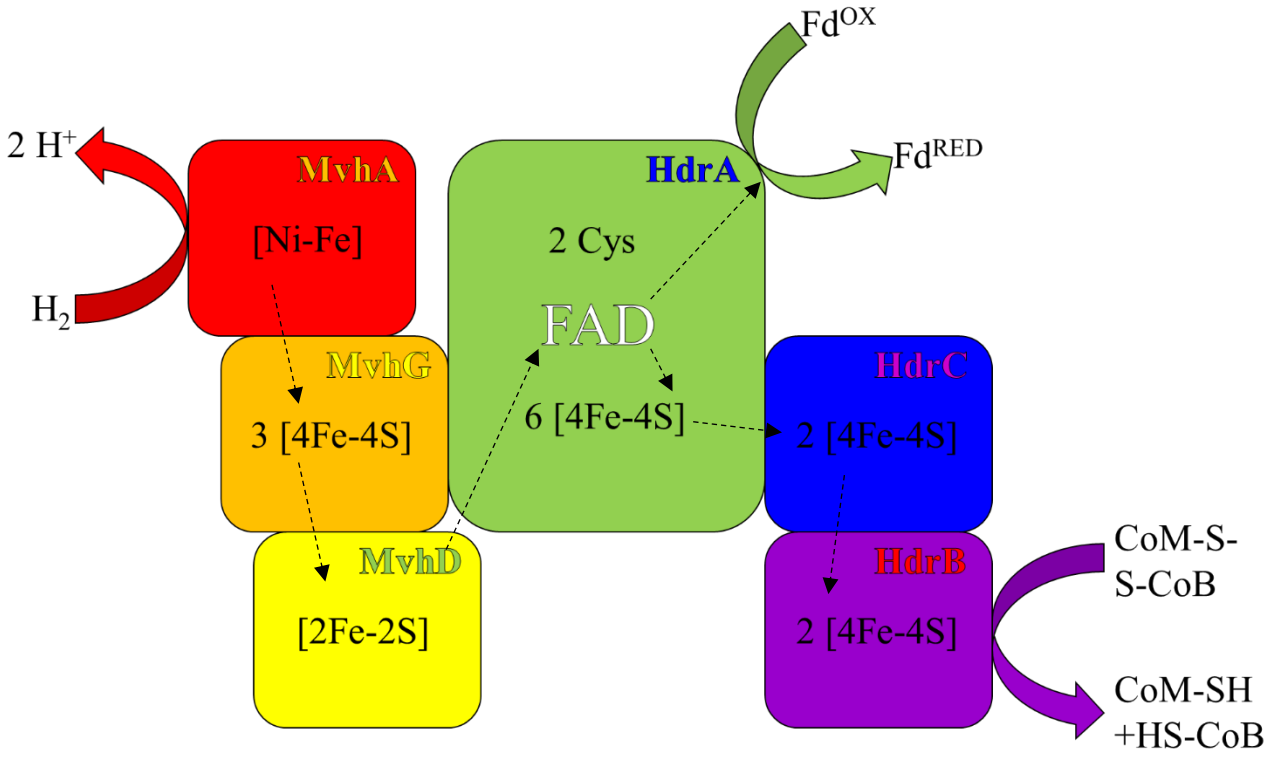

Figure 1.13: A general overview of Mvh:Hdr. The dashed arrows indicate the general electron flow.

1.5.1 Electron Bifurcation

1.5.1.1 Q-Cycle of Oxygenic Photosystems

Inside the thylakoid membrane of most oxygen producing plants, oxygenic photosystems absorb photons from sunlight to use for energy (**Figure 1.14**).[35] Photosystem II splits water to take in low energy electrons to become excited by the photons to a higher energy level (i.e. lower in potential). These electrons are transferred to in the following order: 1) the quinone pool, 2) cytochrome-b_6f, 3) plastocyanin, and 4) photosystem I. The Q-cycle in cytochrome-b_6f drives proton translocation from the stroma into the lumen. Excitation in photosystem I brings the

electrons to a higher energy level (low potential) again to reduce Fd which acts as an electron donor to the enzyme Fd-$NADP^+$ reductase to reduce $NADP^+$ to NADPH. $NADP^+$, however, requires two electrons to be fully reduced and, therefore, the photosynthesis process must occur twice to complete this action. Protons are removed through ATP synthase where ADP and a phosphate group (P_i) bind to ATPase to create ATP and to allow for equilibrium between the two environments.[36] ATP and NADPH both aid in the splitting of the water in the organism to create the product O_2 and H^+. O_2 is required by most organisms to survive today, however, researchers, have been working toward theories on how organisms survived on Earth millions of years ago when oxygen was obsolete.

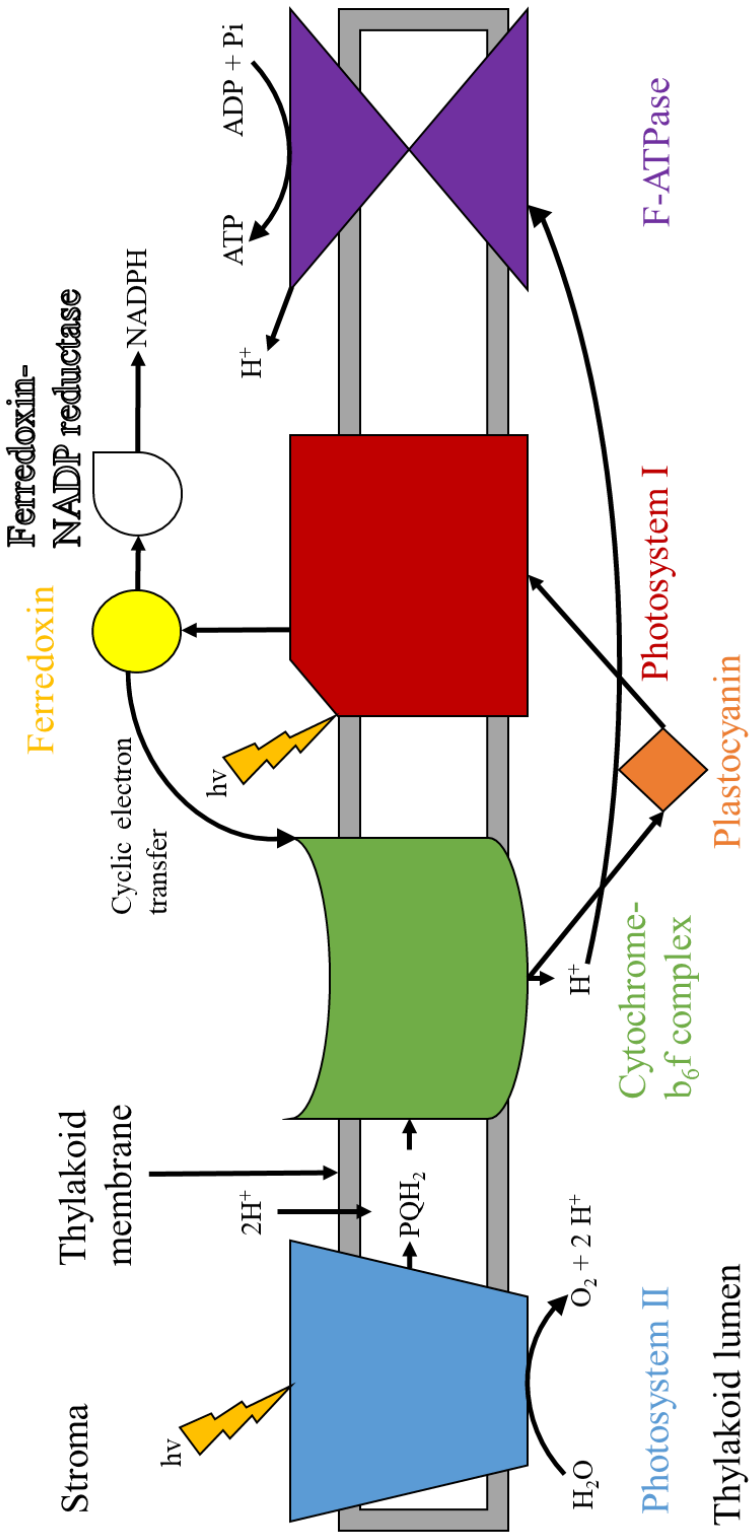

Figure 1.14: Layout of the oxygenic photosystem within the thylakoid membrane.[35,36]

There have been several theories to explain this phenomenon, one being that ancient organisms used H_2 and/or CO_2 as an energy source.[2,37] However, this theory lacks information pertaining to the chemical mechanism used to explain how organisms consume these molecules for energy. Methanogenic *Archaea* or methanogens have the ability to take in H_2, formate, methanol or acetate as energy and carbon sources and convert this into CH_4.[38] These organisms are located in habitats where anaerobic degradation of organic compounds occurs such as anaerobic waste digesters, marine and freshwater sediments, and even human and animal intestinal tracts.[38] A unique characteristic to the species studied in this research is the absence of NADPH. Several decades passed before scientists discovered that these organisms survive such conditions via a process called electron bifurcation.

Electron bifurcation allows the creation of electrons with low redox potentials without coupling to ATP hydrolysis or input from other 'high-energy' compounds. First adopted by Peter Mitchell in 1975, electron bifurcation was formulated as the Q-cycle to represent the cytochrome bc_1 dehydrogenase complexes of the mitochondria.[39] Further research increased the knowledge of this cycle into what is known as Complex III today (**Figure 1.15**). Ubiquinol (QH_2) attaches to Complex III to release two electrons into the complex while two protons (E_m= +110 mV) enter the intermembrane space. Electrons prefer to proceed from a negative potential to a positive potential which rationalizes the first electron transfers to the Rieske cluster (E_m=+290 mV) initially. Upon reduction, the cluster moves away, forcing the $Q^{\bullet}$ form to transfer the second electron to heme b_L (E_m=-20 mV). If the Rieske cluster did not move away from QH_2, the electrons would continuously flow to this cluster because of its preferred potential. Lastly, the Rieske cluster transfers the electron to cytochrome *c* while heme b_L transfers its electron to heme b_H which transfers to a separate ubiquinone (Q) to create a semiquinone radical ion ($Q^{\bullet-}$).

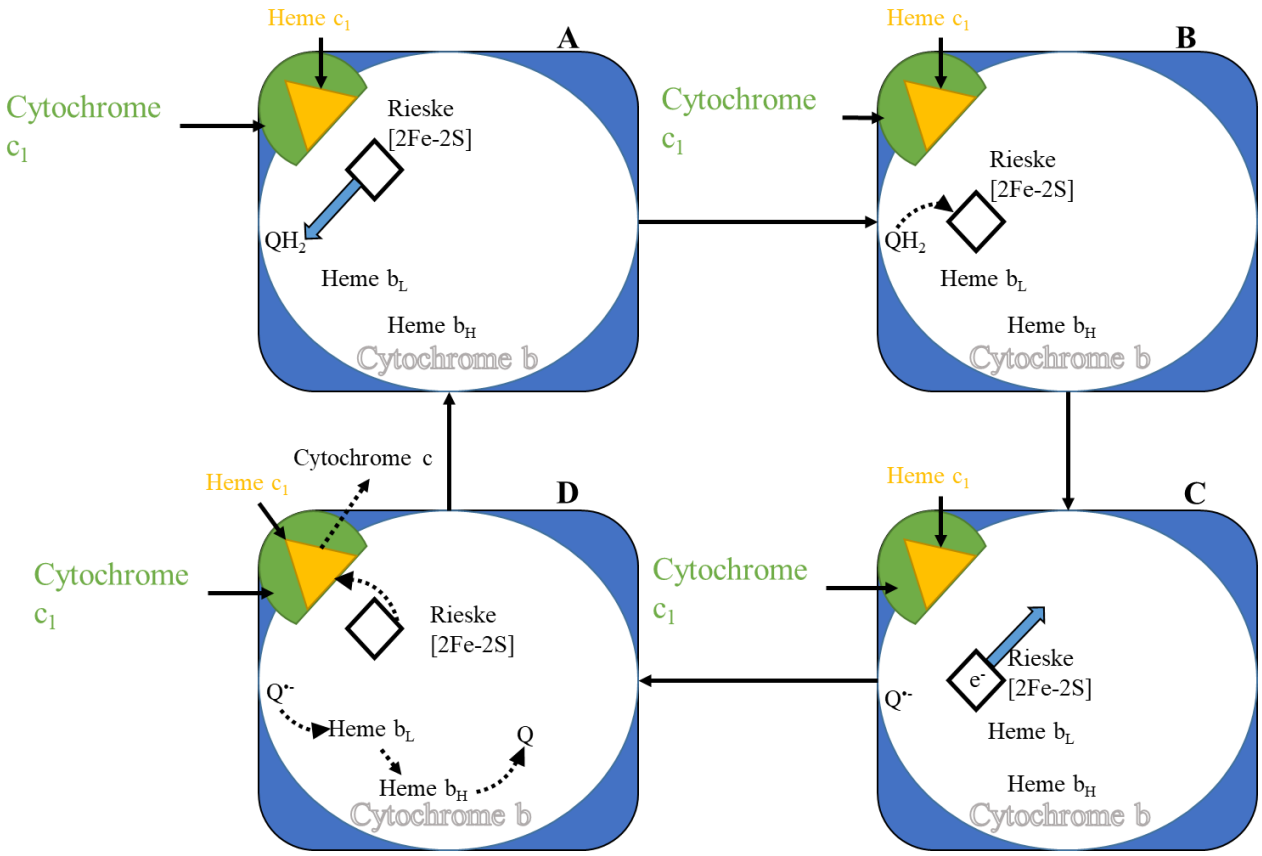

Figure 1.15: Electron bifurcation mechanism schematic overlay within complex III.[36] The solid arrow curve represents a conformational change the enzyme performs to put the Rieske iron-suflur cluster closer to the ubiquinol (QH_2). The dashed arrow lines represent electron transfer between the cofactors. The Q-cycle is quite similar to Hdr in that both contain an outside electron accepting source (i.e. a Rieske cluster for cytochrome b_6f and Fd for Hdr) which reduces other substrates unrelated to these enzymes while the internal electron accepting source (i.e. heme b_L for cytochrome b_6f and [4Fe-4S] cluster for Hdr) proceeds with reducing the substrate. (Adapted from Lehninger)[40]

This whole process repeats to reduce a second cytochrome *c* and for $Q^{\bullet-}$ to become QH_2.[40] The crucial part of this path indicates the potentials of each cofactor must straddle the potential of the FAD as it obtains the electrons simultaneously. [41] A "red hot" semiquinone (i.e. very unstable semiquinone) is created after the first electron transfers to the more positive potential cofactor. This "red hot" semiquinone will, then, transfer the second electron to a cofactor within proximity and willing to accept the electron. In this second step, the acceptor can have a much more negative potential than in the first electron transfer step.

1.5.1.2 Discovery of Flavin-Based Electron Bifurcation

In 2008, Gloria Herrmann et al. proposed a two-step process for a flavin-based electron bifurcation.[42] The authors stated that the exergonic reduction of crotonyl-CoA drives the endergonic reduction of Fd through FAD.[42] Electron transferring flavoprotein-butyryl-CoA dehydrogenase (Etf-Bcd) is the first enzyme for which the mechanism of flavin-based electron bifurcation was determined.[43] Etf (**Figure 1.16**) contains three domains: Domain I which contains no flavin, Domain II which contains an α-FAD, and Domain III contains a NADH binding site and β-FAD. **Figure 1.17** gives a schematic diagram of how this bifurcation process occurs. Once the β-FAD becomes reduced by NADH, the α-FAD accepts the electrons from the now reduced β-$FADH_2$. The unstable radical form of α-$FAD^{\bullet-}$ in Domain II is described by the authors as going through a conformational change by 'twisting' towards γ-FAD in Bcd to donate the electron to this molecule. This conformational change forces the β-$FAD^{\bullet}$ to donate the second electron to Fd and is now fully oxidized once again. The γ-FAD now becomes γ-$FAD^{\bullet}$ but is not able to reduce crotonyl-A crotonyl-A with one electron. Therefore, this process must occur one more time to fully reduce crotonyl-A into butyryl-CoA. Buckel and Thauer further elaborated the FAD molecule's involvement within this enzyme might follow a "cross-over" path.[41] In this model the FAD picks

up two electrons at once at an intermediate potential. These are, then, released one-by-one. The first electron reduces a cofactor with a more positive potential. This now generates a “red-hot” semi-quinone radical that is capable of reducing a second different cofactor with a very negative redox potential.[11,43] This model will be explained in full detail for Hdr in the following sections.

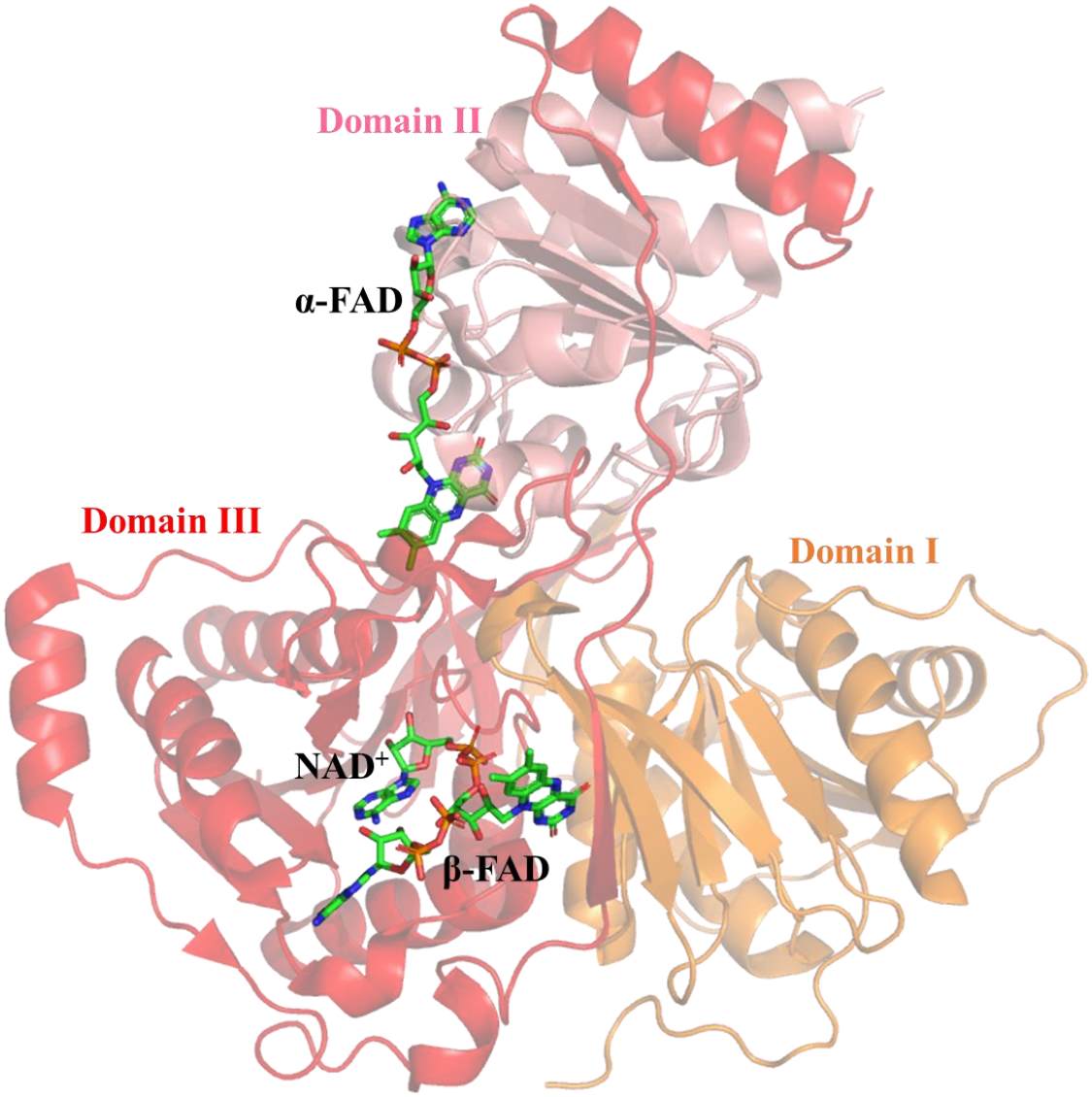

Figure 1.16: Protein crystal structure of Electron transferring flavoprotein (Etf) (PDB: 4L2I).[43]

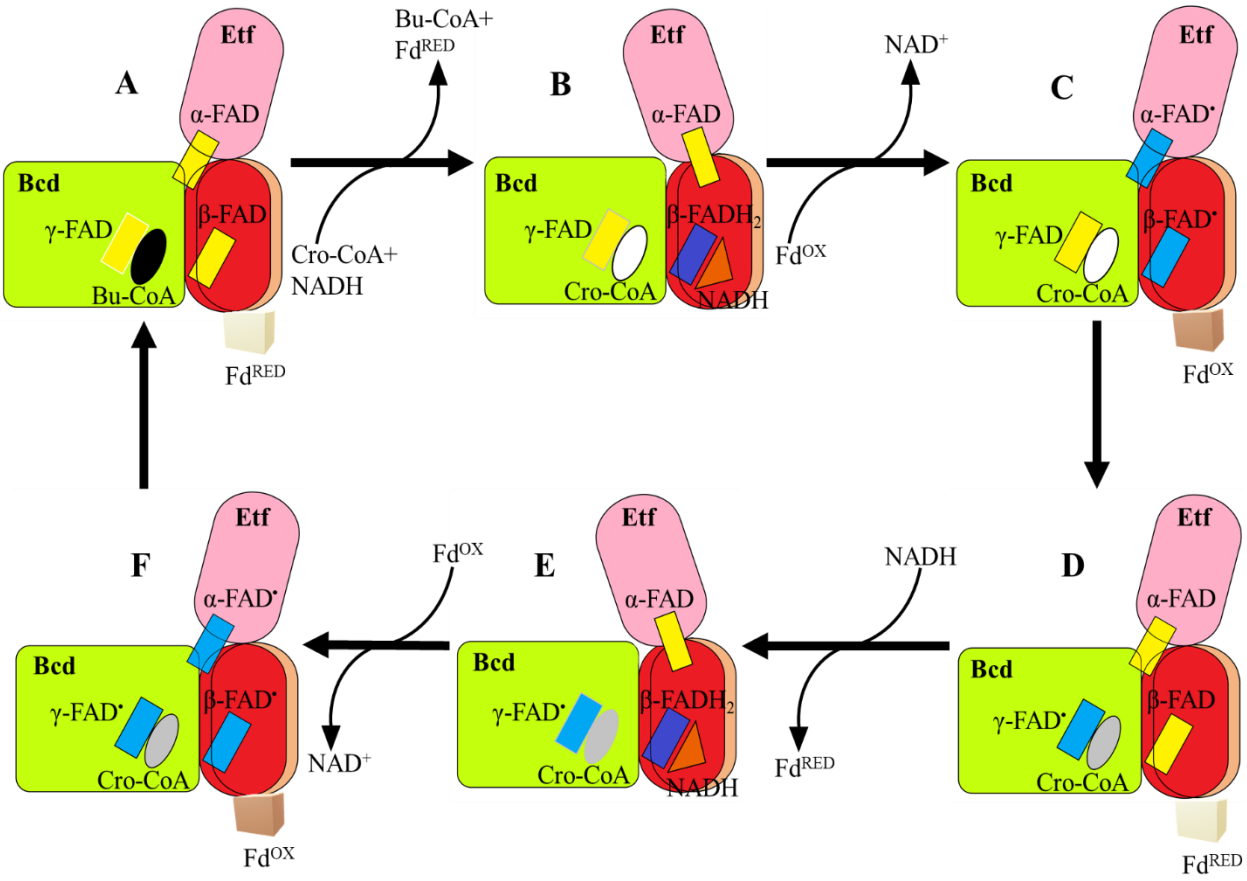

Figure 1.17: Cartoon mechanism diagram of flavin based-electron bifurcation performed within Etf: Bcd. The different ovals of Etf are the same colors as the domain colors seen in **Figure 1.16.** NADH is represented by the orange triangle, the yellow rectangles oxidized flavins, light blue represents the radical form of FAD, and dark blue represents the fully reduced FAD. Once the β-FAD becomes reduced by NADH, the α-FAD in 'B' shows the electron is accepted from the now reduced β-$FADH_2$. Crotonyl-CoA is represented by the white oval, the semi-reduced crotonyl-CoA is represented by the gray oval and the fully reduced crotonyl-CoA or butyryl-CoA is represented by the black oval. Fd^{OX} is the dark brown cube and Fd^{RED} the cream color cube.

1.5.1.3 Flavin-Based Electron Bifurcation in Hdr

Before the crystal structure was solved, our lab developed three different theories as to where the electron traveled during the bifurcation process. The first problem is how the FAD would be able to get reduced by two electrons. In the HdrA sequence there are four sequence motives (CxxCxxCxxxC(P)) that indicate the presence of [4Fe-4S] clusters. Ten more Cys residues are present but not in obvious sequence motive. However, one pair is present as CxC, one pair as CxxC, on one pair as CC. In principle these could form active site disulfides that could be involved in some of the catalytic processes. In particular the last Cys in the CxxC motive is a selenocysteine in *Methanococcus maripaludis* indicating a possible function for this Cys/Sec residues. It can be proposed that electron from molecular hydrogen end up reducing the disulfide to the respective thiols and the FAD is directly involved in the reoxidation forming FADH2 in the process. Similar chemistry is displayed by FAD-dependent sulfhydryl oxidases.[44]

The next problem is to figure out how to separate the flow of electron to the HDS and Fd reduction sites. [45] In Model I, (**Figure 1.18**) the flexible ribose chain allows the isoalloxazine ring to move towards a [4Fe-4S] cluster due to its higher potential the first electron would transfer. Upon movement of the isoalloxazine ring away from the FAD, the $FADH^{\bullet}$ has to deliver the second electron to the bound Fd^{OX} which creates Fd^{RED}. In model II, the [4Fe-4S] is the group that can change position and first moves towards $FADH_2$ to accept the first electron. This model is very similar to the Complex III discussion. The cluster moves away upon reduction which forces the semi-oxidized flavin to transfer the second electron to the Fd^{OX}. HdrA does not contain a [2Fe-2S] cluster and, therefore, we use a [4Fe-4S] cluster in this model. However, in *Methanosarcina acetivorans* the MvhD and HdrA subunits are fused. In *Methanococcus maripaludis*, a variant of the Hdr complex is found that shows that when the cells are grown on formate the complex consists

of formate dehydrogenase, formyl methanofuran dehydrogenase, HdrABC and the D subunit of the hydrogenase.[10] It appears that the HdrA and MvhD subunit function as one unit which leaves room for a possible role of the [2Fe-2S] cluster in the direction of electron flow. In the third model there is no actual movement. For the Hdr complex, when the cluster is reduced, the electron transfer to HdrB is so slow that the "red hot" $FADH^{\bullet}$ state is not able to transfer the second electron to the acceptor cluster since this would create a $[4Fe\text{-}4S]^{0}$ cluster. The possibility of obtaining a '0' state for the [4Fe-4S] cluster is very low, but when it is obtained, the potential for the 1+/0 state is very low. Therefore, the bound Fd^{OX} forces the second electron to transfer to it instead and no movement from any group is necessary.

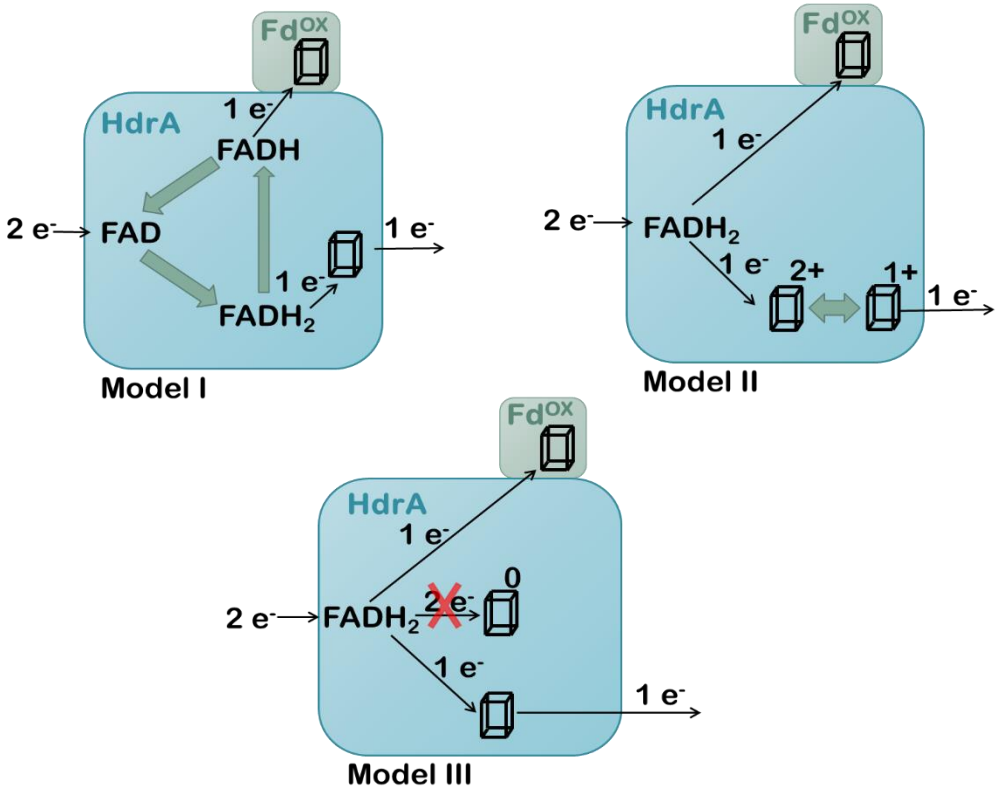

Figure 1.18: Three models for flavin based-electron bifurcation in Hdr. In Model I, the green arrows represent the isoalloxazine ring rotating around towards the internal [4Fe-4S] and Fd^{OX} with the aid of the ribose chain attached to $FADH_2$. In Model II, the double headed green arrow represents the internal $[4Fe\text{-}4S]^{2+}$ going towards $FADH_2$ to accept the first electron. Once the cluster accepts it, it moves away from the flavin compound. In Model III, the thin, black arrows represent the electrons travelling on their own without any conformational change occurring.

1.5.1.4 Theoretic Model for Flavin-Based Electron Bifurcation in Hdr

Flavoproteins (FP) can exhibit three different redox potentials, namely an E'_0 for the FP/FPH_2 couple (n = 2), an E'_0 for the FP/FPH couple (n = 1), and an E'_0 for the FPH/FPH_2 couple (n = 1). E'_0 (FP/FPH) is generally more positive and E'_0 (FPH/FPH_2) more negative than E'_0 (FP/FPH_2).[41] Oxidation of FPH_2 by two one-electron acceptors with different redox potentials thus

leads to a bifurcation of the two electrons in FPH_2. Initially, it was proposed that the reaction follows the scheme on the right in **Figure 1.18**, a sequential reduction of the low potential ferredoxin by the fully reduced flavin and, then, a redox transition to oxidized flavin-reducing crotonyl-CoA or the HDS.[41] However, this does not explain the effect observed that the endergonic reduction of ferredoxin is driven by the exergonic reduction of the high potential acceptor. There is no real reason why the fully reduced flavin needs the second oxidation step to perform the first one. In addition, in this n = 1 model for the flavin the reduced flavin can only be generated by reducing the semi-oxidized form which is not possible with molecular hydrogen as the electron source. The proposed energy conserving bifurcation works can be easily explained by the cross over model on the left side of **Figure 1.19**. The 2-electron transition of the flavin is, in general halfway between the two formal redox potentials of the individual 1-electron steps. Now the potential of molecular hydrogen is sufficient to make $FADH_2$. If both the high potential acceptor and the ferredoxin are simultaneously close to the $FADH_2$, the first oxidation reaction cannot reduce the ferredoxin but will be driven by the high potential acceptor. This, however, leaves the flavin in its ‘‘red hot’’ flavosemiquinone state, mentioned above, that can reduce the low potential ferredoxin.

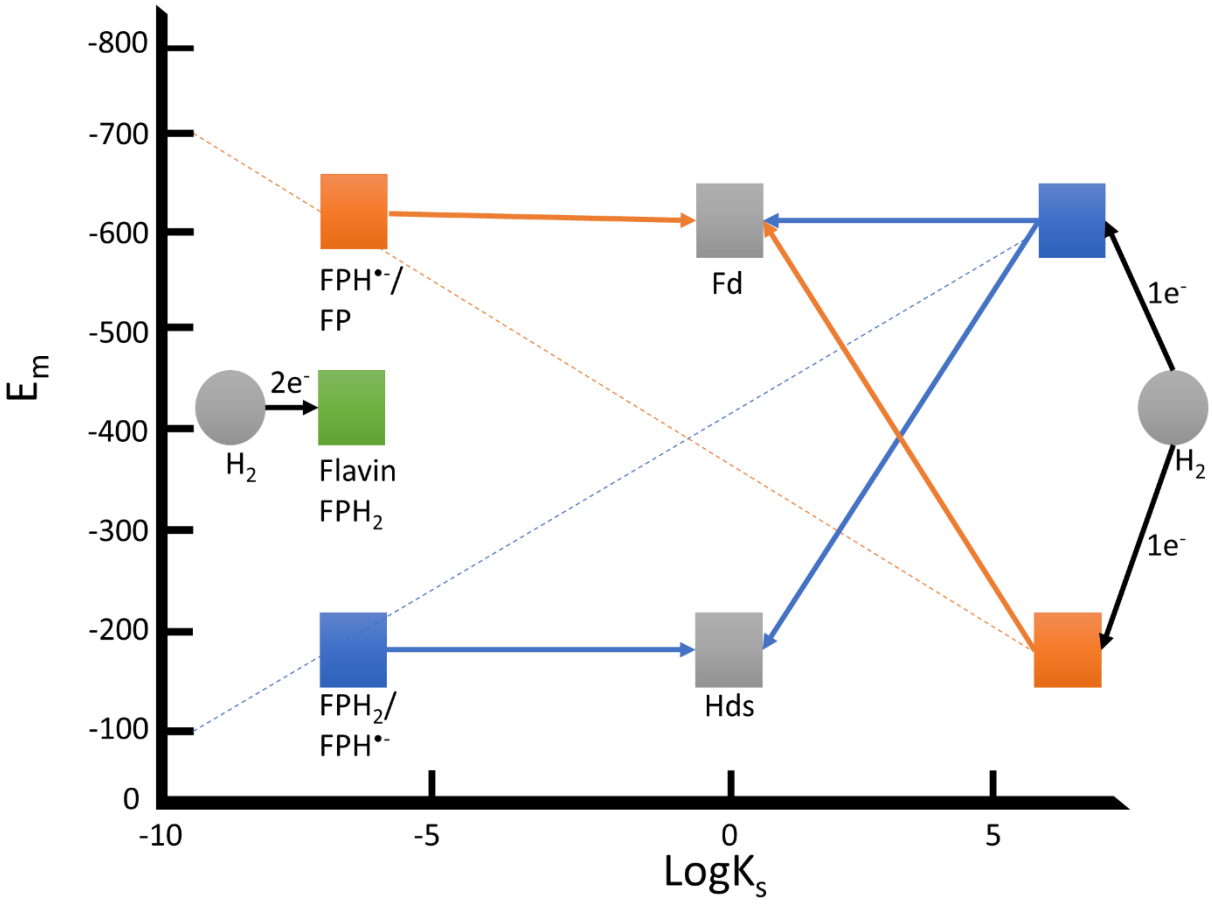

Figure 1.19: Cartoon diagram on the theory of how flavin based-electron bifurcation occurs with Hdr in connection to its redox potentials. (Adapted from Thauer.)[46]

1.5.1.5 Crystal Structure of the Mvh:Hdr Complex

Figure 1.20 represents the protein crystal structure of Mvh:Hdr from *M. thermolithotrophicus* and **Figure 1.21** shows the series of iron-sulfur clusters within the structure. Once Wagner et al. determined the protein crystal structure of Mvh:Hdr, they hypothesized The initial start begins as discussed earlier in this section except instead of going from MvhG to MvhD, they propose that the electron travels from cluster 'G3' to cluster 'A1' in HdrA instead. 'A1'

transports it to ‘A2’ which sends the electron to the cluster in MvhD. From there, three different scenarios were proposed for the electron pathway through the enzyme.

Each scenario incorporates conformational changes since the clusters between the [2Fe-2S] and the [4Fe-4S] clusters and FAD are too far away from one another to transfer the electron. The first scenario suggests the [2Fe-2S] cluster is destabilized by a homodisulfide bridge formed between two Cys. Once this occurs, the N-terminal domain of HdrA rearranges to electronically bridge the ‘A3’ cluster between the [2Fe-2S] cluster and the FAD.[34] The second scenario states the inserted Fd domain at the periphery of the HdrA complex is flexible enough to form an electronic bridge between the [2Fe-2S] cluster, FAD, and the ‘A5’ and ‘A6’ clusters (**Figure 1.22**).[34] The last scenario suggests the structure of MvhD performs a conformational change. Since this structure sits on a flexible arm, the hypothesis suggests MvhD would twist within a small gap between it and the periphery area of HdrA. The distance between the [2Fe-2S] cluster will, then, be mediated by two Cys in HdrA to reach the FAD molecule.[34] From here, they suggested the electron goes straight to the FAD where the bifurcation occurs. ‘A4’ accepts the first electron to send onto a series of iron-sulfur clusters in HdrC and HdrB to reduce the HDS. The second electron goes from ‘A5’ to ‘A6’ to reduce Fd. Though this predicted pathway shows potential, our lab came up with arguments to this proposal and other ideas for the electron pathway.

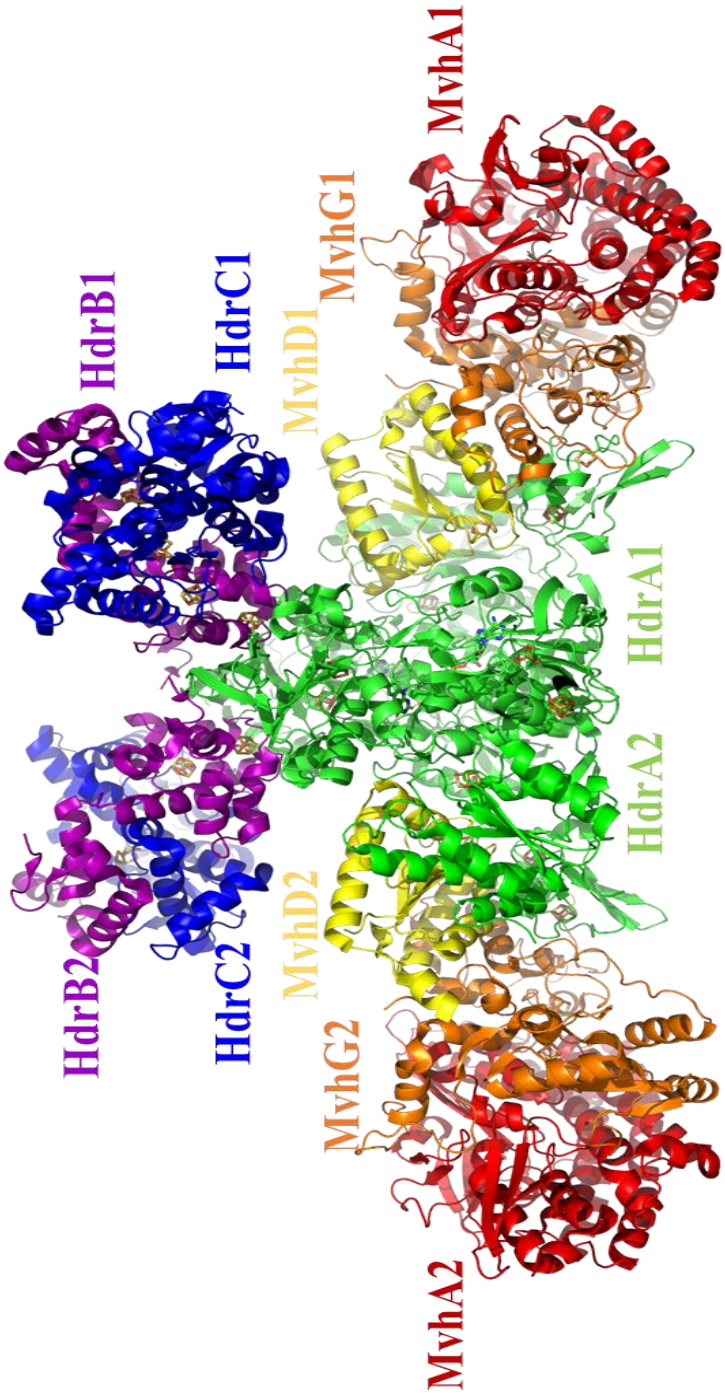

Figure 1.20: Crystal structure of the Mvh:Hdr complex from *Methanothermococus thermolithotrophicus* (PDB: 50DC).[34]. Note that two copies of each enzyme are present.

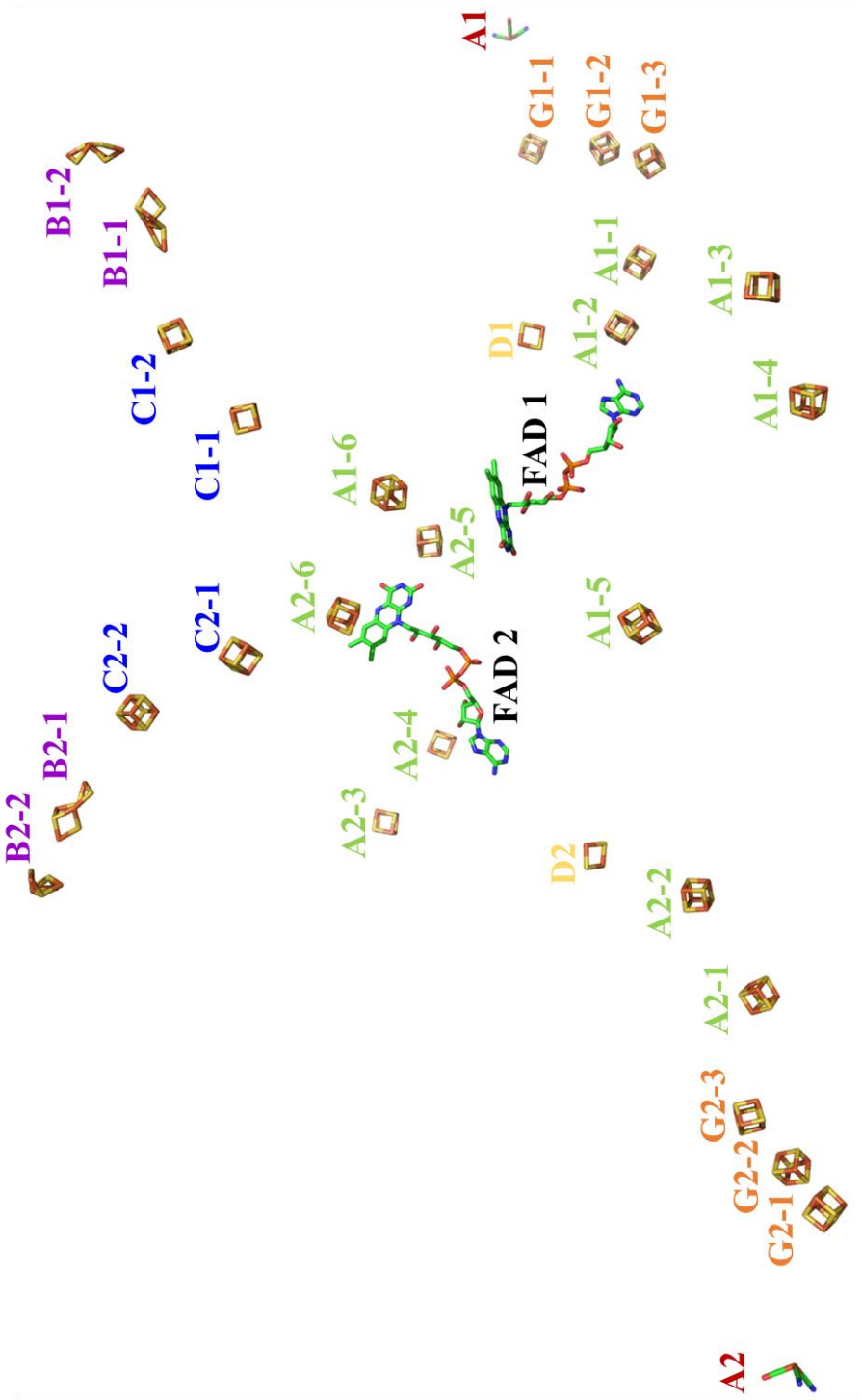

Figure 1.21: Iron-sulfur clusters and FAD present in Hdr.[34] Hdr is a dimer and, therefore, this figure shows both monomers containing iron-sulfur clusters.

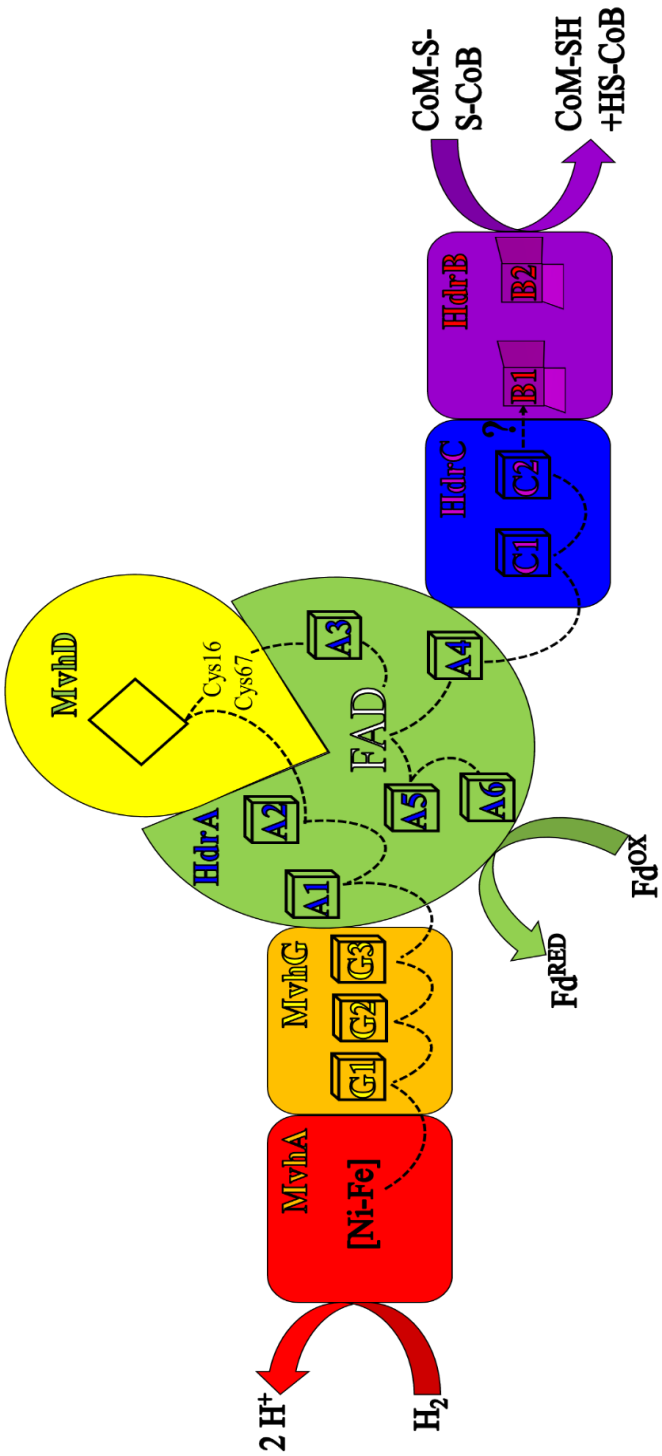

Figure 1.22: A schematic theory of the travel pathway of the electron predicted by Wagner et al.[34] This figure represents the first scenario predicted by the authors. The dashed lines represent the direction at which the electron will travel.

Figure 1.23 represents the predicted mechanism of the flavin-based electron bifurcation suggested in the Duin laboratory. Similar to the cytochrome b_6f enzyme structure, our lab hypothesized the [2Fe-2S] cluster would move within Mvh:Hdr. However, we do not believe this cluster to be a Rieske [2Fe-2S] cluster because the potential would be too high. A higher potential would require more energy to transfer the electron to a lower potential. The second argument to the author's theory was the electronic bridge formed by the two Cys in MvhD. A homodisulfide forming fits in with the theory of the FAD molecule accepting two electrons simultaneously as discussed earlier in section 1.5.1.2 to put it in a more thermodynamically favorable situation. However, the Duin laboratory argues two different Cys form a homodisulfide. Based on the sequence motif CSIC within HdrA, we hypothesized two Cys form a homodisulfide which release two electrons simultaneously to FAD. Therefore, it is suggested that the area of HdrA containing 'A3' performs a conformational change to move this cluster closer to the [2Fe-2S] cluster. 'A3' would have the ability to transfer the electrons to the two Cys to perform the homodisulfide before sending the two electrons to FAD. From there, the first electron is transferred to 'A4' which transfers the electron through other iron-sulfur clusters in HdrC and HdrB to reduce HDS. The second electron is transferred to 'A5' and then onto 'A6' to transfer the electron to Fd^{OX}. This theory came from a docking study had been performed showing the greatest possibility of Fd to have protein-protein interaction with Mvh:Hdr in *M. maripaludis* is on the section of HdrA with 'A5' and 'A6'.[47] Studies on the redox potentials are presented in Chapter 2.

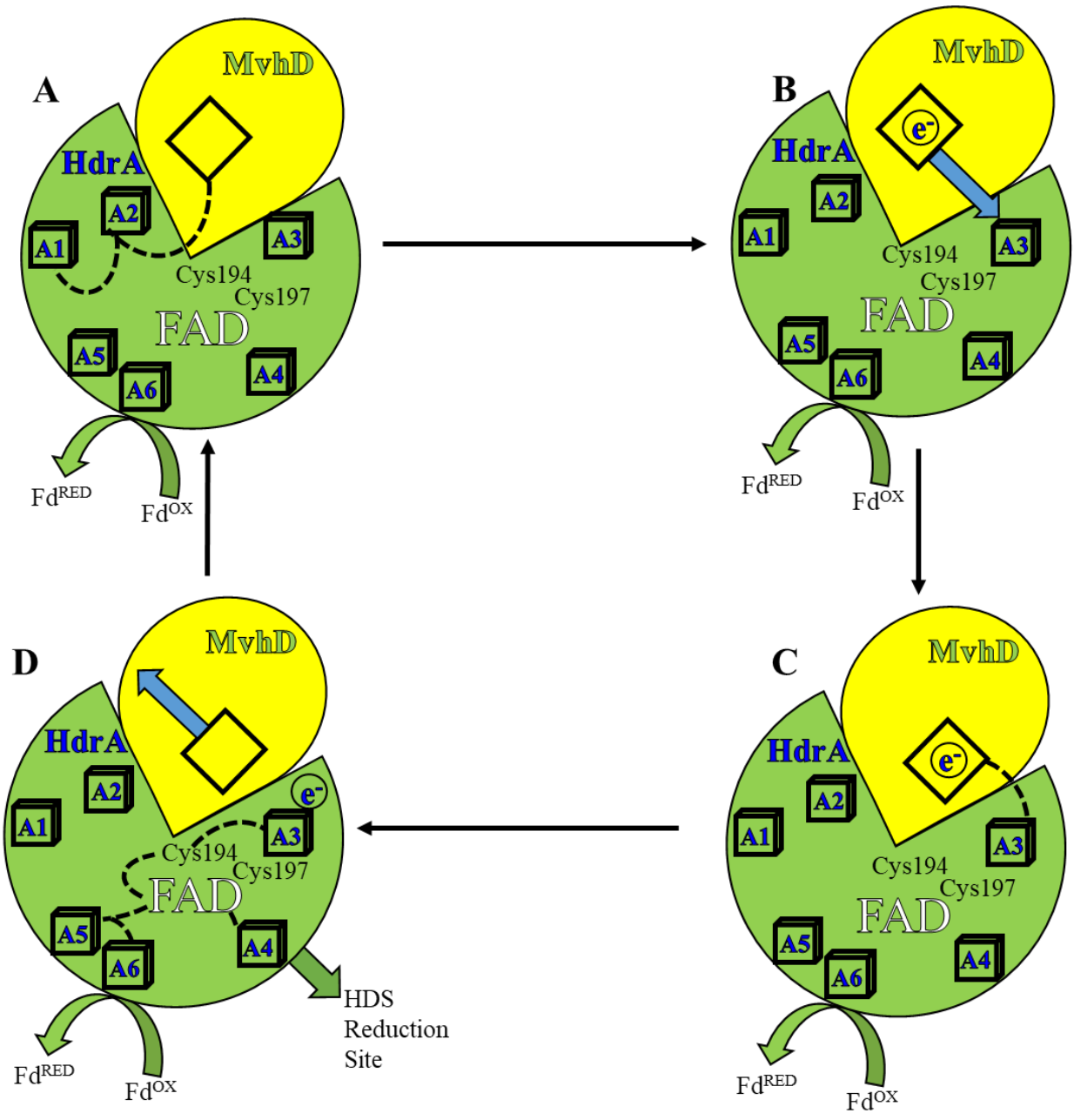

Figure 1.23: Schematic theory of the electron pathway within HdrA developed in the Duin laboratory.

1.5.2 Non-cuboidal Clusters

Many researchers have shown interest in studying HdrB to determine the reduction mechanism of HDS. Madadi-Kahkesh et al. analyzed isolated HdrB in the presence of HDS, CoM, and CoB separately to develop a theory as to which part of the HDS would bind to the [4Fe-4S] cluster.[48] It is important to note during this time the group was under the impression HdrB only had one, cuboidal [4Fe-4S] cluster.

Madadi-Kahkesh et al. performed EPR-monitored redox titrations and steady state conditions to analyze the binding effects of the individual substrates. These researchers were unsure as to what type of iron-sulfur cluster was present in HdrB and what the oxidation state was to reduce the substrate. They found when the cluster is in its oxidized form, CoM binds to an Fe of the cluster and creates a paramagnetic species. The species showed g-values of 2.011, 1.991, and 1.938.[48] In the presences of CoB, the g-values were 2.018, 1.996, and 1.954.[48] These EPR signals did not appear similar to a typical $[4Fe\text{-}4S]^{2+/+}$, $[2Fe\text{-}2S]^{2+/+}$, or a $[3Fe\text{-}4S]^{+}$ signals due to the shape of the signal, the g-values. Therefore, they believed it to be a $[4Fe\text{-}4S]^{3+/2+}$ cluster. [48] Further studies elaborated on the mechanism with this type of cluster.

Mixing Hdr with CoB and CoM, these researchers studied the binding through variable temperature magnetic circular dichroism (VTMCD), ultraviolet-visible spectrophotometry (UV/Vis), Raman resonance, and electron-nuclear double resonance (ENDOR).[49] To their excitement, they confirmed the [4Fe-4S] did indeed have a 3+ oxidation state when comparing to data of another similar enzyme N-ethylmaleimide modified enzyme-ferrodoxin: thioredoxin reductase (NEM-FTR).[49] The difference between these two enzymes came down to their iron-sulfur interactions with the substrates. It was predicted the active-site cluster in Hdr has a direct interaction when reducing HDS. The cluster in FTR mediates the reduction of the substrate

disulfide through an active-site disulfide.[49] With this evidence, Duin et al. hypothesized a mechanism for the reduction of HDS as seen in **Figure 1.24**. In the reduced form, HDS combined and a thiol exchange reaction results in a [4Fe-4S]$^{+}$-CoM complex where the CoM has a strong interaction with one of the S-Cys. Internal electron transfer weakens that bond resulting in the formation of [4Fe-4S]$^{3+}$-CoM. Reduction by an external electron source results in the release of CoM and regeneration of the enzyme.[49]

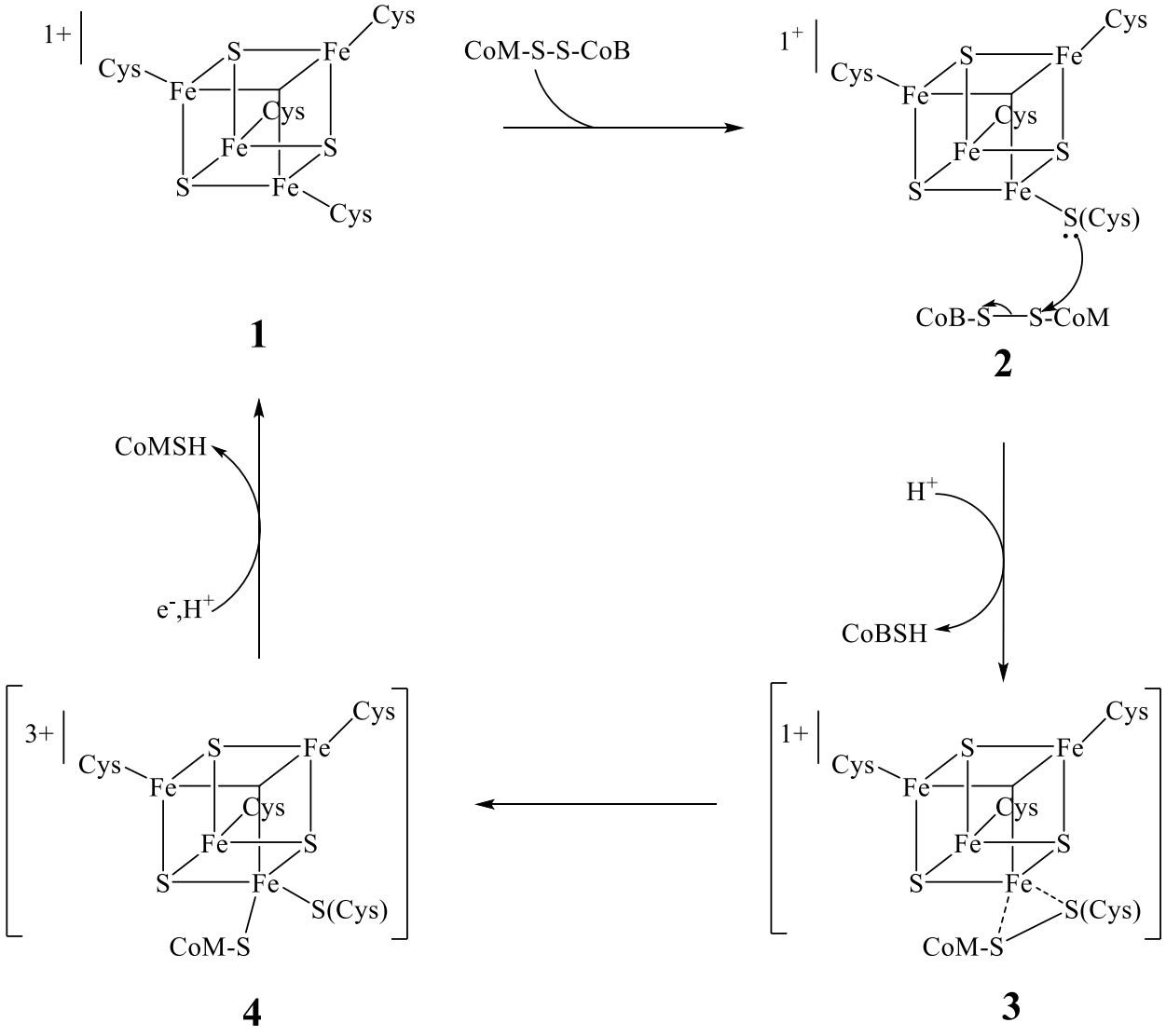

Figure 1.24: Hypothetical reaction mechanism for HDS reduction.[49]

As mentioned in section 1.3.2, iron-sulfur clusters have unique motifs which indicate what type of cluster will form in the enzyme. In contrast, two motifs (i.e. CCG site) found in HdrB were ($CX_{31-39}CCX_{35-36}CXXC$) which show a considerable difference to a typical [4Fe-4S] cluster motif as described in section 1.3.2.[50] Initial studies when purifying HdrB from *M. marurgensis* into *E. coli* showed a [2Fe-2S] present.[51] After reconstitution was performed, a [4Fe-4S] cluster was formed but they still found a Zn metal present. This led the authors to believe the other CCG site to contain a Zn metal binding site. Because Hdr displayed similar functions and sequence motifs to the enzyme succinate: quinone reductase (SQR) and X-ray spectroscopy showed both HdrB and holoenzyme HdrABC contained Zn, the authors believed one site contained a [4Fe-4S] and the other contained a Zn metal binding site.[50,51] In contrast, we hypothesized argues about the similarity between the two CCG motifs in HdrB.

The two motifs in HdrB are $CX_{29}CCX_{35}CX_2C$ and $CX_{38}CCX_{35}CX_2C$ which show how similar these sites are to one another. Therefore, if one motif is an iron-sulfur cluster binding site, why would the other motif be a Zn metal binding site? Reconstitution may reform the iron-sulfur cluster, but it cannot, necessarily, remove the Zn. In addition, a predicted structure calculated by i-Tasser indicated the cysteines to be in similar positions as for each motif and capable of coordinating a cluster (**Figure 1.25**). Lastly, Fielding et al. expressed a recombinant HdrB from *M. maripaludis* into *E. coli*.[50] This host can bind Zn metal due to metal-binding enzymes it contains, and/or the material used to purify the protein. Our hypothesis suggests HdrB from this study likely bound Zn within the CCG motif site due to its expression host. The protein crystal structure proved to indicate both CCG motif sites were iron-sulfur cluster binding sites.[34]

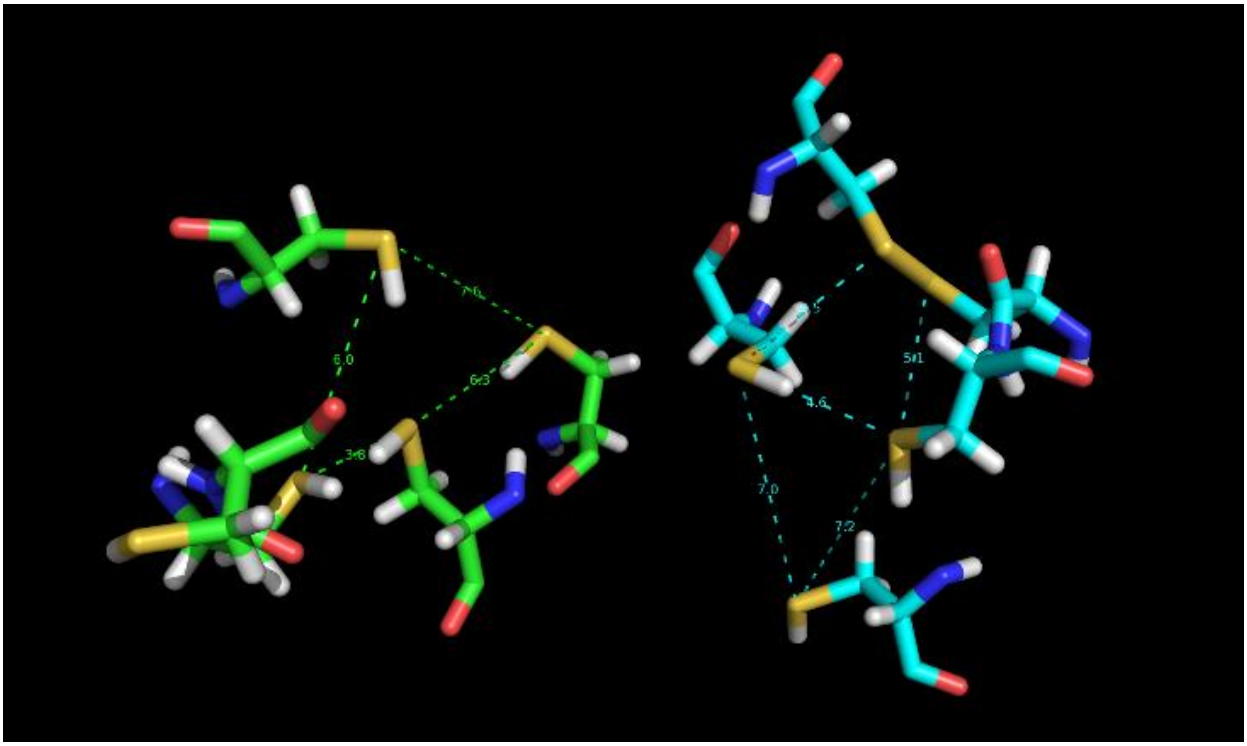

Figure 1.25: i-Tasser predicted structure of HdrB in *Methanothermobacter marburgensis.* Each molecule represents a Cys part of the CCG motif site.

As seen previously in **Figure 1.21**, there are a row of iron-sulfur clusters and at the end of each row are two iron-sulfur clusters which were termed as 'non-cuboidal' (**Figure 1.26**) by Wagner et al.[34] At initial glance, the clusters look like a [3Fe-4S] cluster but the researchers realized there were 4 Fe and 4 S atoms coordinated to one another. The difference between the non-cuboidal and cuboidal clusters is the non-cuboidal look similar to 2 [2Fe-2S] clusters attached at one common Fe atom while the cuboidal, as related to its name, is cubed shaped. The mechanism of the reduction of HDS became even more of a mystery now that researchers knew there were two non-cuboidal iron-sulfur clusters involved in the process. One that had CoM bound and one that had CoB bound. These details are discussed further in Chapter 3.

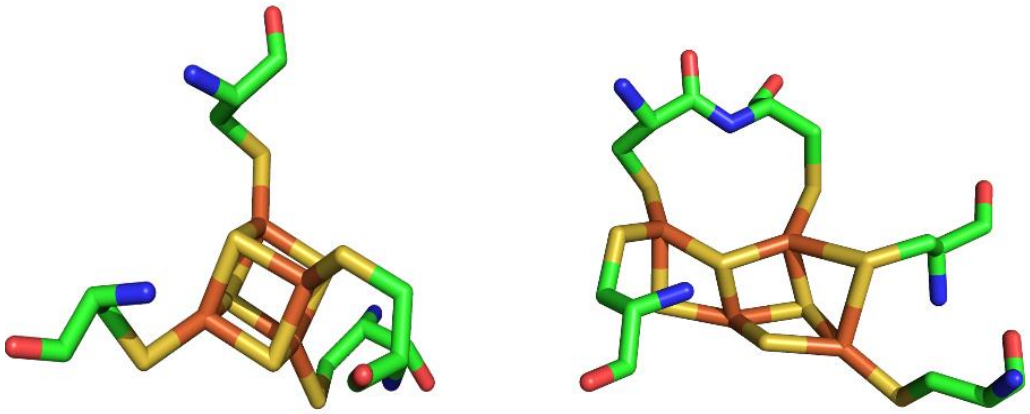

Figure 1.26: Typical cuboidal [4Fe-4S] cluster (Left) and the noncuboidal [4Fe-4S] (Right) cluster discovered in the active site of Hdr.[34]

1.6 Significance of Research

There is an interest in using a reverse methanogenesis pathway to capture methane and convert it into an isoprene-based biofuel. Currently, the criterion to engineer this pathway in methanogens involve an understanding of the enzymes involved in this process and their function. Because the discovery of flavin adenine dinucleotide (FAD)-based electron bifurcation occurred recently in 2008, more research is required to understand the mechanistic pathway of the methane production. The natural, closed carbon cycle averts this gas from entering the atmosphere.[52] Overtime, however, daily human activities, such as oil exploration and increasing husbandry, has caused an imbalance in the carbon cycle. Thus, more and more methane releases into the Earth's atmosphere which traps more ultraviolet light from the sun. Consequently, the Earth's average temperature increases and causes substantial damages to the ecosystem. This occurrence refers to as global warming has been a monumental topic currently in the United States.[53] While some consider global

warming a crisis, others minimize the issue. Recent NASA reports proved daily human activities over the past decades increased the amount of CO_2, CH_4 and N_2O produced which caused significant damage to the Earth's ecosystem (i.e. the increased acidity of the oceans due to the absorption of higher amount of CO_2) and increased the Earth's surface temperature.[54] According to the Natural Resources Defense Council (NRDC), carbon pollution is the main cause of the increase in temperature, weather disasters and health issues.[55] With the continuing rise of these issues today, researching and developing more economical ways in preventing other harmful chemicals from entering the atmosphere have become tremendously important. [56] DSM/Duin are working on the development of inhibitors for MCR and had great success.[57] This work can be further expanded to other unique targets like Hdr and the Mcr accessory enzymes and proteins. EPR monitored-redox titrations and rapid freeze quench experiments were performed on Mvh:Hdr and isolated subunits of Hdr to further analyze the characteristics of the iron-sulfur clusters involved in the reduction of HDS. The redox potentials were established for certain clusters which helped shed some light on the function of Hdr.

Chapter 2: Mvh:Hdr and Isolated Hdr

2.1 Introduction

Methane production by methanogens is a large contributor to increased levels of methane in the atmosphere which causes global warming.[8,57] Understanding this process and finding targets for inhibition is an important theme in the Duin laboratory. Though Mcr is an important target due to its direct role in methane creation, heterodisulfide reductase (Hdr) is an equally important target because of its role in the energy balance in the cell and regeneration of the Mcr substrates. Since Hdr is present as a hydrogenase:Hdr complex (Mvh:Hdr) that performs FAD-based electron bifurcation, this has become a fundamental interest. The available crystal structure shows several electron paths for the electron to travel from the different active sites to and from FAD.

An assumption suggested for the general pathway of the electron begins at MvhA and goes on to HdrA, the location of the FAD molecule. Here, one electron goes onto the active site in HdrB while the second electron transfers to Fd. For an electron to transport between iron-sulfur clusters and other compounds, the preferred distance is <10 Å. The closest distance between the [2Fe-2S] ('D2') cluster in MvhD and the isoalloxazine ring of FAD is ~13Å which is too far away to transport the electrons successfully. Theories suggest an area of HdrA containing the 'A5' cluster twists to move closer to the 'D2' cluster (**Figure 2.1**).[34] This would put a closer distance for the 'D2' cluster to transfer the electron. In addition, our lab advises, based on the sequence motif, that two cysteines next to 'A5' form a homodisulfide bond to create a thermodynamically favorable situation.[46,58] The acceptance of these two electrons, simultaneously, will put the flavin's potential between the two formal redox potentials (**Figure 2.2**).[41,46] 'A6' sequentially accepts the electron from FAD for the reduction of HDS and, subsequentially, 'A3' would accept the second

electron for the reduction of Fd. For the electron transfer to ‘A3’, questions remain as to how this process occurs over a distance >30 Å.

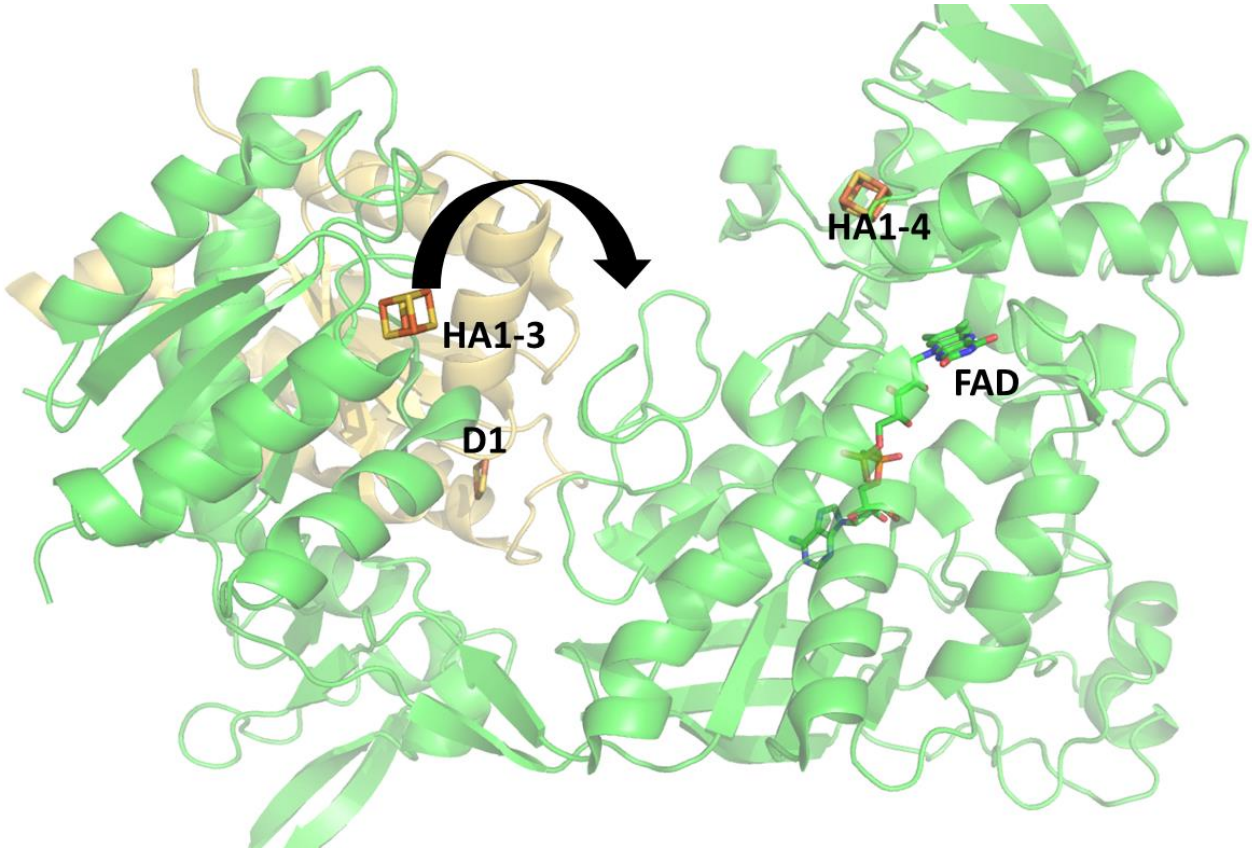

Figure 2.1: Theory suggesting a conformational change before the flavin based-electron bifurcation occurs. Since there is a small amount of coil in the area ‘A5’ as indicated by the black oval, it is believed the part of this structure twists to put the ‘A5’ cluster closer to the ‘D2’ cluster. This would allow the clusters to be closer together and transfer the electron on to the two cysteines near ‘A5’.[34]

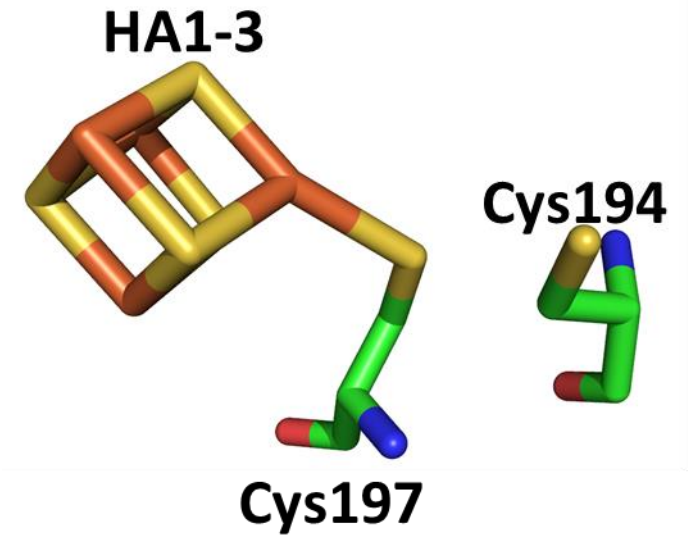

Figure 2.2: Two cysteines responsible for forming a homodisulfide to transfer two electrons to FAD. These cysteines are next to 'A5' which is near FAD after the conformational change potentially occurs.

Computational studies indicated the highest probability based on hydrophobic interactions is for Fd to bind near the 'A5' and 'A6' clusters (**Figure 2.3**). The issue at hand is the large distance between 'A3' and FAD. One theory suggests a possible second conformational change.[34] Similar to the Rieske [2Fe-2S] cluster in Complex III, this area consists of mostly coils which makes it flexible to move. The coils would, potentially, stretch up towards the isoalloxazine ring of FAD, putting the iron-sulfur clusters closer to accept the second electron during the flavin based-electron bifurcation. The other suggestion would be electron tunneling through aromatic amino acids. Looking further into the sequence of Mvh:Hdr, 3.4% of the total amino acids are tyrosines and are evenly distributed throughout the structure. This aromatic amino acid has been shown affective in

electron tunneling over larger distances.[58] This provided our lab with the idea that electron tunneling could occur during the electron transfer between FAD and 'A3'.

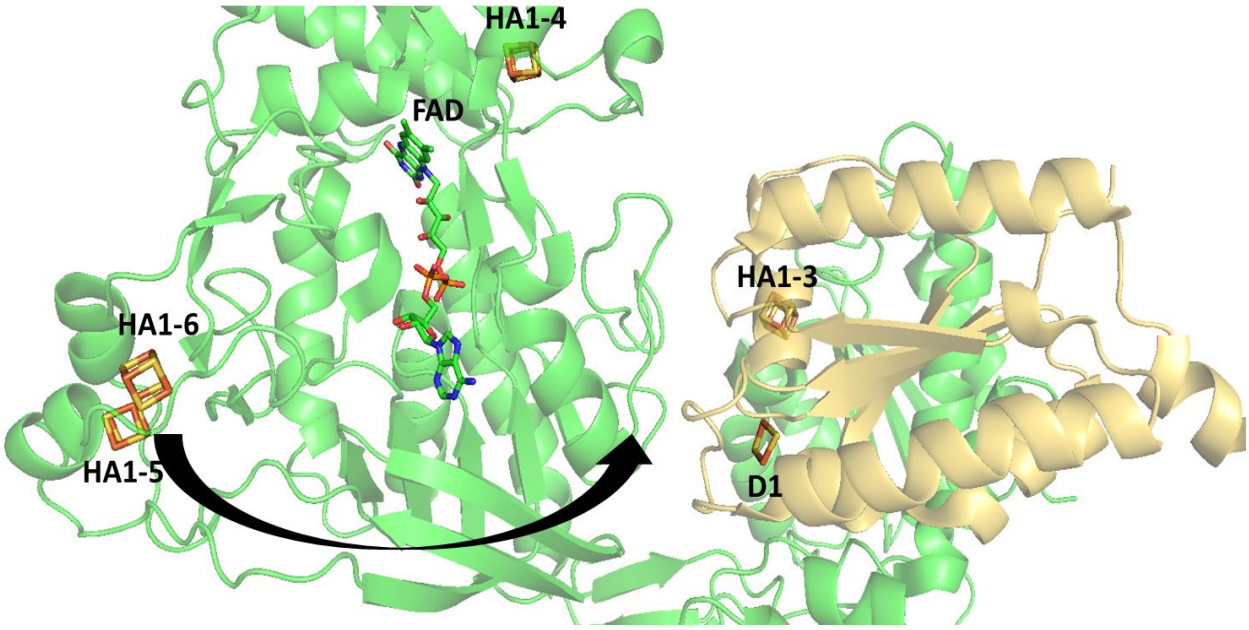

Figure 2.3: Area of HdrA in which computational results indicated Fd would bind. The suggested conformational change is indicated by the green arrow.[34]

In addition to solving this complex mechanism, studies on the active site, HdrB, has increased in interest to determine the reduction mechanism of HDS. For years, researchers believed this subunit only contained one iron-sulfur cluster present and found isolated redox potentials for this cluster.[49,59] After isolating HdrB from *Bacillus subtillis*, Madadi-Kahkesh and other researchers mixed CoMSH, CoMS[33]H, and CoBSH to determine which compound would bind to the iron-sulfur cluster and analyze this binding effect through EPR.[59,60] Since the new discovery of the second iron-sulfur cluster present in HdrB, our lab has wondered what redox potential this

second cluster consists of and which one was being detected by EPR. This information is vital for inhibition studies.

The overall research goal is to determine the mechanism of the flavin-based electron bifurcation and the reduction of HDS through EPR monitored-redox and kinetic studies. Previous studies have been performed on isolated Mvh and Hdr which established certain EPR signals.[27,51,59] Therefore, studying the whole complex was necessary to see if any additional signals would appear when Mvh is removed or if the splitting of the complex had an effect on any of the detected signals. For this research, we purified Mvh:Hdr from *M. marburgensis* considering this organism is a fast-growing organism that reaches high density ($O.D._{627}$=8) within ~13 hours and provides ample enzyme for these studies. For comparison of the Hdr EPR signals, we isolated Mvh and Hdr to see if the separation of the two had any effect on the cofactors.[45,61] Based on our studies, the redox potentials for some of the clusters can now be assigned.

2.2 Materials and Methods

2.2.1 Reagents

The following chemicals were ordered from Sigma Aldrich: N-hydroxysuccinimide, dicyclohexyl carbodiimide, neutral red, benzyl viologen, 1,10-phenanthroline, safranin O, phenosafranin, methyl viologen, 2-hydroxy-1,4-napthoquinone, 1,2-napthoquinone-4-sulphonate, triethylamine, and metronidazole. Chemicals ordered from Alfa Aesar located in Ward Hill, MA: thiourea, dithionite (DIT), benzene, and anthraquinone-2-sulphonate. The chemicals ordered from VWR were tris, HEPES, Chaps, sodium hydroxide, sodium chloride, potassium iodide, sodium dodecylsulfate, glycine, ammonium chloride, sodium bicarbonate, acetonitrile, acetone, dichloromethane, and iodine. The following chemicals were ordered from TCI located in Portland, OR: sodium 2-mercaptoethane sulfonate (Coenzyme M, CoM), flavin adenine dinucleotide

(FAD), indigo carmine, thionine, and 1,4-benzoquinone. Sodium carbonate, ammonium persulfate, and potassium phosphate monobasic were ordered from Amresco located in Solon, OH. Magnesium chloride hexahydrate and ethyl acetate were ordered from Macron Fine Chemicals located in Center Valley, PA. Potassium phosphate dibasic, *p*-dioxane, methanol, hydrochloric acid, deuterium oxide, and methyl butane were ordered from EMD Millipore located in Billerica, MA. Lastly, deuterated chloroform was ordered from Acros Organics located in New Jersey and 7-bromoheptanoic acid was ordered from Matrix Scientific located in Columbia, SC.

2.2.2 Synthesis of Heterodisulfide (CoM-S-S-CoB; HDS)

2.2.2.1 7,7'-Dithiobisheptanoic acid[62]

In separate flasks, 7-bromoheptanoic acid (**12**) (9.6 g, 46.6 mmol) with thiourea (**13**) (17.4 g, 228 mmol) and ethanol were purged with N_2 gas for 30 minutes to dry the reactants and solvents. Compound **12** and **13** were dissolved in ethanol (110 mL) and the solution was heated to reflux at 90°C for 17 hours. Once the reaction was complete, the mixture was cooled to room temperature and 60% NaOH (w/v; 25 mL) was added. The solution was heated to reflux for an additional 2 hours and cooled to room temperature once again. The reaction mixture was concentrated under vacuum at 60-70°C to half the original volume. 1 M HCl (100 mL) was added to neutralize any excess NaOH and was followed by 12.1 M HCl (20 mL) to acidify the compound to produce the thiol intermediate. The thiol was extracted three times with dichloromethane (DCM, 100 mL). The organic layer of this extraction was extracted three times with 1 M sodium bicarbonate (150 mL). The aqueous layer was acidified using HCl to a pH of 1-2. This mixture was extracted three times with DCM (200 mL). The organic layer was concentrated under vacuum at 25°C to 70 mL. The thiol was oxidized by titrating in an aqueous solution of 10% iodine (w/v) and 20% KI (w/v) (i.e. KI_3) until the brown color persisted. This mixture was washed three times with 1 M sodium

thiosulfate (100 mL) to react with the excess KI_3 and then washed with DI water (100 mL) to remove any other impurities. The organic layer was concentrated under vacuum at 25°C to obtain a crude residue of 7,7'-dithiobisheptanoic acid (**15**). The crude residue was recrystallized using benzene, and the crystals were collected by filtration and washed with cold benzene. The product (compound **15**) was dried under high vacuum for two days to furnish ~3.3-4 g (46%-61%). **Scheme 2.1** shows the full synthesis of compound **15** while **Figure 2.4** shows the ^1H NMR result which was confirmed by literature.[62]

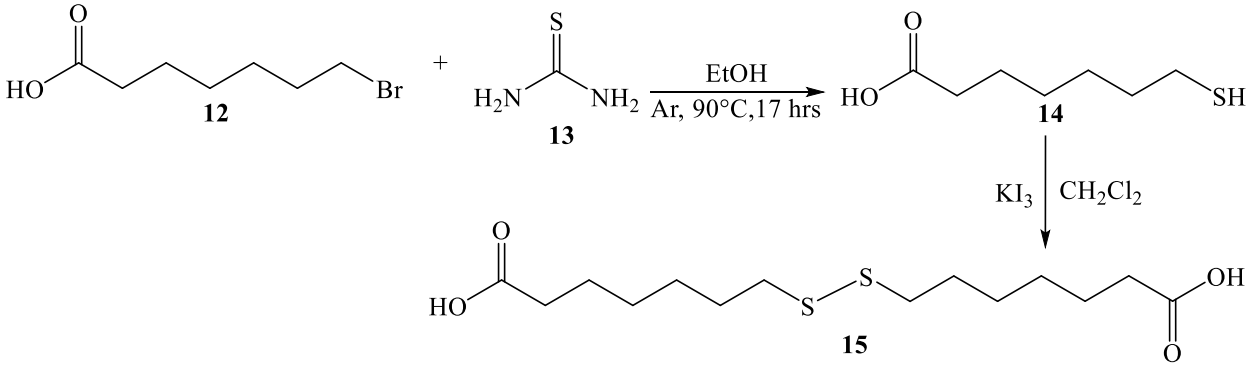

Scheme 2.1: Synthesis of 7,7'-dithiobisheptanoic acid.

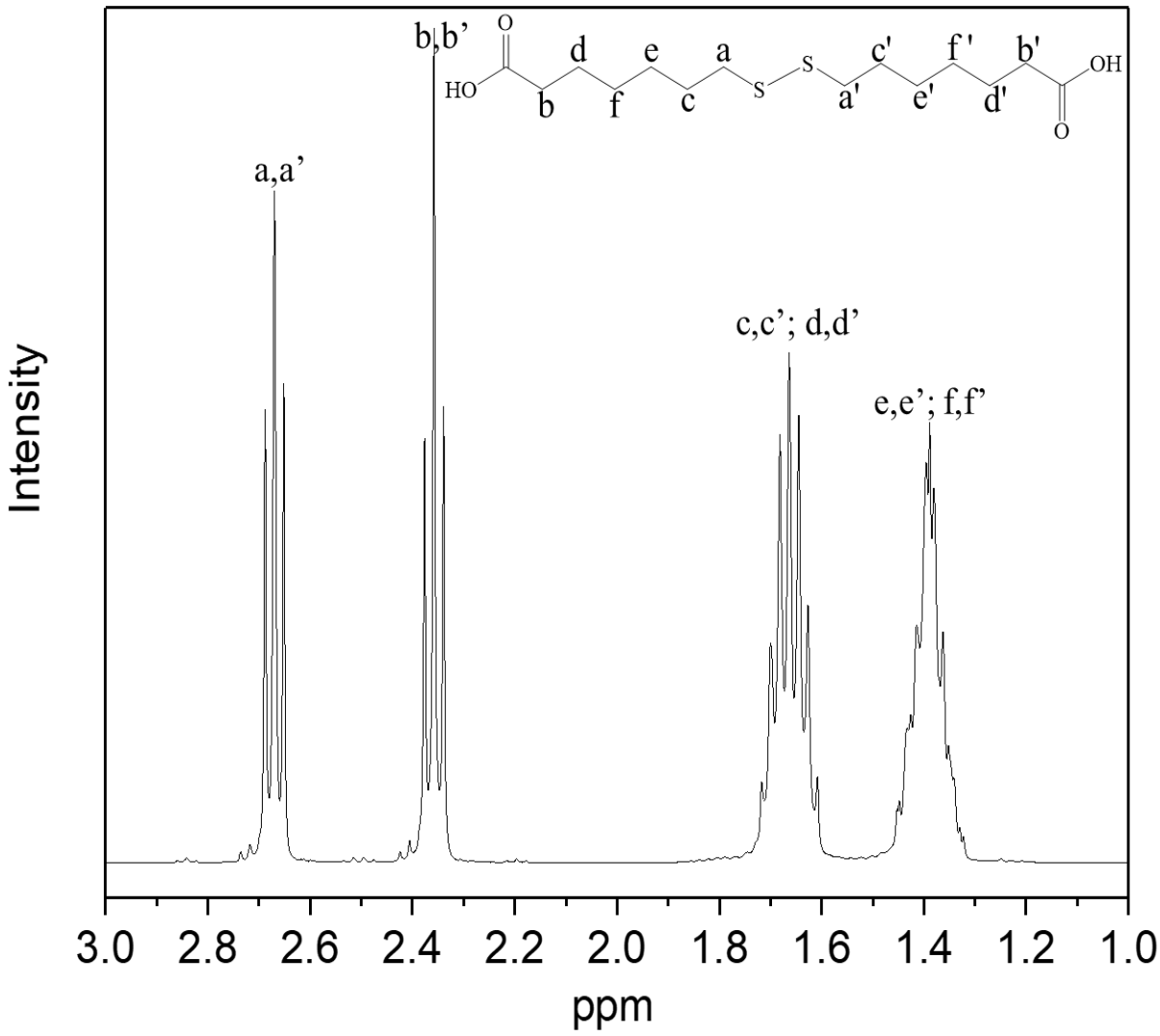

Figure 2.4: ^{1}H NMR ($CDCl_3$, 400 MHz) of 7,7'-dithiobisheptanoic acid: 2.69 (t, 4 H); 2.37 (t, 4 H); 1.62-1.72 (m, 8 H); 1.37-1.43 (m, 8H).

2.2.2.2 7,7'-dithiobis(succinimido-oxyheptanoate)[62]

Compound **15** (388 mg, 1.2 mmol) was dissolved in *p*-dioxane (8 mL) at room temperature. N-hydroxysuccinimide (**16**) (290 mg, 2.5 mmol) was added to this mixture until the solid dissolved. Finally, dicyclohexylcarbodiimide (505 mg, 2.4 mmol) was dissolved in *p*-dioxane (3

mL) and added dropwise to the mixture to allow this compound to react with the reactants without creating too many unwanted by-products.[63] The reaction was stirred at room temperature for 16 hours. The dicyclohexylurea residue was removed by filtration. The filtrate was concentrated under vacuum at 70°C to obtain a crude oil of 7,7'-dithiobis(succinimido-oxyheptanoate) (**17**). The compound was recrystallized twice using isopropanol and the product was collected by filtration. Compound **17** yielded ~384 mg (62%). **Scheme 2.2** shows the synthesis of compound **17** which was continued from **Scheme 2.1**. The NMR spectrum (**Figure 2.5**) was also compared to literature articles to ensure the correct product was synthesized.[62]

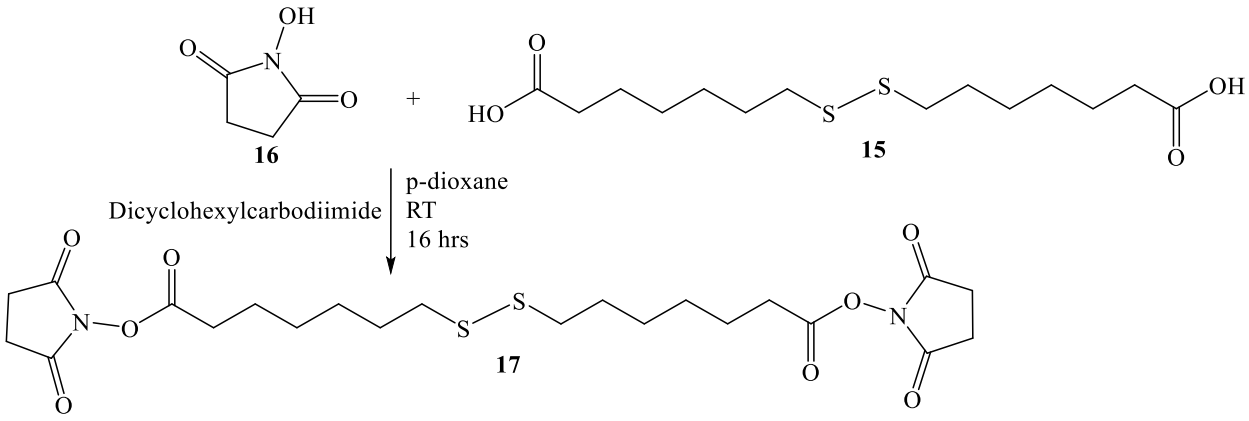

Scheme 2.2: Synthesis of 7,7'-dithiobis(succinimido-oxyheptanoate).

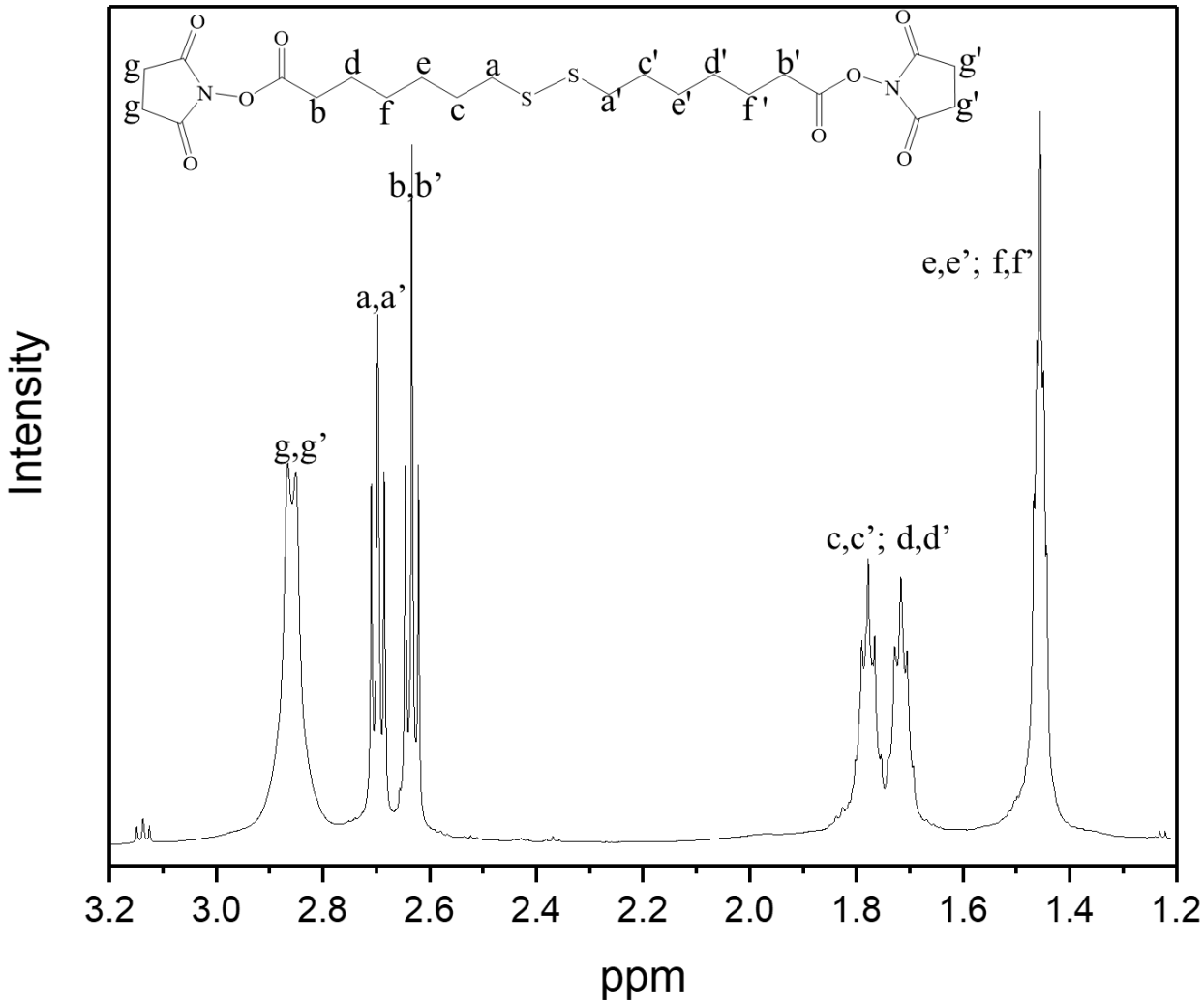

Figure 2.5: ^{1}H NMR ($CDCl_3$, 400 MHz) of 7,7'-dithiobis(succinimido-oxyheptanoate): 2.86 (s, 8 H); 2.70 (t, 4 H); 2.63 (t, 4 H); 1.70-1.79 (m, 8 H); 1.44-1.46 (m, 8 H).

2.2.2.3 (+)-N,N'-(7,7'-dithio-diheptanoyl)bis(O-phospho-L-threonine) (CoB-S-S-CoB)[62]

DI water, triethylamine, tetrahydrofuran (THF), acetonitrile, compound **17** (400 mg, 2 mmol), and O-phospho-L-threonine (**18**) (362 mg, 0.7 mmol) were purged in separate flasks under N_2 for 30 minutes to achieve anoxic conditions. Compound **18** was dissolved in triethylamine (0.56 mL, 4 mmol) and DI water (4 mL) under Ar. Compound **17** was dissolved in THF (18 mL) and acetonitrile (4 mL) and added to the compound **18** solution under stirring in an Ar atmosphere. The reaction was stirred at room temperature under Ar for 36 hours. Next, the reaction was concentrated under vacuum at 30°C until a residue was obtained. The residue was dissolved in 1 M HCl (25 mL) and washed three times with DCM (8 mL). The aqueous layer was loaded onto a polymetric adsorbant (PAD-II) column (equilibrated overnight with 1 M HCl) followed by 1 M HCl (100 mL) and DI water (150 mL) to wash impurities off the column. The eluents were as followed: 1) 4:1 water: MeOH (80 mL), 2) 1:1 water: MeOH (120 mL), 3) 1:4 water: MeOH, and 4) MeOH. Product eluted with 1:1 and 1:4 water: MeOH solutions and was concentrated at 50°C to 1/10 of the original volume. 2 M ammonia (2 mL) was added to obtain CoB-S-S-CoB (**19**) and concentrated under high vacuum until a solid was obtained. This reaction yielded ~15% of product (**Scheme 2.3, Figure 2.6-2.7**).

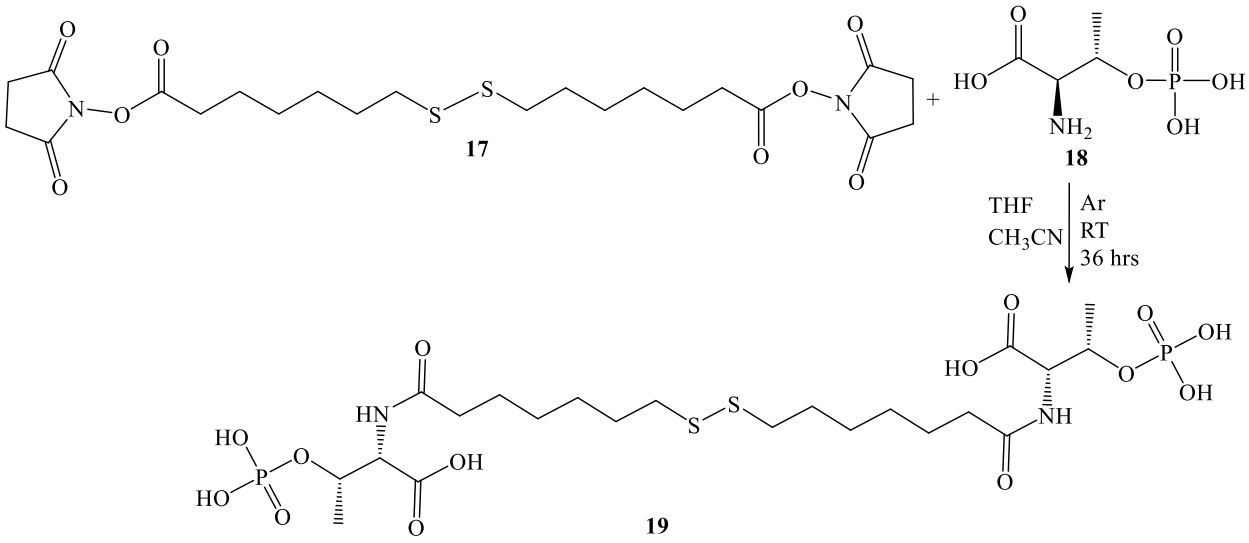

Scheme 2.3: Synthesis of CoB-S-S-CoB.

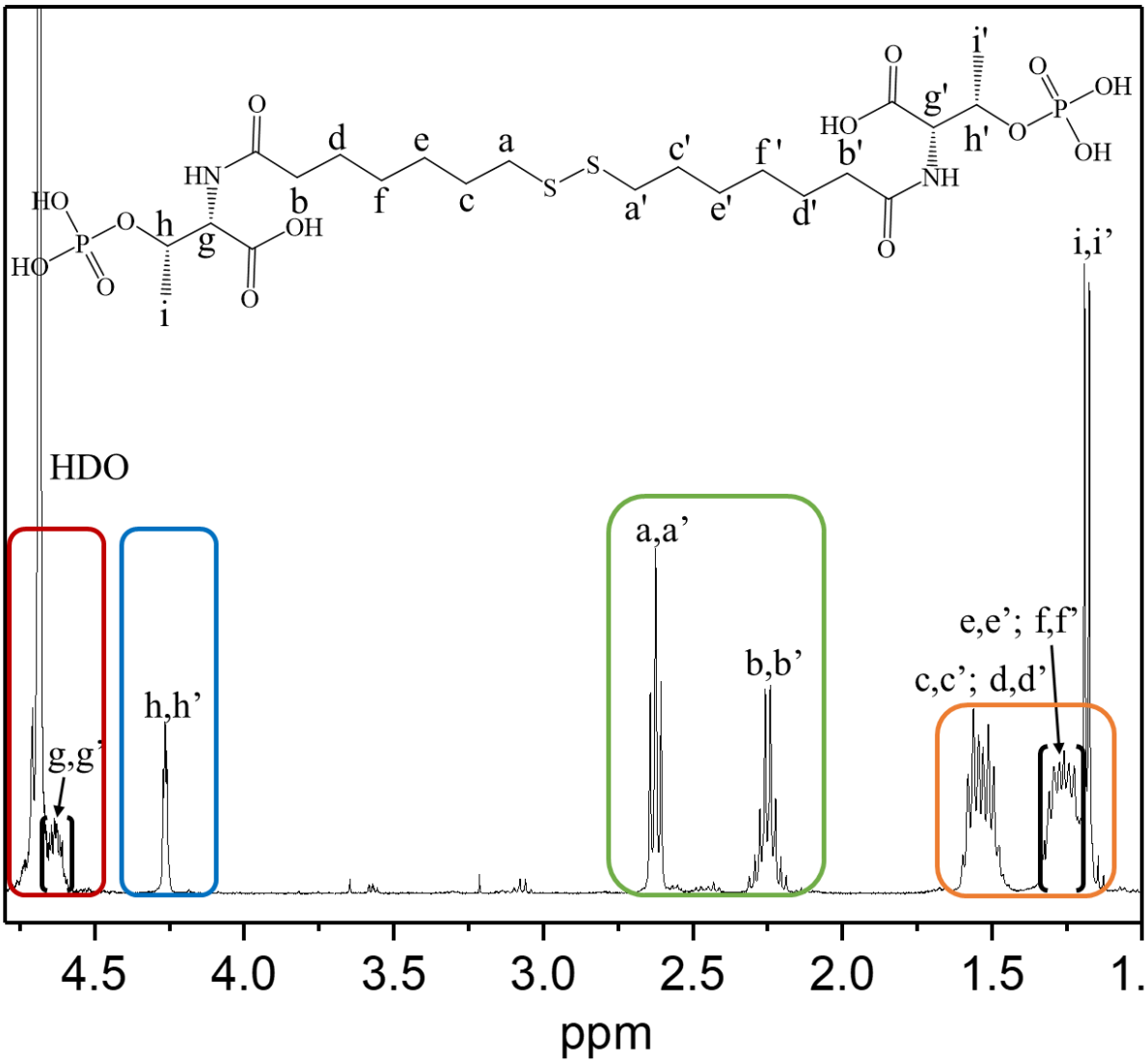

Figure 2.6: ^{1}H-NMR (D2O, 400 MHz) of (+)-N,N'-(7,7'-dithio-diheptanoyl)bis(O-phospho-L-threonine): 4.20 (s, HDO), 4.61-4.63 (m, 1H), 4.27 (d, 2H), 2.62 (t, 4H), 2.18-2.32 (m, 4H), 1.47-1.60 (m, 8H), 1.20-1.34 (m, 8H), 1.18 (d, 6H). Colored regions can be seen in **Figure 2.7** at a closer range.

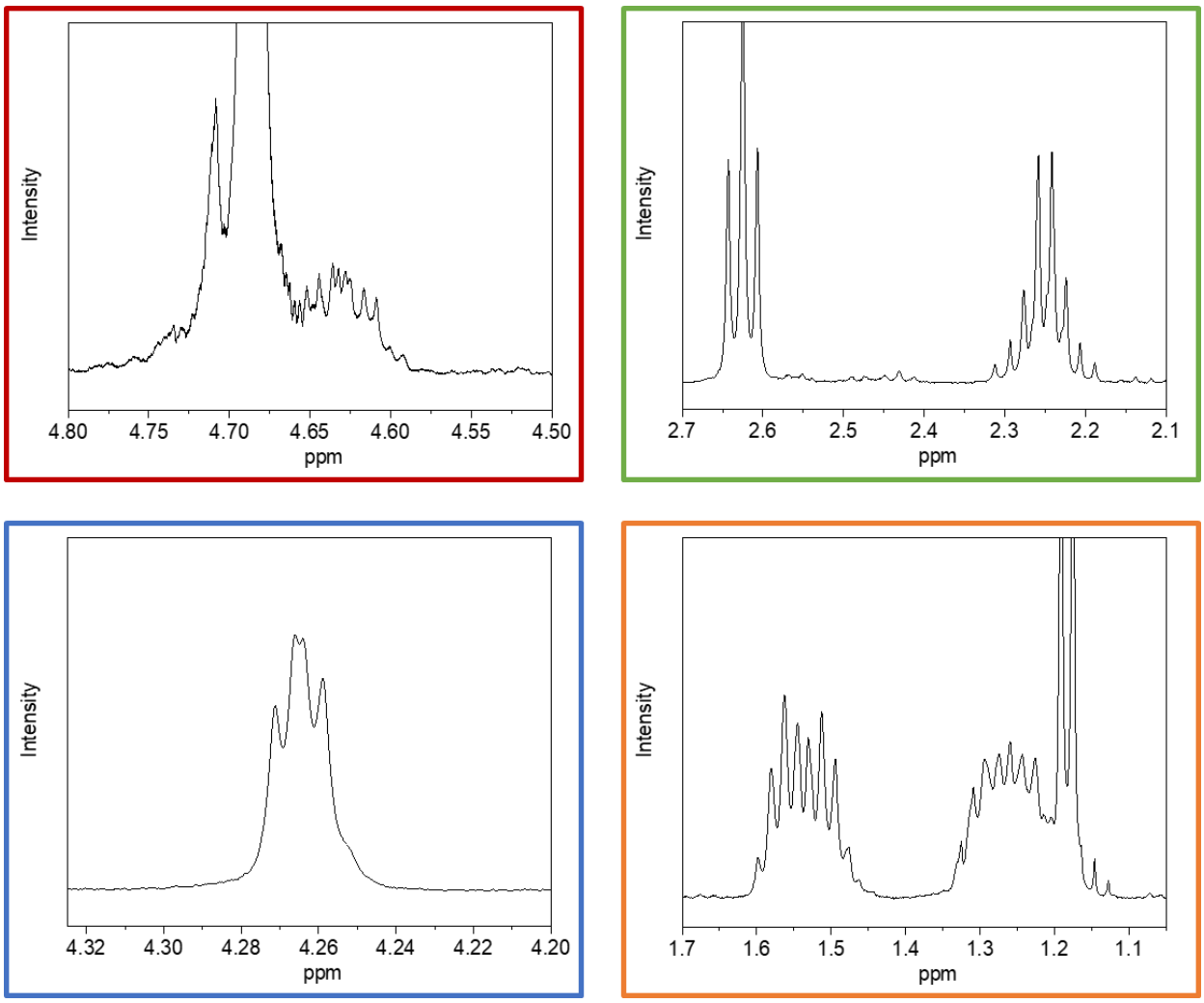

Figure 2.7: Zoomed in ranges of the ^{1}H NMR of (+)-N,N'-(7,7'-dithio-diheptanoyl)bis(O-phospho-L-threonine). The colored outline coordinates with the colored regions highlighted in **Figure 2.26**.

2.2.2.4 CoMSSCoB

Compound **19** (73 mg, 0.097mmol) and CoM (**8**) (330 mg, 2.0 mmol) were dissolved in water (5 mL) and concentrated NH_3 (0.5 mL) and stirred for one hour at room temperature. 0.5 M KI_3 was titrated in until its brown color fades slowly. The mixture was acidified with 20% HCl to a pH 0 and loaded onto a PAD-II (2 cmX13 cm) column which had been equilibrated with 20% HCl overnight. The column was washed with 1 M, 0.5 M, 0.2 M, 0.1 M, and 0.025 M HCl consecutively (100 mL each). The elution solvents were 0%, 10%, 25%, and 50% methanol in water. Solutions are dried under high vacuum to obtain HDS (**11**). Product **11** eluded mostly with 50% MeOH but at times a small amount would elute at 25% MeOH. All peaks from the ^{1}H NMR indicate compound **11** was synthesized after comparing to literature articles (**Scheme 2.4**, **Figure 2.7**-**2.8**).[14] The singlet peak at 3.52 ppm was most likely due to methanol still left on the product.[64]

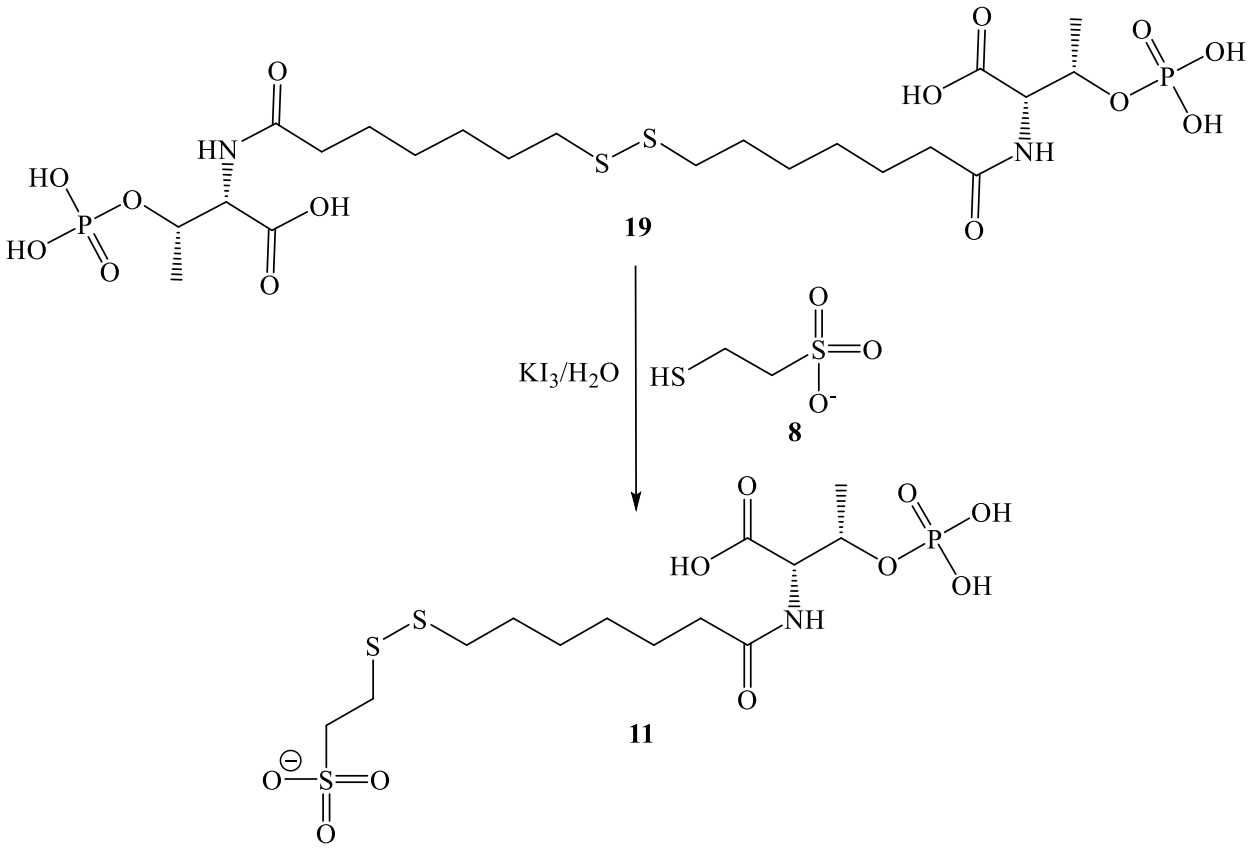

Scheme 2.4: Synthesis of CoM-S-S-CoB.

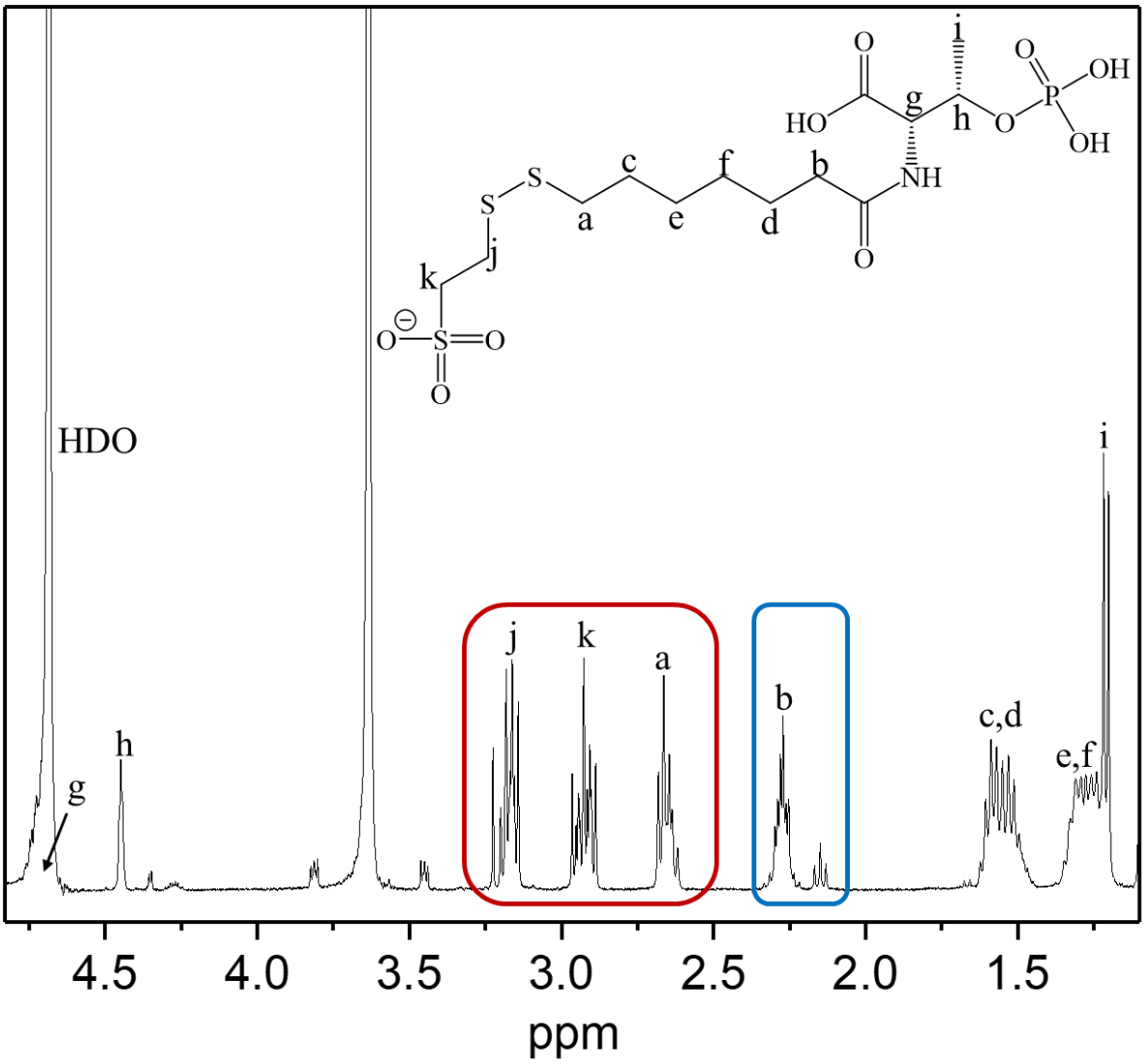

Figure 2.8: ^{1}H NMR (D_2O, 400 MHz) of CoM-S-S-CoB: 4.74 (overlapping with the solvent signal at 4.72 ppm), 4.41 (dd, 1H), 3.15-3.22 (m, 2H), 2.88-2.98 (m, 2H), 2.75 (t, 2H), 2.21-2.32 (dt, 2H), 1.48-1.63 (quintet, 4H), 1.23-1.36 (quartetoid, 4H), 1.21 (d, 3H).

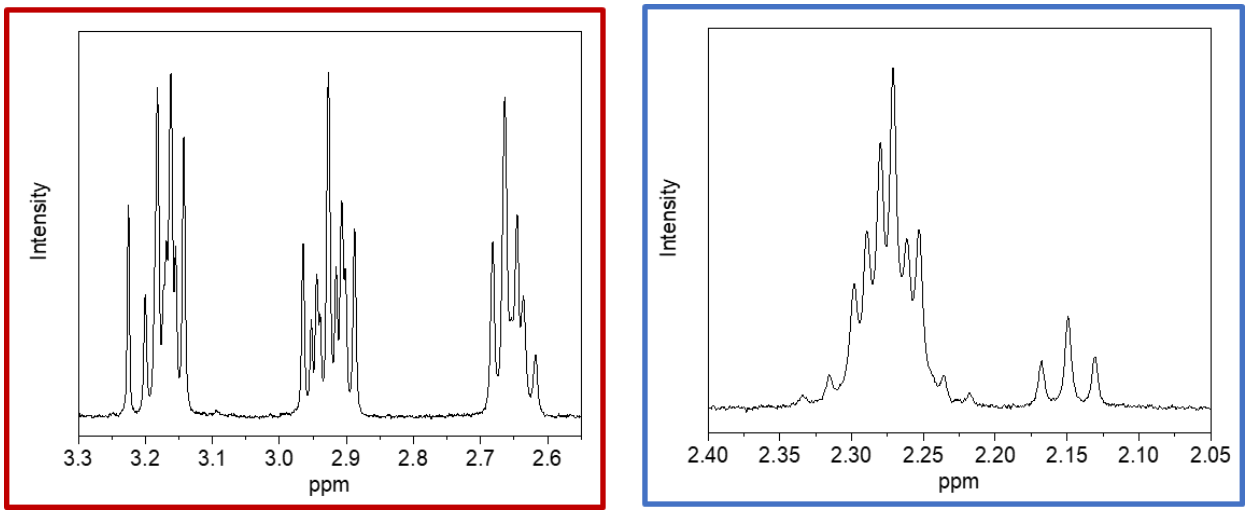

Figure 2.8: Zoomed in areas of the ^{1}H NMR of CoM-S-S-CoB. Colored outlines coordinate with the highlighted regions from **Figure 2.27**.

2.2.3 Growing *Methanothermobacter marburgensis*[61]

(Note*: All buffers were boiled, purged with N_2, stirred under vacuum for three hours, and then pressurized with Ar to 0.3-0.4 psi to provide anoxic buffers for the cells and proteins throughout these experiments.) In a 12 L fermenter, 90 g sodium carbonate, 27 ammonium chloride and 33 g potassium phosphate monobasic were dissolved in DI water. Next, 15 mL of a mineral mixture (final concentrations in the mixture were as follows: 16 mM nitrilotriacetic acid, 20 mM $MgCl_2$*6 H_2O, 8 mM $FeCl_2$*4 H_2O, 0.15 mM $CoCl_2$*6 H_2O, 0.08 mM $NaMoO_4$*2 H_2O, 0.93 mM $NiCl_2$*6 H_2O) and 0.2% resazurin were added and the fermenter was filled to the 10 L mark. Once the lid was fastened to the container, a gas mixture of 80%H_2/20% CO_2 and ~ 1% H_2S was sent through the fermenter to create an anaerobic atmosphere. This mixture was agitated at 1000 rpm and heated to 65°C. Once the temperature and anaerobic conditions were reached, 200-300 mL of *M. marburgensis* culture ($O.D._{568}$=4-5) was innoculated and grown overnight. Once an $O.D._{568}$ of

4-6 was achieved, the cells were harvested with the help of an anaerobic continuous flow centrifuge. 50 mM potassium phosphate (pH 7) was used to fill and "wash" the centrifuge rotor to establish anaerobic conditions inside before the cells were harvested. Harvesting was complete once the entire fermenter was empty (±1.5 hours).

2.2.4 Purifying Mvh:Hdr[61]

(Note*: All buffers mentioned in this section were boiled, purged with N_2, and stirred under vacuum as described in previous section and contained 2 mM dithiothreitol (DTT), 2 mM coenzyme M (CoM), and 20 μM FAD which was added after transferring into the anaerobic glove box.) The harvested cells were transported into an anaerobic glove box where they were resuspended with 10 mM Tris-HCl (pH 7.6) and sonicated for 3.5 minutes with 0.5 second pulsing on and off at 80% amplitude. This method was performed three times with three minutes of cooling periods in between each sonication. This suspension was centrifuged anaerobically at 35,000 rpm for 20 minutes (Beckman Coulter Ultracentrifuge). The supernatant was separated and filtered through a 0.2 μM sterile filter before loading onto a weak anion exchange (diethyl amine ethyl (DEAE)) column. A linear gradient on a fast protein liquid chromatography (FPLC) was utilized to elute the protein using 50 mM Tris-HCl (buffer A) and 50 mM Tris-HCl, 1 M NaCl (buffer B) (**Figure 2.9**). The most active Mvh:Hdr fractions eluded at 35-40% of buffer B which was determined by performing an HDR activity assay.

A buffer exchange was performed on the collected fractions before loading onto a strong anion exchange (Q-sepharose) using the same buffers as before. The most active Mvh:Hdr protein eluted between 45-50% of buffer B which was determined using the same activity assay (**Figure 2.10**). Lastly, this protein is concentrated to 2 mL and loaded onto a size exclusion column (Superdex-200). Buffer C is used to elute the protein which is the same as buffer B except contains

150 mM NaCl (**Figure 2.11**). Mvh:Hdr was analyzed by SDS-PAGE (Shown in section 2.3.1). Once attained, a buffer exchange was performed with buffer A without DTT, FAD, and CoM to remove the excess FAD from the protein. The protein was stored in closed off bottles pressurized with H_2 (0.5 ATM over pressure) and either used immediately or stored in a -20°C freezer.

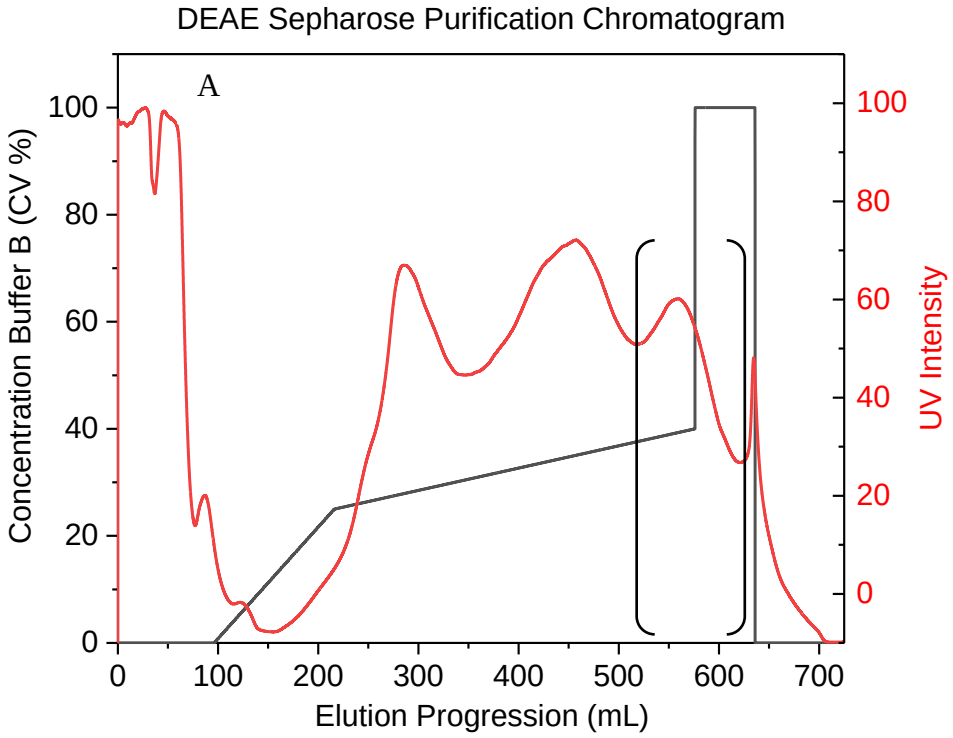

Figure 2.10: DEAE sepharose chromatogram during the purification of Mvh:Hdr. The black brackets show the peak which contained the most Mvh:Hdr activity and was collected for the next chromatographic step.

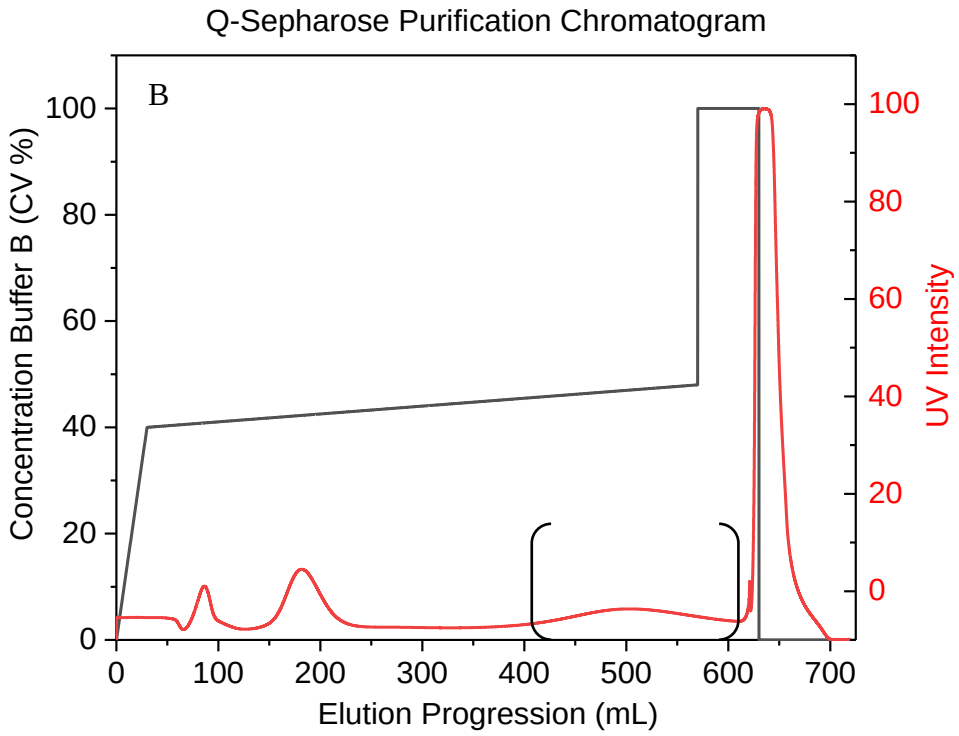

Figure 2.11: Q-sepharose chromatogram during the purification of Mvh:Hdr. The black brackets represent the peak which contained the most active Mvh:Hdr fractions, which were pooled for the next chromatographic step.

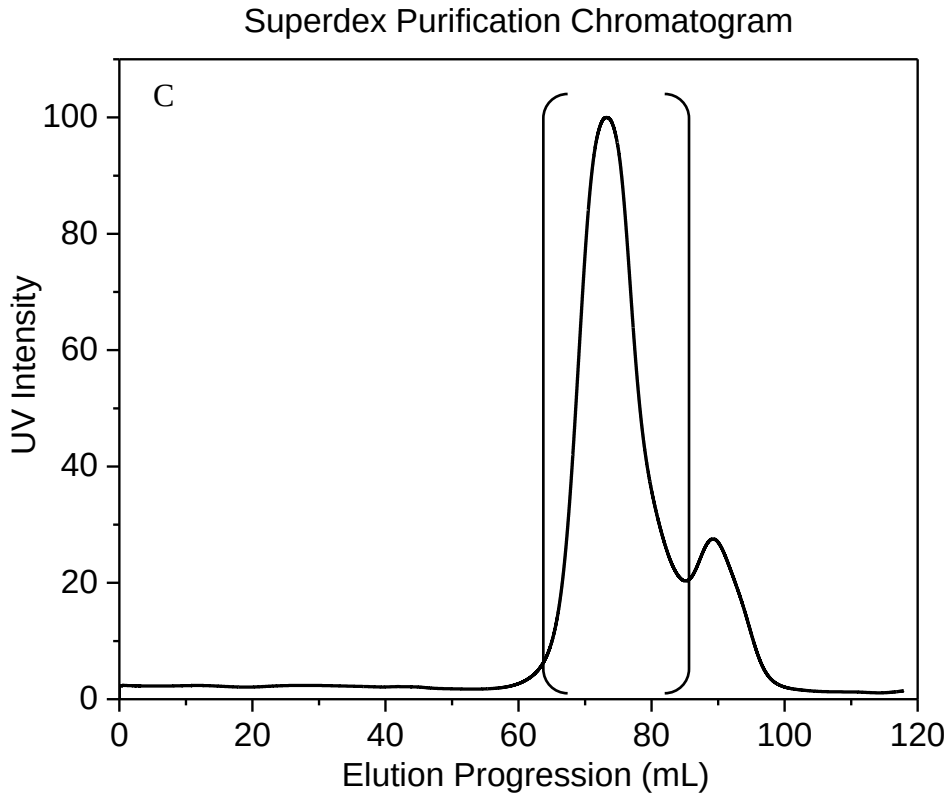

Figure 2.12: Superdex-200 chromatogram during the purification of Mvh:Hdr. Fractions were analyzed through SDS-PAGE to determine the purity of Mvh:Hdr. The SDS-PAGE gel is shown in the 'Results' section.

2.2.6 Separating Mvh from Hdr

We followed the procedures reported by Setzke[61] except that the protein was stirred overnight (12-16 hours) in the presence of Chaps in an anaerobic globe box.

2.2.7 Mvh:Hdr Enzyme Assay

During the purification of Mvh:Hdr, a colorimetric assay was utilized to test activity. This assay involved mixing the following solutions to these final concentrations: 0.33 mM dithionite (DIT), 1 mM methyl viologen, 0.55 μM HDS, 42.5 mM Tris-HCl (pH 7.6) and 10 μL

protein. The most active samples were identified by a quick discoloration as observed by the eye.

The protein concentration was determined by a Bradford assay while the iron concentration was determined by a ferrozine assay. UV/Vis photospectroscopic kinetics were performed measuring the decrease in absorbance of 603 nm with the addition of substrate. HDS was used as the substrate for the Hdr assay while H_2 gas was the substrate for the hydrogenase assay. The Hdr assay involved mixing the following solutions to these final concentrations: 1.28 M potassium phosphate buffer (pH 7), 2 mM methyl viologen, 0.17 mM dithionite, 2 mM HDS, and 14.5 μM protein. For the hydrogenase assay, the anaerobic cuvette with the assay solution inside was purged H_2 gas. The final concentration of the solutions was as followed: 19.3 mM methyl viologen, 14.5 μM protein, and 8 μM dithionite.

2.2.8 EPR analysis of Hdr

Samples were reduced with dithionite (20 mM) and had redox dyes added to analyze the solution at different reduction potentials. Once these were mixed, the sample was frozen in liquid nitrogen to be analyzed by EPR.

2.2.6 EPR monitored-redox titrations

Table 2.1 lists the name of the redox dyes added to the Mvh:Hdr protein. These were added to a final concentration of 50 μM. Dithionite was used to reduce the protein while potassium ferricyanide was used to oxidize the protein. Using a Ag/AgCl electrode, 300 μL was aliquoted from the mixture into a calibrated EPR tube when its potential changed every 30-mV and frozen immediately in liquid nitrogen. These samples were analyzed by EPR and the signals

were corrected for changes in concentration due to this procedure.

Table 2.1: List of the redox dyes utilized during the redox titrations.

Redox Dye	NHE Potential at pH=7 (mV)
Neutral red	-325
Benzyl viologen	-350
Anthraquinone-2-sulphonate	-255
1,4-benzoquinone	274
Phenosafranin	-252
Indigo carmine	-125
Safranin O	-289
1,2-naphthoquinone	134
Methyl viologen	-453
Methylene blue	11
2-hydroxy-1,4-naphthoquinone	-145
Thionine	64
1,4-naphthoquinone	69
Duroquinone	86
1,2-naphthoquinone-4-sulphonate	215

2.2.7 Turn-Over experiments

Two different turn-over experiments were prepared for this section: a timed experiment and one with different substrates. The timed samples were executed to determine how many overlapping EPR peaks would show up. Rapid freeze quench would be impractical to execute if too many iron-sulfur clusters became EPR active and overshadowed the ones transporting the electron at certain time periods. For the alternative electron donor, we purged one set of samples with H_2 gas and added dithionite to the other. Next, we mixed the protein with 1.6 M potassium

phosphate buffer (pH 7), 20 mM dithionite (for one set of samples), and then metronidazole (MTZ)/HDS. The other set of samples mixed with the same solutions but were purged with H_2 for 1-2 minutes and did not contain dithionite.

The samples containing different electron acceptors were made to analyze how this potentially affects the EPR signal. The protein in 1.6 M potassium phosphate buffer (pH 7) was added to an 8 ml bottle. These bottles were purged with H_2 gas and then ~10 mM metronidazole (MTZ) and/or HDS were added. Three different samples were prepared: as such, in the presence of HDS only, and with both HDS and MTZ. Each mixture was put into an EPR tube and frozen in liquid nitrogen to stop the reaction. The timer started once the protein was added to the samples and was stopped once they froze in liquid nitrogen. Each sample was then aliquoted out into EPR tubes to be analyzed.

2.2.8 EPR monitored-rapid freeze quench

Mvh:Hdr (60-80 μM) was incubated with an HDS/MTZ mixture (5 mM for each) using a rapid freeze quench instrument (Kintek) on a millisecond time scale. The instrument was setup in an anaerobic glove box with a 100% Ar atmosphere to maintain anaerobic conditions for the protein and substrate. The protein was reduced with DIT (20 mM) to reach a final concentration of ~5 mM. The mixture was shot into a calibrated EPR tube which sat in cold methylbutane (120-140 K) to ensure this solution would freeze and halt the reaction. This solid was packed at the same temperature into the EPR tube in a chilled methyl butane setup to prevent the reaction from progressing further and for the sample to be analyzed by EPR. Signals were corrected for the dilution factors and tube calibration factor used in this procedure.

2.3 Results

2.3.1 Mvh:Hdr Results

2.3.1.1 SDS-PAGE of Purification

Figure 2.13 shows the SDS-PAGE gel from the purification of Mvh:Hdr. For the EPR studies, the protein was always concentrated between 60-80 μM in a volume of 5-10 mL to receive not only a clear and strong signal but to make multiple samples with varying conditions (i.e. redox potential or time progression).

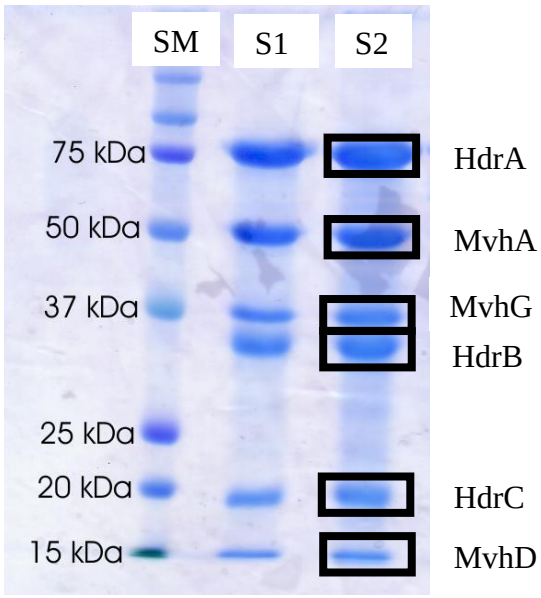

Figure 2.13: SDS-PAGE gel showing Mvh:Hdr after the Superdex-200 column purification. Lane 'SM' represents the standard marker used to compare protein weight sizes of the bands while 'S1' and 'S2' represent samples 1 and 2 collected for the same peak from the FPLC during the Superdex column purification to ensure both fractions not only contained Mvh:Hdr but were both pure.

2.3.1.2 EPR monitored-redox titrations of Mvh:Hdr

A redox titration was performed on the Mvh:Hdr protein from *M. marburgensis* and aliquoted samples were analyzed by EPR (**Figures 2.14-2.17**). **Figures 2.14** and **2.15 A-D** shows a selection of the EPR spectra measured at 8 K and the Nernst curves calculated based on the signal intensities at specific g-values. At this temperature, the cuboidal [4Fe-4S] clusters are typically detected by EPR. 332-335 mT range was eliminated from the graph due to a radical signal formed by methyl viologen and benzyl viologen. The $[4Fe\text{-}4S]^{+}$ cluster signals appear sharper at lower redox potentials but decrease in intensity near -137 mV. Eventually the cluster(s) became damaged and formed a [3Fe-4S] cluster.

Figure 2.15 A-D were the main g-values used to calculate their midpoint potentials. The curves in panels **A**, **B**, and **D** have very similar E_m values or probably represent the three peaks of the EPR signal of a paramagnetic species. At higher potentials, a second species is still detectable but due to overlap, the feature at g=1.85 was used to calculate the E_m value (**Figure 2.15 C**). These values give the specific low redox potential value of the $[4Fe\text{-}4S]^{+}$. One cluster was determined to contain a higher than normal redox potential value (-205 mV). At this time, it was not clear if this iron-sulfur cluster was involved with the HDS reduction or if the cluster was part of the flavin-based electron bifurcation. Further experiments were needed to determine these inquiries. An important note, only two full redox titrations were performed due to time limitations to obtain enough protein for this experiment. Therefore, the midpoint potentials seen in the top right corner of these figures were based on the average between the two titrations performed. In addition, the second value is the standard error average calculated by the computer.

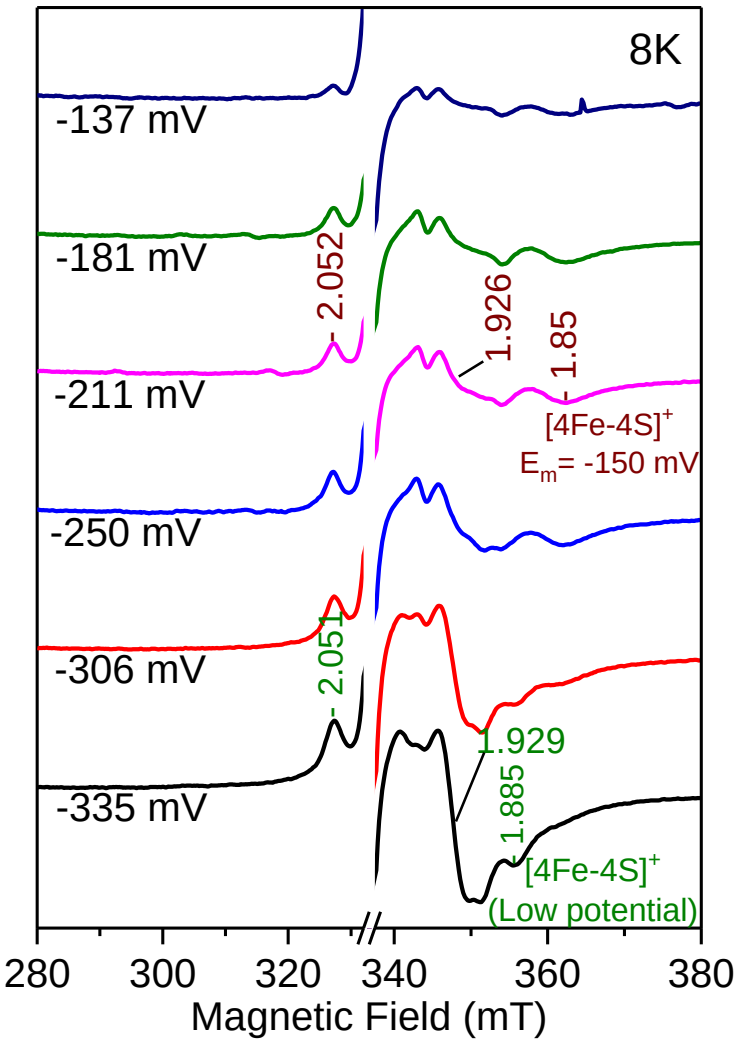

Figure 2.14: Selected EPR spectra overlay from the redox titration of Mvh:Hdr at 8K. Potentials are based on NHE values. The main signals detected at this temperature were [4Fe-4S] clusters.

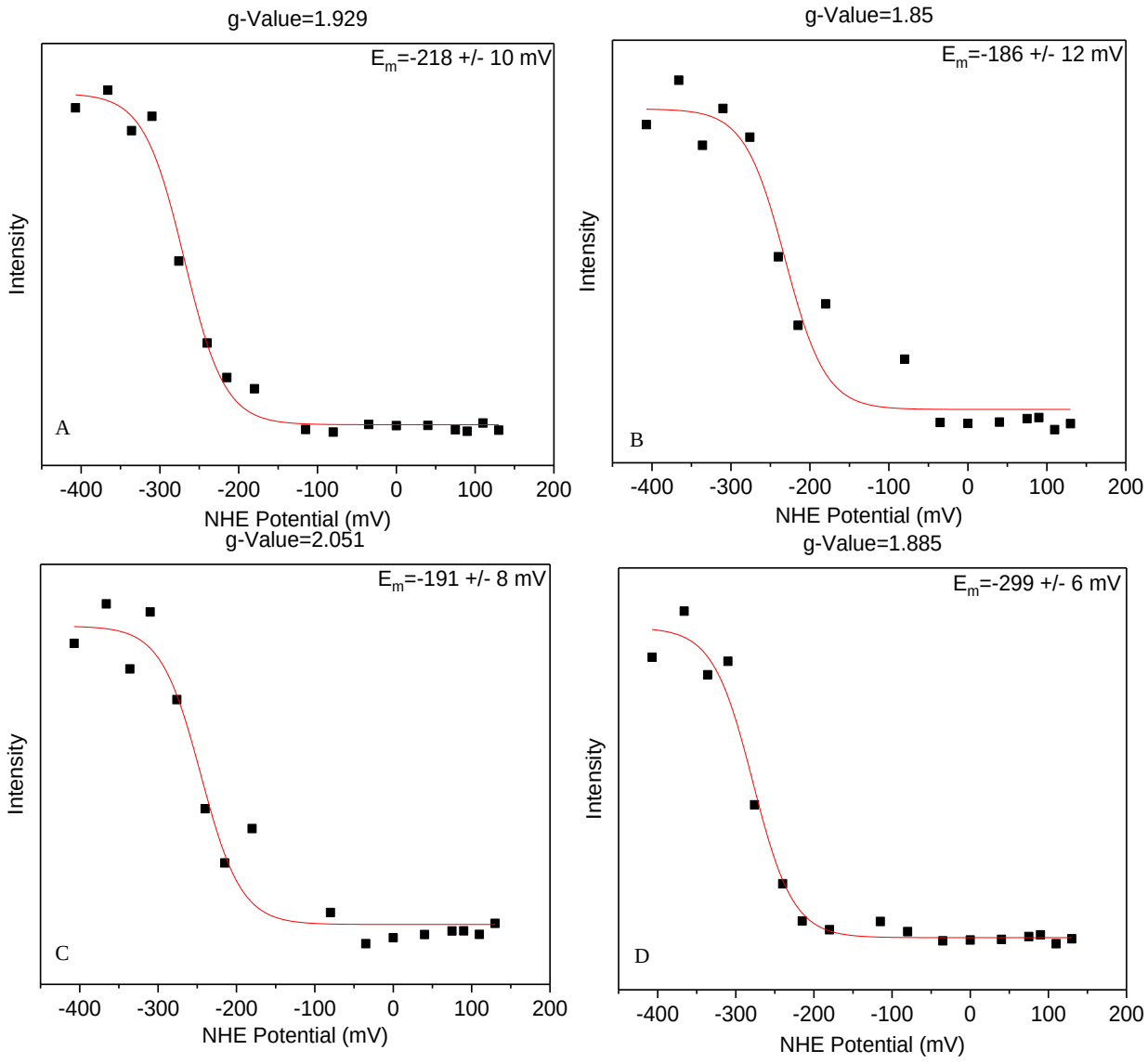

Figure 2.14 A-D: Nernst curves calculated for the g-values determined from the EPR monitored-redox titration spectra at 8K. The midpoint potential correlates with the average of the curves determined from each set of redox titrations and is shown in the upper right corner.

Figures 2.16 and **2.17 A-C** represent selected EPR spectra measured at 70 K and the Nernst curve fits for the different g-values. The g-values for the [Ni-Fe] hydrogenase (Ni-A, Ni-B, Ni-C, and Ni-L) were assigned based on previous studies.[65] The peak with g-value 1.910 was assigned to a 2Fe cluster present in MvhD with a midpoint potential of -265 +/- 5 mV. The species with g-value 1.932 was assigned to the non-cuboidal cluster with CoM bound and contained a midpoint potential of -111 +/- 15 mV.[49,59] The g-value at 1.894 was unassigned to any cluster because this was the first time this signal was detected. Furthermore, this appeared to be a 'transient' species with two different midpoint potential values.

The new signal could be due to the 'A6' cluster that accepts the first electron from $FADH_2$. During the flavin based-electron bifurcation, the flavin must contain a potential between the Fd and 'A6' which would be around -300- -200 mV. Assigning this g-value and redox potential to 'A6' would fit within the flavin-based electron bifurcation theory since this cluster must contain a more positive potential in order to accept the first electron from the flavin. It is also possible this signal came from the 'A5' cluster. This g-value had never been detected during studies with isolated Hdr. Because Mvh was removed from Hdr, MvhD would not be present which would have signaled this section of HdrA to perform the conformational change and allow 'A5' to accept the electron. The [2Fe-2S] cluster was determined to have a potential of -265 +/- 5 mV and, therefore, a potential of -204 mV would be within reduction range for 'A5' to accept the electron. Further experiments would need to be done in order to determine what iron-sulfur cluster produced this signal, specifically isolating the subunits and repeating these redox titrations with each subunit.

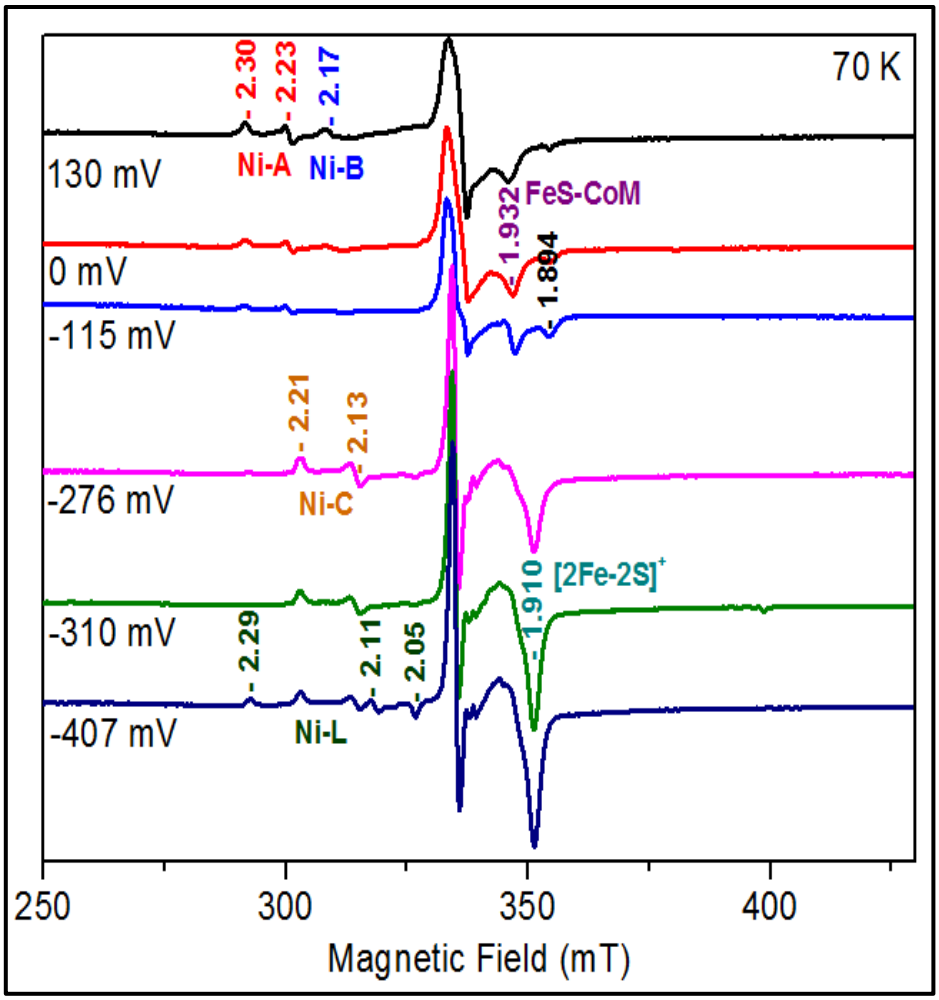

Figure 2.16: EPR overlay of selected spectra during the redox titration of Mvh:Hdr at 70K. g-Values are indicated on the graph along with the correlated metal clusters.

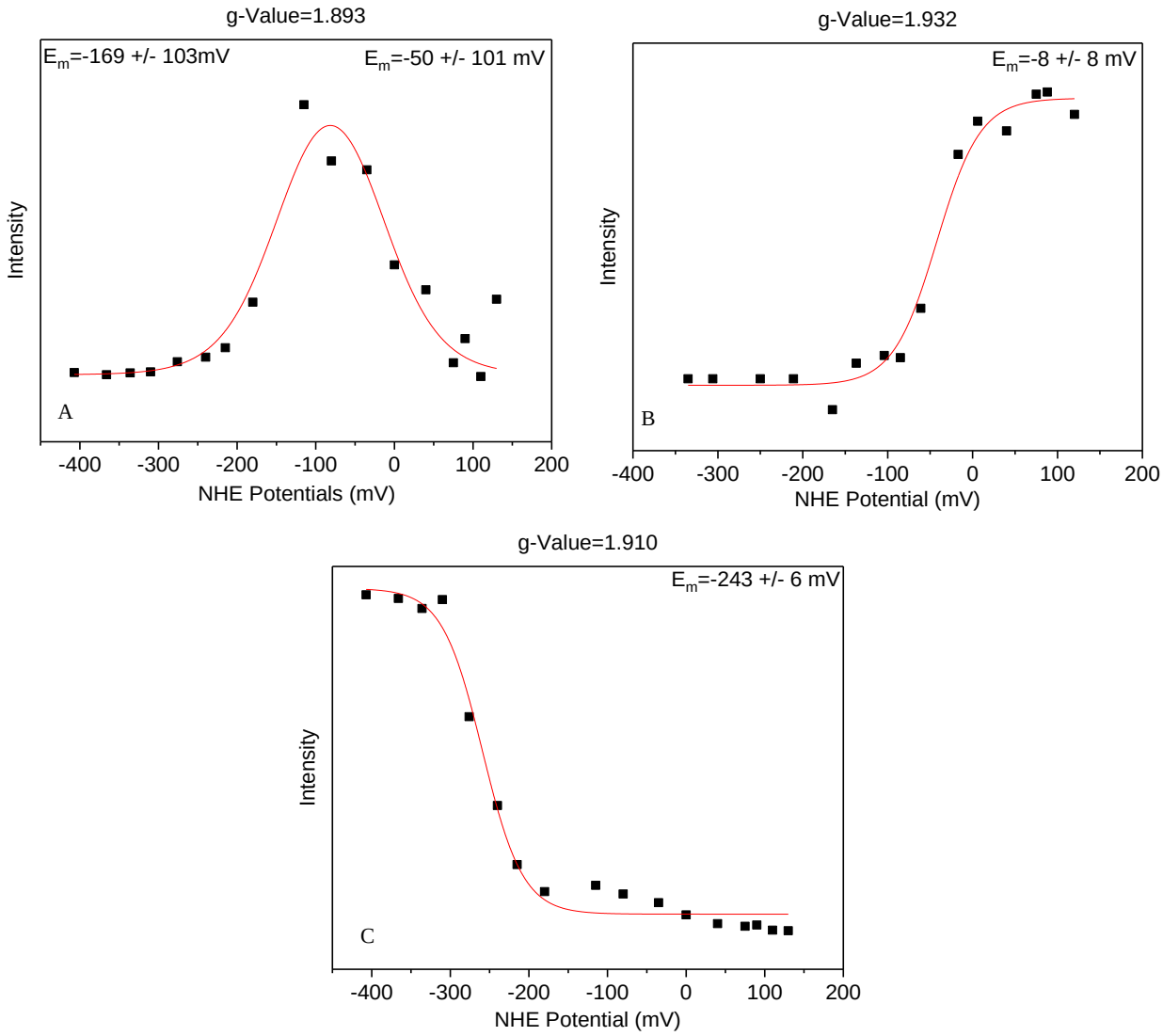

Figure 2.17 A-C: Nernst curves calculated from the g-values found from the EPR monitored-redox titration spectra at 70K. The midpoint potentials are calculated from the average of both sets up redox titrations and appear at the upper right corner of the graphs.

2.3.1.3. Turn-over experiments

Previously there are 28 iron-sulfur clusters total in the Mvh:Hdr complex which increases the chance of spin-spin interaction resulting in broad complex signals. Therefore, pre-steady-state condition experiments were used to test the number of iron-sulfur cluster signals detected by EPR when in the presence of the substrate (**Figure 2.18**). Metronidazole (MTZ) was added with HDS to act as an alternative electron acceptor for Fd.[66] The first step was to analyze the protein in the presence of HDS only and then with HDS and MTZ. These samples were frozen before substrate would run out. We saw the $[4Fe\text{-}4S]^{3+}$-CoM species at g_{zyx}=2.014, 1.986, 1.929, and even, potentially, a CoB bound species at g_{zyx}=2.019, 1.986, 1.955.[48] The spectrum showing Mvh:Hdr in the presence of HDS only showed a small radical peak at g=2.031 which indicates the possibility of either the FAD molecule following the "cross-over" model or a radical formed by the homodisulfide reaction in HdrA (previous studies of these indications were not published). The g-value at 1.863 potentially came from the [4Fe-4S] cluster with E_m=-150 mV.

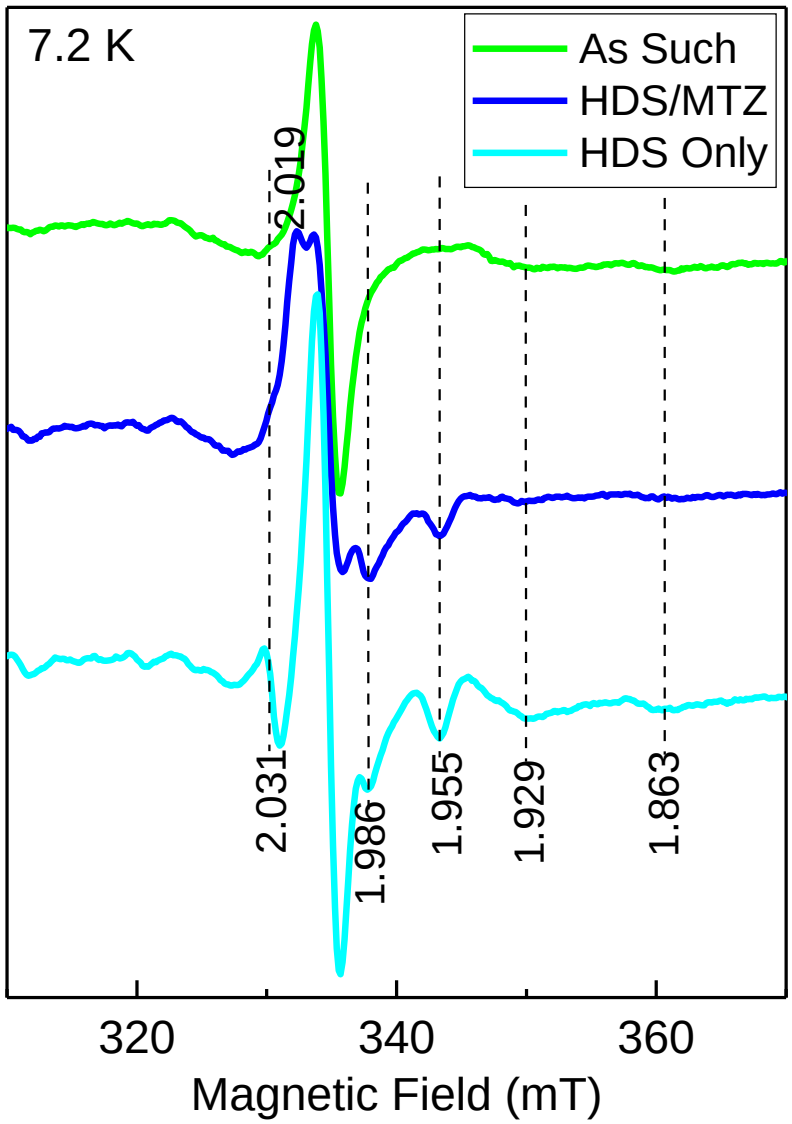

Figure 2.18: EPR overlay of the turn-over experiment with Mvh:Hdr in the presence of different substrate combinations.

The next experiment was to time this reaction (**Figures 2.19** and **2.20 A-D**). Rapid freeze quench would not be useful if the EPR signals were broadened due to the large number of interactions between the clusters. Furthermore, determining how to provide an electron donor was

a challenge. H_2 is used for the protein when it is stored temporarily but we cannot purge the instrument within an anaerobic glove box. We, then, came up with the idea to reduce the protein with dithionite as an alternative and compared these results to the results of the protein purged with H_2. Surprisingly, the signals were fairly narrow even with multiple signals present. At 8K, we saw similar g-values detected for some of the [4Fe-4S] clusters (**Figure 2.19**). More importantly the intensity of the signals for the H_2 purged protein were significantly different compared to the dithionite reduced protein. These samples were measured at 70K (results shown in Appendix for Chapter 2) and 150K (**Figure 2.20 A** and **C**) as well. The most fascinating set of data discovered during this study was when the shortest timed sample measured at 150K was subtracted from the longest timed sample two new rhombic signal were revealed (**Figure 2.20 B** and **D**). The samples with H_2 showed a signal with g_{123}=2.046, 2.018, and 1.986. Less intense (see ovals in **Figure 2.20**) is a species with g_{123}=2.039, 1.935, 1.889. These values are very similar to that of the 'transient' species detected in the redox titrations. This species is much more abundant in the samples with dithionite as the electron donor. Thus, we decided to reduce the protein with dithionite for the rapid freeze quench experiments. The peaks detected from the protein purged with H_2 (noted by the black oval in **Figure 2.20 A** and **C**) were similar to the protein utilizing dithionite but less intense. To provide convenience for this study and to further analyze the rhombic signal found at 150 K, dithionite was used as the alternative electron donor.

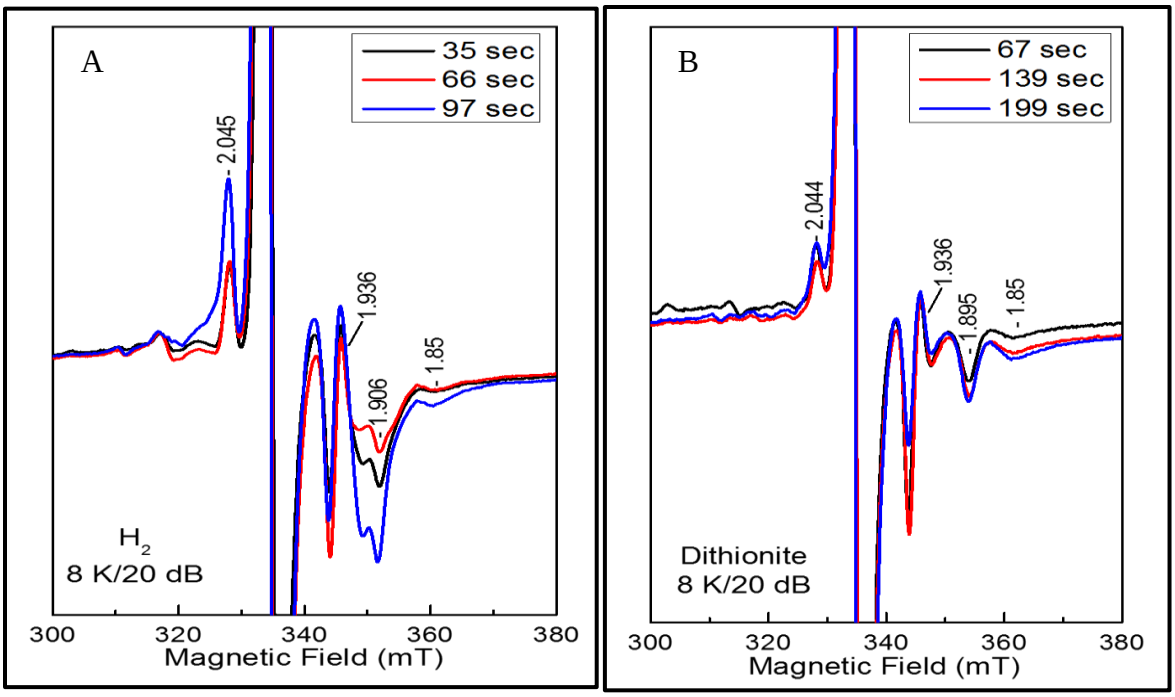

Figure 2.19: EPR spectra detected from the timed turn-over experiments at 8K. The bottom left corner indicates the electron donor source used during the experiment.

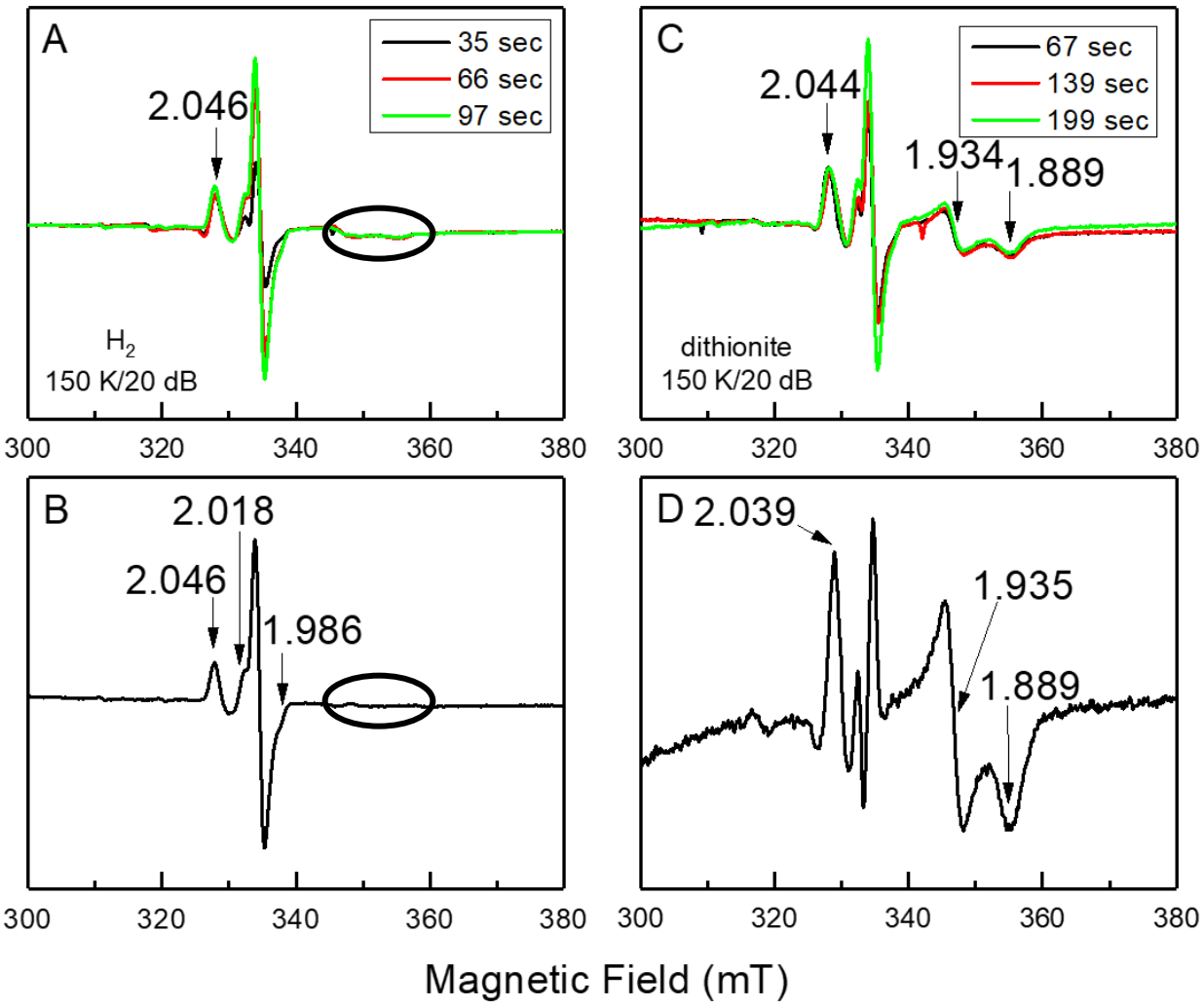

Figure 2.20 A-D: EPR spectra detected from the timed turn-over experiments of Mvh:Hdr at 150K. A and C represent the detected signals of Mvh:Hdr during the experiment while B and D are difference spectra. For each subtraction, the shortest timed spectra was subtracted from the longest timed spectra.

2.3.1.4. EPR-monitored rapid freeze quench

Figure 2.21 overlays the spectra of the samples measured at 8K. In the 'As Such' sample several [Ni-Fe] hydrogenase (Ni-C and Ni-L) signals were detectable, as well as the [2Fe-2S] cluster and low-intense signals due to [4Fe-4S] clusters. Though the [2Fe-2S] cluster overpowered the majority of the signals, there were multiple peaks around it indicating spin-spin interactions. At 4.6 ms, the broad peak at g-value 1.910 is believed to be part of the [2Fe-2S] clusters. This signal disappeared at 200 ms when the $[4Fe\text{-}4S]^{3+}$-CoM species and the new unassigned signal (g-value=1.893) appeared. The [2Fe-2S] signal appeared again at 50 seconds. In **Figure 2.22,** only Ni-C and the [2Fe-2S] cluster were clearly detectable at 70K. Both disappeared as the $[4Fe\text{-}4S]^{3+}$-CoM and unassigned signal began to appear. The reappearance of the [2Fe-2S] signal indicates that the substrate becomes limiting.

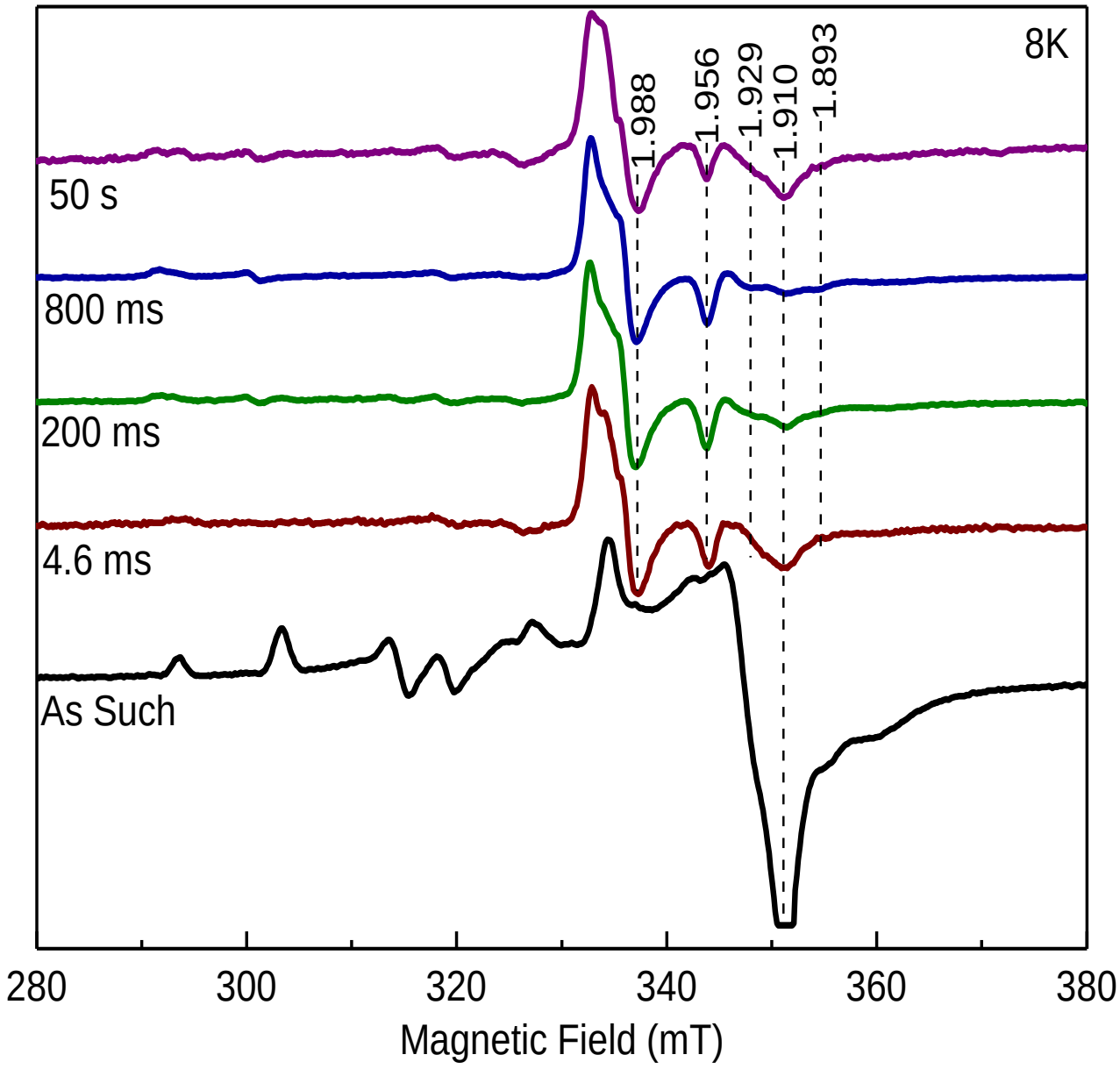

Figure 2.21: Selected EPR spectra overlay of the EPR monitored-rapid freeze quench experiments performed on Mvh:Hdr at 8 K.

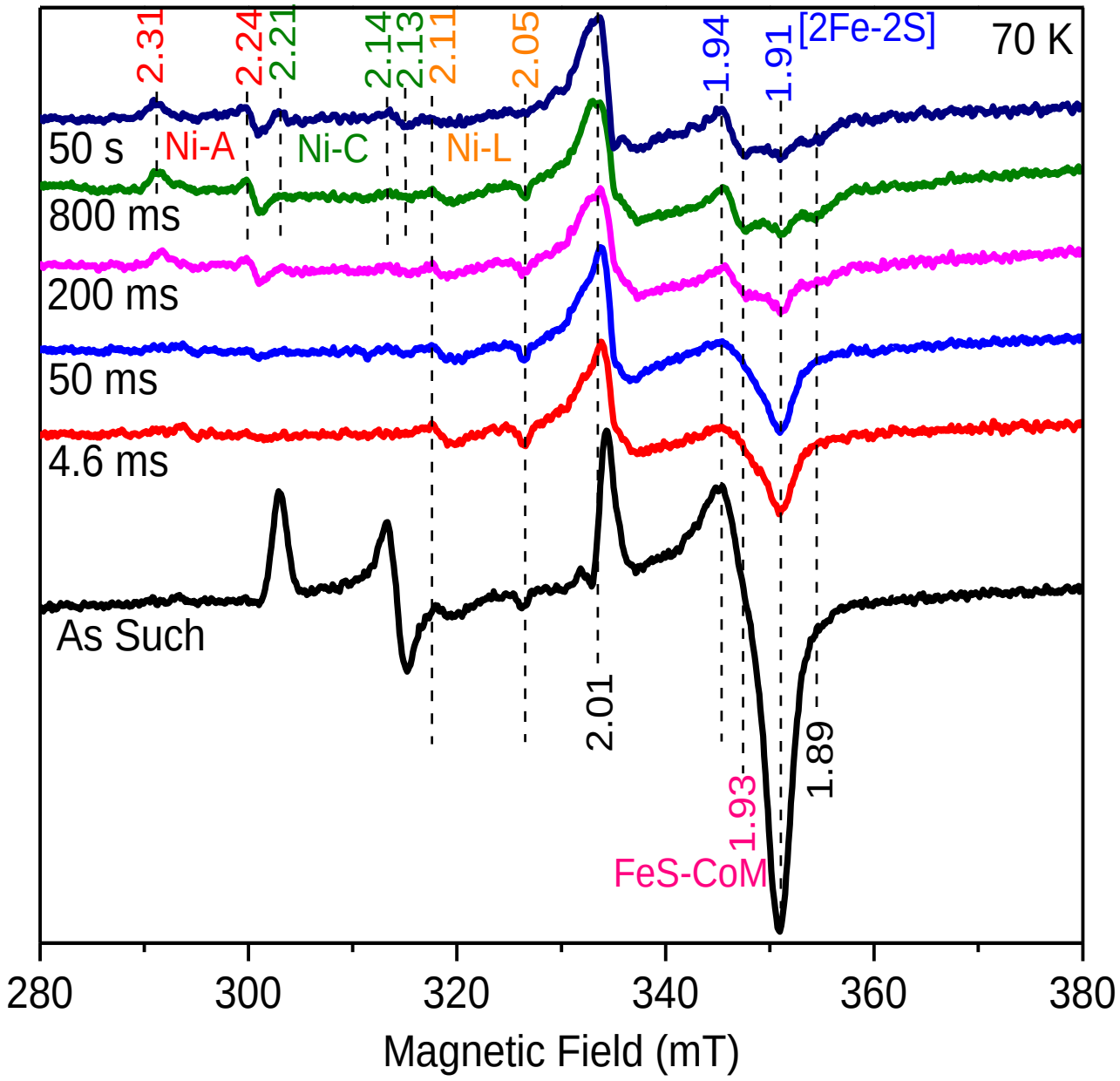

Figure 2.22: EPR spectra overlay of the EPR monitored-rapid freeze quench experiments performed on Mvh:Hdr at 70 K.

2.3.2 Separated Mvh and Hdr Results

2.3.2.1 SDS-PAGE Gel Results

Figure 2.23 shows the SDS-PAGE gel after the separation and purification of Mvh and Hdr. The Hdr sample did show small amounts of Mvh but because the bands appeared much smaller compared to the isolated Hdr, we continued with the EPR studies. The protein concentration averaged ~250 μM in 1 mL for Mvh while Hdr was ~80 μM in 1 mL.

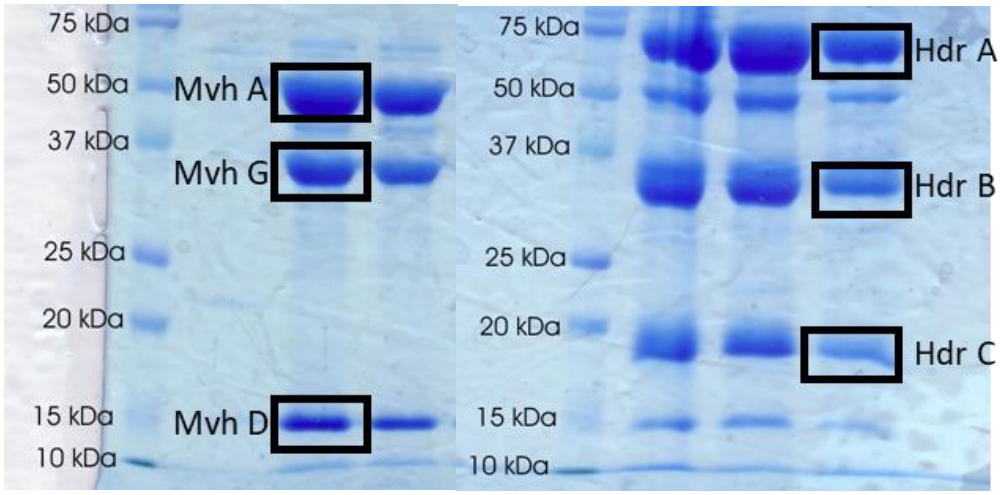

Figure 2.23: SDS-PAGE gel results after the MonoQ purification when separating Mvh from Hdr.

2.3.2.2 EPR Analysis During the Separation of Mvh from Hdr

2.3.2.2.1 Mvh Only

During the redox and kinetic studies, we assumed the [2Fe-2S] was a rhombic signal but was partially hidden by other signals. Instead, the more axial signal was detected. The same signal was also present in Mvh. Though uncommon, [2Fe-2S] clusters may form a rhombic or axial shape[20] The signal, nevertheless, is very unique and this could be the result of the unique coordination found in the crystal structure. The Mvh sample was measured at 8 K to detect the

[4Fe-4S] clusters (**Figure 2.24**) in MvhG and 70 K to detect the [2Fe-2S] cluster (**Figure 2.25**). Because there was a clear [2Fe-2S] cluster detected at 8 K, a simulation was created and then subtracted from the original sample. Unfortunately, none of the [4Fe-4S] clusters were seen which lead us to determine these clusters most likely contain potentials from -500- -300 mV. Further studies would involve obtaining more protein to perform a full redox titration to confirm the low potentials of these clusters. The measurement performed at 70 K allowed us to determine the official g_{zyx} of the [2Fe-2S] cluster which would be used for any future studies involving MvhD.

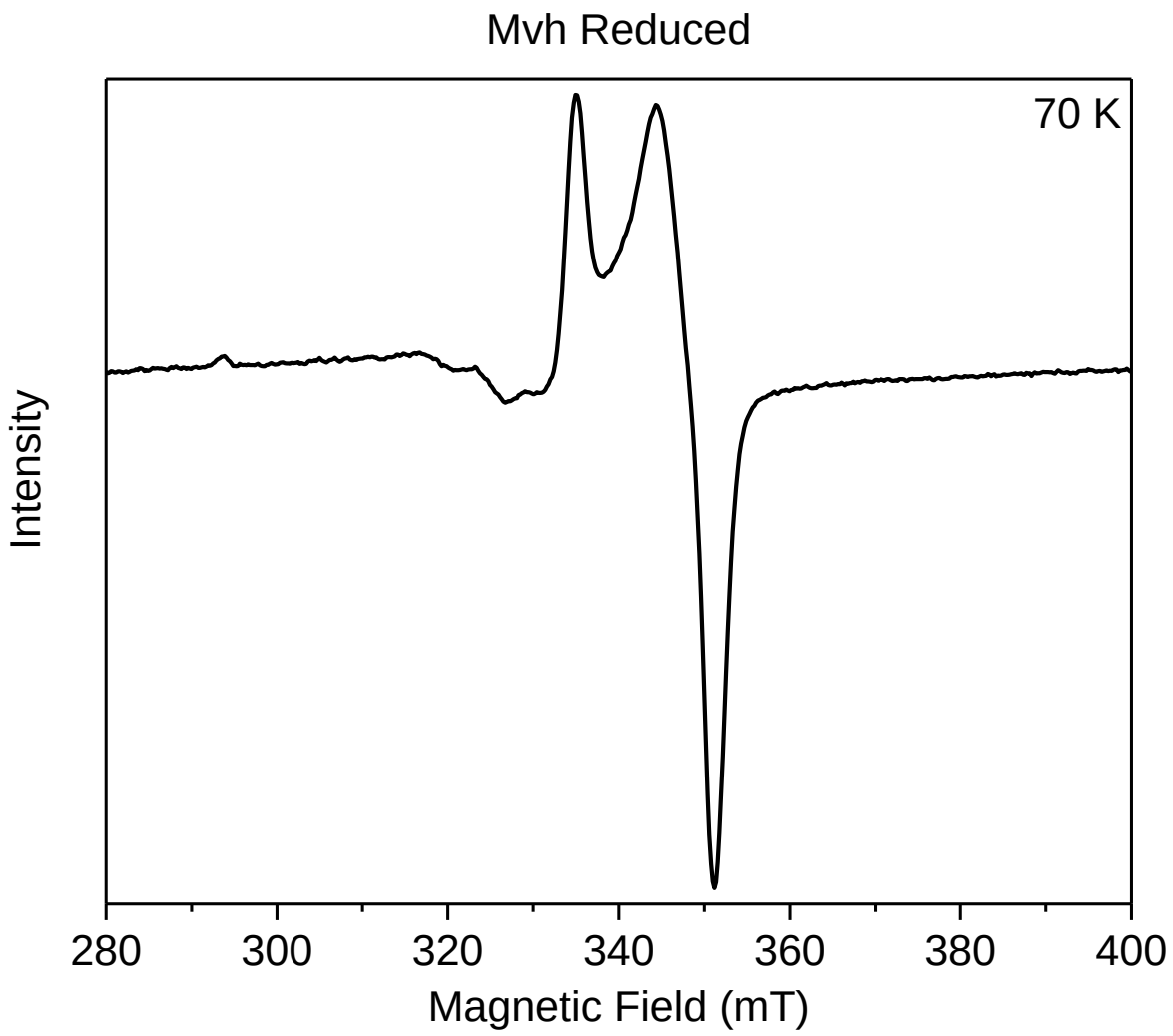

Figure 2.24: EPR spectra of Mvh enzyme reduced after separation from the Hdr complex. Signal shown at this temperature resembles the [2Fe-2S] cluster based on the shape and g-values found.

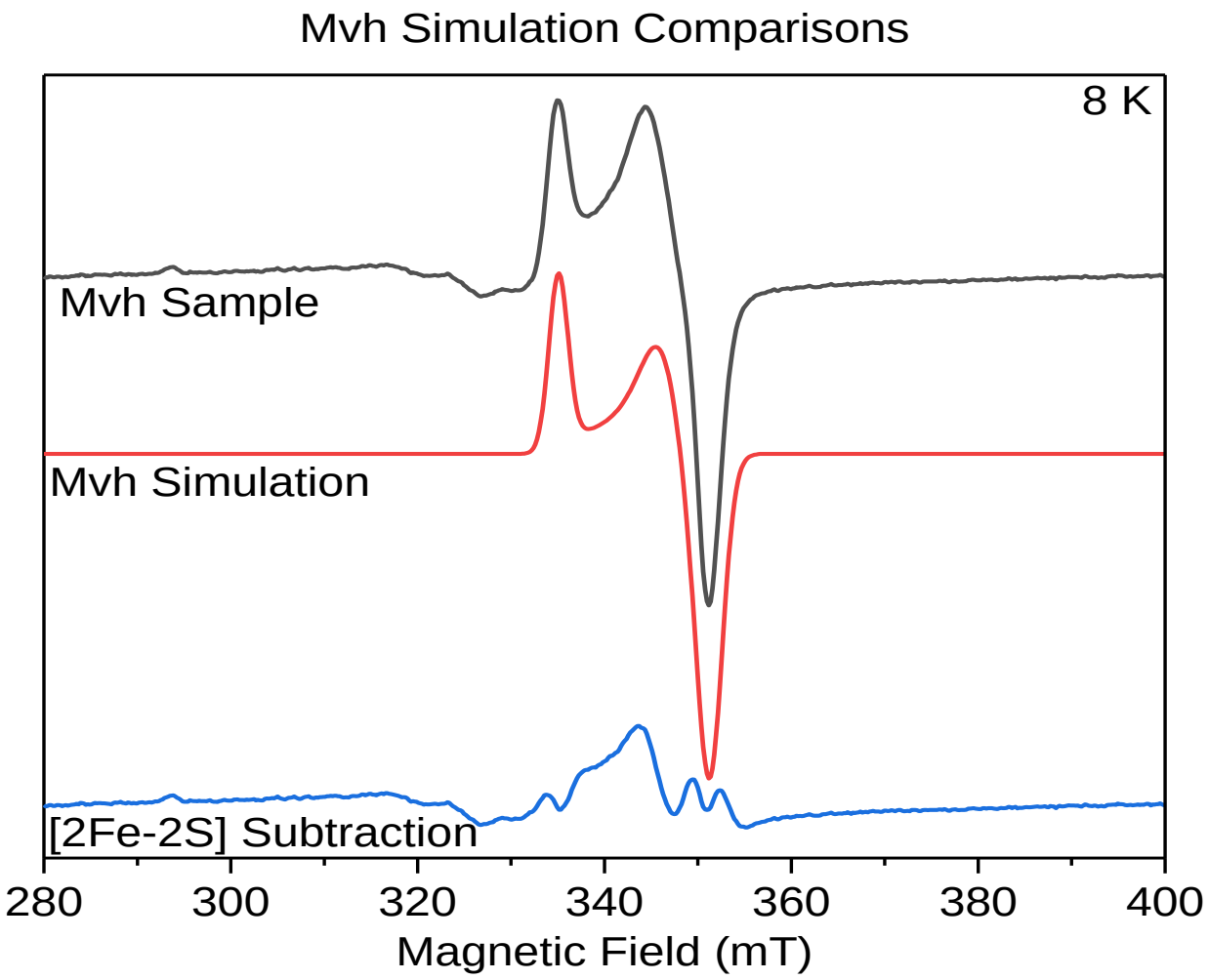

Figure 2.25: Mvh EPR spectra measured at 8 K compared to simulations created for the signal. The blue spectra was the result of when subtracting the Mvh simulation from the sample.

2.3.2.2.2 Hdr Only

Hdr was reduced similar to Mvh (**Figure 2.25**) yet [4Fe-4S] clusters were easily seen at 8 K. We believed a portion of the signal contained the [2Fe-2S] cluster since its g-values lined up with areas of the Hdr sample. With the simulated [2Fe-2S] signal, we subtracted it from the Hdr sample to reveal a portion of the spectra which had shifted slightly. Though both spectra were normalized to enable a more accurate comparison, their receiver gains were slightly different which could have changed the intensity of the signal to some extent. Measuring this sample at higher temperatures, such as 20 K, only revealed the [2Fe-2S] cluster which could have overpowered the noncuboidal clusters in HdrB. Unfortunately, there is still some Mvh present. No further attempts were made since the Hdr by itself was extensively studied by Evert Duin in collaboration with Reiner Hedderich.

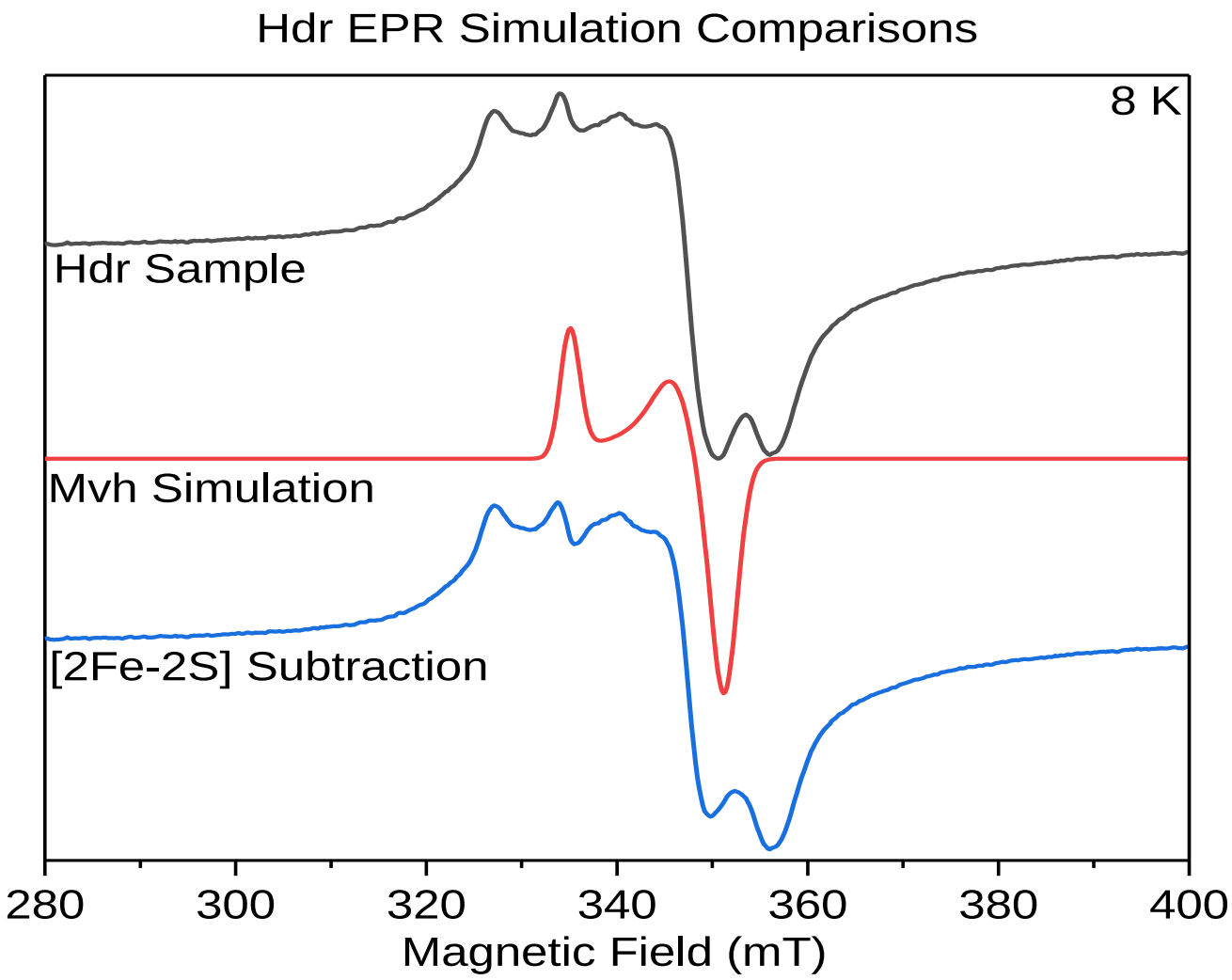

Figure 2.26: Hdr EPR spectra measured at 8 K with simulation containing, ideally, no [2Fe-2S] cluster.

2.4 Conclusion

Mvh:Hdr was studied in *M. marburgensis* because the organism is fast to grow, and one can obtain enough protein to perform EPR monitored-redox titration and rapid freeze quench experiments. The objectives of these experiments were to isolate the iron-sulfur cluster signals to develop the mechanistic pathway of the electron during the flavin-based electron bifurcation and the reduction of HDS. The results gave some indications of the midpoint potentials at which these clusters accept/donate the electron.

During the redox studies of Mvh:Hdr, different midpoint potential values were assigned to different species. For the $[4Fe\text{-}4S]^{+}$ clusters, we determined the midpoint potentials to be around -200 +/- 10 mV at g-values=2.051, 1.926, 1.85 and -299 +/- 6 mV at g-value=1.885. The midpoint potential for the [2Fe-2S] cluster was determined to be -243 +/- 6 mV. The CoM-FeS cluster was determined to be -8 +/- 8 mV. A new signal at g-value 1.894 had never been seen in other studies and indicated to reduce at a potential of -169 +/- 103 mV and oxidize at -59 +/- 101 mV. What cofactor produced this signal remains unknown.

Pre-steady state and turnover experiments revealed dithionite was an effective alternative electron donor. When the rapid freeze quench experiment was performed, the only signals that appeared were the [2Fe-2S] cluster, the CoM-Fe-S cluster, and the unknown cofactor signal at g-value 1.894. If [4Fe-4S] clusters were EPR active, they were overlapping with the other signals. Nevertheless, the [2Fe-2S] cluster appeared first and, then disappeared as the CoM-Fe-S cluster and the unknown cofactor began to appear, simultaneously.

With the separation of Mvh from Hdr, only the [2Fe-2S] cluster was seen in the Mvh sample while mostly [4Fe-4S] clusters were seen in the Hdr sample. Because the samples were only reduced by dithionite, these results revealed most likely the [4Fe-4S] clusters in MvhG are more

EPR active at -500- -300 mV while the [4Fe-4S] clusters present in Hdr are more EPR active at -300- 100 mV.

2.5 Future Studies

2.5.1 Mvh:Hdr

The redox titrations on the whole Mvh:Hdr complex gave valuable information on the cofactors in the complex. Unfortunately, the redox dyes that allow the potential to reach much lower potentials were not available when these titrations were performed. One 4Fe cluster has a value at around -320 mV and one 4Fe cluster has a value at around -205 mV. We assume that the rest of the cluster have values below -400/-450 mV. The non-cuboidal clusters do not show a 1+/2+ transition but only a 2+/3+ transition in the presence of a ligand. This was confirmed by the titrations performed on the HdrB2 C194S-C195S mutant (See chapter 3).

The 2Fe cluster in MvhD has a E_m value of -265 mV. The titrations also revealed a new signal at g-value 1.894, which had not been noted previously. The CXXC is also a binding motif for Zn-finger proteins and the expression of both HdrB and SdhE in *E. coli* might have resulted in the insertion of Zn^{2+} in one site. In addition, excess FAD and CoM was not removed from the protein after the purification and, therefore, removing this possible influencer will show what effect this may had on the EPR signals.

Rapid freeze quench was performed on the whole complex using dithionite as the electron donor. The [2Fe-2S] and CoM-bound Fe-S cluster were detected and indicated the electron switching from the [2Fe-2S] to the CoM-bound Fe-S cluster. No $[4Fe\text{-}4S]^+$ clusters were detected which hindered the process of developing a theory for the electron pathway. What was not known during that time was being able to saturate water with H_2. Therefore, we want to repeat this experiment utilizing H_2-saturated buffer to see if this changes the EPR signals. Using this method would ideally start the electron pathway at the [Ni-Fe] hydrogenase site and end at the HDS active site which could aid in reducing the $[4Fe\text{-}4S]^+$ during the electron transfer. Still we can speculate

that the 4Fe cluster with E_m=-320 mV would be a good candidate to donate electrons to the cluster, although it is not clear how it would transfer two at a time. The cluster with E_m-205 mV would be a good candidate to accept the first, high potential, electron from FAD in the bifurcation process.

The next step is to purify Vhc:Hdr from *M. maripaludis* and crystallize the structure. A selenocysteine is found bound to the [Ni-Fe] hydrogenase and as a replacement during the homodisulfide formation in HdrA. We hope to see a change in the EPR signals which would sequentially isolate certain iron-sulfur clusters while transferring the electron. We are, currently, in collaboration with a crystallographer interested in performing Cryo-EM on this enzyme, as well.

Our funder, DSM, initially started providing different compounds to analyze their inhibition effects on Mcr. During the crystallization of Mvh:Hdr , it was found 3-bromosulfonate was present in the active site similar to the position as CoM.[34] As a result, DSM provided additional compounds similar in structure to 3-bromosulfonate and CoM to analyze their inhibition effect on Mvh:Hdr. [34] Once the reduction mechanism of HDS is determined, we will be able to understand how these inhibitors bind at the active site. We have already performed the same in-vitro colorimetric assays discussed in section 2.2.7, but the inihibitors alone in the presences of methyl viologen and dithionite caused a color change from blue to black. Therefore, a hydrograph is the best instrument to track the activity since methyl viologen will not be needed to track the activity. Similar to the rapid freeze quench experiment, H_2 saturated water must be used to track the intake of this gas by Mvh:Hdr.

2.5.2 Isolated Mvh

Isolation of Mvh was successful and samples were created for EPR analysis. Mvh showed a clear $[2Fe\text{-}2S]^+$ cluster which allowed for isolation of the g-values. However, there was not enough protein to perform redox titrations. Hopefully this can be repeated with more protein.

Extensive redox titrations have been performed on hydrogenases. These studies did not detect a signal at g-value=1.894. Most likely the species is formed in HdrB but the data presented here does not support that idea. In future work, the Hdr complex should be used in freeze quench studies. It might be more complicated, however, since metronidazole could react at more sites and the experiments might have to be done with ferredoxin instead.

Chapter 3: Studies on the isolated subunits of Hdr

3.1 Introduction

With methane being the most potent greenhouse gas and it increases daily, researchers are highly interested in resolving the mechanism at which the subunit HdrB reduces HDS. A cysteine-rich sequence motif called the CCG domain has been found to be conserved in nearly 2000 archaeal and bacterial proteins.[50] $CX_{31-32}CCX_{33-38}CX_2CX_{46-71}CHX_{31-38}CCGGGVX_{30}CPFC$ represents the sequence motif of the CCG domain which was suggested to coordinate iron-sulfur clusters at the site. Fielding et al stated that although HdrB contained two CCG domains ($CX_{35-38}CCX_{35}CX_2C$), one site binds a [4Fe-4S] cluster, based on EPR studies, while the other a Zn metal ion, based on Zn K-edge X-ray absorption spectroscopy (XAS) studies. Furthermore, they defended their theory by arguing recombinant subunit E of succinate dehydrogenase (SdhE) from *Sulfolobus solfataricus* also contained two CCG domains where one site indicated a [4Fe-4S] cluster and the other site contained a Zn metal with a $S_3(O/N)_1$ coordination. Before the crystal structure was solved for Mvh:Hdr, this model was questioned by our group. Previous studies by our group indicated the CXXC is also a binding motif for a Zn-finger protein and the expression of both HdrB and SdhE in *E. coli* may have resulted in the insertion of Zn^{2+} in one site. The Hedderich group also showed that expression of HdrB in *E. coli* resulted in the insertion of a [2Fe-2S] cluster. When the host organism was changed to *Bacillus subtilis* a [4Fe-4S] cluster was inserted showing that the CCG domain is not always properly recognized. The Mvh:Hdr structure was still a surprise since two non-cuboidal clusters were detected.

For years, researchers believed that this subunit only contained one iron-sulfur cluster and developed mechanisms based on this single cluster.[49,59] After isolating HdrB from *Bacillus subtillis*, Madadi-Kahkesh and other researchers mixed CoMSH, $CoMS^{33}H$, and CoBSH to

determine which compound would bind to the iron-sulfur cluster and analyze this binding effect through EPR.[59,60] Based on these labeling studies, a mechanism was suggested as to how HDS would be reduced (**Figure 3.1**).[48,49] This mechanism involved a 'transient' species $[4Fe\text{-}4S]^{2+/+}$.[49] $[4Fe\text{-}4S]^{+}$ immediately reacts to the substrate and cleaved through a nucleophilic substitution reaction via a ligating cysteinate. The nucleophilic attack results in the formation of CoBSH and a weakly coordinated CoM-S-S-Cys.[49] The $[4Fe\text{-}4S]^{+}$ cluster donates two electrons to cleaves the disulfide finally resulting in CoMSH and a $[4Fe\text{-}4S]^{3+}$ cluster. The $[4Fe\text{-}4S]^{3+}$ transitions back to $[4Fe\text{-}4S]^{2+}$ by accepting one electron which allows for the reduction process to repeat. Since the identification of the second iron-sulfur cluster in HdrB, Wagner et al suggested a new mechanism involving both iron-sulfur cluster to reduce HDS (**Figure 3.2**).[34] The heterodisulfide enters near the two exposed iron atoms of the two separate noncuboidal clusters and, then, homolytically cleaved to bind to the clusters. These clusters, as a result, become oxidized transitioning from $[4Fe\text{-}4S]^{2+}$ to $[4Fe\text{-}4S]^{3+}$. Since the reduction of HDS requires two electrons, the first electron reduces CoBSH and the second electron reduces the CoMSH. The argument we present with this hypothesis is if isolated HdrB reduced HDS with one cluster present, then why would a second cluster need to be incorporated in the reduction mechanism? If a second cluster was vital for the reduction of HDS, then HdrB would not have been active and HDS would not have been reduced. Our lab was interested in learning the function of this second cluster in HdrB and what role it plays in the reduction of HDS.

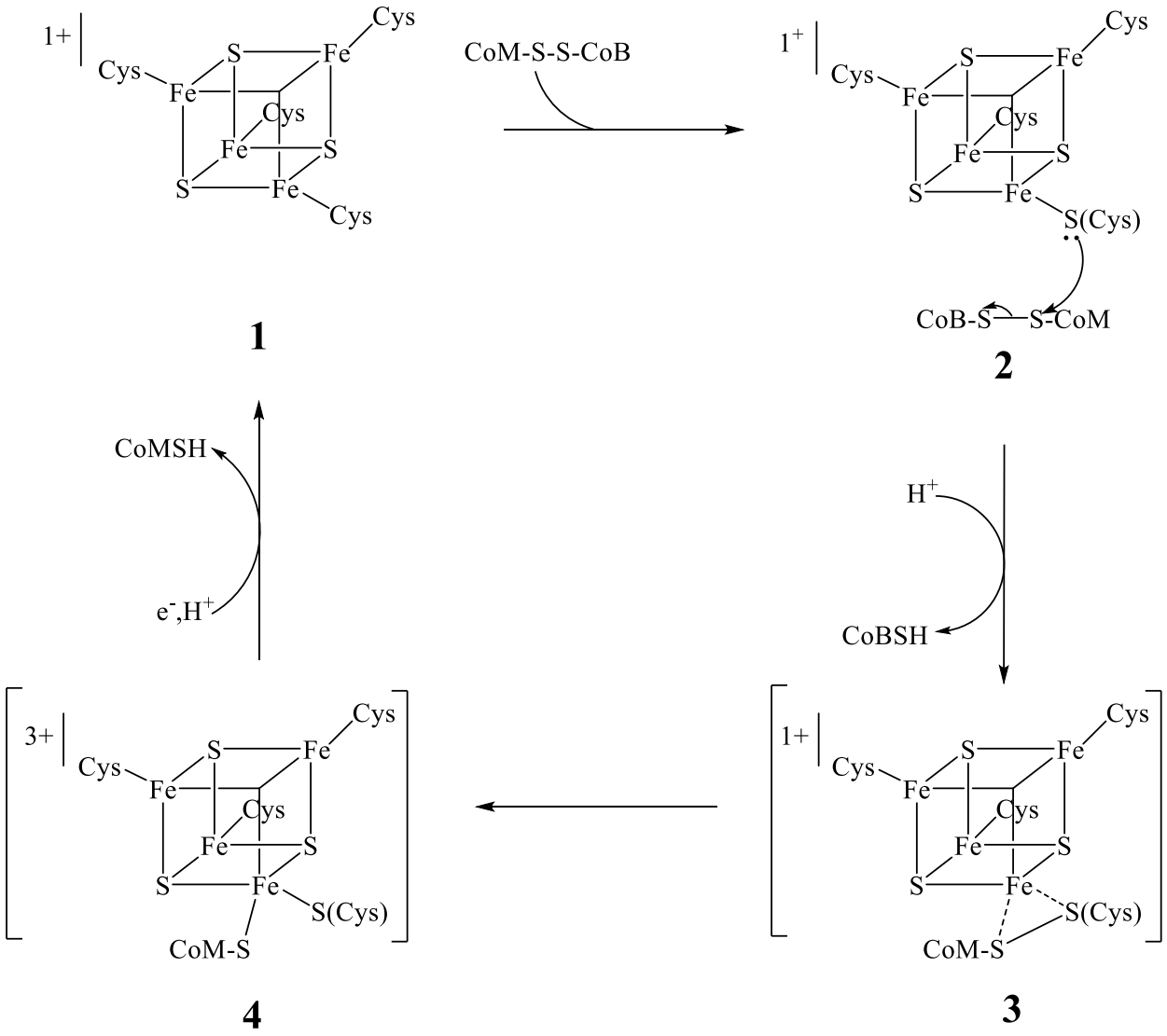

Figure 3.1: HDS reduction mechanism proposed by and adapted from Duin et al.[49] Because these researchers only determined one cluster was present in HdrB, they wrote the mechanism with only one cluster present.

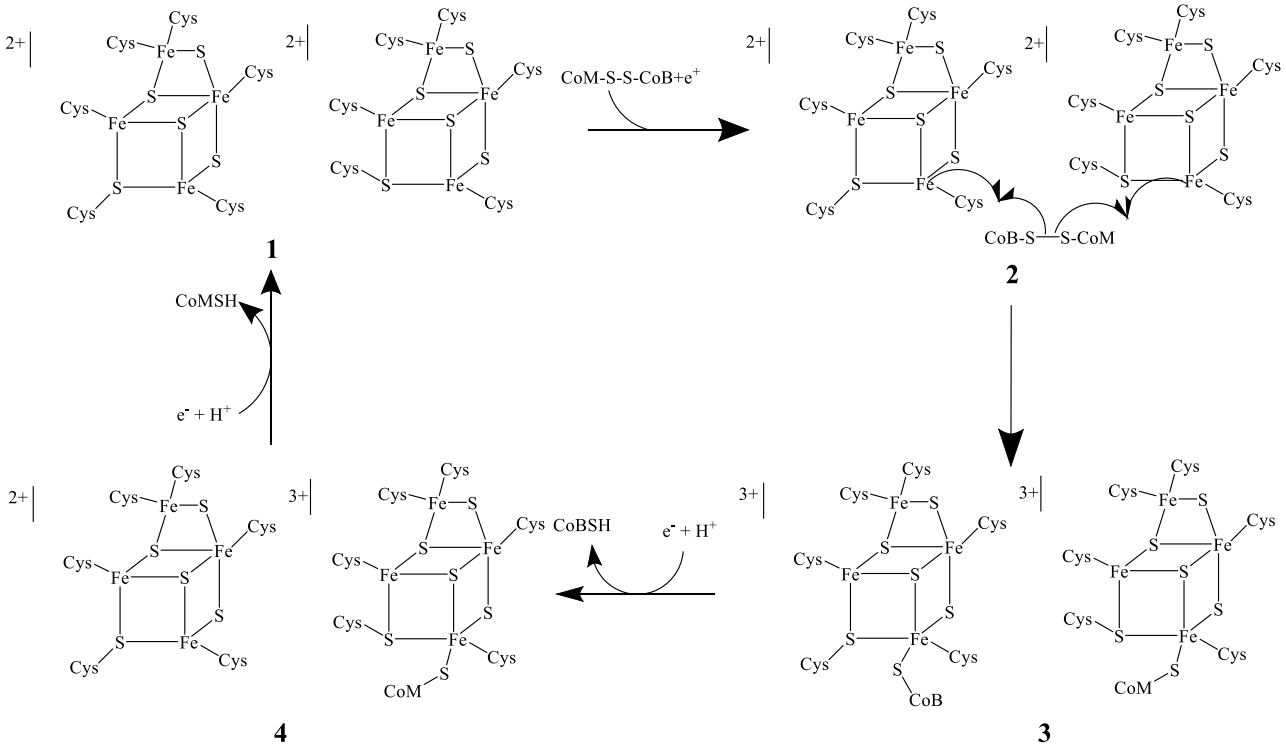

Figure 3.2: HDS reduction mechanism proposed by Wagner et al.[34]

The crystal structure generated a new set of questions that need to be answered. 1) How is the HDS reduction performed? 2) Why is expression of HdrB in *E. coli* not successful? Would co-expression of the *isc* genes fix this problem or is there a specialized cluster insertion gene? 3) Is the [4Fe-4S] cluster in recombinant HdrB a cuboidal or a non-cuboidal cluster? There is some debate whether these iron-sulfur clusters could be cuboidal but because of the harsh environment during crystallization, these clusters potentially fell apart. Recombinant HdrB was utilized in redox and rapid freeze quench studies to determine the coordination of the iron-sulfur cluster and to identify other characteristics about these clusters that may not have been observed during studies on the whole Hdr complex studies.

3.2 Materials and Methods

3.2.1 Reagents

4,4-bipyridyl and 2,2'-bipyridyl were purchased from Acros Organics located in New Jersey. 1,3-dibromopropane was purchased from Beantown Chemical located in Hudson, NH. Iodomethane, diethylenetriaminpentaacetic acid (DTPA), and europium (II) chloride was purchased from Sigma Aldrich located in St. Louis, MO.

3.2.2 Synthesis of Redox Dyes

3.2.2.1 1-methyl-4,4'-bipyridinium

4,4'-bipyridinium (**20**, 784 mg, 5.0 mmol) and methyl-iodide (**21**, 0.41 mL, 6.5 mmol) were mixed in DCM (10 mL) and refluxed at 30°C for two hours. After cooling to room temperature, the precipitate formed during the reflux was filtered off and washed with ethyl acetate. The solid was recrystallized in MeOH and then dried under lyophilization. The reaction for 1-methyl-4,4'-bipyridinium (**22, Scheme 3.1**) yielded 780 g (90%). Results from the ^{1}H NMR (**Figure 3.3-3.4**) showed the product was synthesized. The unlabeled peaks at 7.5 and 8.4 ppm potentially indicate unreacted 4,4'-bipyridinium.

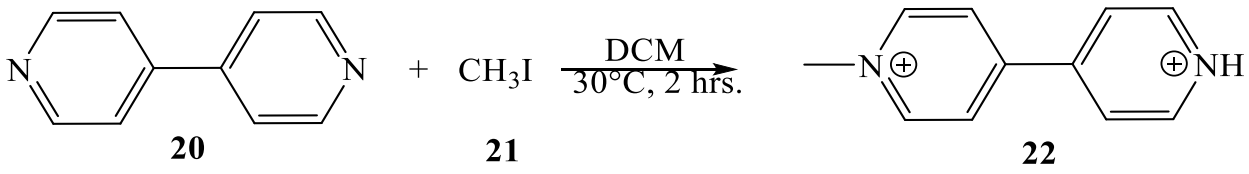

20 **21** **22**

Scheme 3.1: Synthesis of 1-methyl-4,4'-bipyridinium.

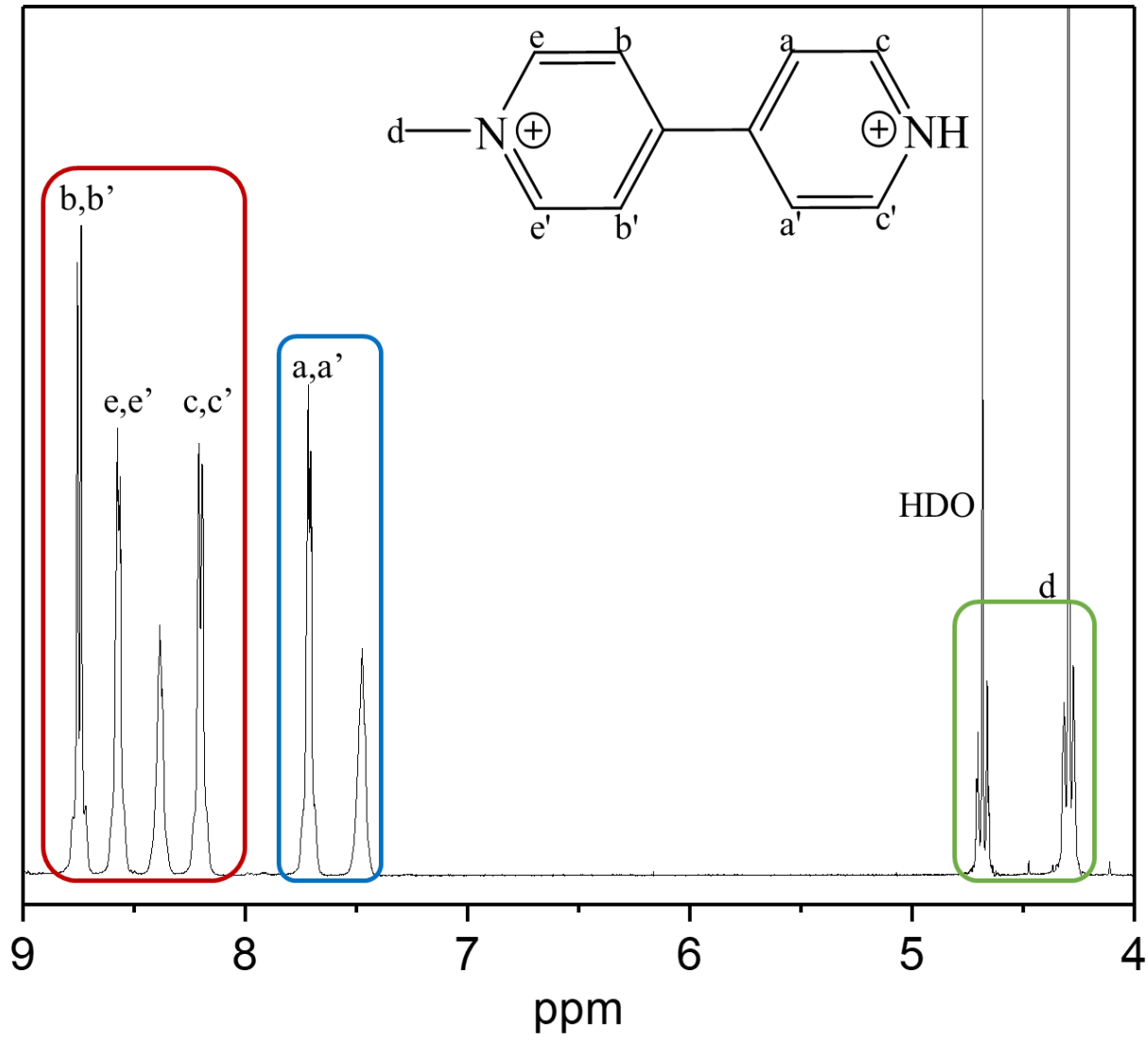

Figure 3.3: [1]H-NMR (D2O, 400 MHz) of 1-methyl-4,4'-bipyridinium: 8.74 (d, 2 H), 8.62 (d, 2 H), 8.23 (d, 2 H), 7.76 (d, 2 H), 4.28 (s, 3 H).

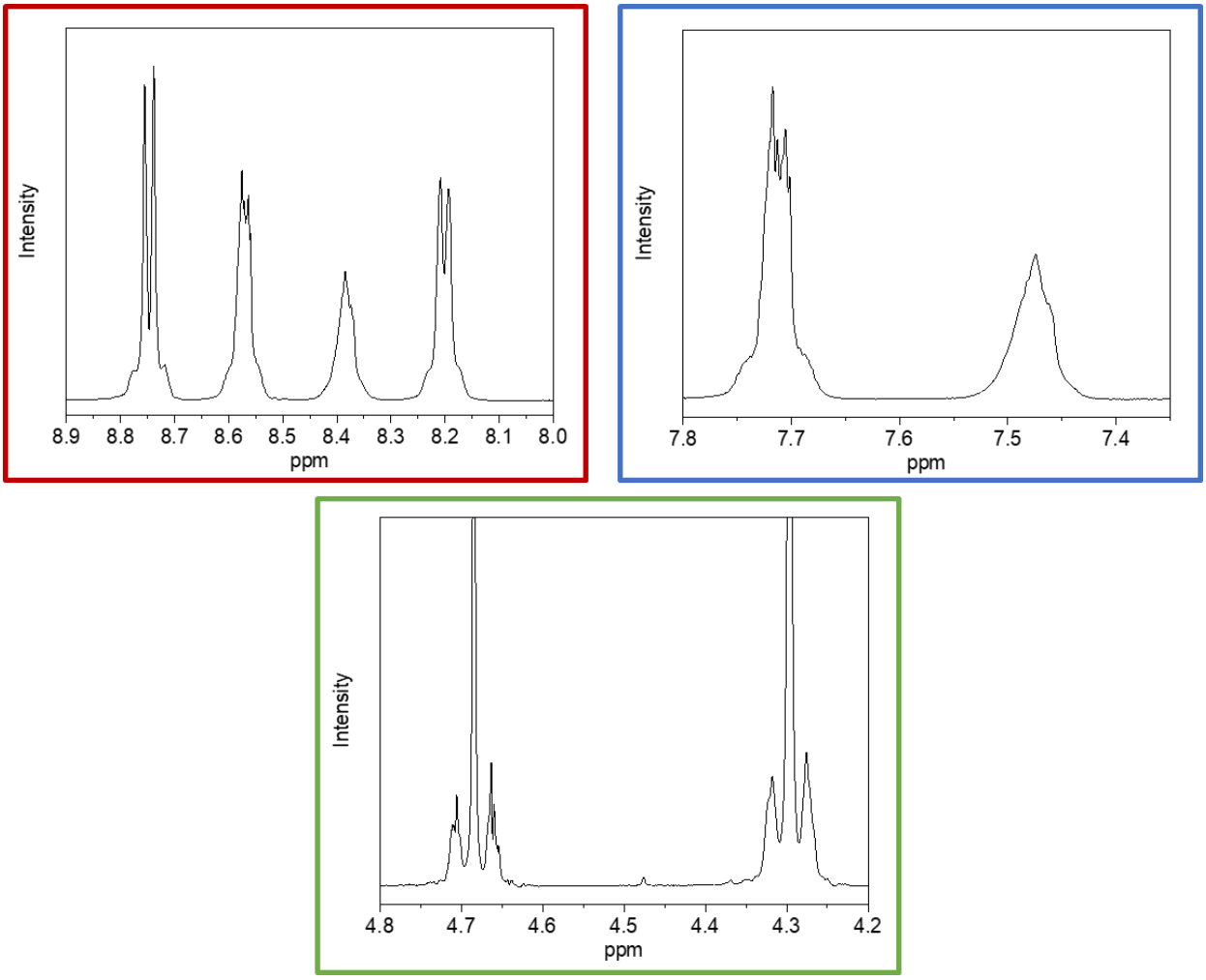

Figure 3.4: Zoomed in ranges of the ^{1}H NMR of 1-methyl-4,4'-bipyridinium. Colored outlines coordinate with the highlighted regions in **Figure 3.3**.

3.2.2.2 7,8-Dihydro-6H-dipyrido[1,2-a:2',1'-c][1,4]diazepinediium

2,2'-dibipyridinium (**23**, 250 mg, 1.7 mmol) was mixed with 1,3-dibromopropane (**24**, 6 mL) and refluxed at 167°C for 12 hours. Once the reaction was cooled to room temperature, the precipitate was filtered off and washed with cold acetone and hexane. This reaction (**Scheme 3.2**) yielded 542 mg (172%) of 7,8-Dihydro-6H-dipyrido[1,2-a:2',1'-c][1,4]diazepinediium (**25**). ^{1}H NMR (**Figure 3.5-3.6**) spectrum indicated the product was synthesized. Peaks shown in this ^{1}H

NMR spectrum indicate the drawn structure was synthesized based on the peaks formed. The reason for the HDO triplet peak and the multiplet at 4.4 ppm was determined to be unreacted compound **24** during the reaction. The ^{1}H NMR of pure **24** contains a triplet at 3.5 ppm and a quintet at 2.3 ppm. The peaks found in this spectrum appear further down field because **25** potentially provides a type of shield which makes the protons on **24** more resistant and causes them to appear further down the spectrum. With this evidence, this would explain the reason for over 100% yield as well.

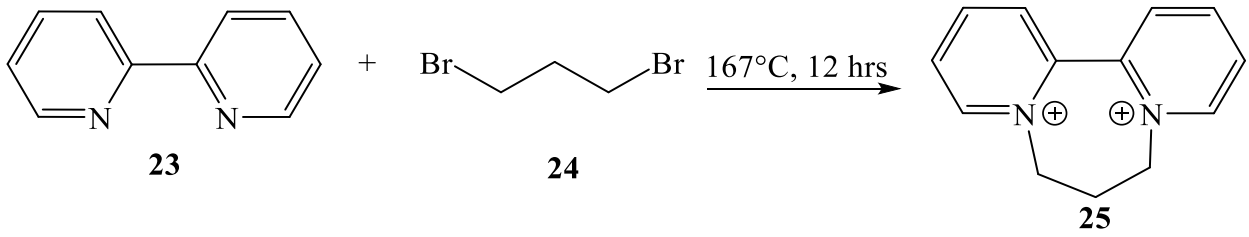

Scheme 3.2: Synthesis of 7,8-Dihydro-6H-dipyrido[1,2-a:2',1'-c][1,4]diazepinediium.

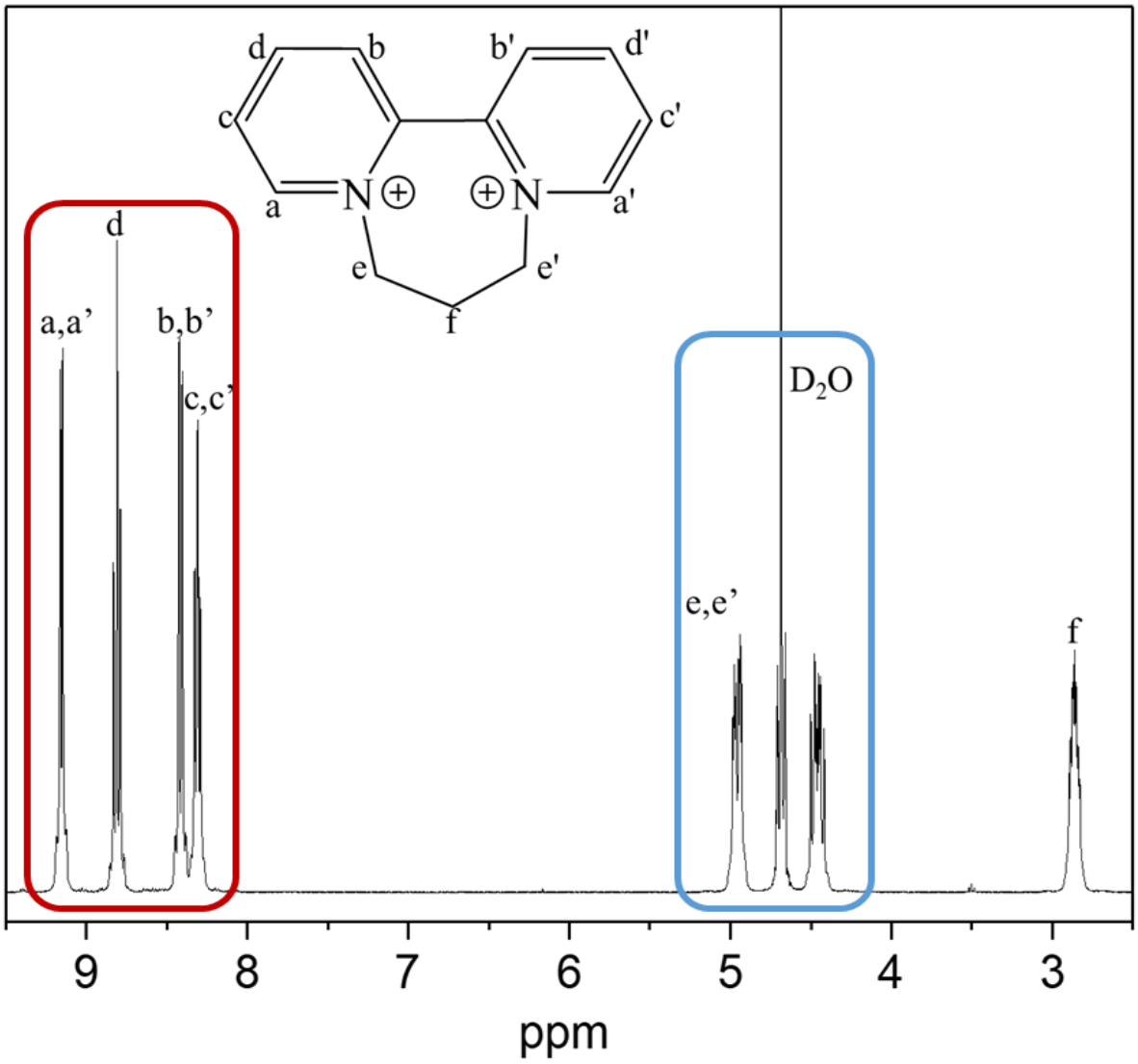

Figure 3.5: ^{1}H-NMR (D2O, 400 MHz) of 7,8-Dihydro-6H-dipyrido[1,2-a:2',1'-c][1,4]diazepinediium: 9.11 (d, 2 H), 8.78 (t, 2 H), 8.37 (d, 2 H), 8.27 (t, 2 H), 4.89-4.85 (m, 2 H), 4.37-4.46 (m, 2 H), 2.81-2.83 (m, 2 H).

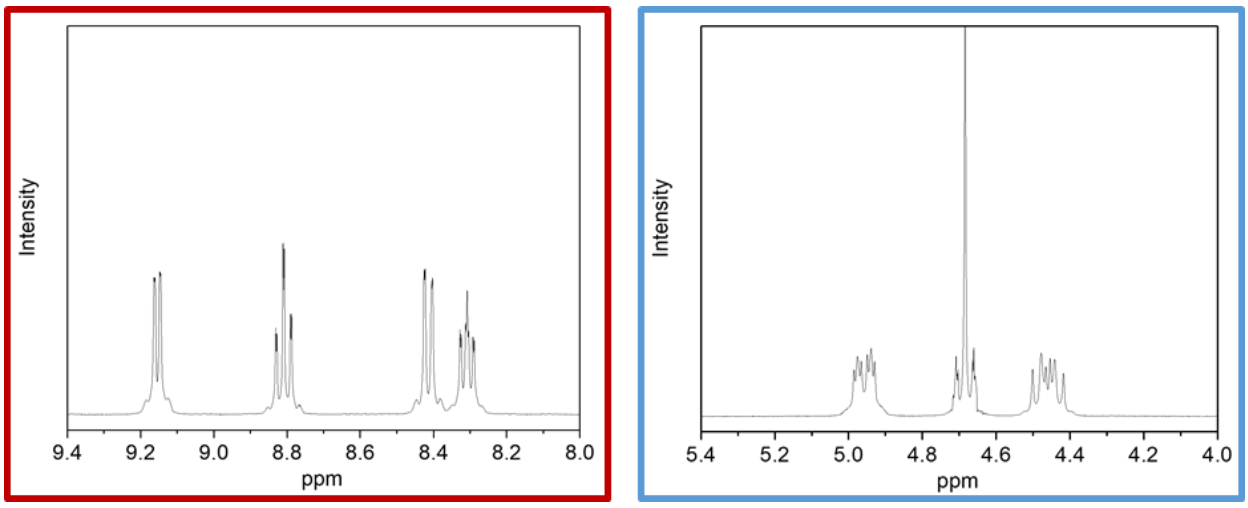

Figure 3.6: Zoomed in regions of the ^{1}H NMR of 7,8-Dihydro-6H-dipyrido[1,2-a:2',1'-c][1,4]diazepinediium. Colored outlines coordinate with the highlighted regions in **Figure 3.5**.

3.2.2.3 2,12-Dimethyl-7,8-dihydro-6H-dipyrido[1,2-a:2',1'-c][1,4]diazepinediium

This synthesis followed the same steps as discussed in section 2.2.3.2 except 4,4'-dimethyl-2,2'-bipyridinium (**26**, 315 mg, 1.7 mmol) was mixed with compound **24** (6 mL) instead. Compared to NMR spectra of the starting reactants, 2,12-Dimethyl-7,8-dihydro-6H-dipyrido[1,2-a:2',1'-c][1,4]diazepinediium (**27**) was synthesized (**Scheme 3.3, Figure 3.7-3.8**) with a yield 580 mg (150%). Similar peaks found in **Figure 3.5** were also found in **Figure 3.7** which gives the same reasoning as to why the percent yield was over 100%.

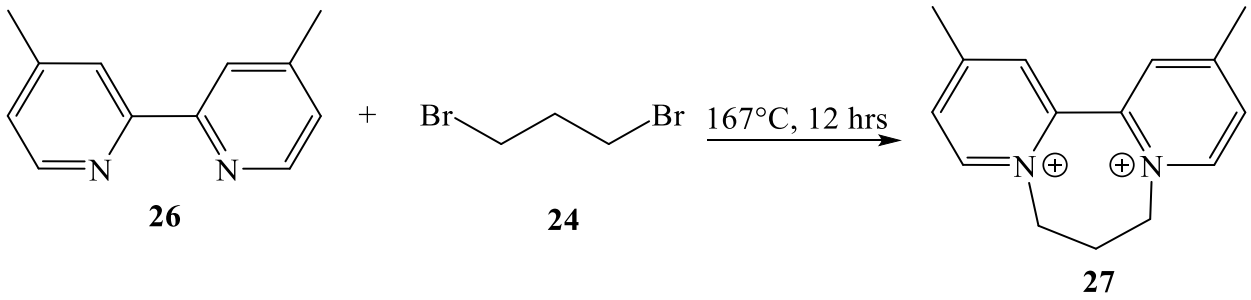

26 **24** **27**

Scheme 3.3: Synthesis of 2,12-Dimethyl-7,8-dihydro-6H-dipyrido[1,2-a:2',1'-c][1,4]diazepinediium.

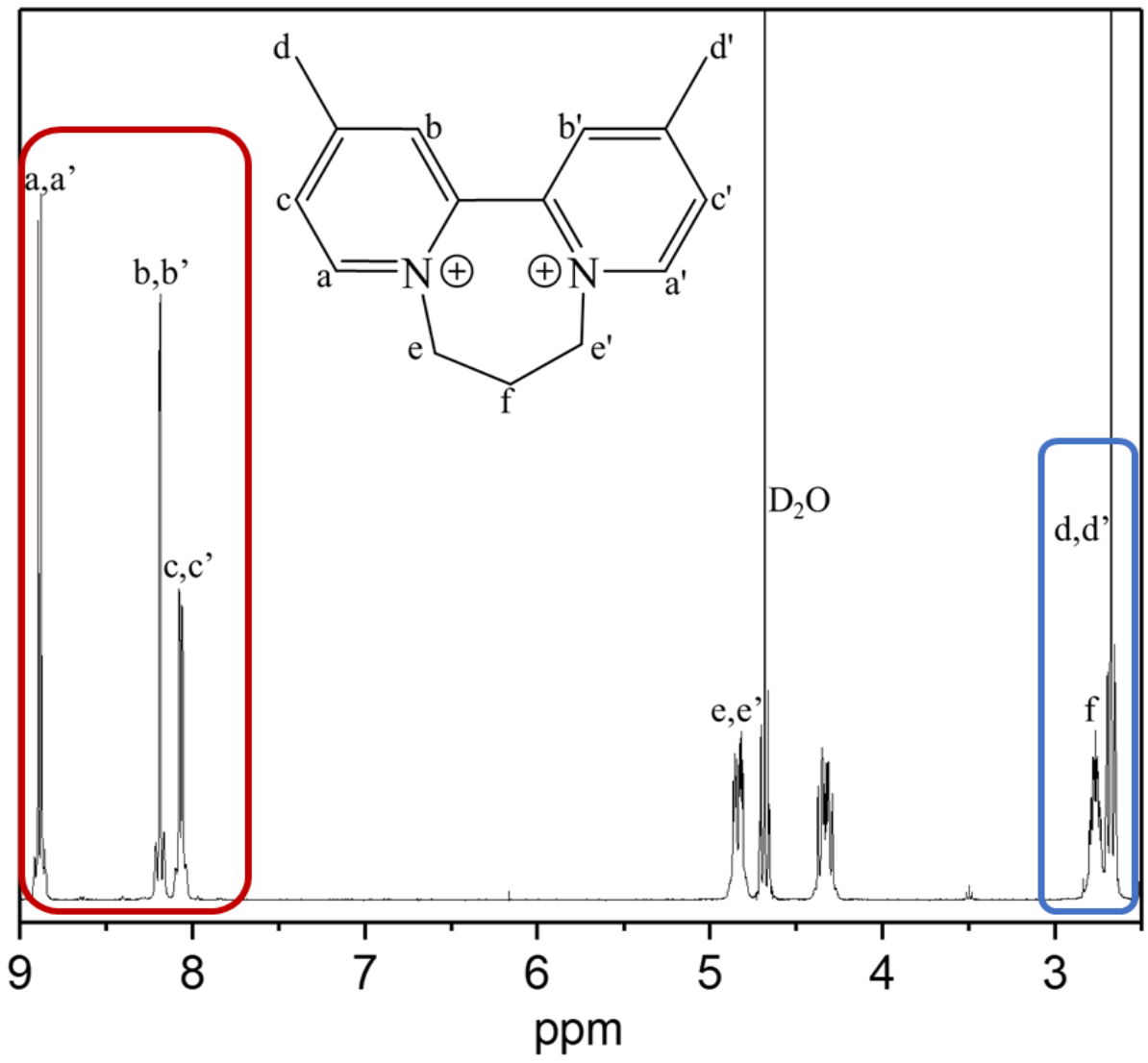

Figure 3.7: ^{1}H-NMR (D_2O, 400 MHz) of 2,12-Dimethyl-7,8-dihydro-6H-dipyrido[1,2-a:2',1'-c][1,4]diazepinediium: 8.95 (s, 2 H), 8.56 (d, 2 H), 8.19 (d, 2 H), 4.79-4.83 (m, 2 H), 4.31-4.39 (m, 2 H), 2.75-2.82 (m, 2 H), 2.54 (s, 6 H).

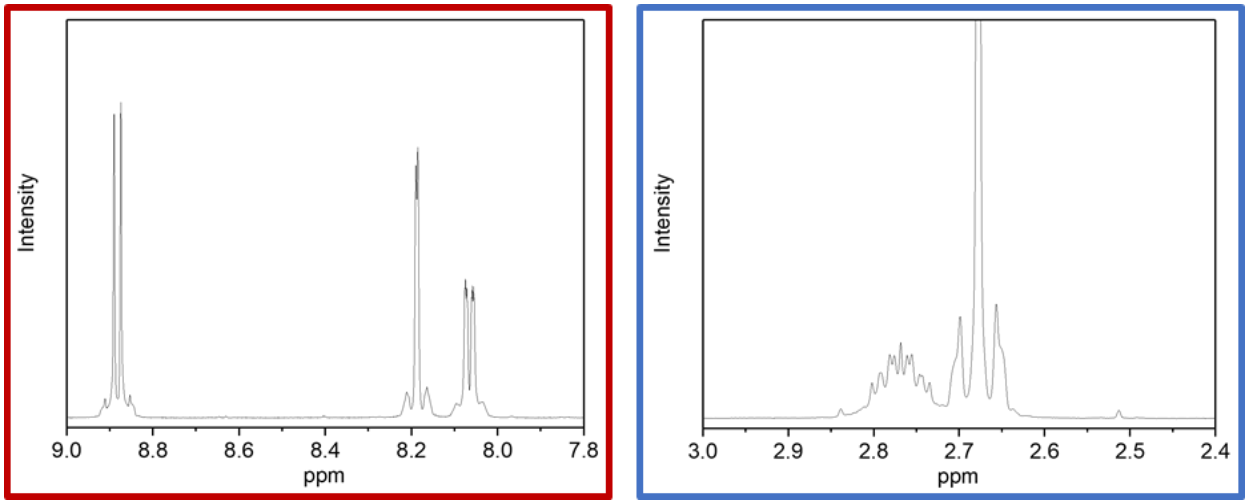

Figure 3.8: Zoomed in regions of the ^{1}H-NMR of 2,12-Dimethyl-7,8-dihydro-6H-dipyrido[1,2-a:2',1'-c][1,4]diazepinediium. The colored outlines coordinate with the highlighted regions in **Figure 3.5**.

3.2.2.4 3,11-Dimethyl-7,8-dihydro-6H-dipyrido[1,2-a:2',1'-c][1,4]diazepinediium

This synthesis was the same as section 2.2.3.3 but this reaction used 5,5'-dimethyl-2,2'-bipyridinium (**28**, **Scheme 3.4**). This reaction synthesized 3,11-Dimethyl-7,8-dihydro-6H-dipyrido[1,2-a:2',1'-c][1,4]diazepinediium **29** which gave a yield of 522 mg (135%) as indicated by the NMR spectrum shown in **Figure 3.9-3.10**. As previously noted, the peaks at 4.4 and 4.7 ppm were from unreacted compound **24**.

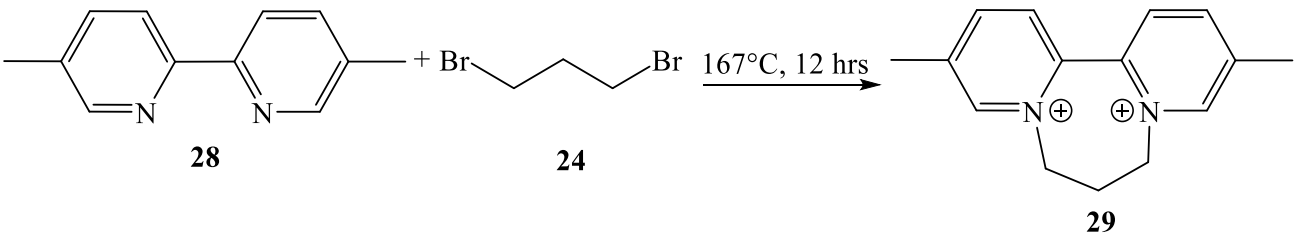

28 **24** **29**

Scheme 3.4: Synthesis of 3,11-Dimethyl-7,8-dihydro-6H-dipyrido[1,2-a:2',1'-c][1,4]diazepinediium.

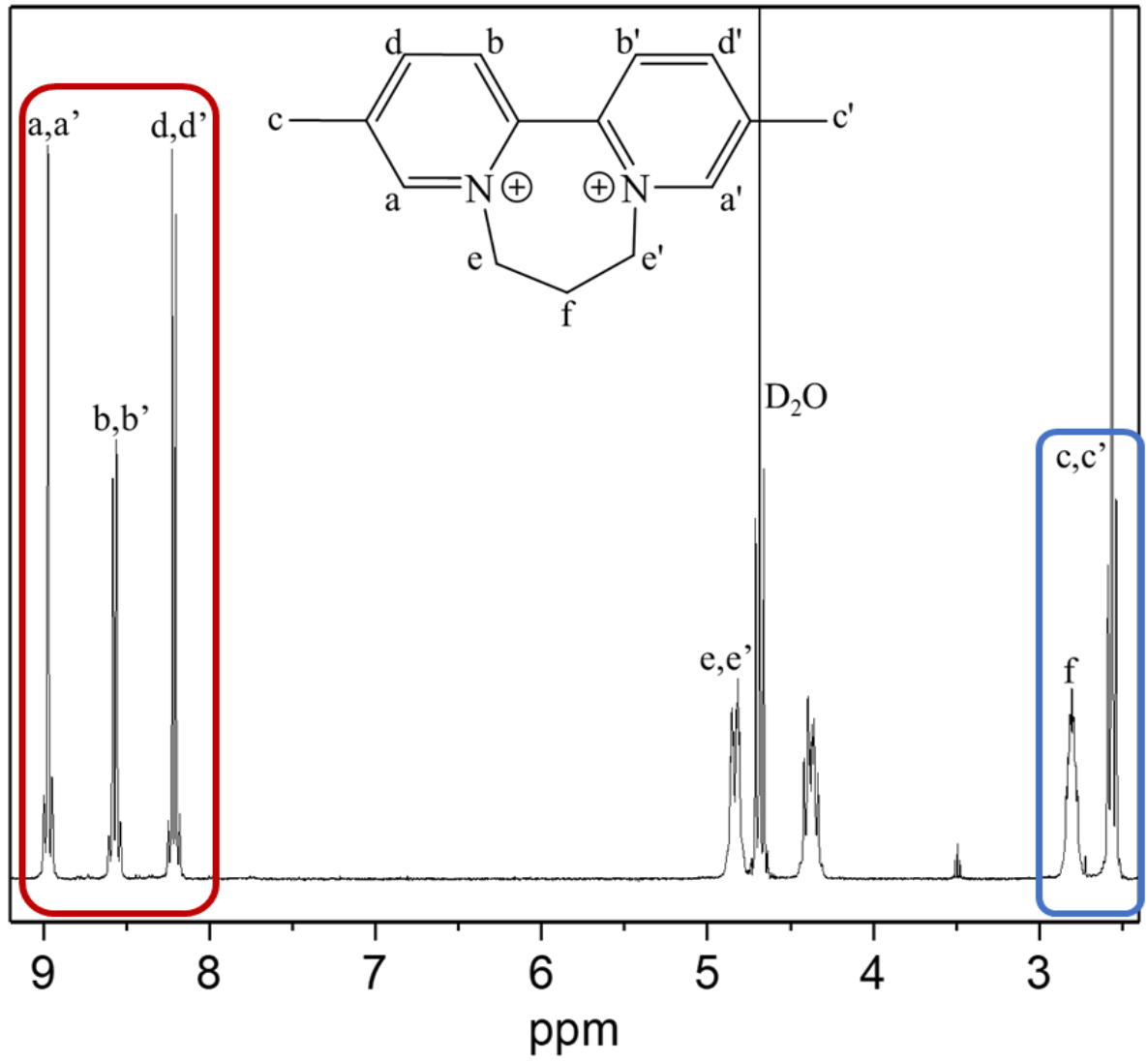

Figure 3.9: ^{1}H-NMR (D_2O, 400 MHz) of 3,11-Dimethyl-7,8-dihydro-6H-dipyrido[1,2-a:2',1'-c][1,4]diazepinediium: 8.42 (d, 2 H), 8.14 (s, 2 H), 8.02-8.04 (m, 2 H), 4.77-4.83 (m, 2 H), 4.24-4.33 (m, 2 H), 2.70-2.75 (m, 2 H), 2.64 (s, 6 H).

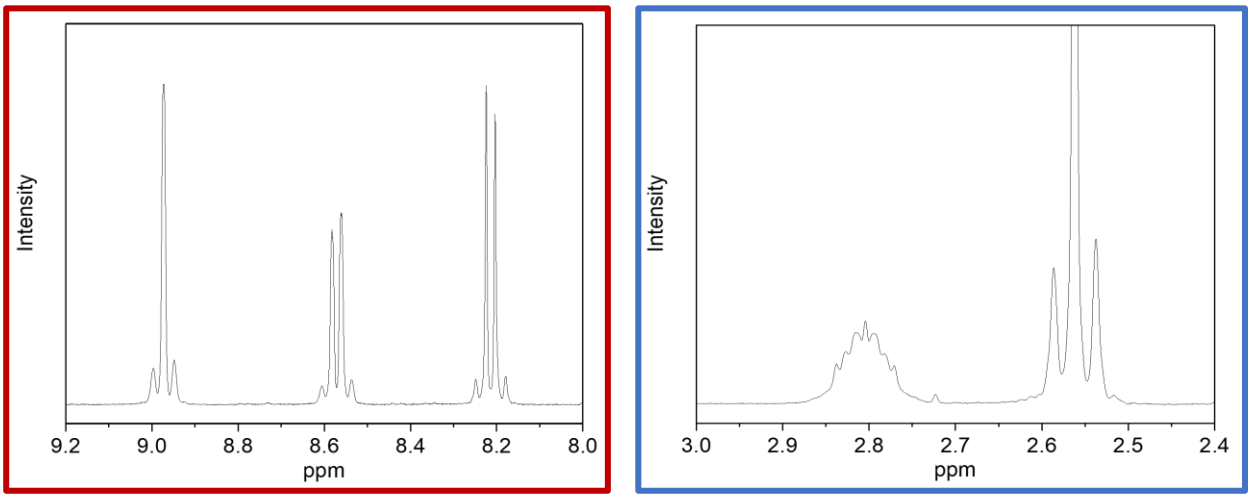

Figure 3.10: Zoomed in region of the ^{1}H-NMR of 3,11-Dimethyl-7,8-dihydro-6H-dipyrido[1,2-a:2',1'-c][1,4]diazepinediium. The colored outlines coordinate with the highlighted regions in **Figure 3.5**.

3.2.3 Synthesis of N-7-Mercaptoheptanoyl-O-phospho-L-threonin (CoB)

Compound **19** (0.1145 mg, 0.032 mmol) was dissolved in 2 mL 50 mM potassium phosphate buffer, pH 7.0, in an anaerobic glove box. 10% KBH_4 (w/v in 50 mM potassium phosphate buffer, pH=7, 8 mL) was added to the reaction and stirred for 16 hours in the anaerobic glove box. 25% HCl (v/v, 2 mL) was added, anaerobically, to quench the excess KBH_4. The mixture was applied to a PAD-II column (1 cm X 10 cm) which had been equilibrated with 1 M HCl overnight. The column was washed with anaerobic water to remove possible impurities. The product (compound **10**) was eluted with 70:30 (v/v) water: methanol. Purity of CoB (**10**) was determined by performing the Ellman's reagent assay. While the percent yield was 55%, the purity was determined to be 47%. A by-product developed during the synthesis of compound **10** is KCl and would explain the low percent purity. This determination was corrected to achieve the

concentration needed for the experiments. The protons on C7 of Compound **10** produced a triplet at 2.42 which is shifted compared to compound **19**'s triplet found at 2.64 due to the sulfur atom having a hydrogen bond versus another sulfur bond (**Scheme 3.5, Figure 3.11-3.12**).

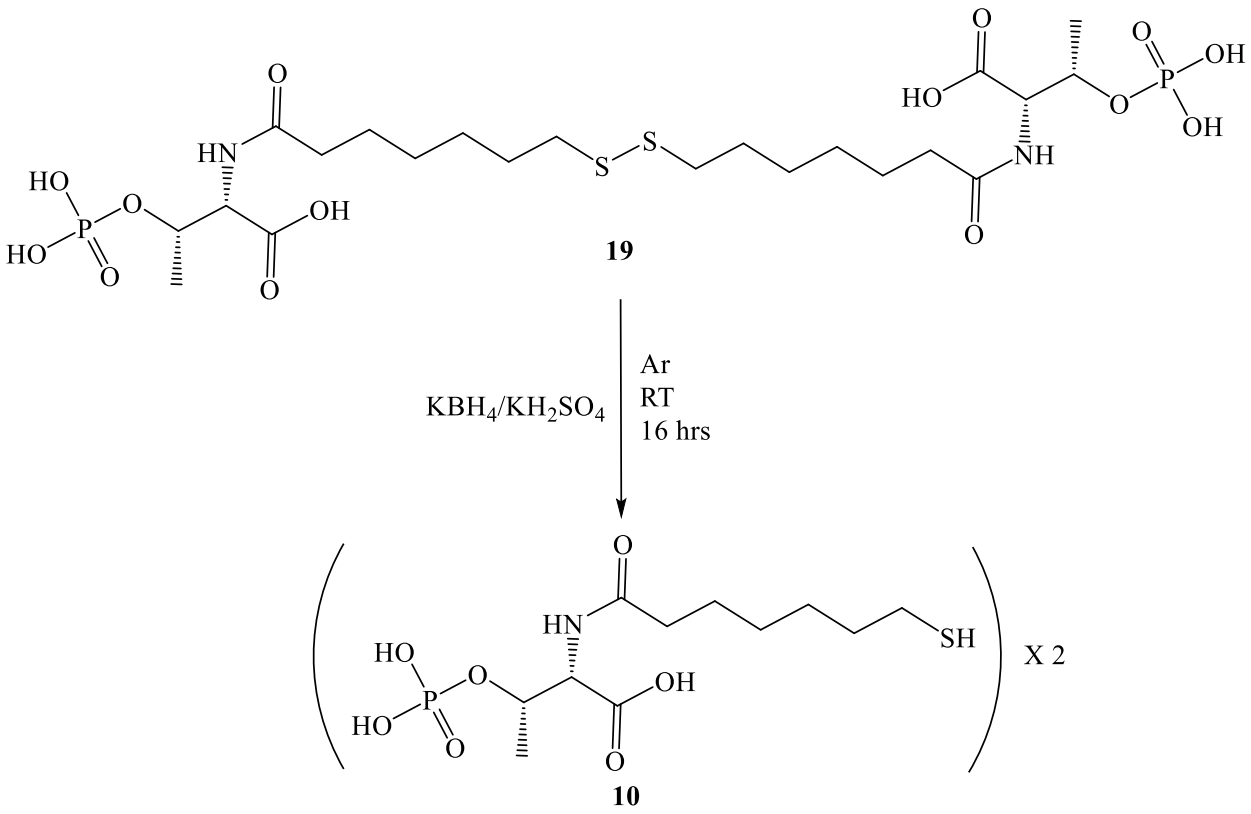

Scheme 3.5: Synthesis of CoB.

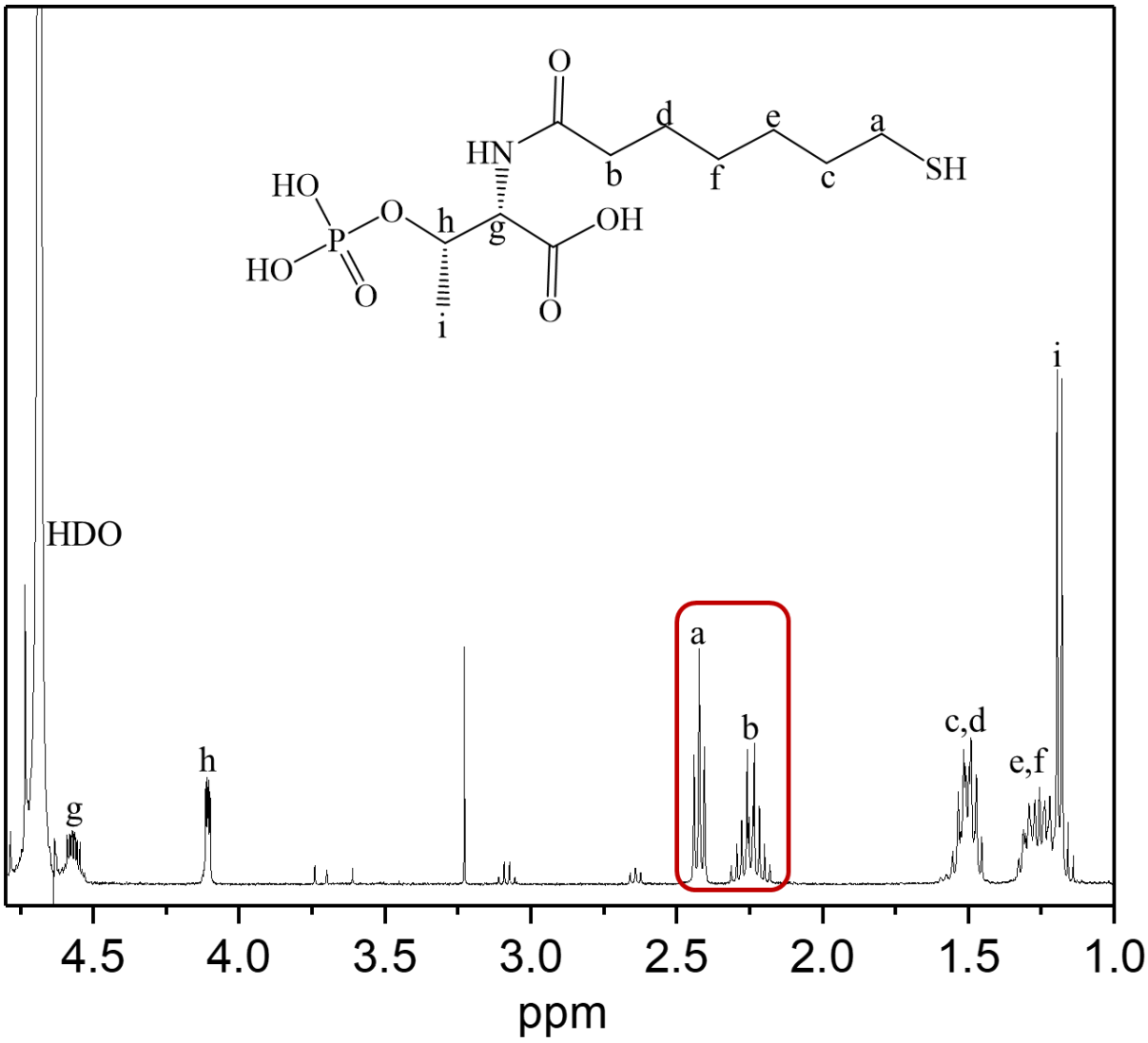

Figure 3.11: ^{1}H NMR (D_2O, 400 MHz) of CoB: 4.52-4.60 (dqd, 1H), 4.10 (dd, 1H), 2.42 (t, 2H), 2.18-2.32 (dt, 2H), 1.44-1.56 (quint., 4H), 1.21-1.34 (q, 4H), 1.19(d, 3H).

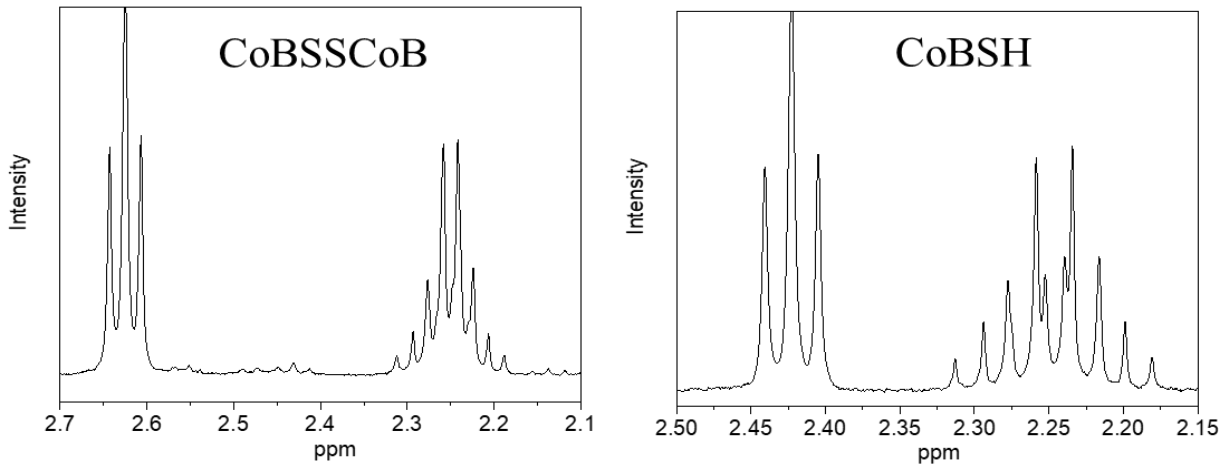

Figure 3.12: Zoomed in region of the ^{1}H NMR of CoB. These areas represent the highlighted region in **Figure 3.11.**

3.2.3 HdrB Methods

3.2.3.1 Cloning hdrB2[67,68]

The cloning was performed by the lab of Dr. James "Greg" Ferry (Pennsylvania State University). *hdrB2* (MA4237) of *M. acetivorans* were amplified by PCR and cloned into pETDuet (Novagen) for coexpression with a C-terminal His_6 tag on HdrB2. Constructs were validated by sequencing.[68]

3.2.3.2 Overexpression and purification of HdrB2[67,68]

These procedures were performed by the Ferry lab. The protein was overexpressed as discussed in section 5.2.2.[68]

3.2.3.3 EPR monitored-redox titration

This experiment was performed the same way as discussed in section 2.2.6.

3.2.3.4 EPR monitored-rapid freeze quench

This experiment was performed the same way as discussed in section 2.2.7. For the reverse direction, 5 mM CoM and CoB were used as the substrate and dithionite was not added.

3.2.4 HdrBC Methods

3.2.4.1 Cloning hdrBC[67,68]

Cloning was completed by the Ferry lab. *hdrB2C2* (MA4236) of *Methanococcus acetivorans* were amplified similar to the procedure mentioned in section 3.2.3.1.[68]

3.2.2.2 Overexpression and purification of HdrBC[67,68]

These procedures were performed by the Ferry lab. The plasmids were transformed into *Escherichia coli* BL21 (DE3) Δ*iscR* and grown with 100 μg/mL ampicillin. A colony was used to inoculate 100 mL of LB medium buffered with 50 mM morpholinepropanesulfonic acid (MOPS) (pH 7.4) and supplemented with 100 μg/mL of ampicillin that was incubated at 37°C for 12 hours.[68]

The starter culture was subcultured (1:50 dilution) in 3 liters of the above medium supplemented with 1 mM ferric ammonium citrate that was contained in a spinner flask (Chemglass) modified to allow sparging with 100% Ar. Cultures were grown aerobically at 37°C to an optical density at 600 nm (OD600) of 0.6 that was then supplemented with 1 mM cysteine and induced with 200 μM isopropyl-β -D-thiogalactopyranoside (IPTG). Anaerobic metabolism was facilitated by the addition of glucose (0.5%, wt/vol) and sodium fumarate (25 mM) followed by incubation at 21°C for 20 h with sparging. Cells were harvested by centrifugation in sealed tubes containing 95% N_2–5% H_2, resuspended (1:5, wt/vol) in 50 mM Tris (pH 8.0) containing 10% glycerol (buffer C), and stored at -80°C until use. [68]

3.2.2.3 EPR-monitored redox titration

This experiment was performed the same way as discussed in section 2.2.6.

3.2.2.4 EPR-monitored rapid freeze quench

This experiment was performed the same way as discussed in section 2.2.7.

3.3 Results

3.3.1 HdrB2 Results

3.3.1.1 *WT HdrB2 Results*

The SDS-PAGE gel (**Figure 3.13**) was provided by the Ferry group along with the iron concentration and specific activity data (**Table 3.1**).[69] When they performed the specific activity assay with CoM-S-S-CoB (**Scheme 3.6**), they did not detect any activity most likely due to the reaction occurring too fast for the instrument to detect. Therefore, the activity assays involved the reverse reaction with CoM and CoB.

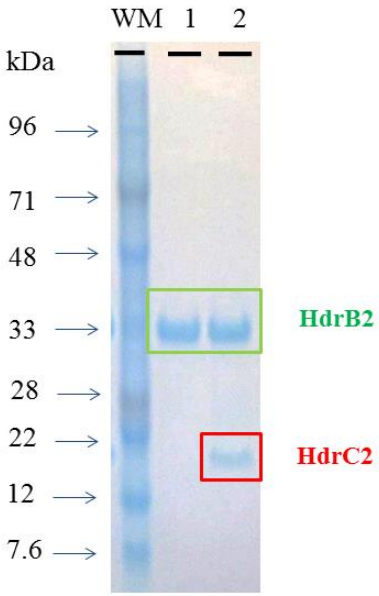

Figure 3.13: SDS-PAGE gel picture provided by the Ferry group.[67] The lane labeled 'WM' represents the weight marker to compare the proteins' weights. Lane #1 shows the HdrB2 protein while lane #2 represents the HdrB2C2 protein.

Table 3.1: Iron concentration, specific activity, and iron content percentage calculated through EPR signals for the WT HdrB2 and variants after reconstitution.[69] Activity assays were executed with the presence of CoM and CoB. * represents the activity was detected after incubation (10 minutes) with both substrates.[69] The more negative and more positive EPR signals were individually calculated by determining the iron concentration through comparison of a Cu standard. Once determined, this value was divided by the iron concentration calculated by Ferry's group which gave the percentage of iron content.

WT HdrB2 and Variants Results				
Protein	Iron Concentrations (μmol Fe/μmol of protein)	Specific Activity (nmol*(min*mg of protein)$^{-1}$)	% Fe Content-Reduced Signal	% Fe Content-Oxidized Signal
WT HdrB2	3.9	460	71%	12%
HdrB2 C42S-C43S	3.8	No Detection	207%	6.9%
HdrB2 C194S-C195S	4.7	428*	31%	17%
HdrB2C2	14.6	600	-	-

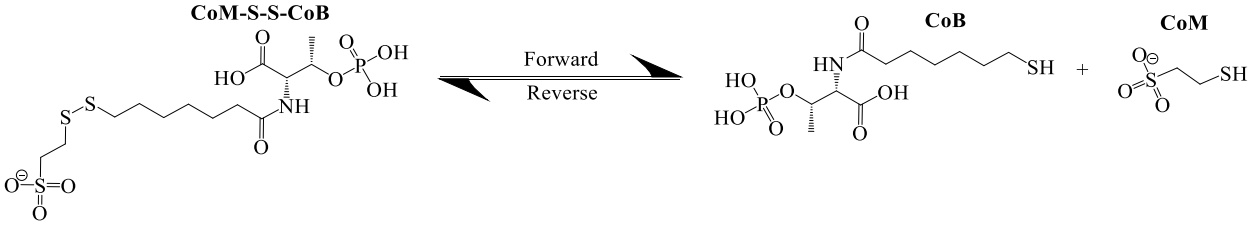

Scheme 3.6: Forward and reverse reaction for the reduction and oxidation of HDS respectively.

3.3.1.1.1 EPR-monitored redox titration

In **Figure 3.14**, an overview of the redox study performed with WT HdrB2 is shown along with the Nernst curves for the more negative and the more positive potential signal. For the entirety of redox studies performed on WT HdrB2, please refer to the 'Appendix for Chapter 3' for the overview of EPR spectra and the Nernst curves calculated for the individual signals. During these studies, two different rhombic signals were detected at two different redox potentials. A rhombic signal with g_{zyx}= 2.053, 1.980, 1.857 and a midpoint potential of -354 +/- 7 mV while the other rhombic signal with g-values of 2.030, 1.970, 1.945 had a midpoint potential of -173 +/- 10 mV. Whether these signals were from two separate iron-sulfur clusters or just one was not clear. For the WT HdrB2, Santiago Martinez reported ~4 μmol Fe/μmol of protein which would result in one [4Fe-4S] cluster, ideally. The EPR signal revealed, however, that 50% of this Fe formed a [2Fe-2S] cluster for the more negative potential. We confirmed this signal to be a [2Fe-2S] cluster through temperature studies and the variant studies which are discussed later in this chapter. We assigned the more positive signal to the noncuboidal [4Fe-4S] cluster. The signal, however, is due to a small amount of the $[4Fe\text{-}4S]^{3+}$-ligand state formed. No signal was detectable for the $[4Fe\text{-}4S]^{1+}$ state unless the extra peak at 350 mT at -528 mV was due to this species. Subtractions, however, did not result in an EPR signal that could be easily assigned (not shown).

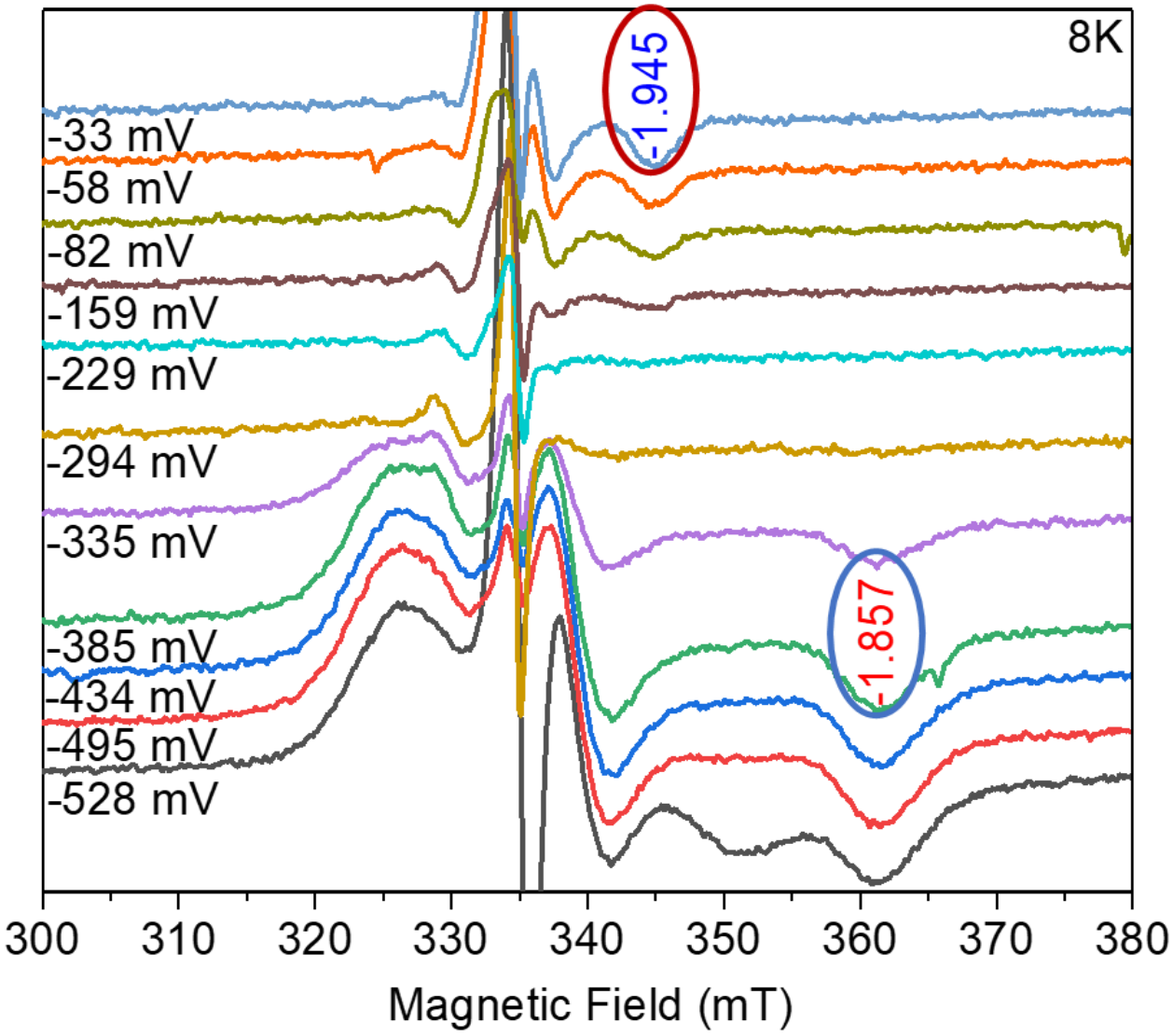

Figure 3.14: Selected EPR monitored-redox titration spectra overlaid of WT HdrB2 measured at 8 K.

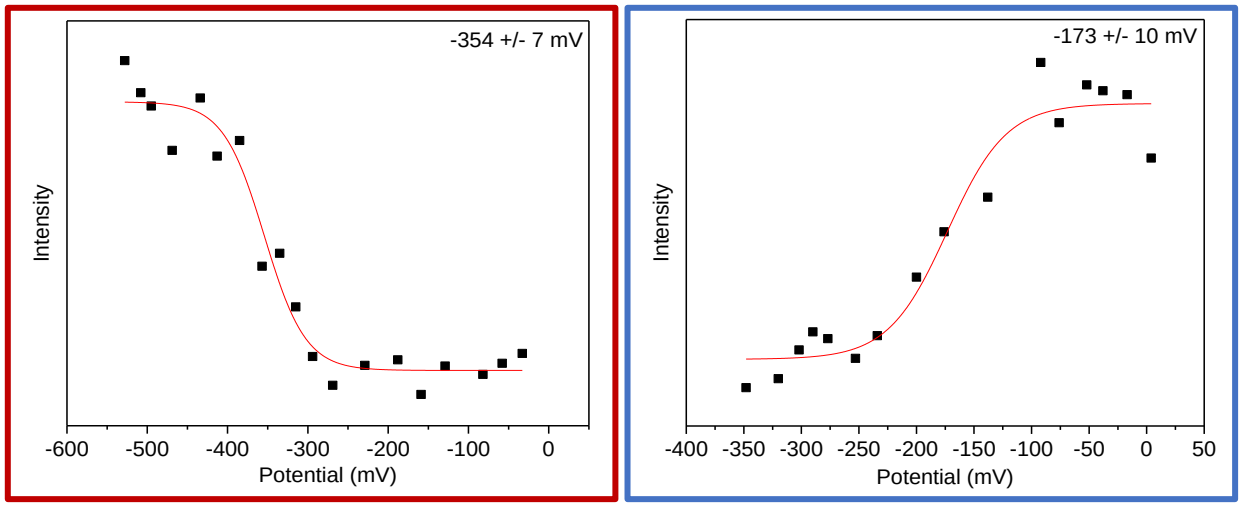

Figure 3.15: The Nernst curves created for the g-values from the redox titrations of WT HdrB2. The midpoint potential values are in the top right corner of each graph. The first values represent the average of all the redox studies performed while the second value gives the standard deviation.

3.3.1.1.2 Temperature Studies

Temperature studies were performed on HdrB (**Figure 3.16-3.17**). The optimal temperature where the signal could be measured without saturation or broadening was ~20-30K, and the signal was detectable up to 60-80 K. Regular [4Fe-4S] clusters have a small window, 5-15 K, where they can be detected without saturation or temperature broadening. This temperature abnormality aided in the determination of the more negative potential EPR signal to be a [2Fe-2S] cluster. The higher potential EPR signal was the non-cuboidal cluster based on the signals found in WT Hdr. Due to the low intensity, no full Curie plot was obtained. The data in **Figure 3.17** indicates that it might behave similar to the 2Fe cluster with an optimum at 20 K and detection all the way up to 70 K.

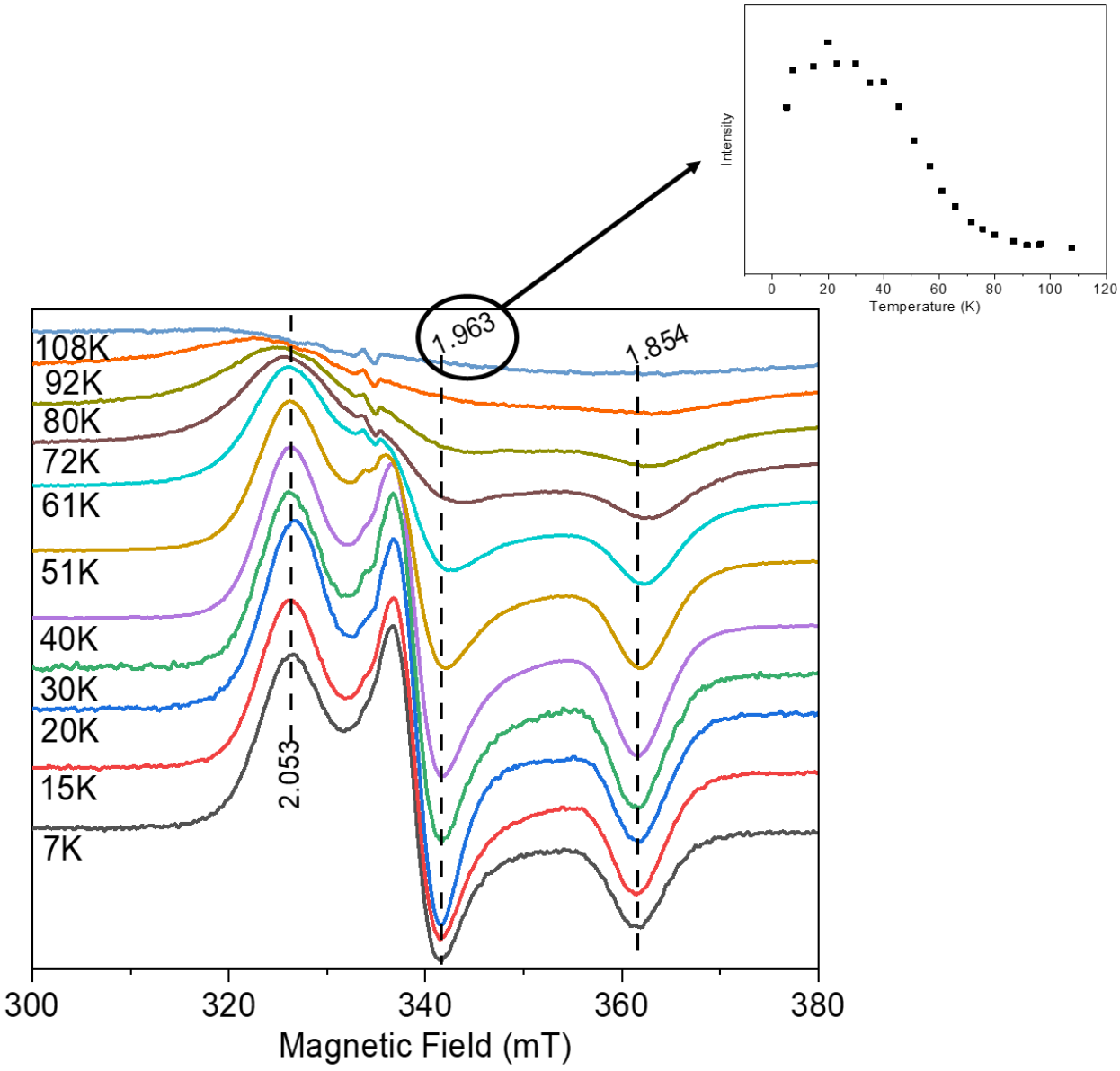

Figure 3.16: Overlay from temperature studies overlay of WT HdrB2 'As Such' sample. Top right corner shows the Curie plot at g-Value 1.963. This plot was created by plotting the intensity at g-Value 1.963 as the temperature increased.

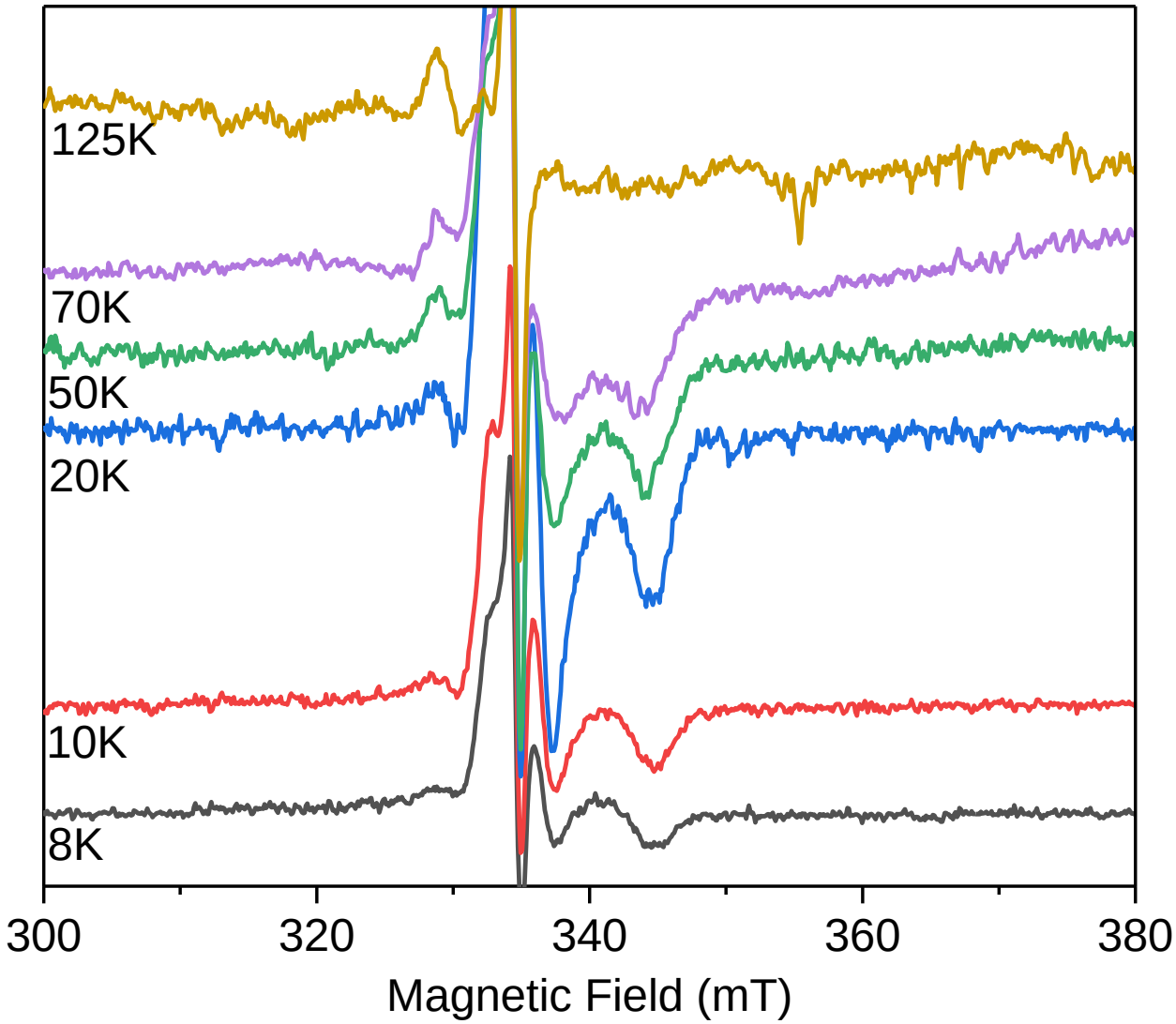

Figure 3.17: Overlay from temperature studies of overlay of WT HdrB2 at -33 mV (NHE value). A Curie plot could not be created because there were not enough temperature measurements made at the time.

3.3.1.1.3 EPR-monitored rapid freeze quench

Both the forward reaction (**Figure 3.18**) and the reverse reaction (**Figure 3.19**) were performed for the rapid freeze quench experiment. Yan et al performed activity assays on HdrB2

but found performing the forward reaction was too fast for their instrument to detect. When they performed the reverse reaction, they determined the turnover rate to be 2 s^{-1}. We performed both experiments to see what the EPR would reveal during these reactions. The forward reaction appeared to complete after just 10 ms. The possible explanation is the [2Fe-2S] EPR signal overpowered the non-cuboidal cluster. Therefore, the HDS was potentially being reduced by the cluster but we could not detect it well enough due to the overwhelming [2Fe-2S] signal.

As for the reverse reaction, the low potential signal disappears as time progresses and the high potential signal begins to appear. The reaction with CoM and CoB should reduce the protein but that is not observed. However, the $[4Fe\text{-}4S]^{3+}$-ligand form only forms under reducing conditions. The issue with this experiment is the data was hard to interpret since most change occurred after 3000 ms.

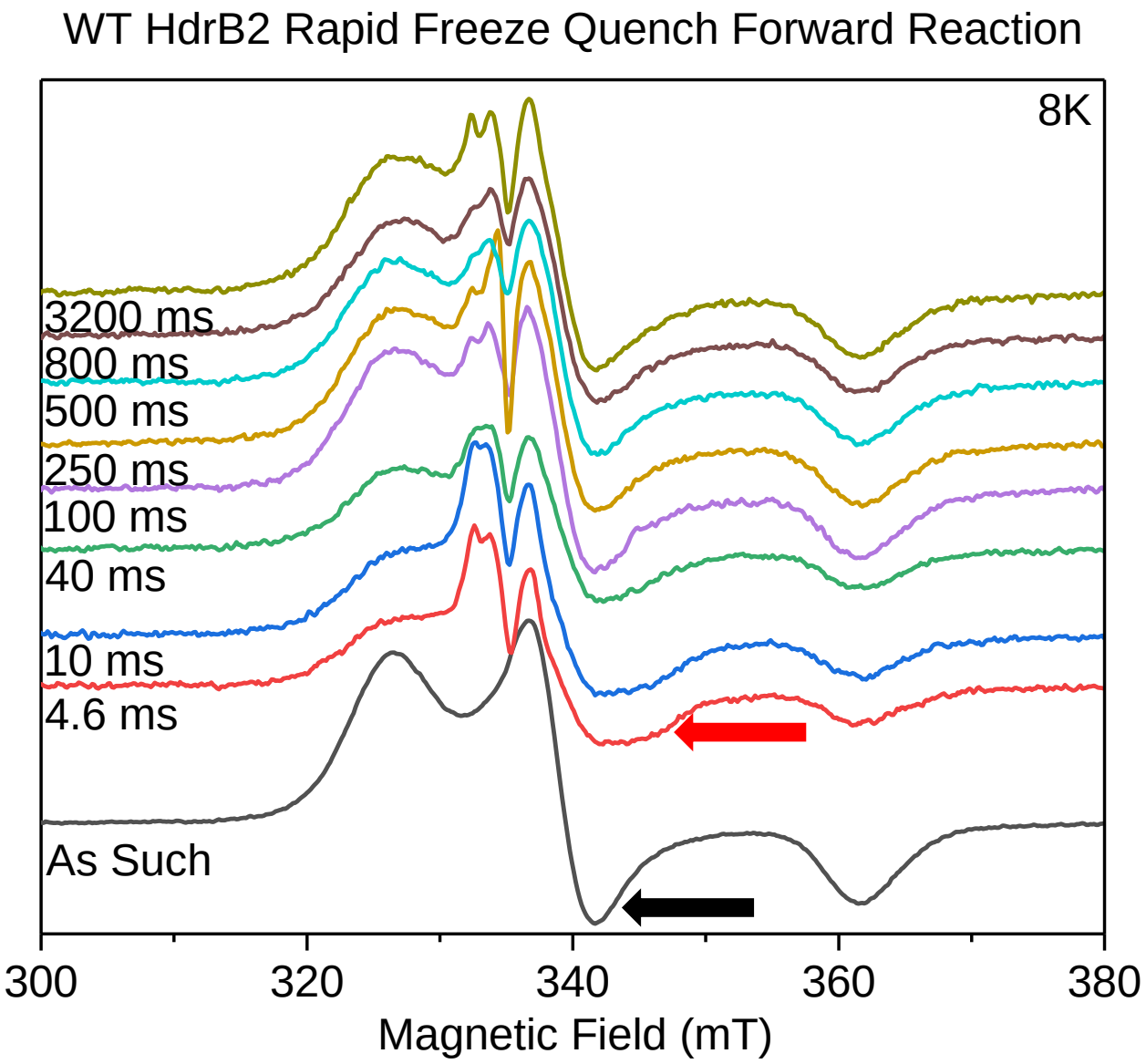

Figure 3.18: Overlay of selected EPR spectra from the rapid freeze quench experiments performed on WT HdrB2 for the forward reaction. The black arrow points to the area where the peak appeared sharp initially. Once the reaction incubates at 4.6 ms, the peak pointed by the red arrow shows some slight broadening. After 10 ms, the peak sharpens again.

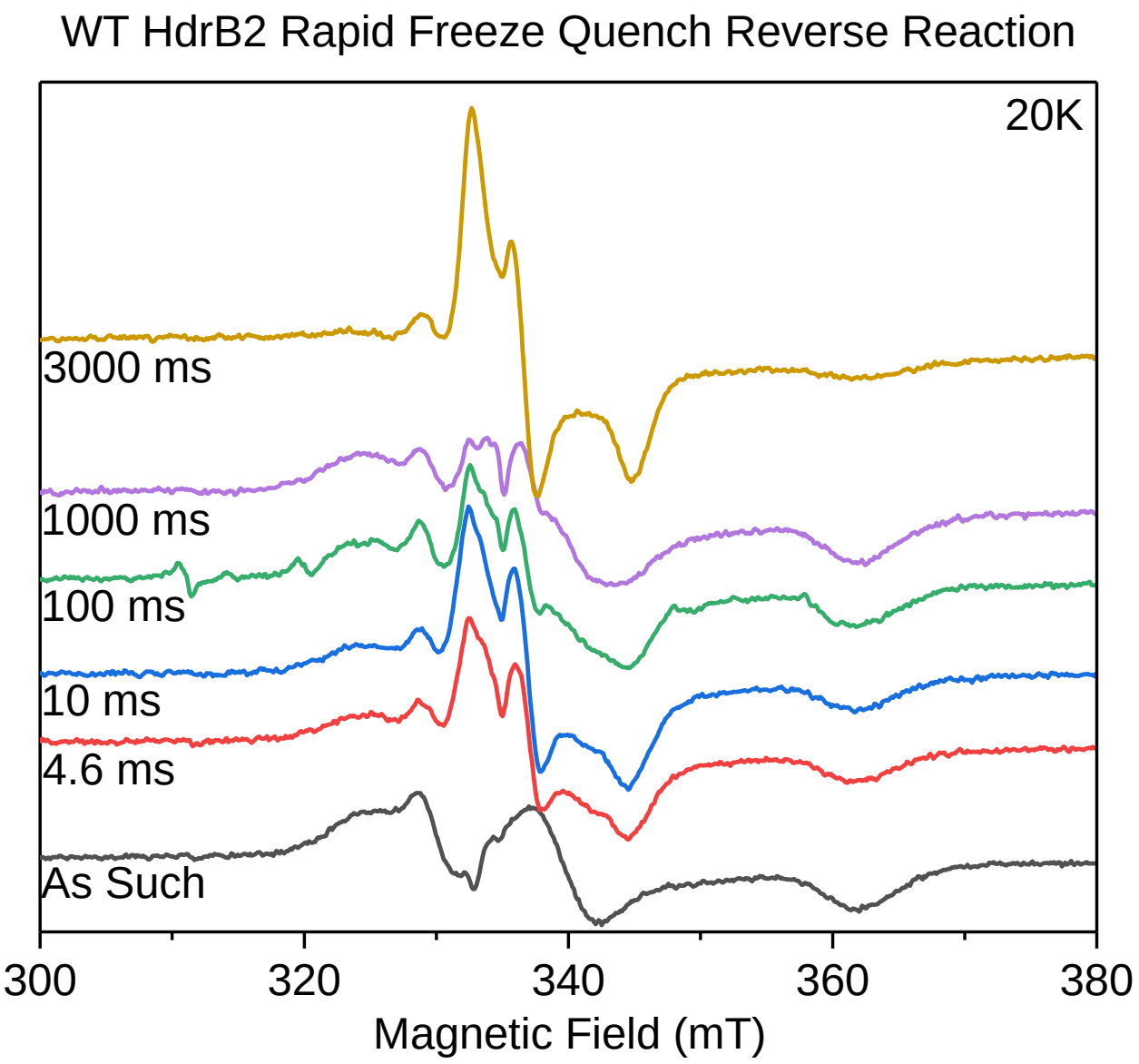

Figure 3.19: Overlay of selected EPR spectra from the rapid freeze quench experiments performed on WT HdrB2 for the reverse reaction. The more reduced cluster signal appears initially during the 'As Such' sample and then the more oxidized cluster signal immediately appears at 4.6 ms. With the later times, the more oxidized cluster signal appears to change back to the more reduced cluster signal.

3.3.1.2 *HdrB2 Variant Results*

3.3.1.2.1 C42S-C43S Results

This variant was created and purified by the Ferry group. They found that this variant had no activity even after reconstitution. The only difference between Ser and Cys is one has an -OH group and the other has a -SH group, that would change the electronegativity which could change the coordination with the iron. A redox titration was performed with the variant to see what EPR signals would appear. Due to time constraints a single titration was performed.

3.3.1.2.1.1 EPR monitored-redox titrations

In **Figure 3.20**, the spectra obtained during the redox titrations are shown. It was determined the more reduced signal was a [2Fe-2S] cluster due to its rhombic shape and optimal temperature which is discussed in the next section. The [2Fe-2S] cluster appears far more abundant than the $[4Fe\text{-}4S]^{3+}$-ligand species appears, this may explain the lack of activity.

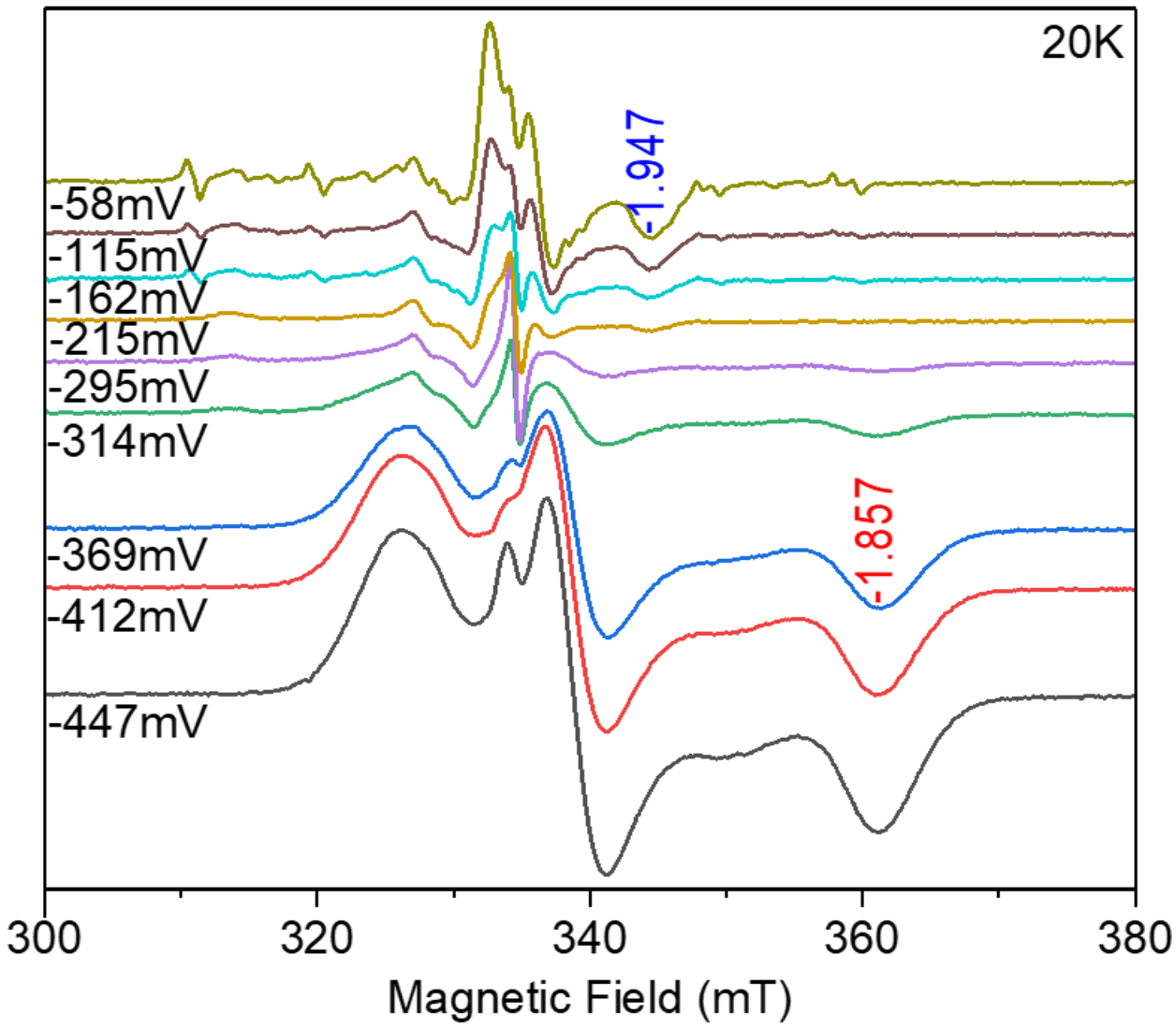

Figure 3.20: Selected EPR spectra overlay of the redox titration of variant HdrB2 C42S-C43S measured at 20K.

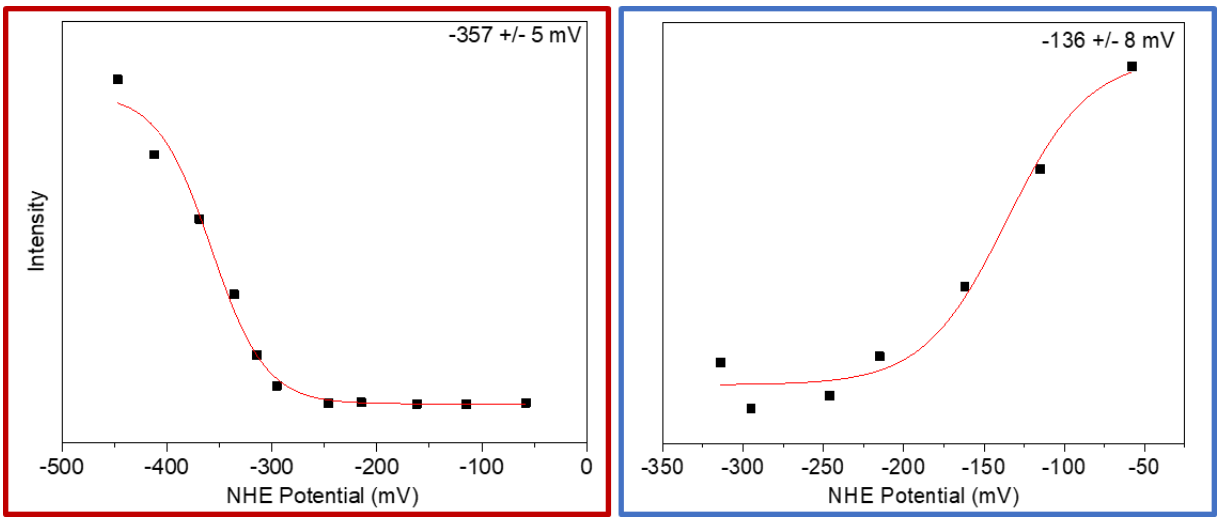

Figure 3.21: The Nernst curves are for the redox titrations performed on HdrB2 C42S-C43S. The colored outline coordinates with the colored ovals in **Figure 3.20**. It is interesting to note the midpoint potentials were similar to those of the WT HdrB2.

3.3.1.2.1.2 Temperature Studies

Temperature studies for the samples with E_m=-456 mV were performed to determine if the lack of activity may be due to the type of iron-sulfur clusters formed as a result of the mutagenesis **Figures 3.22**. Initial analysis revealed the presence of both the 2Fe signal and the 4Fe signal. The cluster did not appear damaged since the signals resembled the same signals found in HdrB2. **Figure 3.22** gives an overview of selected EPR signals of the temperature studies performed on HdrB2 C42S-C43S at -456 mV with the temperature curve in the top right corner.

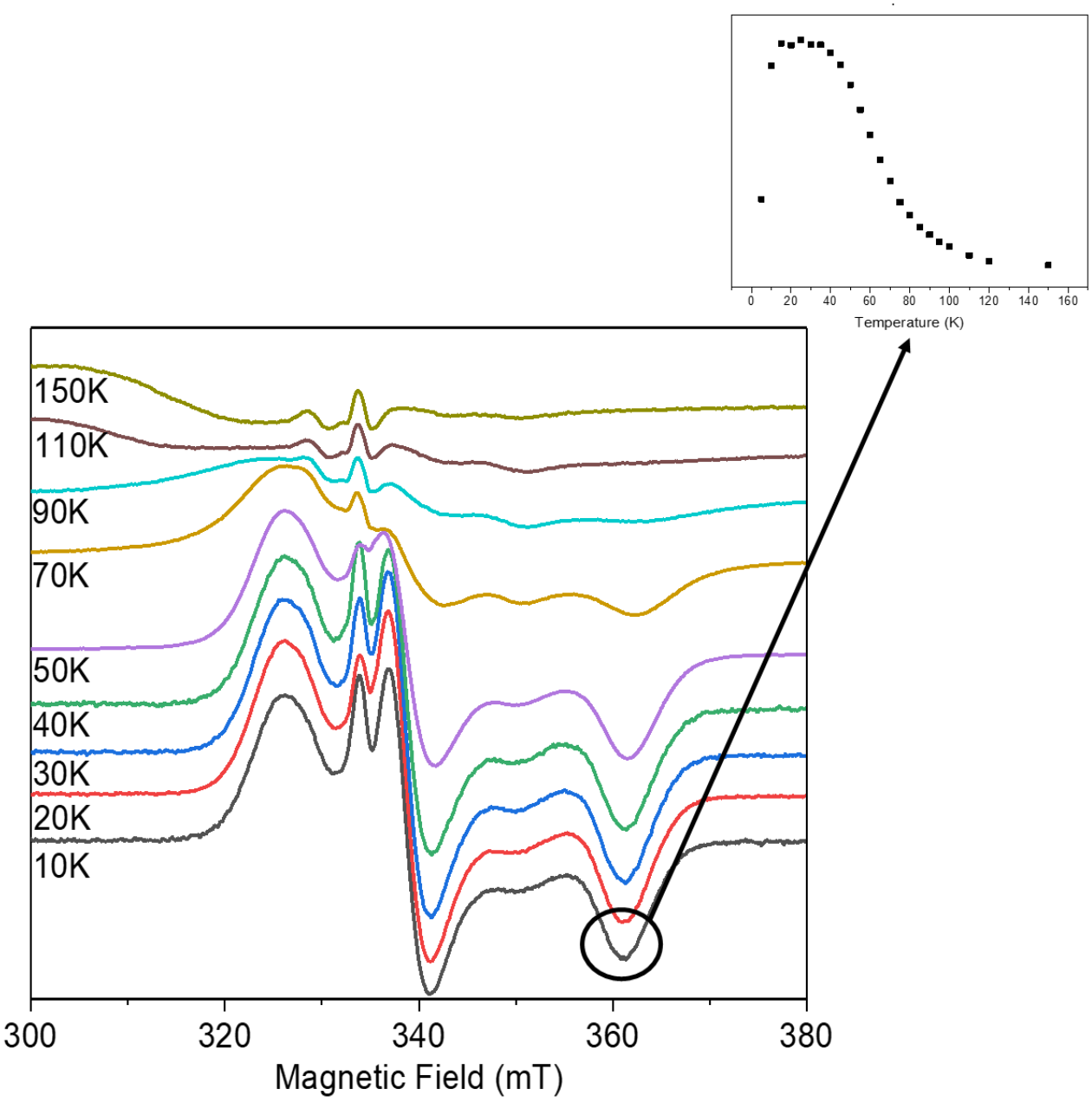

Figure 3.22: Selected EPR signals of the temperature studies for the more reduced cluster signal in the variant HdrB2 C42S-C43S. The type right corner represents the temperature curve for the peak within the black oval. The curve was graphed by plotting the peak intensity vs. the temperature increase.

3.3.1.2.2 C194S-C195S Results

After 10 minutes of incubating with CoM and CoB, the activity of this variant was determined to be 428 nmol*(min*mg of protein)$^{-1}$. Why this protein required an additional 10 minutes to react is not clear.

3.3.1.2.2.1 EPR monitored-redox titrations

Figure 3.23 represents an overview of selected EPR signals during the redox studies of HdrB2 C194S-C195S. The most interesting aspect of this result was the [2Fe-2S] cluster signal was hardly present as seen in the WT and variant HdrB2 C42S-C43S redox studies. Because the more oxidized cluster signal was the predominate EPR signal, we concluded this signal was the non-cuboidal [4Fe-4S] cluster. The midpoint potential determined for this signal (-217 +/- 5 mV) was slightly different from the WT HdrB2. The absence of the [2Fe-2S] cluster may have influenced the non-cuboidal cluster.

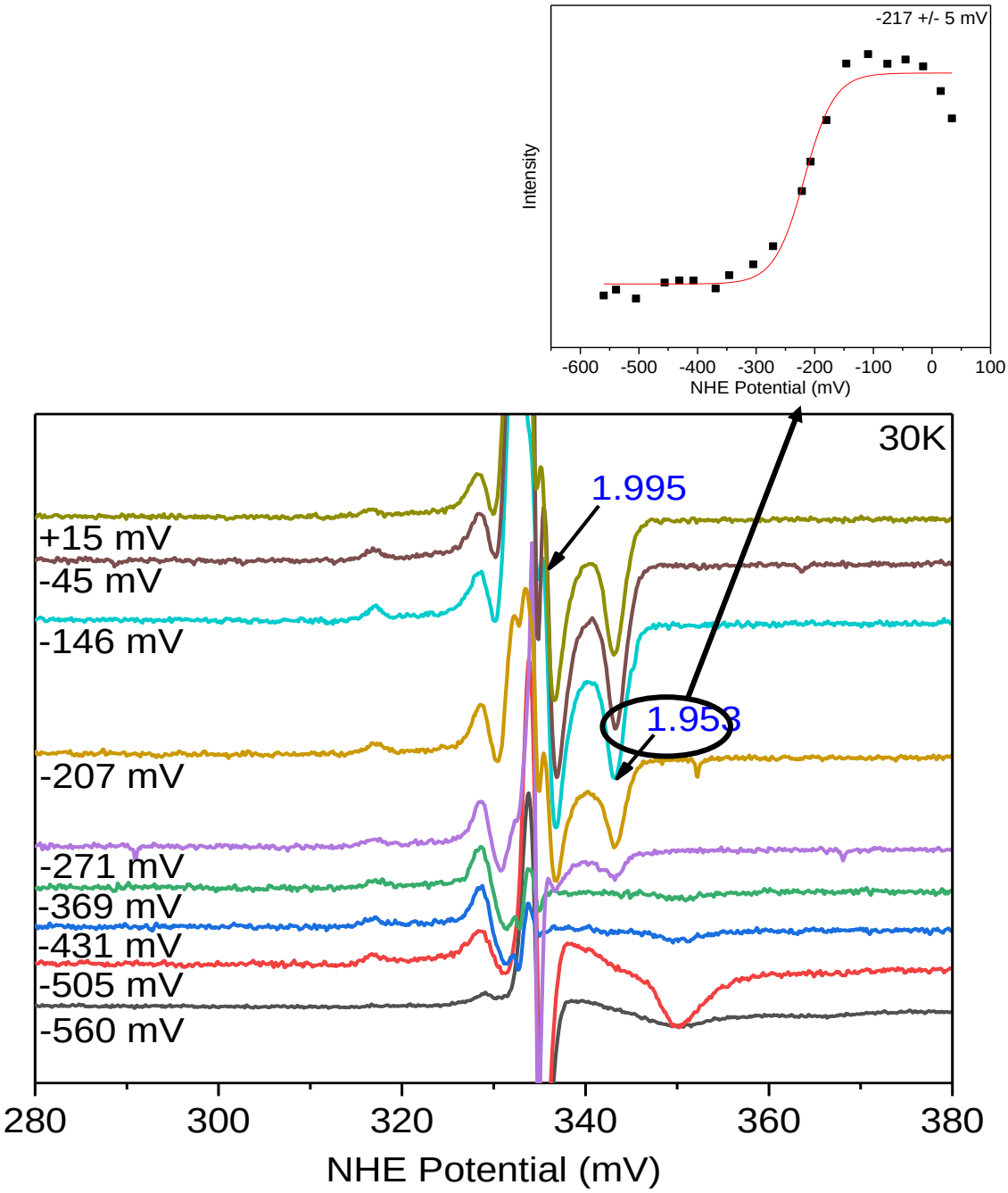

Figure 3.23: Selected EPR spectra of the redox titration performed on the variant HdrB2 C194S-C195S. The Nernst curve was only graphed for the g-Value 1.953 since there was hardly any signal for the g-Value 1.856. The Nernst curve can be found in the top right corner along with the midpoint potential.

3.3.1.2.2.2 Temperature Studies

Figure 3.24-3.25 shows the temperature study of the variant at the more reduced and oxidized potential. The optimal temperature was 20-30 K so the redox studies were measured at 30 K. With the more reduced sample, as the temperature increased, a new signal began to appear slightly noted at g-value 1.933. We believe this could be the substrate bound iron-sulfur cluster.

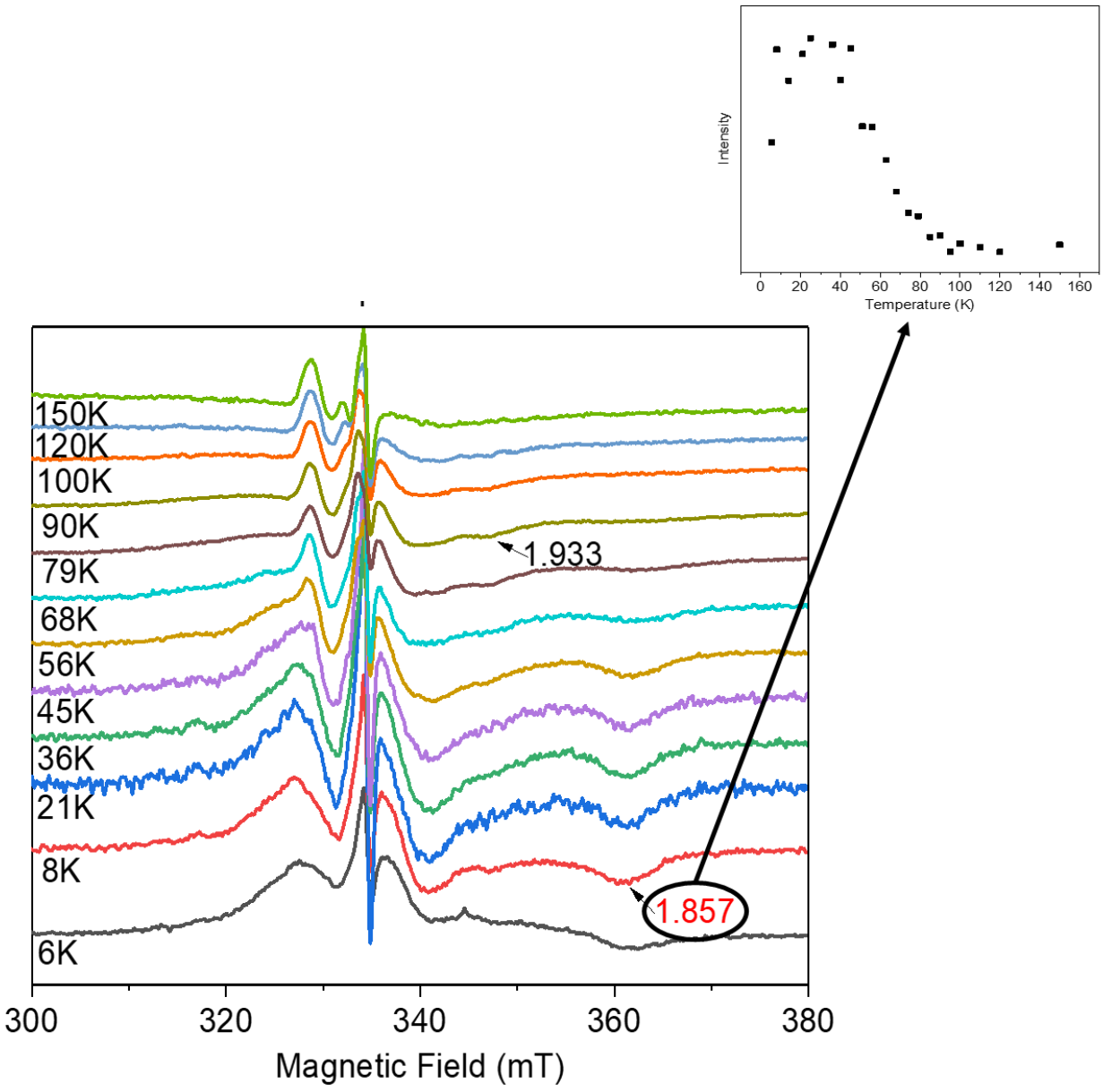

Figure 3.24: Selected EPR spectra overlay of the temperature studies for variant HdrB2 C194S-C195S measured at -456 mV (NHE values). The temperature curve is shown in the top right corner for g-Value 1.857.

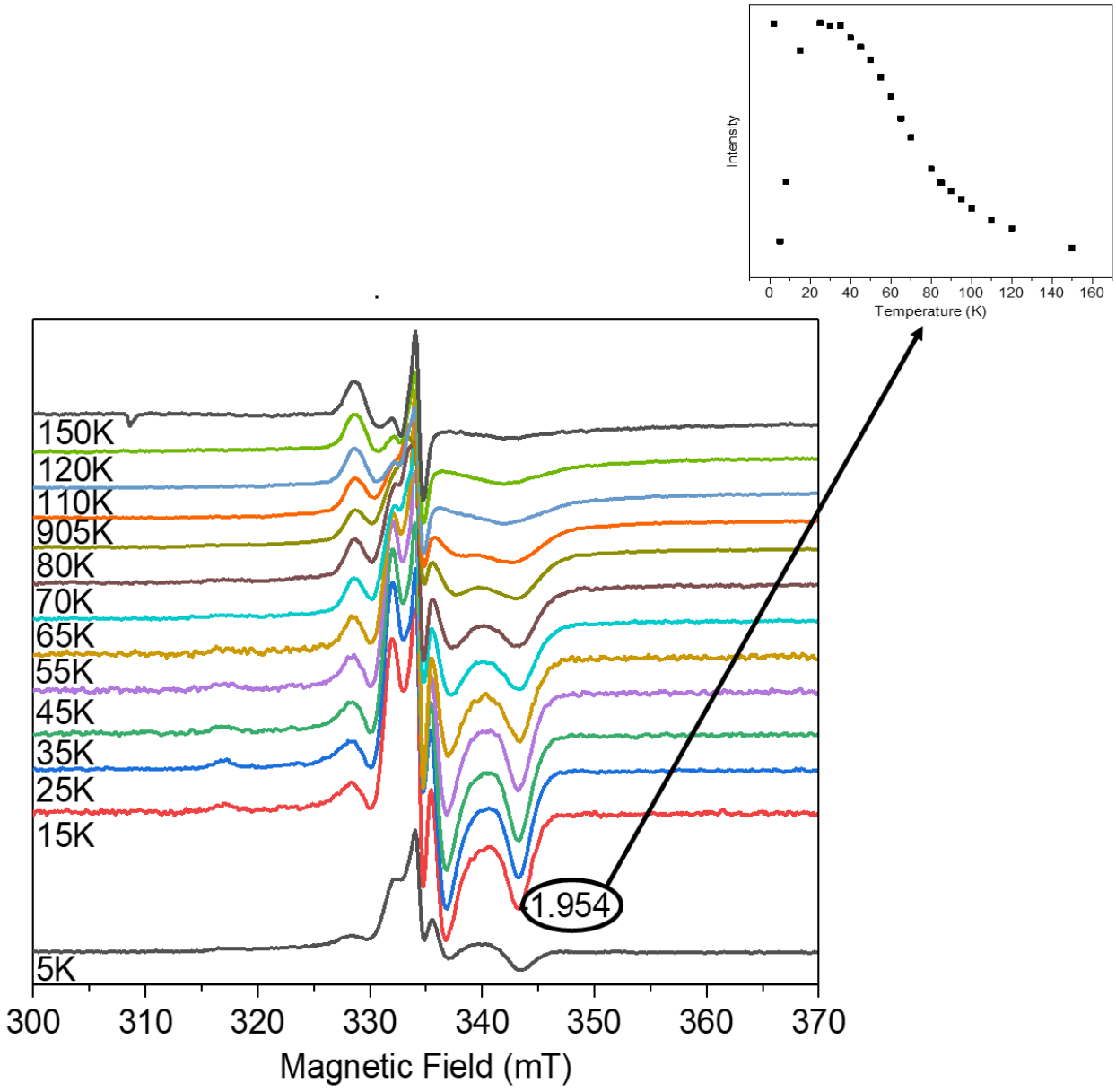

Figure 3.25: Selected EPR spectra of the temperature studies for the more oxidized sample of variant HdrB2 C194S-C195S measured at -76 mV. The temperature curve is shown in the top right corner for the g-Value 1.954.

3.3.2 HdrBC Results

Please refer to **Figure 3.13** and **Table 3.1** for the purification, iron content, and specific activity results. This assay was also performed in the reverse direction and, therefore, the forward and reverse reaction for the rapid freeze quench experiment was performed on this protein. The goal to studying this co-expressed enzyme was to see how the iron-sulfur clusters in HdrC2 could influence the binding of the iron-sulfur clusters in HdrB2. Ferry's group attempted to clone and express HdrC2 by itself, but the protein was never stable. When HdrB2C2 was co-expressed, the protein was stable.

3.3.1.2 *EPR monitored-redox titration*

Initially, the signals at 8K were assigned to the $[4Fe\text{-}4S]^{+}$ in HdrC (**Figure 3.26**). However, when temperature studies were performed (results shown in next section), we discovered this signal was similar to the reduced sample of the HdrB2 protein which had an optimal temperature of 20 K. Measuring the redox study samples showed the same signal as the [4Fe-4S] cluster with CoM bound (**Figure 3.26-3.27**) and a possible artefact signal between g-value 2.134 and 2.051. There was a signal that appeared to be similar to a HiPIP [4Fe-4S] cluster. The difference, though, is the temperature and g-values are lower than a typical HiPIP [4Fe-4S] cluster and it never appeared during the Mvh:Hdr studies. Since a similar signal is also detected in the HdrB2 sample (**Figure 3.14**), we proposed that it is an artifact due to improper cluster insertion. It could even be due to the presence of a cuboidal cluster. No experiments were done to see if this artefact could be removed so we made note of this signal for future experiments. The midpoint potentials were calculated using the Nernst curve equation which indicated the potential of the more reduced cluster (2Fe cluster) was -353 +/- 4 mV while the more oxidized cluster (4Fe cluster) was -98 +/- 13 mV.

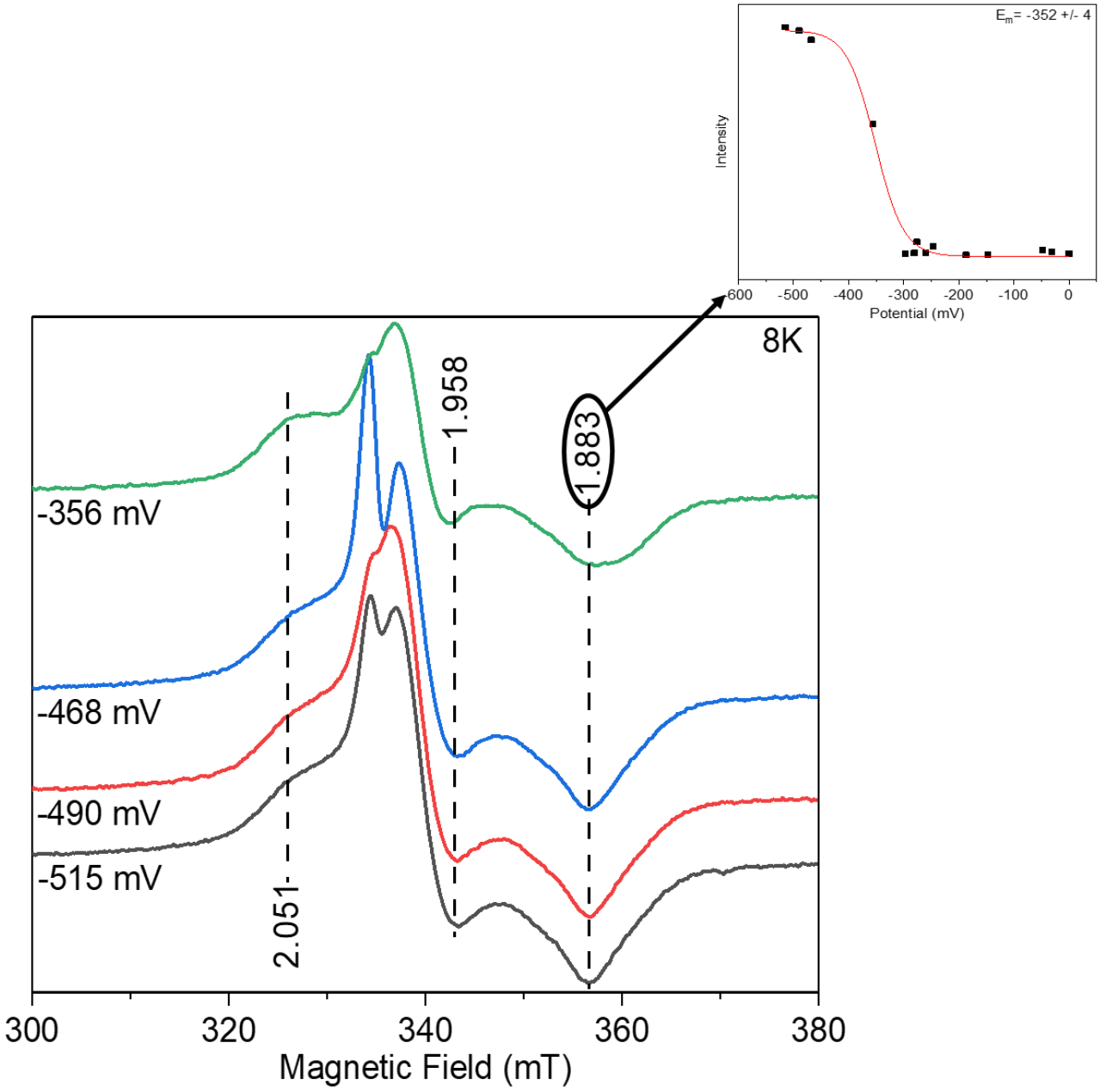

Figure 3.26: Selected EPR spectra overlay from the redox studies of HdrB2C2 at 8 K. The top, right corner shows the Nernst curve created from g-Value 1.883. Any signal higher than -353 mV contained only a radical signal which is why the overlay contained so few signals.

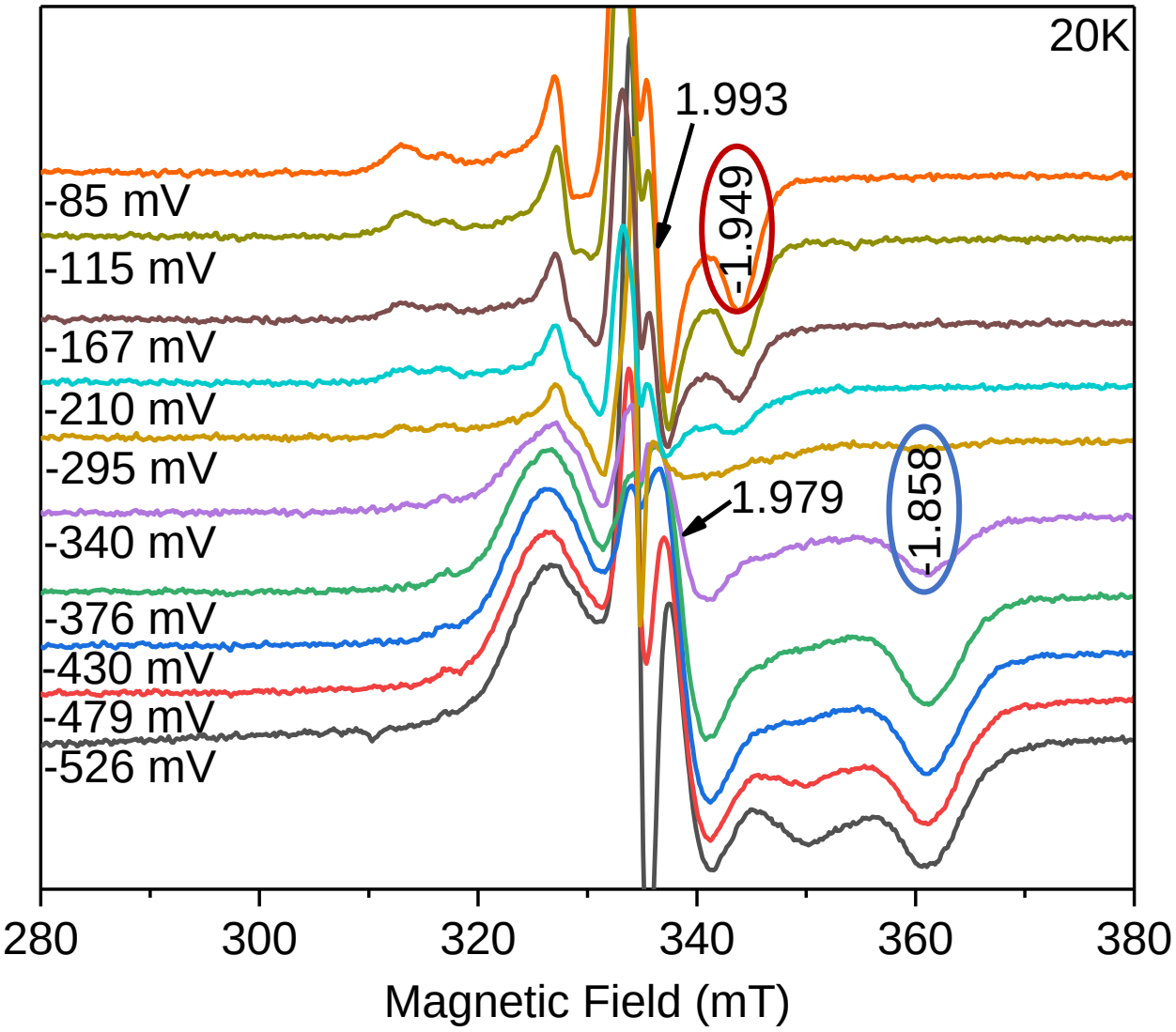

Figure 3.27: Selected EPR spectra overlay from the redox studies of HdrB2C2 at 20 K.

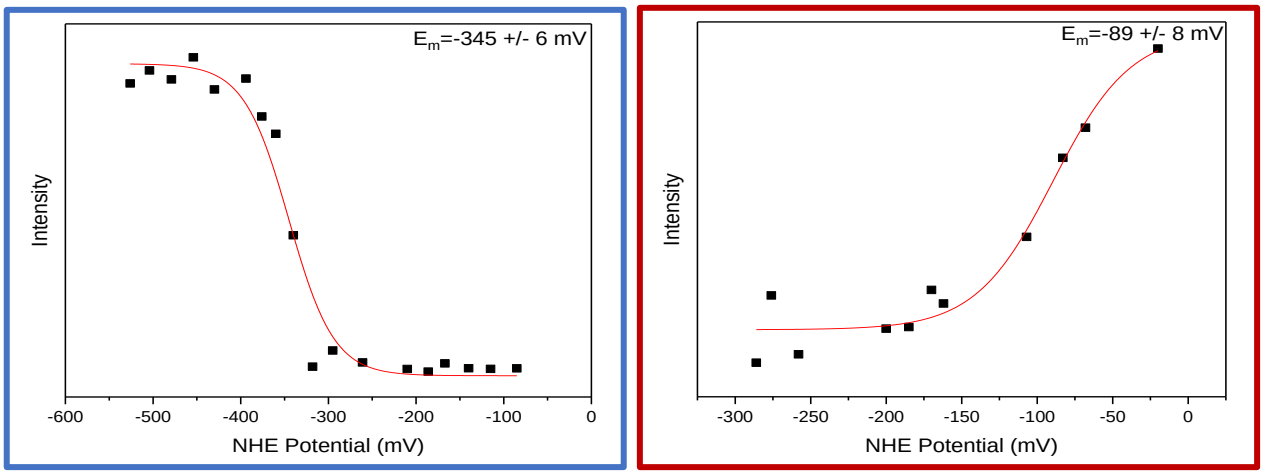

Figure 3.28: The Nernst curves created from the redox titrations of HdrB2C2. The midpoint potentials are shown in the top right corners along with the standard error.

3.3.2.1 *Temperature Studies*

These studies revealed the optimal temperature for HdrBC samples were ~20-25K (**Figure 3.29-3.30**) for both the [2Fe-2S] cluster and the substrate bound iron-sulfur cluster. We do not know why the [4Fe-4S] clusters in HdrC did not appear but this, again, may be due to these enzymes needing an iron-sulfur cluster binding enzyme to help express these clusters properly in these enzymes. This information was beneficial for us to know for the freeze quench experiments which are discussed in the next section.

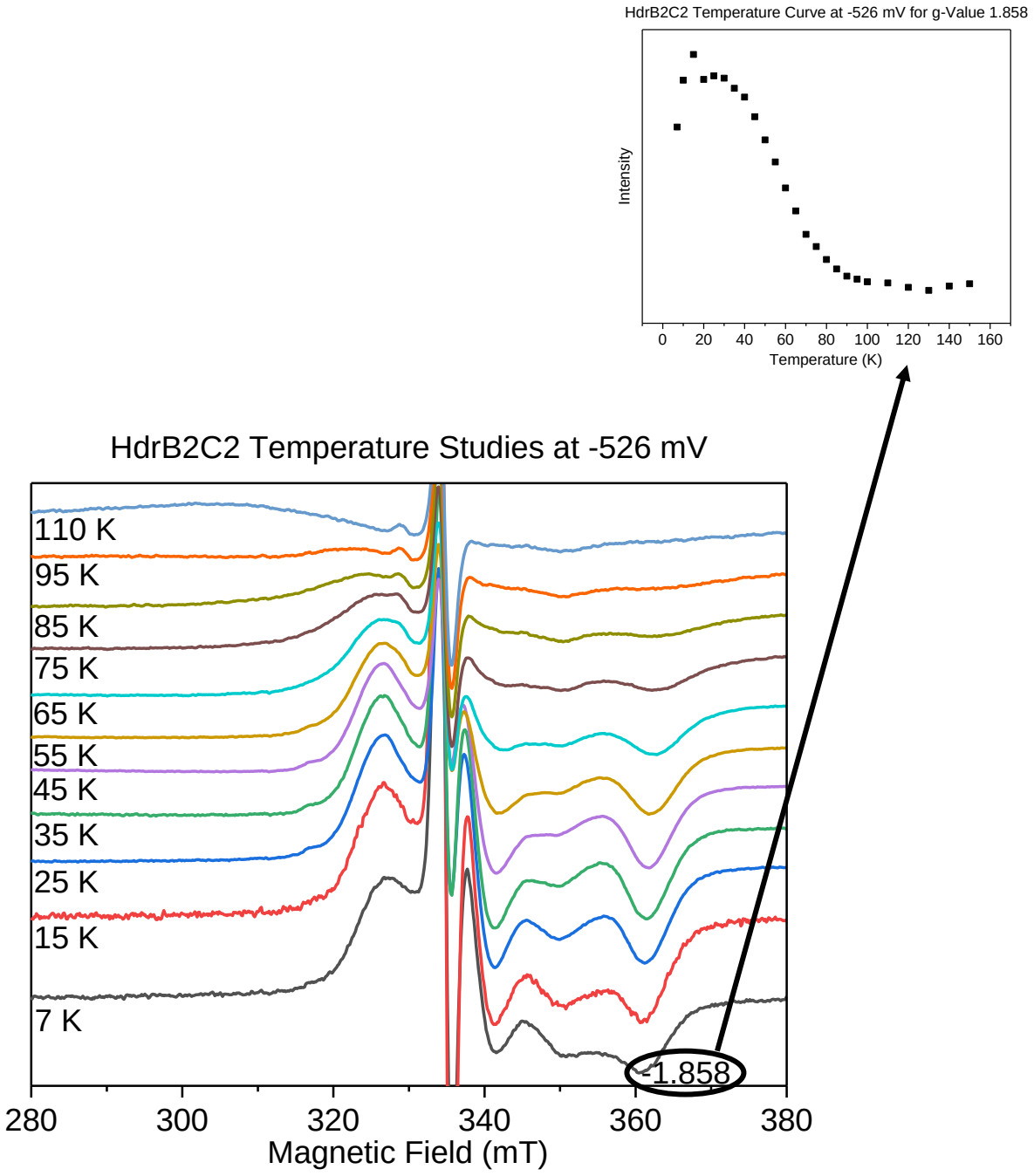

Figure 3.29: Selected EPR spectra overlay of temperature studies performed on HdrBC at -526 mV (NHE potential). Curie plot of the temperature studies for HdrBC. Curve was created based on the intensities of the signal at g-value 2.149.

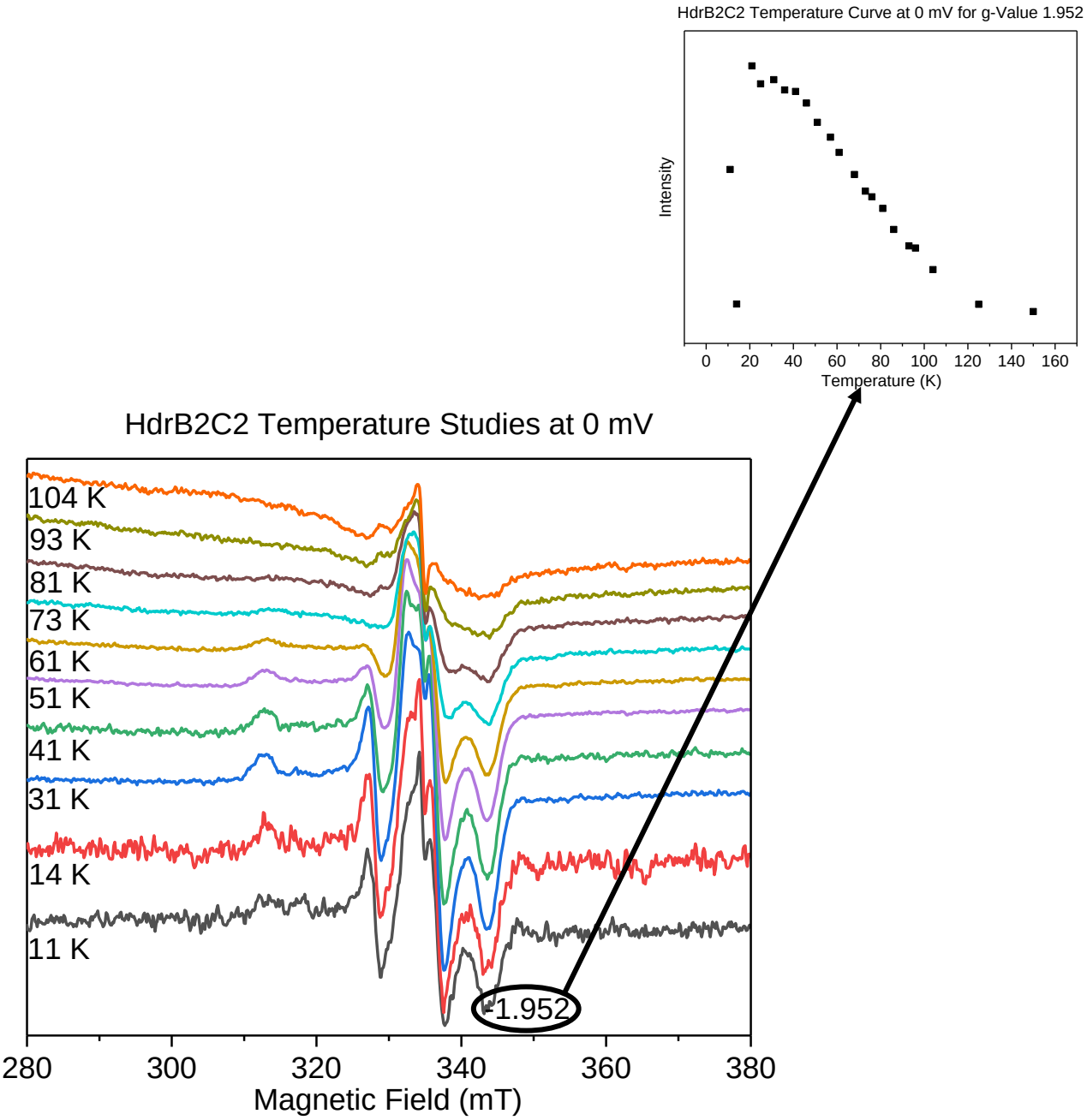

Figure 3.30: Selected EPR spectra of temperature studies for HdrB2C2 at 0 mV. Temperature curve for g-Value 1.952 can be see in the top right corner. According to these results, this signal is measured optimally at 20 K as well.

5.3.2.2 *EPR monitored-rapid freeze quench*

The forward and reverse reaction for rapid freeze quench was performed on HdrB2C2. The forward reaction (**Figure 3.31**) was analyzed at 8 K because this was done before the temperature studies had been done. The broad signals made it too difficult to see any changes as the reaction progressed. As for the reverse reaction (**Figure 3.32**), signals were very noisy since the sample was (and stayed) oxidized. One can see the substrate bound iron-sulfur cluster signal appear and disappear. To confirm these observations and decrease the noise, this experiment needs to be repeated with concentrated protein.

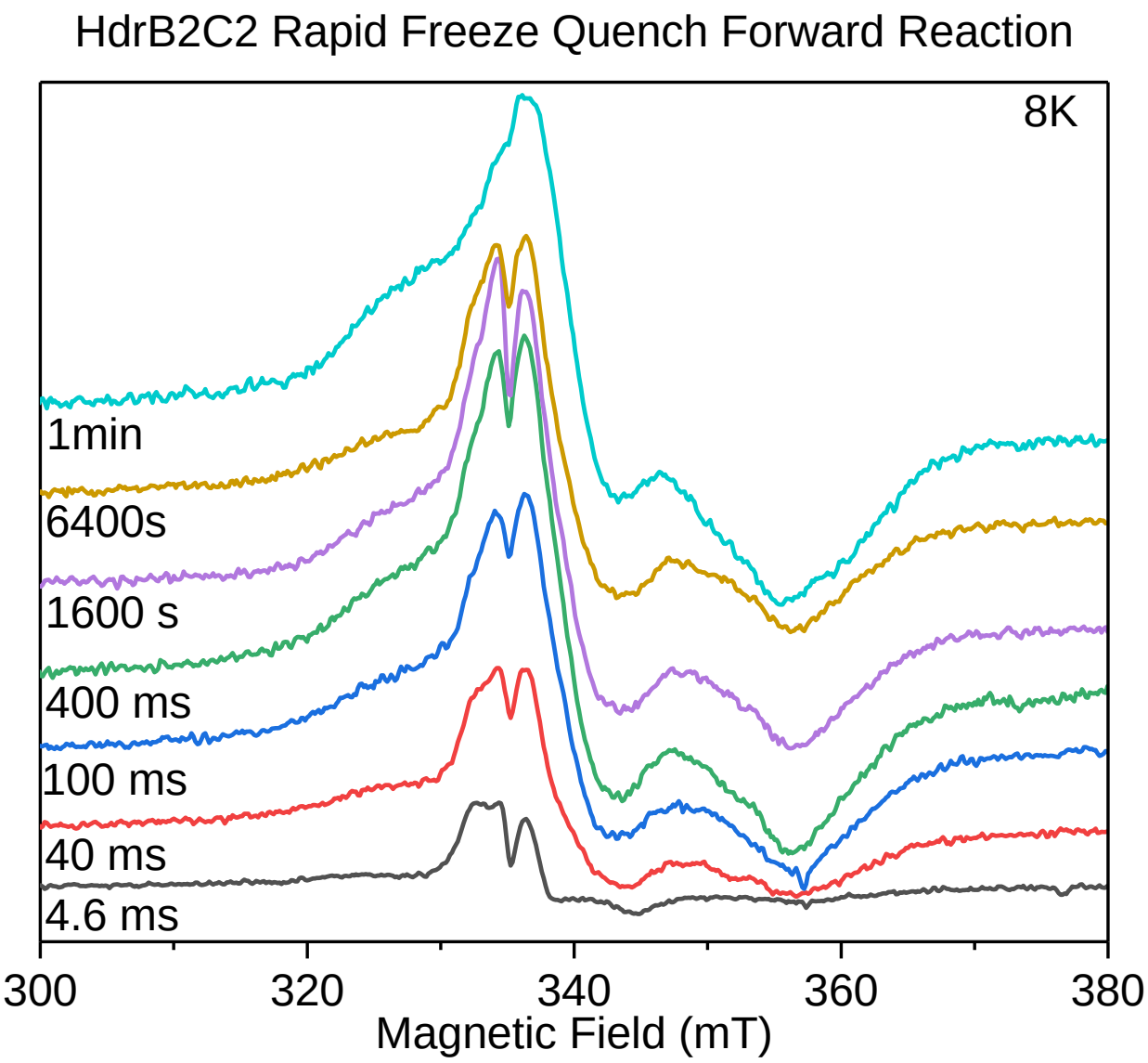

Figure 3.31: Selected EPR spectra overlay of the rapid freeze quench experiment performed on HdrB2C2 for the forward reaction

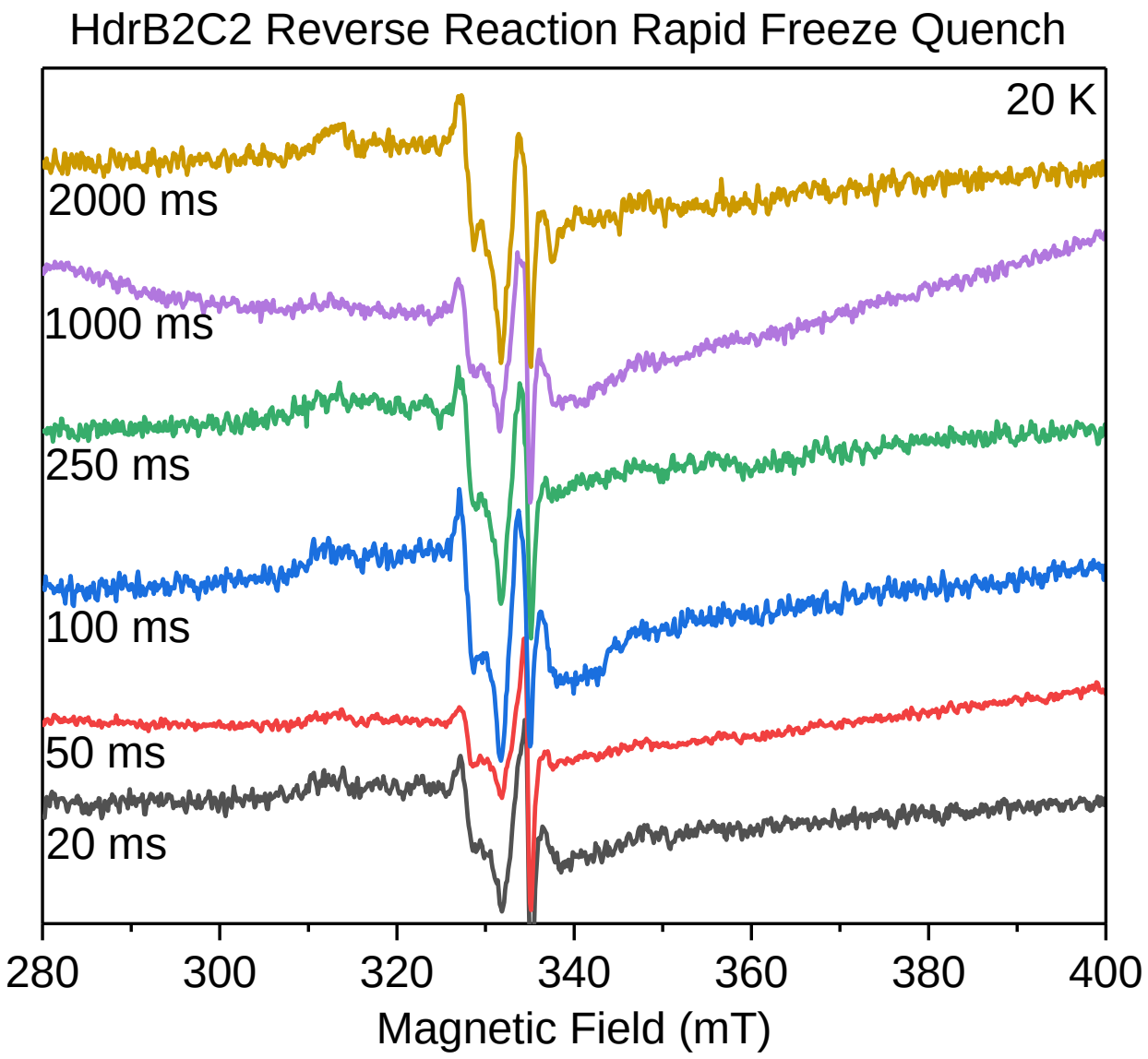

Figure 3.32: Selected EPR spectra of the rapid freeze quench performed on HdrB2C2 for the reverse reaction. The sample is not reduced and, therefore, the signal is weak.

3.4 Conclusion

Since the discovery of the noncuboidal clusters in the active site of HdrB, determining their role during the HDS reduction became a huge priority for researchers. The original hypothesis suggested the CCG domains contained one cuboidal [4Fe-4S] cluster site and one Zn element site

and, therefore, the mechanism for the reduction of CoM-S-S-CoB was based on one cluster. We performed EPR monitored- redox and kinetic studies to further analyze the unique characteristics of these clusters and determine role each cluster plays in HDS reduction. In addition, two different variants were studied to determine which EPR signal correlated to which cluster.

The redox studies for the WT HdrB2 revealed two different signals with midpoint potentials of -354 +/- 7 mV and -173 +/- 10 mV. Based on these potentials and the temperature studies, we determined the more negative midpoint potential was a [2Fe-2S] cluster while the more positive midpoint potential was the noncuboidal cluster. We were not able to determine any characteristics with the binding of HDS from the rapid freeze quench experiments. The broadened signals during the forward reaction prevented us to see the progression as HDS was being reduced and there were some inconsistencies during the reverse reaction due to the tube packing.

The variant C42S-C43S contained no activity even though both the 2Fe and 4Fe EPR signals were present. The lack of activity was potentially due to the 2Fe cluster being more abundant than the 4Fe cluster. A 2Fe cluster will change the potential of the environment and prevent the reduction of the substrate. The variant C194S-C195S was active and contained only traces of the [2Fe-2S] cluster EPR signal and a strong $[4Fe\text{-}4S]^{3+}$-ligand signal. The non-cuboidal cluster is sufficient for activity.

Mössbauer experiments will need to be performed to confirm our theories and to see if the substrate bound iron-sulfur cluster is a [4Fe-4S] cluster or not. This could change the proposed mechanism for CoM-S-S-CoB reduction. In addition to this experiment, cloning HdrB from *M. acetivorans* into *M. maripaludis* would help in expressing the iron-sulfur clusters properly. Our theory is these methanogens contain a unique iron-sulfur cluster binding protein that helps express

the iron-sulfur clusters properly. Using *E. coli* as a host eliminates those important proteins and there results in a [2Fe-2S] cluster instead of a [4Fe-4S] cluster.

3.5 Future Studies

3.5.1 VhcD/HdrA

Initially, Selam Ghebreamlak purified HdrA from *M. marburgensis* into *E. coli* and 45 *M. maripaludis* was the best solution to obtain pure protein. However, the amount of protein obtained was very low. The flavin and several Fe-S clusters were not present which rendered the protein useless. However, Ghebreamlak purified the protein without FAD present in the buffers. Incorporating FAD in the buffers during protein purification allows for the protein to bind the molecule tightly. This procedure should be explored since HdrA was obtained in a pure form while VhcD/HdrA could not be obtained in a pure form. If the protein is still missing some iron-sulfur clusters, then the co-expression of VhcD/HdrA will be examined once again to ascertain if VhcD keeps some of the iron-sulfur clusters in HdrA bound. The purification methods will have to be changed in order to obtain pure protein. Once a pure protein is apprehended and contains the correct number of iron-sulfur clusters and flavin, redox studies can be done to further determine the g-values and redox potentials involved in the flavin-based electron bifurcation.

3.5.2 HdrB2 and HdrB2C2

Lastly, the Ferry group is currently working on performing a Mössbauer analysis on HdrB to confirm the type of clusters present in the enzyme. Once confirmed, we can proceed on with our next idea which is cloning HdrB2 and HdrB2C from *M. acetivorans* into *M. maripaludis*. We suggest there are unique genes that aid HdrB2 into expressing its iron-sulfur clusters. We are actively working on this process with the help of Dr. Barny Whitman at University of Georgia who has cloned Mcr and other related enzymes from *M. maripaludis* and *M. okinawensis* into *M.*

maripaludis. From there, we would repeat the redox and kinetic studies to see how the EPR signals vary compared to the original results.

Appendix for Chapter 2

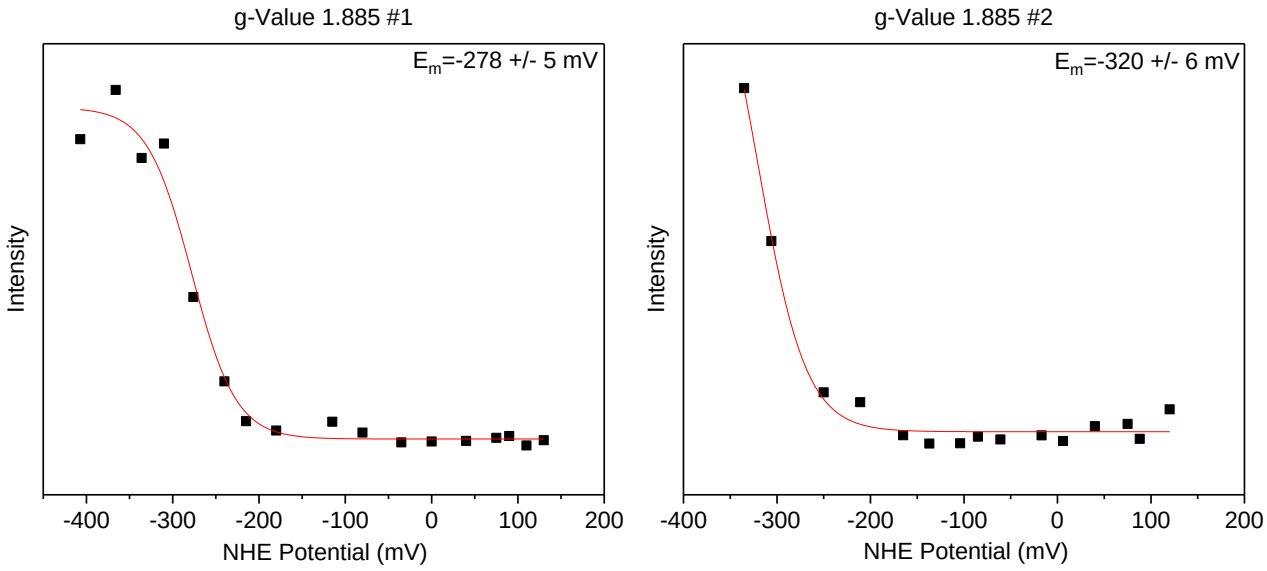

Figure A2.1: Nernst curve for g-value 1.885 from first and second redox titration. This g-value can be found at 8 K.

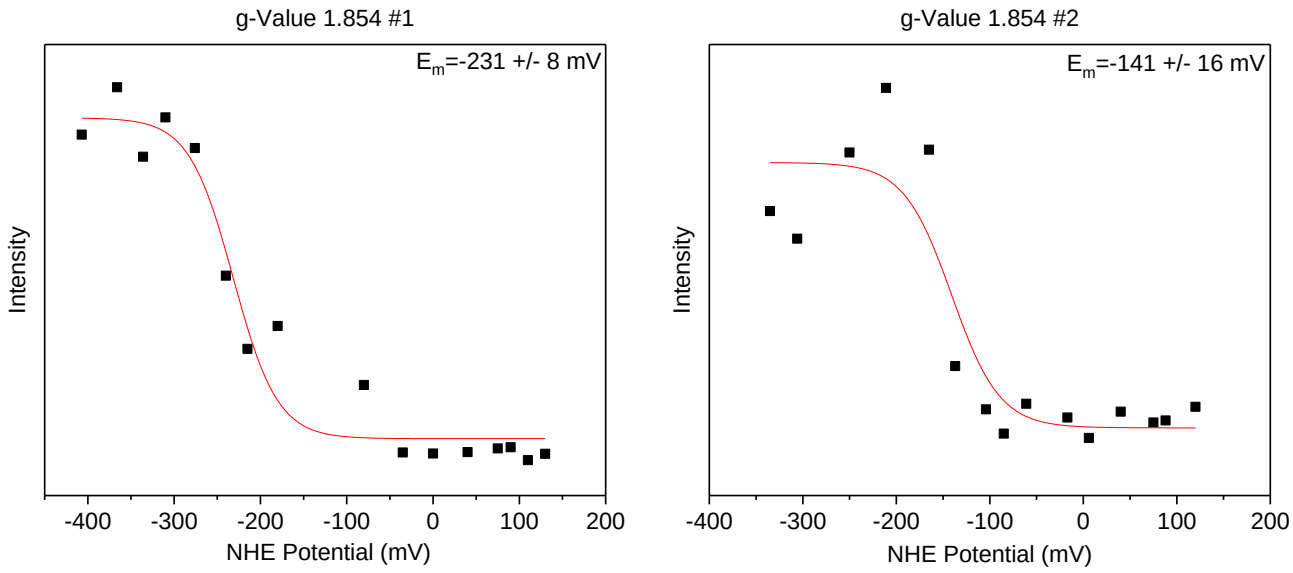

Figure A2.2: Nernst curve for g-value 1.85 from first and second redox titration. This g-value can be found at 8 K.

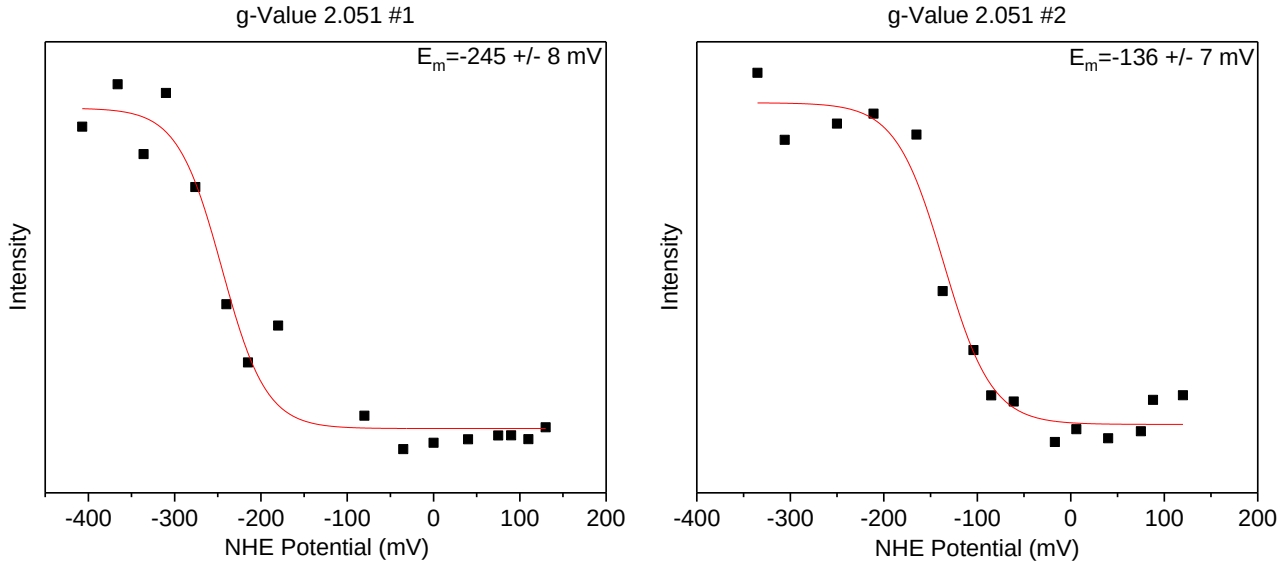

Figure A2.3: Nernst curve for g-value 2.051 from first and second redox titration. This g-value can be found at 8 K.

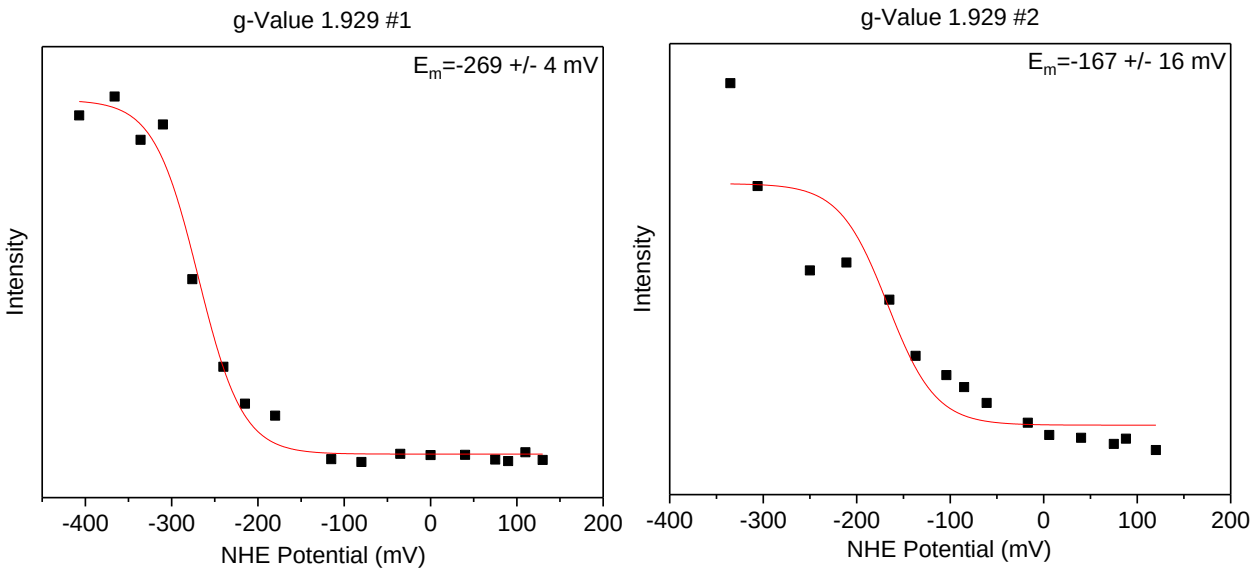

Figure A2.4: Nernst curve for g-value 1.929 from first and second redox titration. This g-value can be found at 8 K.

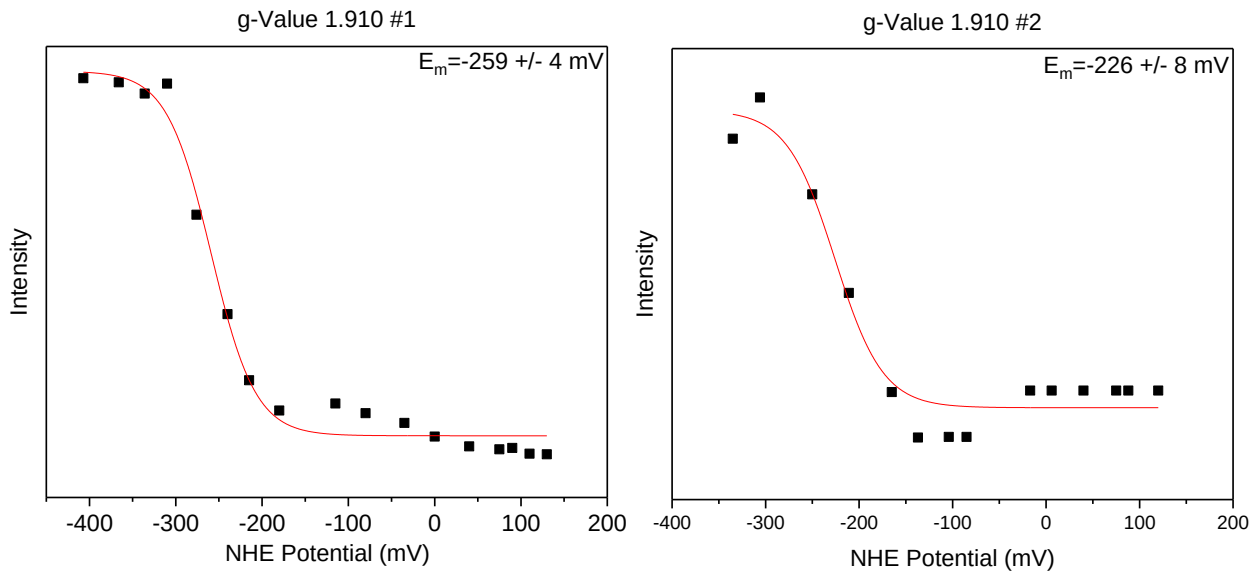

Figure A2.5: Nernst curve for g-value 1.910 from first redox titration. This g-value can be found at 70 K.

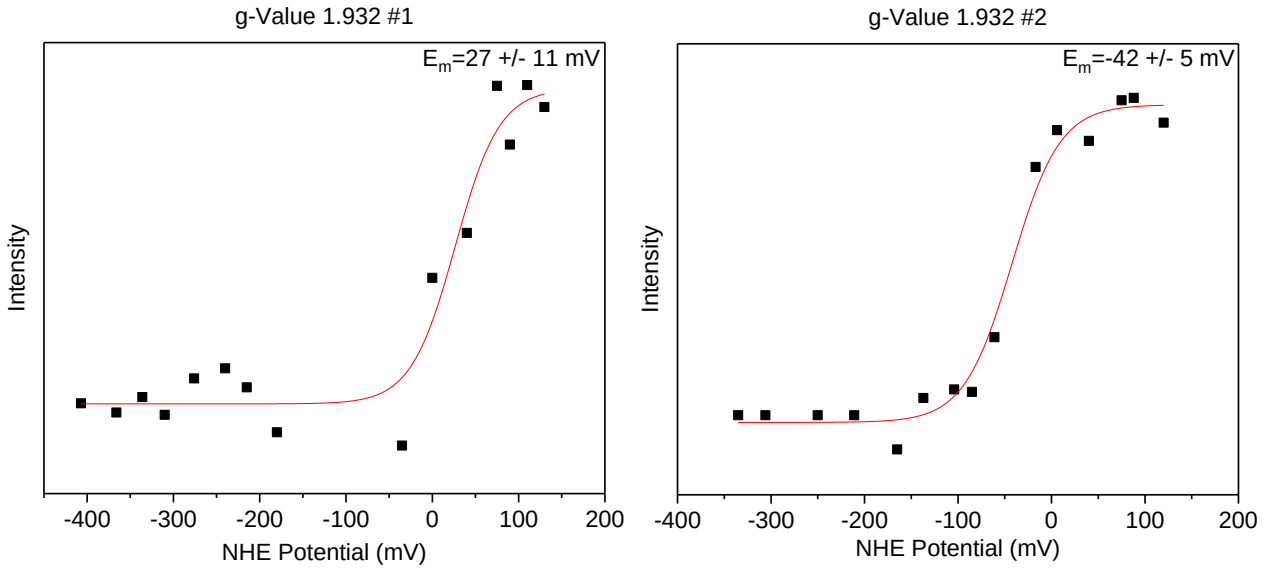

Figure A2.6: Nernst curve for g-value 1.932 from first and second redox titration. This g-value can be found at 70 K.

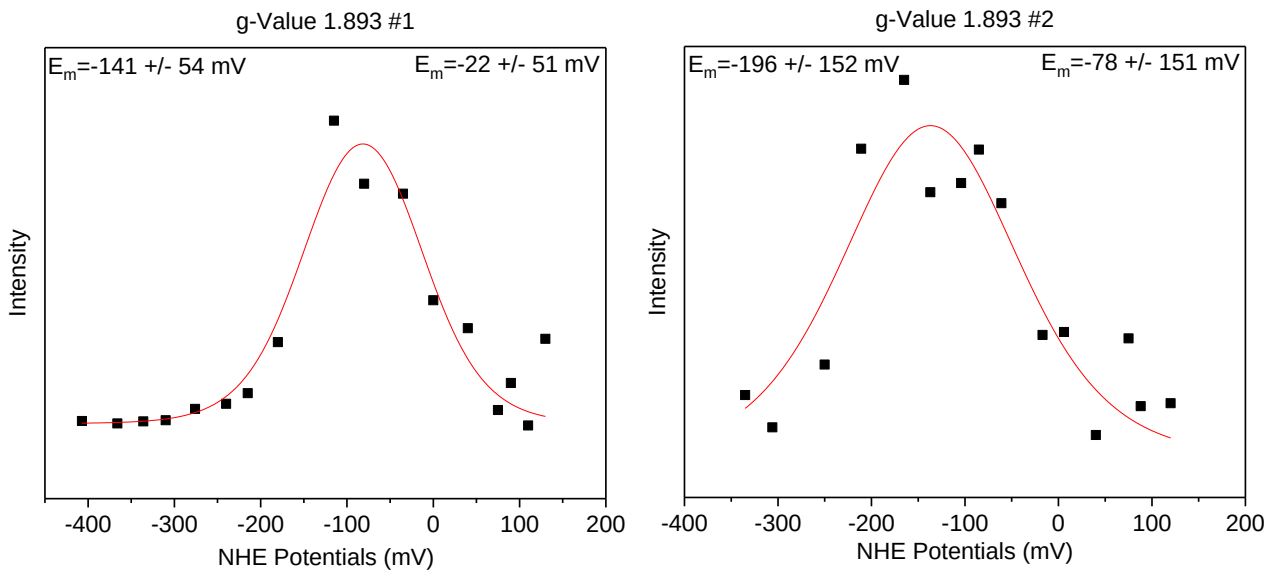

Figure A2.7: Nernst curve for g-value 1.893 from first and second redox titration. This g-value can be found at 70 K.

Appendix for Chapter 3

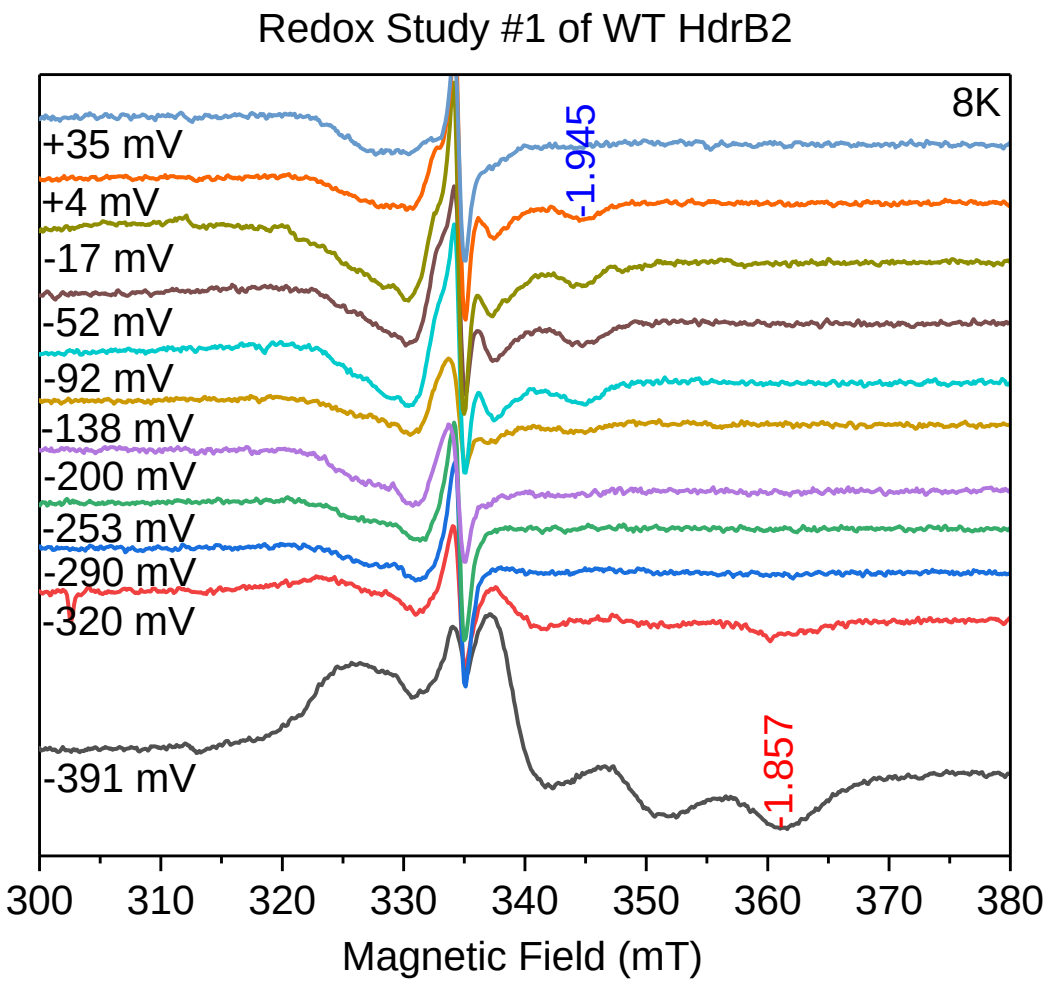

Figure A3.1: Selected EPR spectra overlay of the first redox titration performed on WT HdrB2.

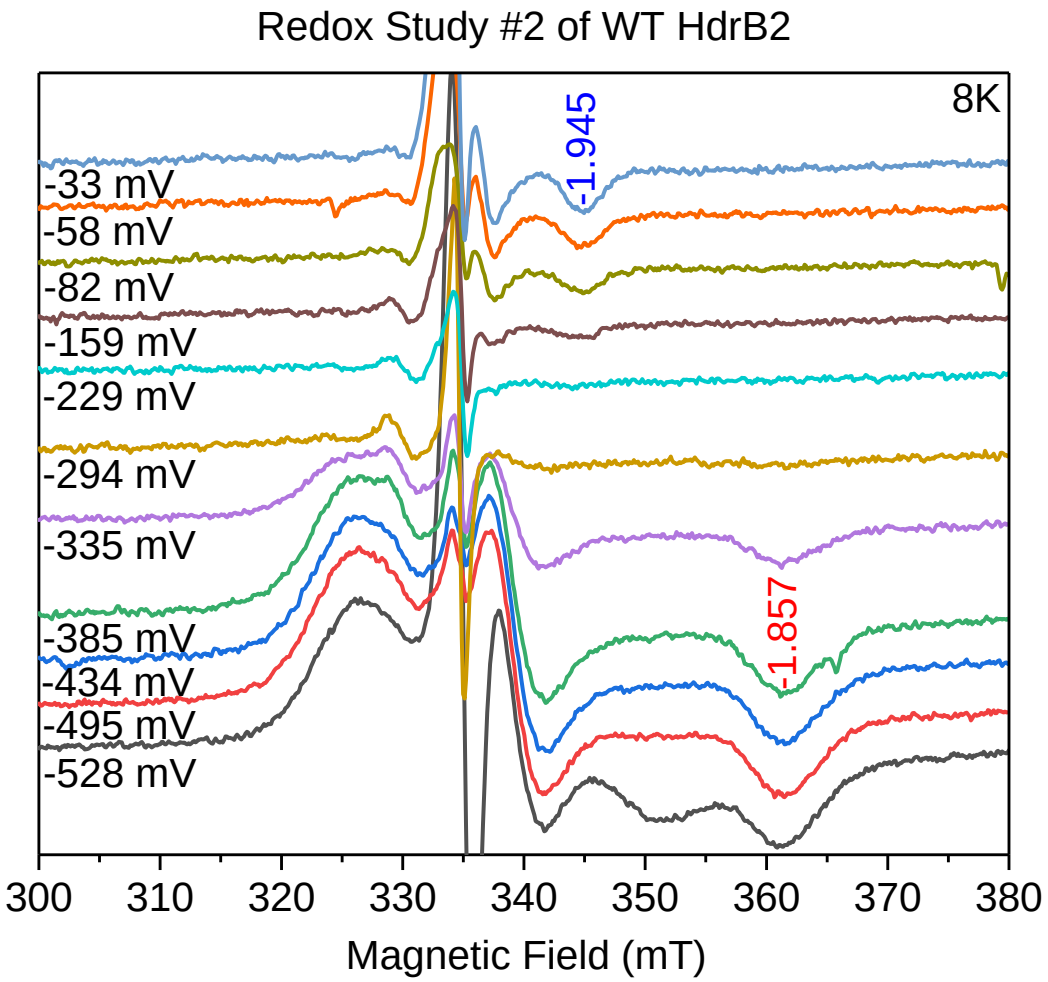

Figure A3.2: Selected EPR spectra overlay of the second redox titration performed on WT HdrB2.

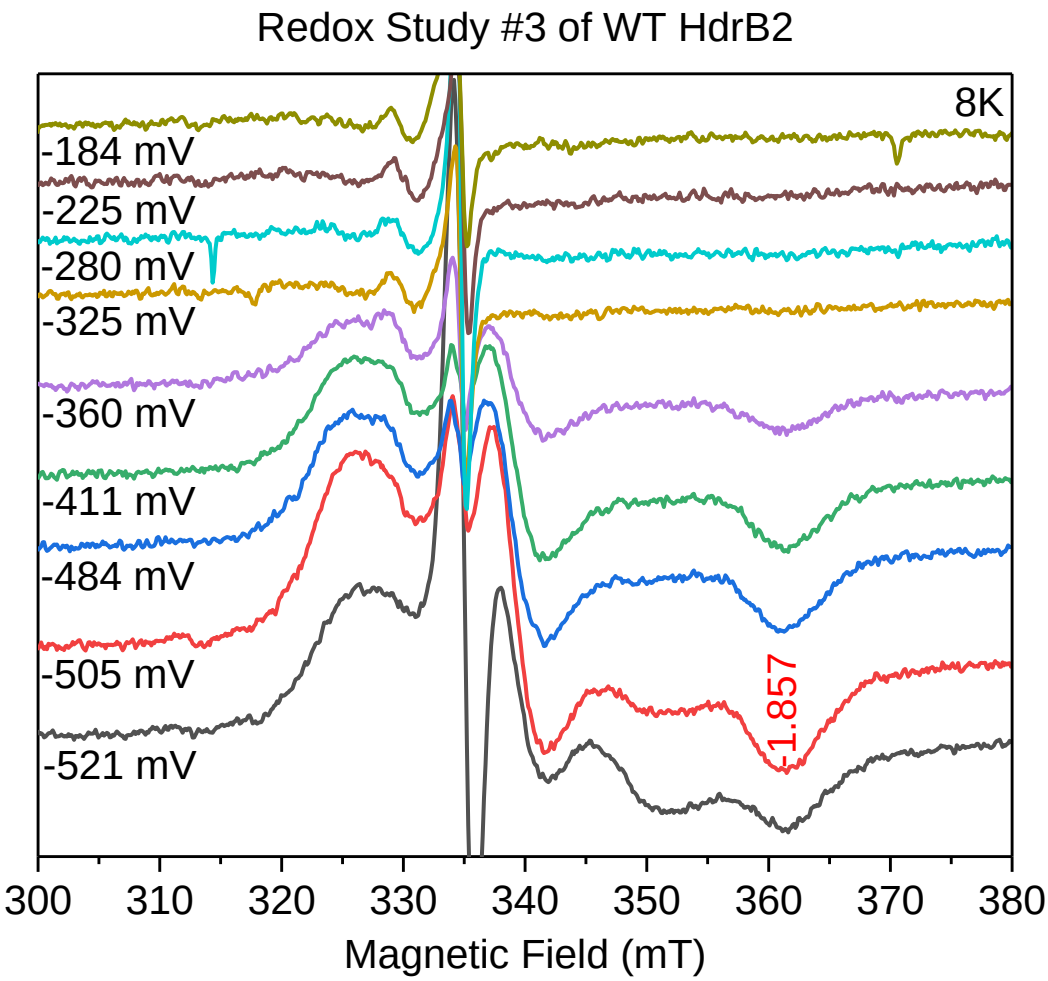

Figure A3.3: Selected EPR spectra overlay of the third redox titration performed on WT HdrB2.

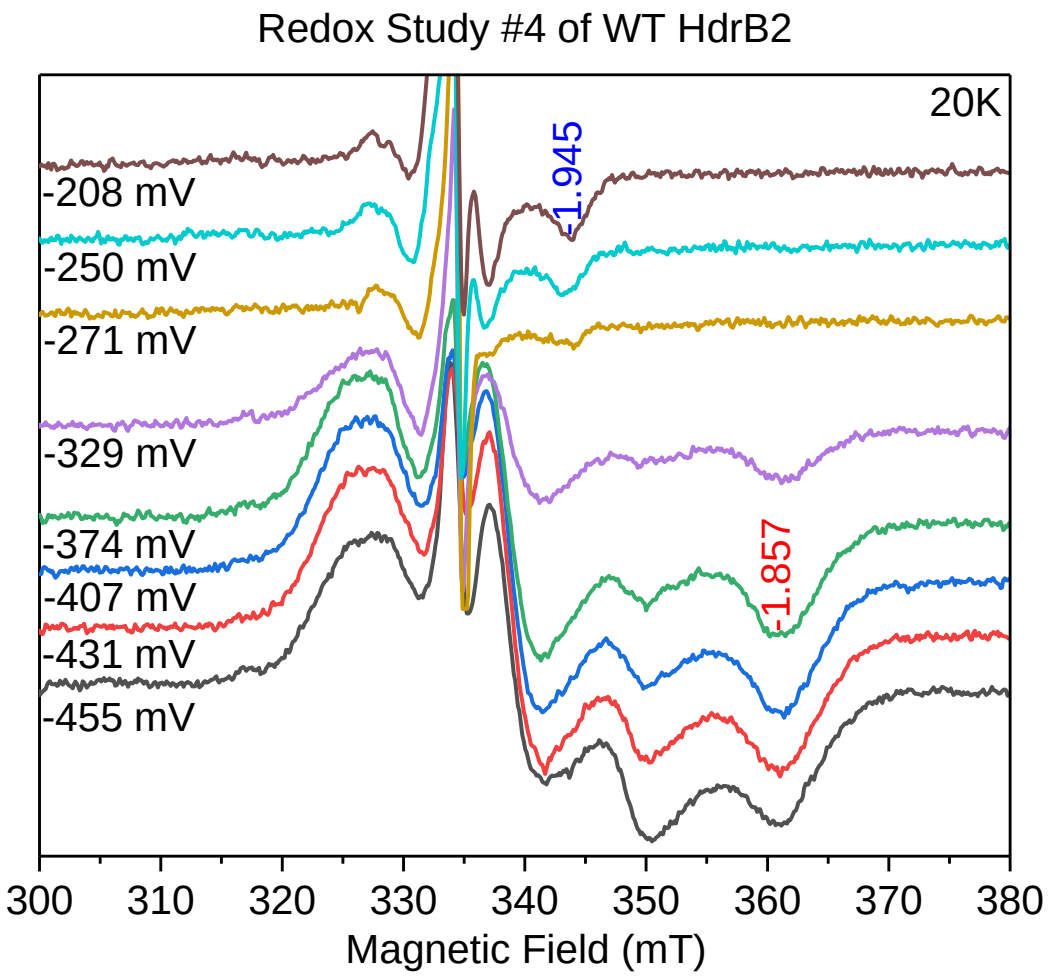

Figure A3.4: Selected EPR spectra overlay of the fourth redox titration performed on WT HdrB2.

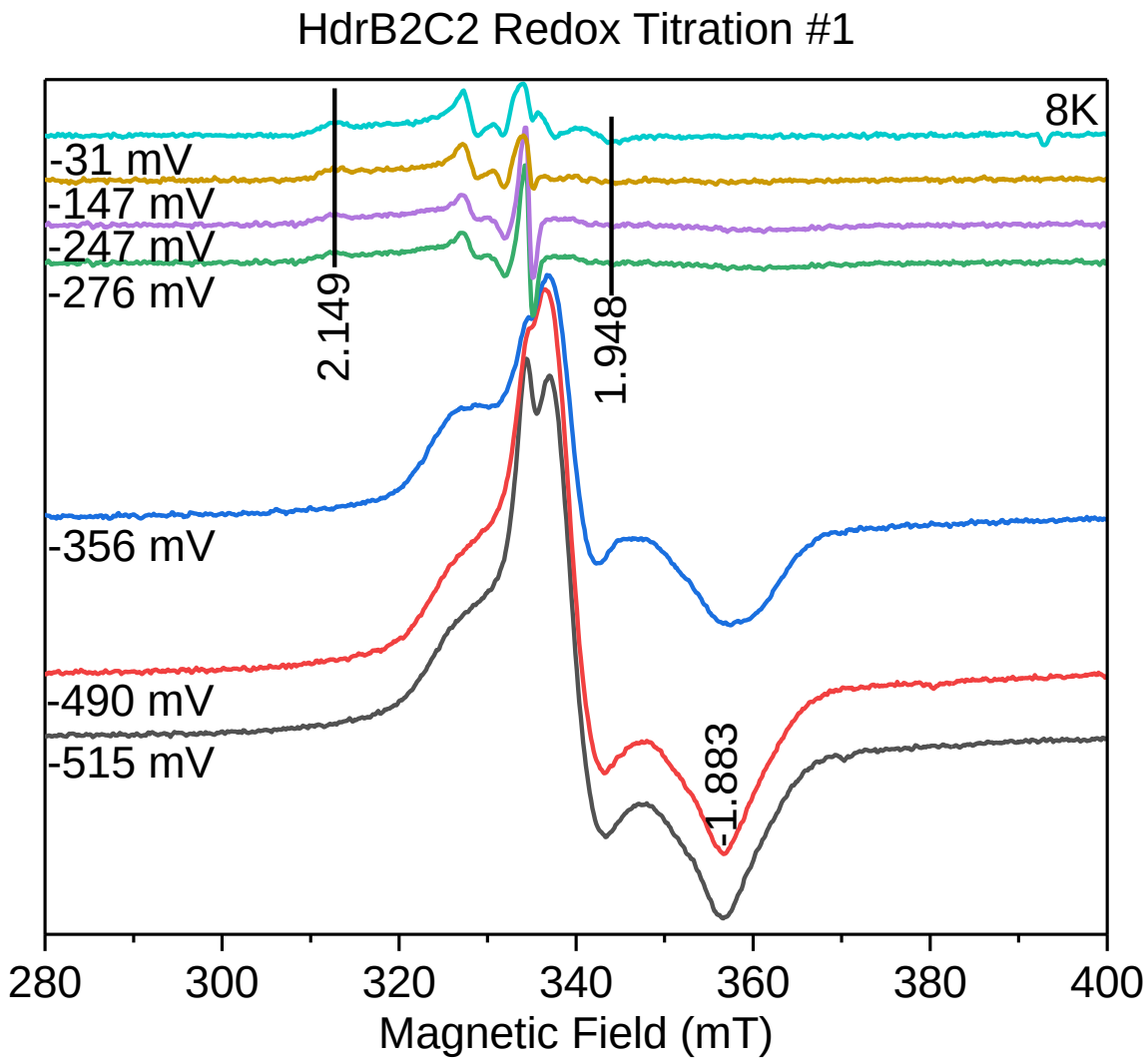

Figure A3.5: Selected EPR spectra overlay of the first redox titration performed on HdrB2C2. The graphs in the top corners represent the Nernst curves graphed to calculate the midpoint potentials of the g-values.

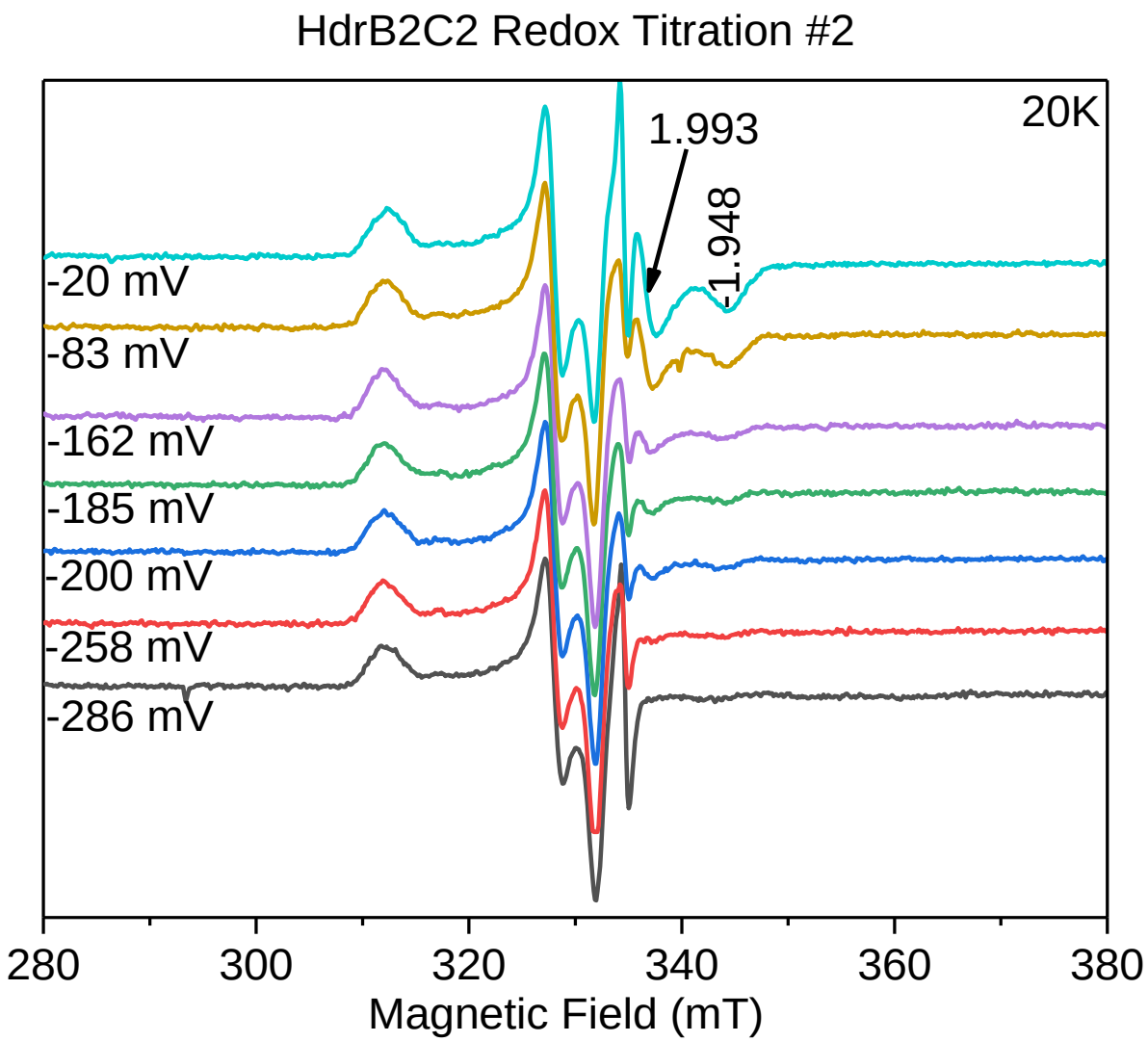

Figure A3.6: Selected EPR spectra overlay of the second redox titration performed on HdrB2C2.

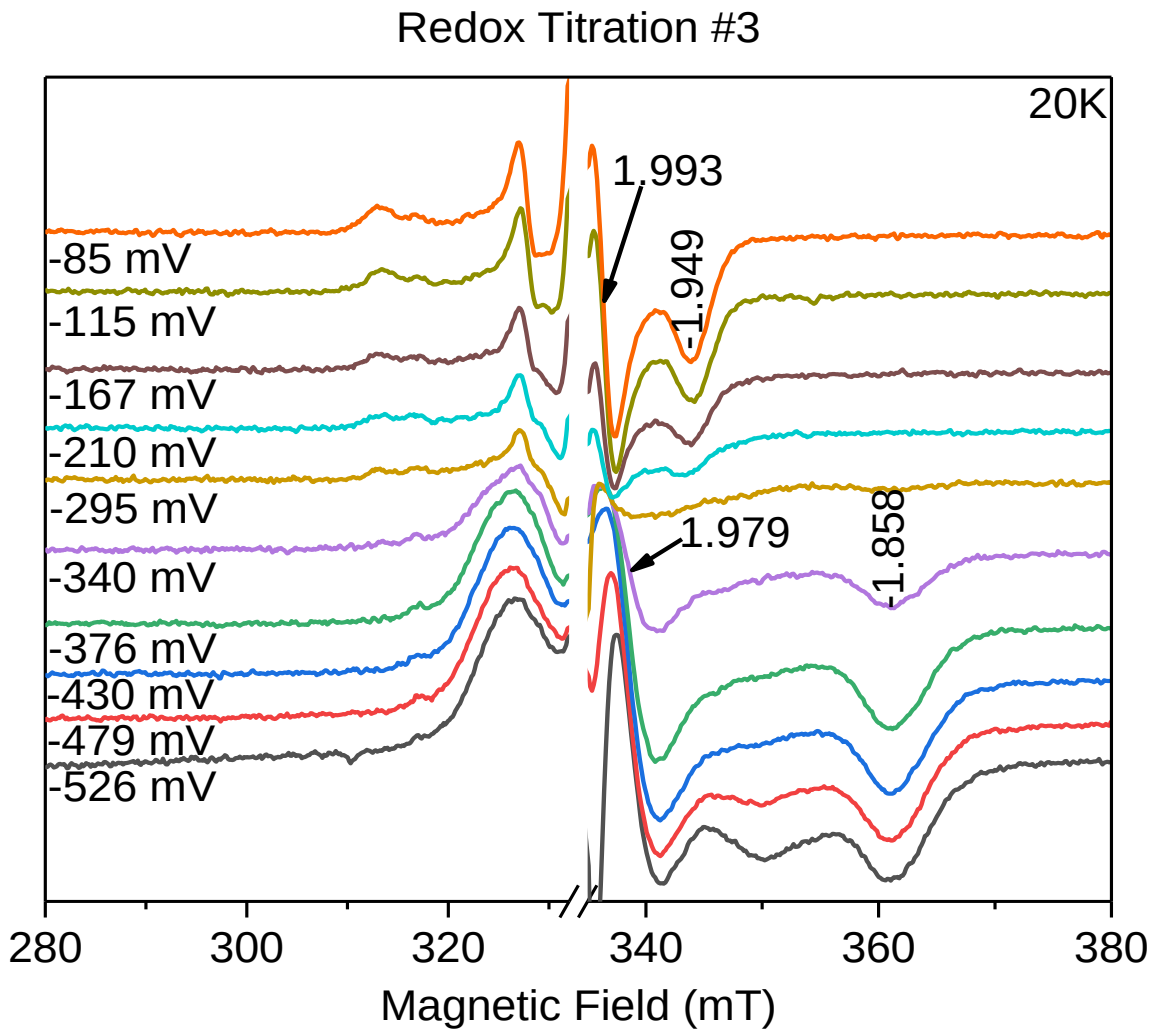

Figure A3.7: Selected EPR spectra overlay of the third redox titration performed on HdrB2C2.

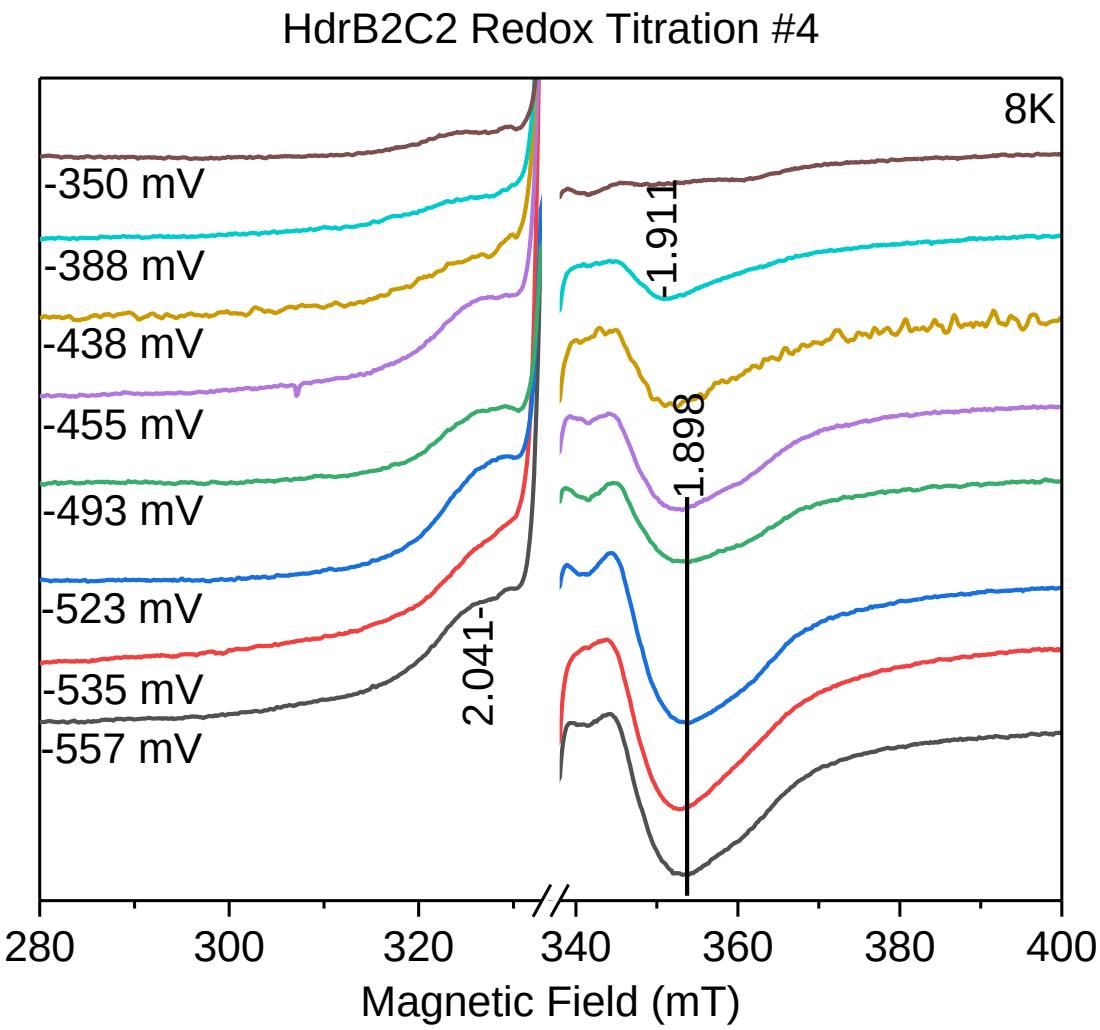

Figure A3.8: Selected EPR spectra overlay of the fourth redox titration performed on HdrB2C2.

References

(1) Rehder, D. (2014) Bioinorganic Chemistry. Oxford University Press.
(2) Enzmann, F., Mayer, F., Rother, M., and Holtmann, D. (2018) Methanogens: biochemical background and biotechnological applications. *AMB Express 8*.
(3) Forterre, P. (2013) The Common Ancestor of Archaea and Eukarya Was Not an Archaeon. *Archaea 2013*, 1–18.
(4) Wongnate, T., Sliwa, D., Ginovska, B., Smith, D., Wolf, M. W., Lehnert, N., Raugei, S., and Ragsdale, S. W. (2016) The radical mechanism of biological methane synthesis by methyl-coenzyme M reductase. *Science 352*, 953–958.
(5) Zheng, K., Ngo, P. D., Owens, V. L., Yang, X., and Mansoorabadi, S. O. (2016) The biosynthetic pathway of coenzyme F430 in methanogenic and methanotrophic archaea. *Science 354*, 339–342.
(6) Prakash, D., Wu, Y., Sang-Jin Suh, and Duin, E. C. (2014) Elucidating the Process of Activation of Methyl-Coenzyme M Reductase. *J. Bacteriol. 196*, 2491–2498.
(7) Abelson, J. N., and Simon, M. I. (2011) Methods in Enzymology First. Elsevier, Inc., Burlington, MA.
(8) Duin, E. C., Wagner, T., Shima, S., Prakash, D., Cronin, B., Yáñez-Ruiz, D. R., Duval, S., Rümbeli, R., Stemmler, R. T., and Thauer, R. K. (2016) Mode of action uncovered for the specific reduction of methane emissions from ruminants by the small molecule 3-nitrooxypropanol. *Proc. Natl. Acad. Sci. 113*, 6172–6177.
(9) (2006, November 23) MetaCyc Pathway: methanogenesis from H2 and CO2.
(10) Costa, K. C., Lie, T. J., Qin Xia, and Leigh, J. A. (2013) VhuD Facilitates Electron Flow from H2 or Formate to Heterodisulfide Reductase in Methanococcus maripaludis. *J. Bacteriol. 195*, 5160–5165.
(11) Thauer, R. K. (2012) The Wolfe cycle comes full circle. *Proc. Natl. Acad. Sci. U. S. A. 109*, 15084–15085.
(12) Rouault, T. A. (2012) Biogenesis of iron-sulfur clusters in mammalian cells: new insights and relevance to human disease. *Dis. Model. Mech. 5*, 155–164.
(13) Weil, J. A., and Bolton, J. R. (2007) Electron Paramagnetic Resonance Second. Wiley and Interscience: A John Wiley and Sons, Inc.
(14) Menghisteab Ghebreamlak, S. (2016, May 4) Iron-Sulfur Cluster-Containing Enzymes Involved in Isoprenoid Biosynthesis and Electron Bifurcation. Auburn University.
(15) Duin, E. C. Electron Paramagnetic Resonance Theory.
(16) Scott, R. A., and Lukehart, C. M. Applications of Physical Methods to Inorganic and Bioinorganic Chemistry. Wiley.
(17) Brudvig, G. (1995) Methods in Enzymology. Academic Press, Inc.
(18) Palmer, G. Methods in Enzymology.
(19) Crichton, R. (2008) Biological Inorganic Chemistry: An Introduction 1st ed. Elsevier.
(20) Johnson, M., and Smith, A. (2006) Encyclopedia of Inorganic Chemistry 2nd ed. Wiley.
(21) Crack, J. C., Green, J., Thomson, A. J., and Brun, N. E. L. (2014) Iron–Sulfur Clusters as Biological Sensors: The Chemistry of Reactions with Molecular Oxygen and Nitric Oxide. *Acc. Chem. Res. 47*, 3196–3205.

(22) Johnson, D. C., Dean, D. R., Smith, A. D., and Johnson, M. K. (2005) STRUCTURE, FUNCTION, AND FORMATION OF BIOLOGICAL IRON-SULFUR CLUSTERS. *Annu. Rev. Biochem. 74*, 247–281.
(23) Bak, D. W., and Elliott, S. J. (2014) Alternative FeS cluster ligands: tuning redox potentials and chemistry. *Curr. Opin. Chem. Biol. 19*, 50–58.
(24) Beinert, H. (2000) Iron-sulfur proteins: ancient structures, still full of surprises. *J. Biol. Inorg. Chem. 5*, 2–15.
(25) Cammack, R., Patil, D., and Fernandez, V. (1985) Electron-spin-resonance/electron-paramagnetic-resonance spectroscopy of iron-sulphur enzymes. *Bio. Soc. Trans. 13*, 572–578.
(26) Zwaan, J. W., Albracht, S. P. J., Fontijn, R. D., and Mul, P. (1987) On the anomalous temperature behaviour of the EPR signal of monovalent nickel in hydrogenase. *Eur. J. Biochem. 169*, 377–384.
(27) Duin, E. C. (1996, April 4) Exploring the Active-Site of Nickel-Hydrogenases. E. C. Slater Institute.
(28) Peters, J. W., Schut, G. J., Boyd, E. S., Mulder, D. W., Shepard, E. M., Broderick, J. B., King, P. W., and Adams, M. W. W. (2015) [FeFe]- and [NiFe]-hydrogenase diversity, mechanism, and maturation. *Biochim. Biophys. Acta BBA - Mol. Cell Res. 1853*, 1350–1369.
(29) Brugna-Guiral, M., Tron, P., Nitschke, W., Stetter, K.-O., Burlat, B., Guigliarelli, B., Bruschi, M., and Giudici-Orticoni, M. T. (2003) [NiFe] hydrogenases from the hyperthermophilic bacterium Aquifex aeolicus: properties, function, and phylogenetics. *Extremophiles 7*, 145–157.
(30) Stojanowic, A., Mander, G. J., Duin, E. C., and Hedderich, R. (2003) Physiological role of the F420-non-reducing hydrogenase (Mvh) from Methanothermobacter marburgensis. *Arch. Microbiol. 180*, 194–203.
(31) Meuer, J., Kuettner, H. C., Zhang, J. K., Hedderich, R., and Metcalf, W. W. (2002) Genetic analysis of the archaeon Methanosarcina barkeri Fusaro reveals a central role for Ech hydrogenase and ferredoxin in methanogenesis and carbon fixation. *Proc. Natl. Acad. Sci. 99*, 5632–5637.
(32) Ogata, H., Nishikawa, K., and Lubitz, W. (2015) Hydrogens detected by subatomic resolution protein crystallography in a [NiFe] hydrogenase. *Nature 520*, 571–574.
(33) Greene, B. L., Wu, C.-H., Vansuch, G. E., Adams, M. W. W., and Dyer, R. B. (2016) Proton Inventory and Dynamics in the Ni_a-S to Ni_a-C Transition of a [NiFe] Hydrogenase. *Biochemistry 55*, 1813–1825.
(34) Wagner, T., Koch, J., Ermler, U., and Shima, S. (2017) Methanogenic heterodisulfide reductase (HdrABC-MvhAGD) uses two noncubane [4Fe-4S] clusters for reduction. *Science 357*, 699–703.
(35) Garrett, R., and Grisham, C. (2010) Biochemistry, Fourth Edition. Brooks/Cole Cengage Learning.
(36) Nelson, N., and Ben-Shem, A. (2004) The complex architecture of oxygenic photosynthesis. *Nat. Rev. Mol. Cell Biol. 5*, 971–982.
(37) Rouvière, P. E., and Wolfe, R. S. (1988) Novel biochemistry of methanogenesis. *J. Biol. Chem. 263*, 7913–7916.
(38) Methanogens in Human Health and Disease - ajgsup20126a.pdf.
(39) Mitchell, P. (1975) The protonmotive Q cycle: a general formulation. *FEBS Lett. 59*, 137–139.
(40) Lehninger. (2008) Principles of Biochemistry, Fifth Edition. N. H. Freeman and Company.

(41) Buckel, W., and Thauer, R. K. (2013) Energy conservation via electron bifurcating ferredoxin reduction and proton/Na+ translocating ferredoxin oxidation. *BBA - Bioenerg. 1827*, 94–113.
(42) Herrmann, G., Jayamani, E., Mai, G., and Buckel, W. (2008) Energy Conservation via Electron-Transferring Flavoprotein in Anaerobic Bacteria. *J. Bacteriol. 190*, 784–791.
(43) Pal Chowdhury, N., Mowafy, A. M., Demmer, J. K., Upadhyay, V., Koelzer, S., Jayamani, E., Kahnt, J., Hornung, M., Demmer, U., Ermler, U., and Buckel, W. (2014) Studies on the Mechanism of Electron Bifurcation Catalyzed by Electron Transferring Flavoprotein (Etf) and Butyryl-CoA Dehydrogenase (Bcd) of Acidaminococcus fermentans. *J. Biol. Chem. 289*, 5145–5157.
(44) Sevier, C. S., Cuozzo, J. W., Vala, A., Åslund, F., and Kaiser, C. A. (2001) A flavoprotein oxidase defines a new endoplasmic reticulum pathway for biosynthetic disulphide bond formation. *Nat. Cell Biol. 3*, 874–882.
(45) Duin, E. C. Electron Bifurcation by Heterodisulfide Reductase. Auburn University.
(46) Nitschke, W., and Russell, M. J. (2012) Redox bifurcations: Mechanisms and importance to life now, and at its origin. *BioEssays 34*, 106–109.
(47) Milton, R. D., Ruth, J. C., Deutzmann, J. S., and Spormann, A. M. (2018) *Methanococcus maripaludis* Employs Three Functional Heterodisulfide Reductase Complexes for Flavin-Based Electron Bifurcation Using Hydrogen and Formate. *Biochemistry 57*, 4848–4857.
(48) Madadi-Kahkesh, S., Duin, E. C., Heim, S., Albracht, S. P. J., Johnson, M. K., and Hedderich, R. (2001) A paramagnetic species with unique EPR characteristics in the active site of heterodisulfide reductase from methanogenic archaea. *Eur. J. Biochem. 268*, 2566–2577.
(49) Duin, E. C., Madadi-Kahkesh, S., Hedderich, R., Clay, M. D., and Johnson, M. K. (2002) Heterodisulfide reductase from Methanothermobacter marburgensis contains an active-site [4Fe–4S] cluster that is directly involved in mediating heterodisulfide reduction. *Febs Lett. 512*, 263.
(50) Fielding, A. J., Parey, K., Ermler, U., Scheller, S., Jaun, B., and Bennati, M. (2013) Advanced electron paramagnetic resonance on the catalytic iron–sulfur cluster bound to the CCG domain of heterodisulfide reductase and succinate: quinone reductase. *JBIC J. Biol. Inorg. Chem. 18*, 905–915.
(51) Hamann, N., Mander, G., Shokes, J., Scott, R., Bennati, R., and Hedderich, R. (12885) A Cysteine-Rich CCG Domain Contains a Novel [4Fe-4S] Cluster Binding Motif As Deduced from Studies with Subunit B of Heterodisulfide Reductase from Methanothermobacter marburgensis. *Biochemistry 46*, 12875.
(52) Scheller, S., Goenrich, M., Boecher, R., Thauer, R. K., and Jaun, B. (2010) The key nickel enzyme of methanogenesis catalyses the anaerobic oxidation of methane. *Nature 465*, 606–608.
(53) (2002) Global Warming. *Am. Herit. Sci. Dict.* Houghton Mifflin Company.
(54) Climate Change: How Do We Know? NASA.
(55) (2014) Extreme Weather: Impacts of Climate Change. NRDC.
(56) Romm, J. NOAA Study Confirms Global Warming Speed Up is Imminent. Center for American Progress Action Fund.
(57) Prakash, D. (2014, December 13) Methyl-coenzyme M reductase: Elucidating the process of activation and study of the effect of the methanogensis inhibitor 3-nitrooxypropanol. Doctor of Philosophy, Auburn University, Auburn, AL.
(58) Gray, H. B., and Winkler, J. R. (2015) Hole hopping through tyrosine/tryptophan chains protects proteins from oxidative damage. *Proc. Natl. Acad. Sci. 112*, 10920–10925.
(59) Duin, E. C.; Bauer, C.; Jaun, B.; Hedderich, R. *Febs Lett.* **2003*, *538* (1-3), 81.

(60) Shokes, J. E., Duin, E. C., Bauer, C., Jaun, B., Hedderich, R., Koch, J., and Scott, R. A. (2005) Direct interaction of coenzyme M with the active-site Fe–S cluster of heterodisulfide reductase. *Febs Lett. 579*, 1741–1744.
(61) Setzke, E., Hedderich, R., Heiden, S., and Thauer, R. K. (1994) H2: heterodisulfide oxidoreductase complex from Methanobacterium thermoautotrophicum Composition and properties. *Eur. J. Biochem. 220*, 139–148.
(62) Noll, K., Donnelly, M., and Wolfe, R. S. (1987) Synthesis of 7-Mercaptoheptanoylthreonine Phosphate and Its Activity in the Methylcoenzyme M Methylreductase System. *J. Biol. Chem. 262*, 513–515.
(63) Steglich Esterfication. Organic Chemistry Portal.
(64) Singh, P., and Sinha, M. Determination of Residual Solvents in Bulk Drug and Formulations. *Am J PharmTech Res 3*, 289–295.
(65) Stojanowic, A., Mander, G. J., Duin, E. C., and Hedderich, R. (2003) Physiological role of the F 420 -non-reducing hydrogenase (Mvh) from Methanothermobacter marburgensis. *Arch. Microbiol. 180*, 194–203.
(66) Church, D. L., and Laishley, E. J. (1995) Reduction of Metronidazole by Hydrogenase from Clostridia. *Anaerobe 1*, 81–92.
(67) Yan, Z. (2016, December 13) HdrA and HdrB Expression Methods.
(68) Yan, Z., Wang, M., and Ferry, J. G. (2017) A Ferredoxin- and $F_{420}H_2$ -Dependent, Electron-Bifurcating, Heterodisulfide Reductase with Homologs in the Domains *Bacteria* and *Archaea*. *mBio* (Ruby, E. G., Ed.) *8*, e02285-16.
(69) Santiago Martinez, M. G. Results HdrB2 and variants.
(70) Lane, N., and Martin, W. F. (2012) The Origin of Membrane Bioenergetics. *Cell 151*, 1406–1416.